AFRL-SN-HS-TR-2000-008 (I)

Proceedings of the 1999 Antenna Applications Symposium
Volume I

Daniel H. Schaubert, et al.

University of Massachusetts
Department of Electrical and Computer Engineering
Amherst, MA 01003

September 1999

AIR FORCE RESEARCH LABORATORY
Sensors Directorate
80 Scott Dr
AIR FORCE MATERIEL COMMAND
Hanscom AFB, MA 01731-2909

Title of Report: PROCEEDINGS OF THE 1999 ANTENNA APPLICATIONS SYMPOSIUM

PUBLICATION REVIEW

This report has been reviewed and is approved for publication.

APPROVED:

ZACHARY O. WHITE
Contract Monitor
Antenna Technology Branch
Electromagnetics Technology Division

APPROVED:

Robert V. McGahan

ROBERT V. McGAHAN
Division Technical Advisor
Electromagnetics Technology Division

REPORT DOCUMENTATION PAGE

Form Approved
OMB No. 0704-0188

1. AGENCY USE ONLY *(Leave blank)*	2. REPORT DATE	3. REPORT TYPE AND DATES COVERED
	September 1999	Final Report

4. TITLE AND SUBTITLE
PROCEEDINGS OF THE 1999 ANTENNA APPLICATIONS SYMPOSIUM

5. FUNDING NUMBERS
C: F19628-99-C-0053
PE: 62702F
PR: 4600
TA: 01
WU: 01

6. AUTHOR(S)
Daniel H. Schaubert, et al

7. PERFORMING ORGANIZATION NAME(S) AND ADDRESS(ES)
University of Massachusetts
Department of Electrical & Computer Engineering
Amherst, MA 01003

8. PERFORMING ORGANIZATION REPORT NUMBER

9. SPONSORING/MONITORING AGENCY NAME(S) AND ADDRESS(ES)
Air Force Research Laboratory/SNHA
80 Scott Drive
Hanscom AFB, MA 01731-2909

10. SPONSORING/MONITORING AGENCY REPORT NUMBER
AFRL-SN-HS-TR-2000-008 (I)

11. SUPPLEMENTARY NOTES
SNHA Project Engineer: Zachary O. White, AFRL/SNHA, (781) 377-3191
Volume I contains pages 1-279
Volume II contains pages 280-538

12a. DISTRIBUTION AVAILABILITY STATEMENT
Approved for Public Release; Distribution Unlimited

12b. DISTRIBUTION CODE

13. ABSTRACT *(Maximum 200 words)*

The Proceedings of the 1999 Antenna Applications Symposium is a collection of state-of-the-art papers relating to phased array antennas, multibeam antennas, satellite antennas, microstrip antennas, reflector antennas, HF, VHF, UHF and various other antennas.

14. SUBJECT TERMS
Antennas, Microstrip, Multibeam Antenna, Satellite Antennas, Reflector, Array Antennas, Broadband Antennas, HF, VHF, UHF

15. NUMBER OF PAGES
290

16. PRICE CODE

17. SECURITY CLASSIFICATION OF REPORT	18. SECURITY CLASSIFICATION OF THIS PAGE	19. SECURITY CLASSIFICATION OF ABSTRACT	20. LIMITATION OF ABSTRACT
Unclassified	Unclassified	Unclassified	UL

Standard Form 298 (Rev. 2-89) (EG)
Prescribed by ANSI Std. 239.18
Designed using Perform Pro, WHS/DIOR, Oct 94

1999 ANTENNA APPLICATIONS SYMPOSIUM

*Not Included In This Volume

*Not Included In This Volume

Identifiers for Proceedings of Symposia

The USAF Antenna Research and Development Program

Year	Symp. No.	Identifier
1951	First	
1952	Second	C054 520
1953	Third	AD63794
1954	Fourth	AD63139
1955	Fifth	AD90397
1956	Sixth	AD114702
1957	Seventh	AD138500
1958	Eighth	AD301151
1959	Ninth	AD314721
1960	Tenth	AD244388 (Vol. 1) AD319613 (Vol. 2)
1961	Eleventh	AD669109 (Vol. 1) AD326549 (Vol. 2)
1962	Twelfth	AD287185 (Vol. 1) AD334484 (Vol. 2)
1963	Thirteenth	AD421483
1964	Fourteenth	AD609104
1965	Fifteenth	AD474238L
1966	Sixteenth	AD800524L
1967	Seventeenth	AD822894L
1968	Eighteenth	AD846427L
1969	Nineteenth	AD860812L
1970	Twentieth	AD875973L
1971	Twenty-First	AD888641L
1972	Twenty-Second	AD904360L
1973	Twenty-Third	AD914238L

Antenna Applications Symposium

		TR#	ADA#
1977	First	None	955413
1978	Second	None	955416
1979	Third	_____	077167
1980	Fourth	_____	205907
1981	Fifth	_____	205816
1982	Sixth	_____	129356
1983	Seventh	_____	142003; 142754
1984	Eighth	85-14	153257; 153258
1985	Ninth	85-242	166754; 165535
1986	Tenth	87-10	181537; 181536
1987	Eleventh	88-160	206705; 206704
1988	Twelfth	89-121	213815; 211396
1989	Thirteenth	90-42	226022; 226021
1990	Fourteenth	91-156	237056; 237057
1991	Fifteenth	92-42	253681; 253682
1992	Sixteenth	93-119	268167; 266916
1993	Seventeenth	94-20	277202; 277203
1994	Eighteenth	95-47	293258; 293259
1995	Nineteenth	96-100	309715; 309723
1996	Twentieth	97-189	341737
1997	Twenty First		
1998	Twenty Second	1999-86	
1999	Twenty Third		

INITIAL BISTATIC MEASUREMENTS OF ELECTROMAGNETIC PROPAGATION IN AN ENCLOSED SHIP ENVIRONMENT

E. L. Mokole, M. Parent, J. Valenzi, E. Tomas, B. T. Gold, T. T. Street
Naval Research Laboratory
4555 Overlook Avenue, SW
Washington, DC 20375

S. N. Samaddar
SFA, Inc.
1401 McCormick Street
Largo, MD 20774

Understanding the propagation of RF energy in confined naval shipboard environments is extremely important to the operability and effectiveness of communication systems used by the Navy. It is known that single-frequency communication systems suffer from multipath interference that can render them ineffective in confined spaces. Spread spectrum and frequency-hopping systems, currently used in wireless local area networks (LANs), have been shown to operate effectively in confined shipboard environments; however the transfer characteristics of these signals relative to bulkheads, watertight doors, ducts, mask cable transits, compartment penetrations and obstructions, and steel deckplates are not fully understood. To address these issues for systems between 800 MHz and 3 GHz, a broadband bistatic measurement system was developed, and initial measurements were taken on the ex-USS SHADWELL (23-25 February 1998) in Mobile AL. In excess of 100 sets of data were collected for various open/closed door configurations on three levels of the ex-USS SHADWELL. The measurement system and the measurements will be discussed. Initial observations indicate that received power levels over reasonably long propagation distances were sufficient to ensure communication, even when all passageway doors were closed.

1. Introduction

Understanding the propagation of RF energy in confined naval shipboard environments is extremely important to the operability and effectiveness of communication systems used by the Navy. It is known that single-frequency communication systems suffer from multipath interference that can render them ineffective in confined spaces. Spread spectrum and frequency-hopping systems, currently used in wireless local area networks (LANs), have been shown to operate effectively in confined shipboard environments; however the transfer characteristics of these signals with respect to steel bulkheads, watertight doors, ducts, mask cable transits (MCTs), and steel deckplates are not fully understood. To understand and characterize the underlying radiation and propagation mechanisms of signal sources at frequencies between 800 MHz and 3 GHz in confined ship spaces, a broadband bistatic measurement system was developed. On completion of the initial measurement system, data were taken on the USS BARRY (28 January 1998) in Washington DC to help refine the system and to understand the measurement process. Then the improved system was transported to the ex-USS SHADWELL, the Naval Research Laboratory's Advanced Fire Research Vessel in Mobile AL,[1] where data were collected (23-25 February 1998) to ascertain how a ship's structure affects signal propagation over the aforementioned frequencies. The ex-USS SHADWELL is beached on Little Sand Island in Mobile, Alabama, and serves as a test vessel for the U. S. Navy's Systems Commands, under the control of the Navy Technology Center for Safety and Survivability (NTCSS) at the Naval Research Laboratory (NRL).[2]

Because this work is sponsored by the program on Damage Control - Automation for Reduced Manning (DC-ARM) of the NTCSS, an underlying purpose of this study is to determine the limitations of shipboard emergency communications, especially during fires when compartment doors are closed. To quantify the distribution of energy from a source in ship compartments, data were sampled and received power levels were collected for various open/closed door configurations, for selected locations of the transmitter and receiver on three levels of the ex-USS SHADWELL, and for different signal polarizations. Each data set consisted of 23 values of received power at equally spaced frequencies between 800 MHz and 3 GHz, inclusive.

Section 2 discusses some of the problems and issues associated with RF communication that have been experienced on Navy ships and provides some historical background on RF propagation in confined ship spaces. In Section 3, the bistatic measurement system is described. Then the measurement methodology on the ex-USS SHADWELL is discussed in Section 4, and the data analysis and associated theory is addressed in Section 5. In particular, the underlying electromagnetic theory for the experiment is summarized, and an

algorithm is provided for extracting the effective propagation loss from the measured received power at each of the 23 transmission frequencies. The propagation-loss parameter is chosen because it is essentially independent of the measurement system. Consequently, the results should be applicable for arbitrary measurement systems. In the final section, the observations of test results are summarized.

2. Shipboard Communication Background

Ships of the future will require vast, state-of-the-art, communication networks that are capable of integrating a multitude of communication architectures with numerous communication sources and technologies to ensure communication capabilities at any time throughout the ship. These systems must have the ability to transfer vast amounts of sensor data related to a ship's condition, damage control operation, and C^3 functions. The systems must also be survivable in the event of damage from casualty or conflict, must be resistant to hostile electronic attack and to electromagnetic interference (EMI) from other ownship radio-frequency (RF) sources, and must not cause EMI problems for other devices on the ship. Communication systems can be programmed to perform operational testing to determine current coverage, to reroute data as necessary to reestablish coverage, and to reprogram or reconfigure itself to continue operation by shedding non-functional and/or destroyed segments to recover communication capabilities. Specifically, wireless RF communications can provide a flexibility not offered by wired and cabled systems when interruptions occur from damage to wire and fiber-optic conductors. With the implementation of spread-spectrum direct-sequence and frequency-hopping systems, wireless RF LANs have become leading candidates for use in the highly multipath environment of confined shipboard spaces. Although these RF communication systems cannot match the data throughput available in wired systems, they currently can achieve rates in excess of 10 Mb/s, with large throughput improvements on the horizon. However, the commercial-off-the-shelf (COTS) wireless LANs that are currently being deployed on Navy ships are susceptible to eavesdropping, electronic attack (EA), and ownship EMI. The impact of these vulnerabilities could be substantial.

Clearly, this propagation problem has ramifications for a variety of competing shipboard interests: communications, radar, jamming, and EMI. Unfortunately, after undertaking an extensive search of the literature, very little characterization and documentation exists on the propagation of RF signals in confined ship spaces. Although current communication systems apparently work well in confined ship spaces for many situations and for a broad range of frequencies, it is not known exactly how or why this is true. In fact, it is unclear

whether signals from different sources in this environment can be discriminated. Since communication systems will share the RF spectrum with devices like radars and electrically driven machinery, one must know when a communication system will work and when problems can be expected.

In a related area, much speculation exists on whether ion-producing fires enhance, attenuate, or do not affect RF signals. It is well known that ion production in fires is a function of fuel type.[3-5] In particular, no ionization occurs for alcohol-based fuels; whereas heptane and diesel fuels induce ionization near the flame. Data exist which support the contention that an RF signal can be enhanced by traveling through an ionized medium. Specifically, trans-ionospheric data shows that an RF signal is enhanced on the line-of-sight path through the ionosphere.[6] However, it is unclear whether this phenomenon is significant for shipboard fires, because the ionization levels and the thickness of the ionized medium should be much less than that of the ionosphere. In fact, one might well argue that the signal attenuation from soot, smoke, steam, and water mist is more important than the flame ionization. Questions regarding possible interruptions or enhancements caused by ion production, smoke, soot, steam, and water mist from large-scale and extremely hot fires to RF communications need to be answered, especially if these systems are to be used in support of damage control operations.

The propagation of electromagnetic (EM) waves below deck aboard Naval vessels has been a concern of shipboard personnel and test teams for many years. The most common application is the use of hand-held walkie talkies between personnel situated in different locations of a ship. The cables and piping which pass through a ship's space provide excellent conduits for RF energy to pass from one location to another. Despite allowing good communication, these propagation channels have apparently lead to EMI problems on ships. For example, the USS OAK HILL (LSD 51) was surveyed for below-decks EMI from 23 September 1996 through 4 October 1996 as part of a Shipboard Electromagnetic Compatibility Improvement Program (SEMCIP). Mild-to-severe EMI was experienced by COTS PC monitors and televisions from portable VHF and UHF transceivers, and the AN/SPS-49 radar (851 MHz - 942 MHz) caused severe EMI to a weather-deck phone and mild EMI to pilot-house phones.[7]

EMI from shipboard portable transceivers are known to cause degradation in the performance of other shipboard systems. A case in point is the measured EMI (27-28 August 1997) from the AN/SRC-55 (XN-1) HYDRA UHF communication system on the USS PONCE (LPD 15) to the SPS-40E, a two-dimensional air-search radar aboard amphibious ships. HYDRA operates from 406 MHz through 420 MHz, with channels separated by 25 kHz. The Radar Division of the NRL (Code 5300) was tasked by SPAWAR Systems Center, Charleston Detachment (Code 514), to determine the severity of the EMI on the SPS-40E and to

recommend appropriate filters to remedy the EMI effects. The levels of EMI were quantified for each channel, and a design for a bandpass filter was developed to correct the problem.[8] Testing the filter is scheduled for the summer of 1999. Moreover, to estimate the degradation of the performance of an electronic system by EMI, Code 5300 of the NRL has developed the Advanced Technology Chamber (ATC) to simulate the RF modes of propagation both on a ship's topside and in a shipboard compartment. The ATC is a completely enclosed, welded, aluminum chamber (2.73m x 4.64m x 5.33m) with access panels on its bulkheads that can be modified to feed cables or other objects into its interior. This chamber provides an accurate model of a tightly sealed ship compartment in a controlled laboratory setting. In fact, it is capable of providing 110 dB of effective shielding; whereas typical compartments on ships attain roughly 20 dB of shielding effectiveness. The chamber is equipped with its own measurement system consisting of a LabVIEW interface, a scalar network analyzer, electric-field intensity probes, a frequency synthesizer, and power amplifiers. The ATC is capable of modeling the effects of wireless communications inside the hull of a ship for frequencies between 200 MHz and 40 GHz.[9]

Over the last four years, the NTCSS has sponsored a limited number of tests of wireless, spread-spectrum, RF LANs on the ex-USS SHADWELL to determine the capabilities and limitations of such systems when they are operated in the highly multipath environment of confined ship spaces.[10-12] During these tests, it was observed that the expected major interruption of RF communications by the ship's steel structure (bulkheads, overheads, and decks), closed watertight doors, and compartment penetrations/obstructions did not occur. An example of a confined ship space is the photograph of the Main Deck of the ex-USS SHADWELL in Fig.1. Instead, the dominant effect appeared to be an approximate 10-dB signal loss for each closed watertight door and/or bulkhead. It was therefore determined that an understanding of the basic propagation characteristics of signals onboard ships is necessary to understand signal transmission in this environment, which lead to the work that is discussed in this paper.

As noted in the introduction, preliminary investigations were conducted on the ex-USS SHADWELL (23-25 February 1998) to investigate the contributions from the various modes of transfer of RF signals in a shipboard environment: (1) distributed cable networks, (2) watertight door seals, (3) compartment penetrations/obstructions (MCTs, ducts, gratings, vents, etc.), (4) the waveguide-like nature of ship compartments and passageways, (5) the coaxial transmission behavior of shielded cable in compartments and passageways, and (6) the effects of multipath. These tests determined the necessary measurement equipment and verified the ship-compartment geometries and types of tests that are required to investigate the modes of transfer of RF signals in confined ship spaces properly.

The preliminary findings are presented in this paper and are partially documented in an NRL Letter Report.[13]

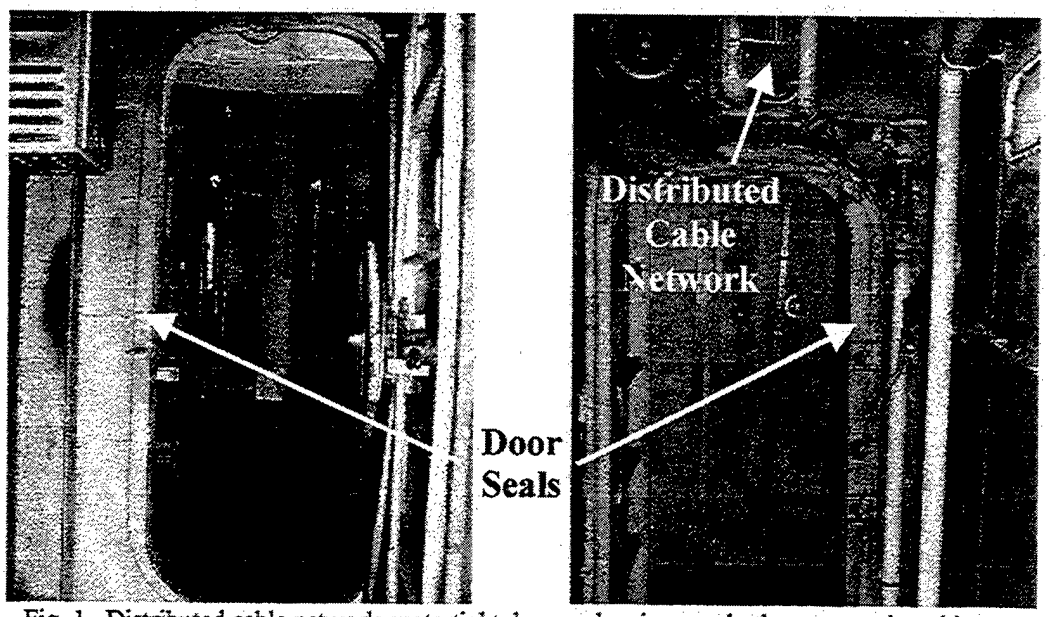

Fig. 1. Distributed cable network, watertight door seals, pipes, and other penetrating objects on the Main Deck of the ex-USS SHADWELL.

Concurrent with the RF propagation testing on the ex-USS SHADWELL, two other measurement campaigns were conducted. Lucent Technologies took CW measurements at 2.48 GHz to determine the performance of their Modulated Backscatter (MBS) radios for ambient and fire environments, and the results were excellent. The other group (Penn State - ARL/INVOCON) tested the effects of a compartment fire on four RF spread-spectrum communications systems: two over the interval [902 MHz,928 MHz], one at 2.4 GHz, and one at 5.6 GHz.

3. Bistatic Measurement System

The bistatic measurement system used in this study consists of an HP8592L spectrum analyzer, an HP83752A synthesized signal source (10 MHz to 20 GHz), an HP8347A RF amplifier (100 kHz to 3 GHz), a broadband disc-cone transmitting antenna, a laptop computer, a broadband batwing receiving dipole,

and a small coaxially tipped receiving probe. The system is depicted by the block diagram in Fig.2. Both the disc-cone (Fig.3) and the batwing dipole (Fig.4) can be repositioned to have a dual-polarization capability. The signal source is stepped in 100-MHz frequency increments from 800 MHz through 3000 MHz, inclusive, so that the transmitting antenna emits a stepped CW signal at the indicated 23 frequencies. The broadband disc-cone, which also covers 800 MHz to 3000 MHz, is attached to the signal source to form the transmitter, and the receiving antennas are connected to the spectrum analyzer to form the receiving system. The batwing dipole is the receiving antenna for most measurements, while the smaller coaxial probe (Fig.4) is used to measure the electric field intensities very close to an object's surface, such as near cable networks and hard-to-reach places. The spectrum analyzer is controlled through an HPIB interface that is connected to the laptop computer and measures the absolute signal-amplitude levels. The computer then transfers the data from the spectrum analyzer to a file. Measurement software was developed and was integrated with the receiving system through the LabVIEW interface.

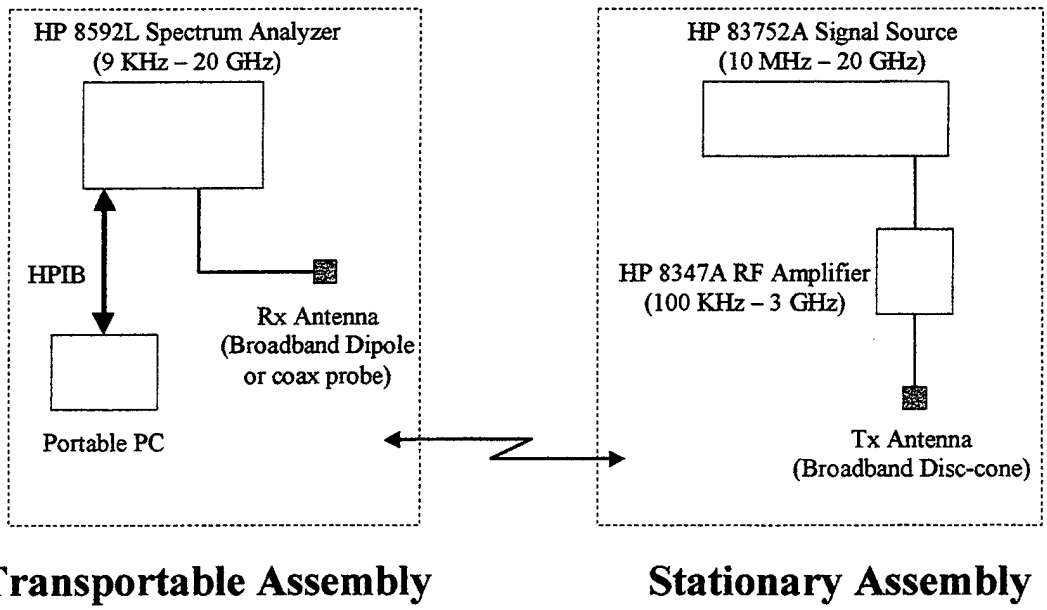

Fig.2. Block diagram of bistatic measurement system.

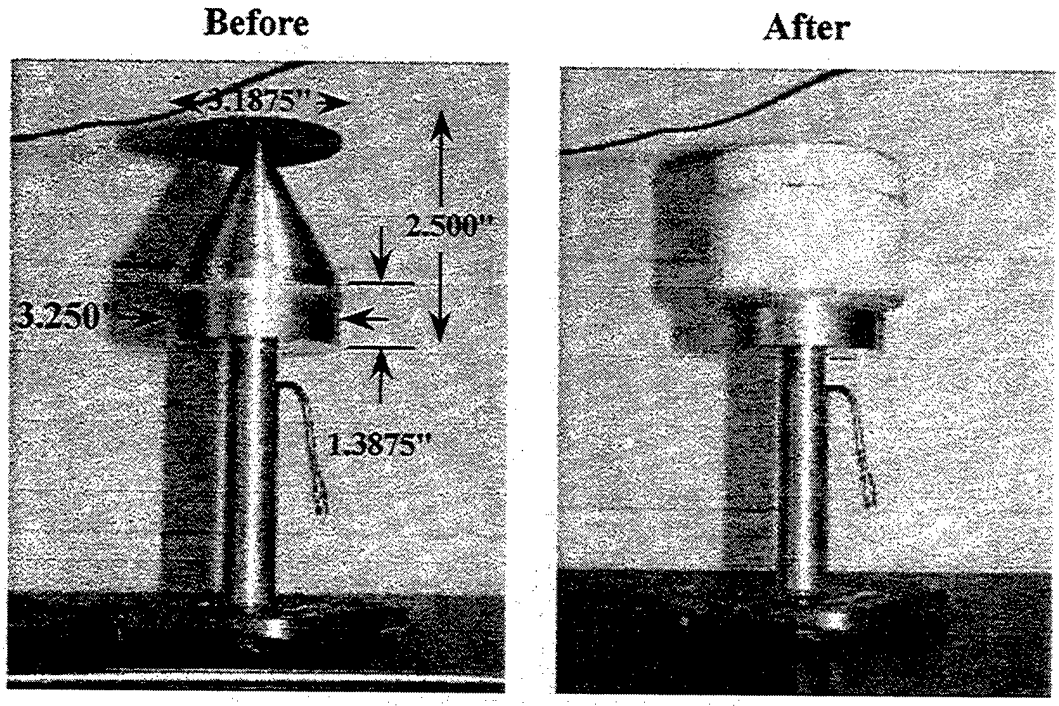

Fig.3. Broadband disc-cone transmitting antenna with and without a protective styrofoam cover.

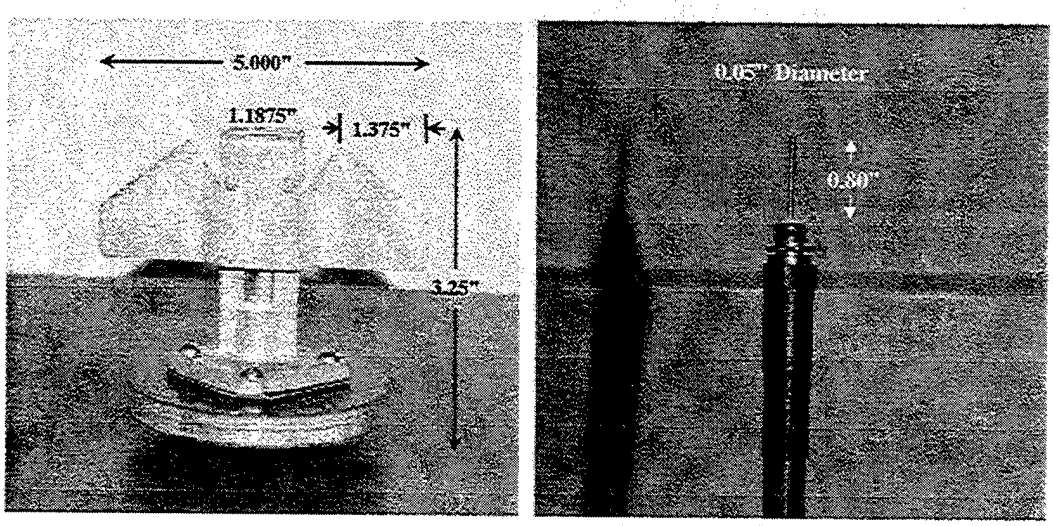

Fig.4. Receiving antennas: broadband batwing dipole on left and coaxially tipped probe on left.

The transmitting antenna is mounted on a tripod so that the center of the radiator is 5 ft above the ground. For this system, the disc-cone is a composite structure that consists of a truncated half-cone, a cylinder, and a circular disk (Fig.3.). The circular disk has a 3.1875-in diameter and sits atop the apex of the half-cone portion of the structure. The height and diameter of the half-cone are 1.1125 in and 3.250 in, respectively. The cylindrical portion has height and diameter of 1.3875 in and 3.250 in, respectively, and lies below the half-cone. As Fig.3 indicates, most of the antenna is protected by an outer layer of styrofoam. General properties of the disc-cone antenna are found in [14].

From Fig.4, one can see how the batwing dipole[15] got its name. This receiving antenna is mounted on a 7.5-ft rectangular post, with notches at one-inch intervals for different placements of the antenna. Of course, this antenna has a favored polarization. To receive vertically, the straight edge of the dipole is parallel to the post as shown in Fig.5. For horizontally polarized reception, the antenna is oriented so that the straight edge is parallel to the floor and perpendicular to the post. Fig.5 also displays the laptop computer and spectrum analyzer, which are mounted on a two-wheel dolly for portability. The watertight door in Fig.5, labeled 1-28-1 in Fig.6, opens into compartment $D_{1,3}$, and the view is from compartment $D_{1,2}$. This door figures prominently in subsequent discussion of the data. For places that are inaccessible to the batwing dipole, a probe is connected to a coaxial cable. The probe is 1-ft long with a tip that is a 0.8-in long and has a 0.05-in diameter.

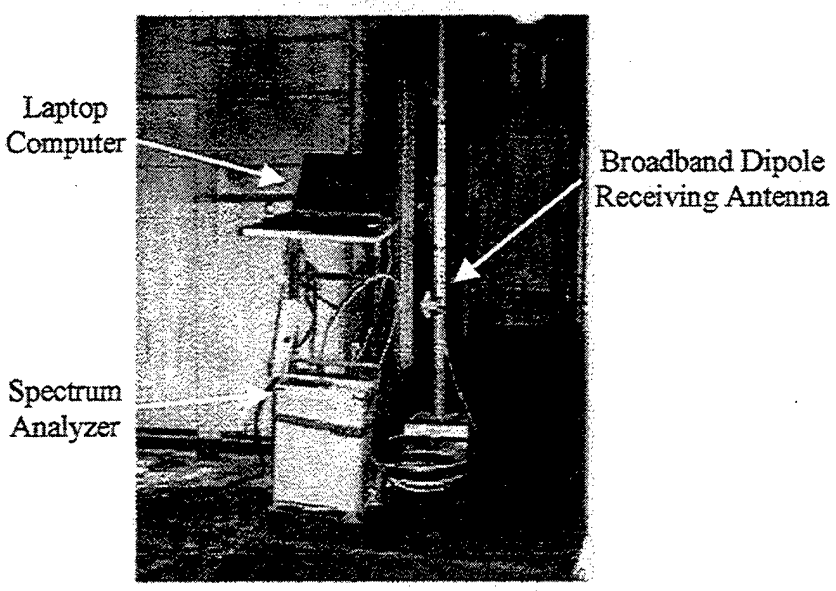

Fig.5. Integrated bistatic measurement system on the Main Deck of the ex-USS SHADWELL.

Because the transmitter and receiver are not locked to a reference, the measurement is not coherent. The signal source in the transmitter executes a fast sweep through the designated frequency interval (800 MHz to 3 GHz) about 5 times in a 7-second time frame. Simultaneously, the spectrum analyzer also samples the received signal spectrum by sweeping frequency. To register a received signal at a given frequency, the sweep windows for both devices must overlap, which takes approximately 7 seconds. Thus the total time for acquiring the received signals at a specified number of frequencies exceeds seven times the number of frequencies. This lack of synchronization necessitated a tradeoff between the number of frequencies and the total acquisition time for a given measurement configuration. Consequently, the number of frequencies was restricted to 23, because of the lengthy acquisition time. Collecting the received signals at the 23 specified frequencies took approximately 3 minutes.

4. SHADWELL Geometry and Test Configurations

For the SHADWELL measurements of 23-25 February 1998, 113 sets of data were collected. All but two of the data sets correspond to specific placements of the receiving and transmitting antennas, and each data set consists of twenty-three values of the received power in dBm, one for each frequency. The measurements were taken in the forward half of the 01, 1, and 2 Levels of the SHADWELL between Frame 13 and Frame 29. The separation between adjacent frames is 4 feet, where the frame number appears at the bottom of Fig.6. In Navy nomenclature, the 1 Level is called the Main Deck, the 01 Level is the deck above the Main Deck, and the 2 Level is the deck below the Main Deck. To keep track of the data, Levels 1, 2, and 01 are identified with Decks 1, 2, and 3, respectively. The compartments of each deck are designated $D_{L,n}$, which is compartment n on Deck L for L = 1,2,3.

For most of the measurements, the transmitter was placed at one location (Compartment $D_{1,3}$ of Fig.6) on the Main Deck (1 Level), and the receiver was moved about the three levels, but was predominantly on the Main Deck. However, for seven of the measurements, the receiver was placed near the starboard stairwell halfway between Frames 28 and 29 of the Main Deck, and the transmitter was moved aft (rearward) along the SHADWELL's centerline from the forecastle area toward the receiving antenna. The locations of all measurements on the Main Deck are indicated by the large solid dots in Fig.6. The solid triangles in this figure note the locations of the receiving dipole and probe positions, and the solid circles with '**T**' above them correspond to transmitter positions. For most of the measurements, the transmitting antenna is located in $D_{1,3}$.

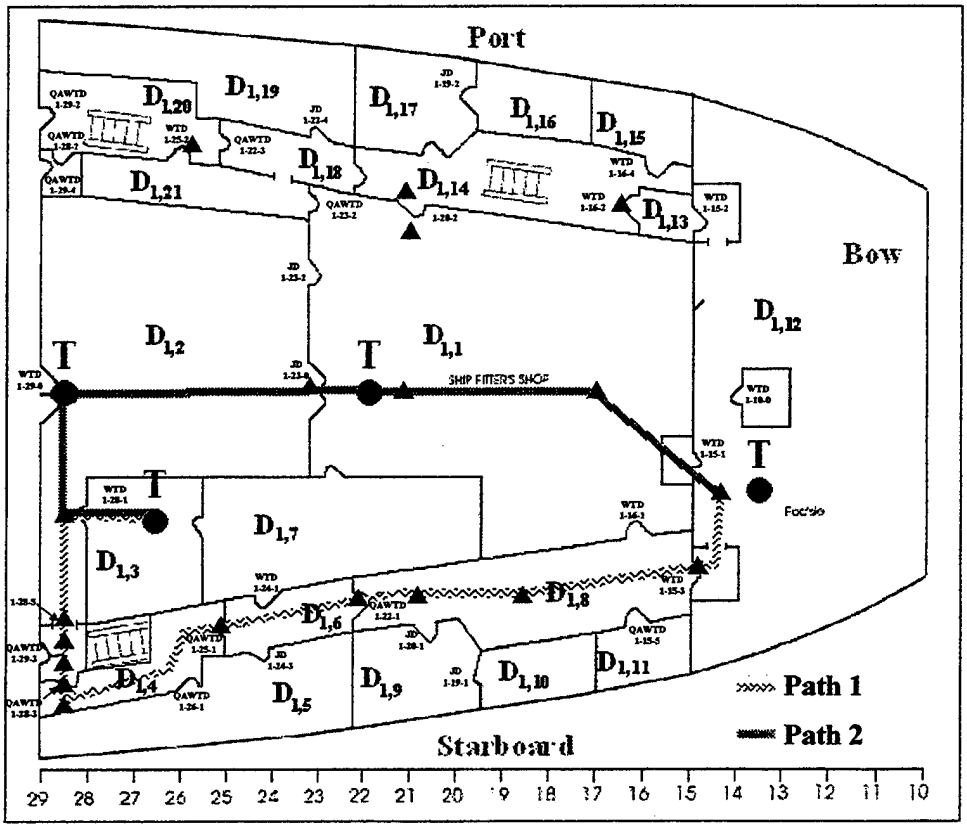

Fig. 6. Locations of receiver (triangles) and transmitter (circles) positions in compartments ($D_{1,n}$) on the 1 Level of the ex-USS SHADWELL.

Essentially, seven classes of data were collected: (A) five classes with the transmitter at a fixed position in $D_{1,3}$ and (B) two classes with the receiver at a fixed position in the foyer of $D_{1,2}$ at the head of the starboard stairwell to the 2 Level (Fig.6). The various classes of A and B are:

A1. Fifty-five measurements at receiver points just outside $D_{1,3}$ around door 1-28-1 in the corridor of $D_{1,2}$ to determine if energy escapes through the door seal;

A2. Thirty measurements in the corridor consisting of $D_{1,2}$, $D_{1,4}$, $D_{1,6}$, and $D_{1,8}$ to determine if energy propagates along the corridor of $D_{1,2}$ outside $D_{1,3}$ and through the starboard corridor. These measurements are also intended to determine whether energy propagates along the cables that pass through the MCTs in the starboard passageway;

A3. Five measurements in the forecastle ($D_{1,12}$) with doors 1-15-1 and 1-15-3 in appropriate open-closed configurations to determine if the transmitted signal propagates through the large central area en route to the forecastle ($D_{1,3} \rightarrow D_{1,2} \rightarrow D_{1,1} \rightarrow D_{1,12}$) or through the slanted L-shaped corridor ($D_{1,3} \rightarrow D_{1,2} \rightarrow D_{1,4} \rightarrow D_{1,6} \rightarrow D_{1,8} \rightarrow D_{1,12}$) to the forecastle;

A4. Ten measurements in the large central area and the port passageway to determine signal levels in the port passageway;

A5. Four measurements on the 01 and 2 Levels near the starboard stairwells to test inter-deck propagation;

B1. Five measurements with the transmitter in the forecastle to test propagation along different paths;

B2. Two measurements with the transmitter moving along the centerline of $D_{1,1}$ and $D_{1,2}$ toward the receiver.

The final two data sets are measurements of the background noise on the SHADWELL and the received power when the transmitter and the receiver are connected directly.

5. Theory and Results

5.1 Analysis

Instead of directly analyzing the raw data, which are received power readings in dBm at the twenty-three frequencies for the 111 locations of interest, the effective propagation loss L_{SP} is studied because it is essentially independent of the measurement system, which follows from Eq. (1). Therefore, the results should be applicable to any radar, communication, or surveillance system on the SHADWELL. The effective propagation loss embodies the losses from all modes of propagation that are generated in this complex environment. These propagation modes include multipath scattering from the bulkheads, scattering from compartment penetrations and obstructions, surface waves along cables, waveguide effects from the nature of the ship spaces like the corridors, free-space propagation, and possibly coaxial-cable effects. The last mode may arise from having a cable in a corridor behave like a coaxial cable, where the cable is the inner conductor and the steel bulkheads of a corridor form the outer conductor.

The propagation loss L_{SP} is extracted from the SHADWELL data and the system calibration measurements by applying a variation of the Friis Transmission Equation that incorporates system losses and by solving for L_{SP}. For a different system of interest, the derived values of L_{SP} and the pertinent parameters of the different system can then be substituted into the appropriate

transmission equation to obtain predicted values of the received power for the transmitter-receiver locations of our measurements. The pertinent equation is

$$L_{SP} = \frac{P_{S1}}{P_{S2}} \left(\frac{\lambda}{4\pi R_{C1}} \right)^2 \left(\frac{P_{C1}}{P_{C2}} \right)^{-1}, \tag{1}$$

where P_{C1} is the measured received power in a Compact Range when the transmitting and receiving antennas are separated by R_{C1} (5.6388 m for the batwing dipole and 4.699 m for the probe), P_{C2} is the measured received power in a Compact Range when the transmitting antenna is connected directly to the receiving antenna, λ is the wavelength corresponding to the specified frequency f, P_{S1} is the measured received power on the SHADWELL, and P_{S2} is the measured received power on the SHADWELL when the transmitting antenna is connected directly to the receiving antenna. Although P_{C2} and P_{S2} are equal, both are included in Eq.(1) because P_{C1}/P_{C2} was the quantity that was measured in the Compact Range. Further, P_{C1}/P_{C2} contains the effect of the transmitting and receiving antennas. The squared quantity is the free-space propagation loss for the Compact-Range measurement and is denoted L_{0C}. Let P_{C12} be the ratio P_{C1}/P_{C2}, take $10\log_{10}$ of Eq.(1), and let lower case letters represent the resulting expressions for the losses and powers. For example, $p_{C12} = 10\log_{10}(P_{C1}/P_{C2})$. Equation (1) becomes

$$l_{SP} = p_{S1} + l_{0C}(f) - p_{S2} - p_{C12}. \tag{2}$$

Fig.7 provides the measured background noise level p_N on the SHADWELL for the 23 frequencies. The noise power has small variations between -90.67 dBm and -88.67 dBm.

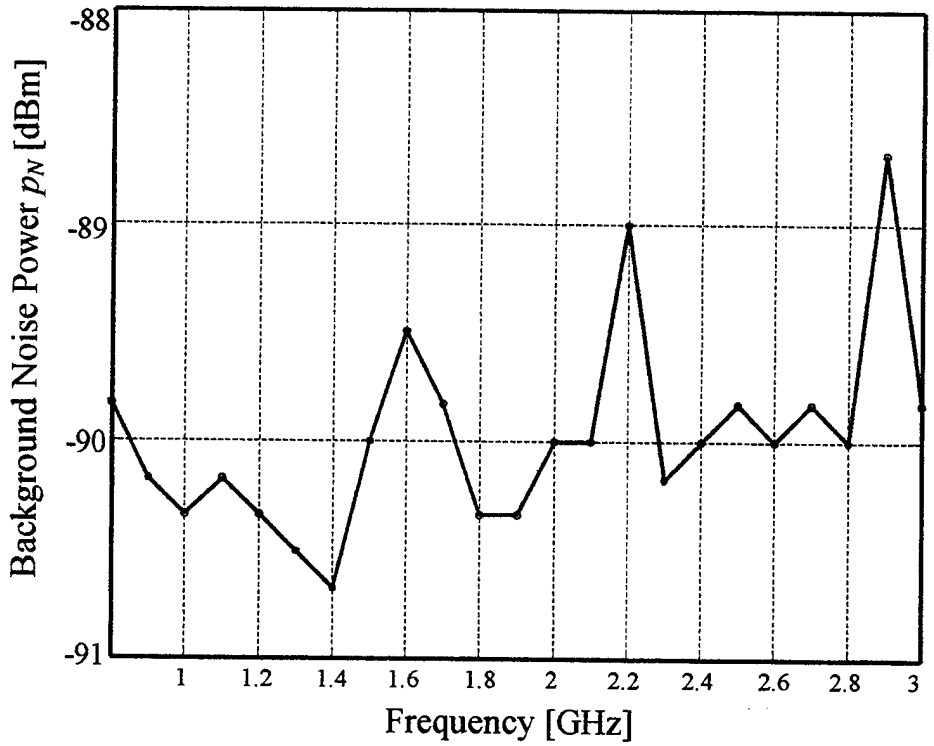

Fig.7. Background noise power p_N vs frequency on the 1 Level of the SHADWELL

As long as the received signal power exceeds the noise power by 20 dB, the data is acceptable. In fact, the accuracy of a measurement increases as the signal-to-noise ratio increases. The true signal lies in the interval $[\varepsilon_L, \varepsilon_U]$, where

$$\varepsilon_L = p_{S1} + 20\log_{10}\left(1 - \sqrt{\frac{P_N}{P_{S1}}}\right),$$

$$\varepsilon_U = p_{S1} + 20\log_{10}\left(1 + \sqrt{\frac{P_N}{P_{S1}}}\right), \qquad (3)$$

$$\alpha = 10\log_{10}\left(\frac{P_{S1}}{P_N}\right).$$

For different values of the measured signal-to-measured noise ratio α, upper and lower bounds of the true signal relative to the measured signal p_{S1} are plotted

in Fig.8, and specific values are provided in Table 1. Thus the value of the true signal minus p_{S1} lies between the bounding curves of Fig.8. For a given value of p_{S1}, one can associate an error bar with the data point p_{S1} by connecting ε_L and ε_U with a vertical line segment through p_{S1}. Because of the logarithmic scale, the error bar is not symmetric about p_{S1}. Moreover, the error bar decreases as α increases. For reasonable accuracy, one would like α to exceed 20 dB.

Table 1 – Error Bounds on Measured Signal p_{S1}

α [dB]	$\varepsilon_U - p_{S1}$ [dBm]	$\varepsilon_L - p_{S1}$ [dBm]	$\varepsilon_U - \varepsilon_L$ [dBm]
1	5.535	-19.271	24.806
5	3.876	-7.177	11.053
10	2.387	-3.302	5.688
15	1.422	-1.701	3.122
20	0.828	-0.915	1.743
25	0.475	-0.503	0.978
30	0.270	-0.279	0.550
35	0.153	-0.156	0.309
40	0.086	-0.087	0.174
45	0.049	-0.049	0.098
50	0.027	-0.028	0.055

Recall that p_{S2} is the received power when the transmitter and receiver are connected directly. This parameter measures the response of the bistatic measurement system without the antennas. As Fig.9 indicates, p_{S2} decreases monotonically across the frequency band, with a maximum of 20.75 mW (13.17 dBm) at 800 MHz and a minimum of 7.36 mW (8.67 dBm) at 3 GHz. Except for the effective propagation loss and the measured power, the remaining parameters of Eq. (2) are shown in Tables 2 and 3. On including the measured data, one obtains the various plots of l_{SP} that appear in the next subsection.

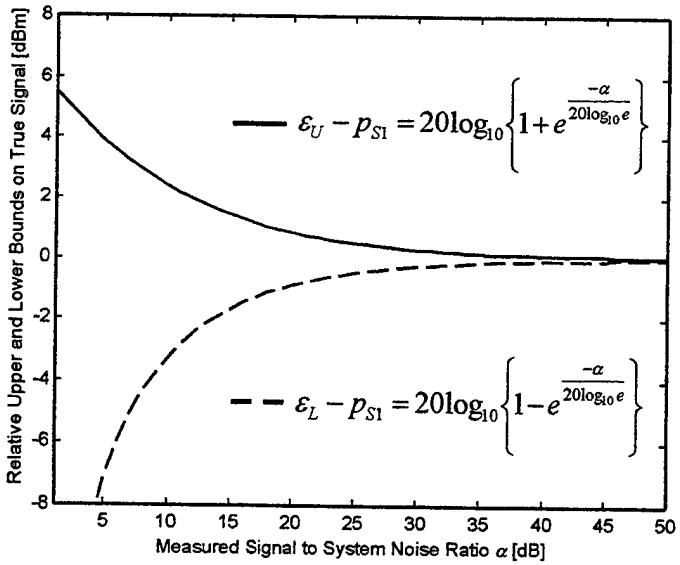

Fig.8. Relative upper bound ε_U - p_{S1} and relative lower bound ε_L - p_{S1} for the true received signal power versus the measured signal-to-noise ratio α given the measured signal power p_{S1} and the noise p_N.

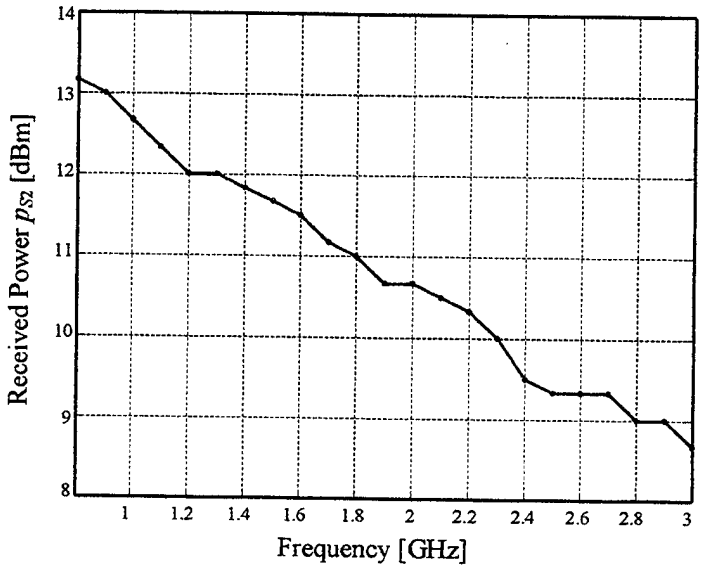

Fig.9. Measured received power p_{S2} vs frequency f when the transmitter and receiver are connected directly.

Table 2 – Parametric Values for Effective Propagation Loss when Receiving Antenna is Coaxial Probe

f [MHz]	$l_{0C}(f)$ [dB]	p_{S2} [dBm]	p_{C12} [dB]	$l_{0C}(f) - p_{S2} - p_{C12}$
800	-43.950	13.17	-62.50	5.380
900	-44.973	13.00	-59.21	1.237
1000	-45.888	12.67	-73.47	14.907
1100	-46.716	12.33	-62.63	3.581
1200	-47.472	12.00	-67.87	8.395
1300	-48.167	12.00	-63.94	3.774
1400	-48.811	11.83	-56.96	-3.677
1500	-49.410	11.67	-56.99	-4.090
1600	-49.970	11.50	-62.91	1.437
1700	-50.497	11.17	-62.47	0.804
1800	-50.993	11.00	-59.74	-2.255
1900	-51.463	10.67	-56.19	-5.943
2000	-51.909	10.67	-60.40	-2.181
2100	-52.332	10.50	-68.67	5.833
2200	-52.736	10.33	-62.94	-0.130
2300	-53.123	10.00	-63.32	0.198
2400	-53.492	9.50	-61.22	-1.771
2500	-53.847	9.33	-60.84	-2.339
2600	-54.187	9.34	-62.16	-1.367
2700	-54.515	9.35	-62.98	-0.882
2800	-54.831	9.00	-66.01	2.181
2900	-55.136	9.01	-61.92	-2.225
3000	-55.430	8.67	-59.71	-4.386

The values for the probe in Table 2 differ from the values for the batwing dipole (Table 3) in two respects: the chamber calculations of l_{0C} (column 2) and p_{C12} (column 4). Recall from Eq. (2) that l_{0C} is the free-space propagation loss and p_{C12} is the combined effective gain of the transmitting and receiving antennas. The difference in the values of l_{0C} is the same (1.584 dB) at each frequency, because chamber measurements of the probe and the batwing dipole were taken at 4.699 m and 5.6388 m, respectively. The 1.584-dB differential corresponds to 20 $\log_{10}(5.6388/4.699)$ and is independent of the antenna type. In contrast, the

differences in p_{C12} for the two receiving antennas are directly attributable to antenna type. The values of p_{C12} for the probe oscillate between –56 dB and – 74 dB. Furthermore, the probe suffers greater losses relative to the dipole, ranging from 3.54 dB at 2.7 GHz to 30.03 dB at 1 GHz, across the entire frequency interval. The batwing dipole has fairly constant values up to roughly 2 GHz (typical of broadband antennas), steadily decreases until 2.8 GHz, and rises again at the upper end of the band.

Table 3 – Parametric Values for Effective Propagation Loss when Receiving Antenna is Batwing Dipole

f [MHz]	$l_{0C}(f)$ [dB]	p_{S2} [dBm]	p_{C12} [dB]	$l_{0C}(f) - p_{S2} - p_{C12}$
800	-45.533	13.17	-47.11	-11.593
900	-46.556	13.00	-47.64	-11.916
1000	-47.472	12.67	-43.39	-16.752
1100	-48.299	12.33	-43.32	-17.309
1200	-49.055	12.00	-44.52	-16.535
1300	-49.750	12.00	-45.56	-16.190
1400	-50.394	11.83	-47.25	-14.974
1500	-50.993	11.67	-44.05	-18.613
1600	-51.554	11.50	-43.85	-19.204
1700	-52.081	11.17	-44.23	-19.021
1800	-52.577	11.00	-45.15	-18.427
1900	-53.047	10.67	-44.61	-19.107
2000	-53.492	10.67	-45.39	-18.772
2100	-53.916	10.50	-46.93	-17.486
2200	-54.320	10.33	-51.09	-13.560
2300	-54.706	10.00	-52.58	-12.126
2400	-55.076	9.50	-52.86	-11.716
2500	-55.430	9.33	-55.49	-9.270
2600	-55.771	9.34	-58.78	-6.331
2700	-56.099	9.35	-59.44	-6.009
2800	-56.415	9.00	-61.72	-3.695
2900	-56.720	9.01	-57.99	-7.740
3000	-57.014	8.67	-54.26	-11.424

5.2 Effective Propagation Losses Derived from SHADWELL Data

For Class A1, listed at the end of Sec. 4, forty of the measurements correspond to receiver locations on a grid about 9" from the door 1-28-1 outside $D_{1,3}$, where the grid points are spaced every 12" in the vertical and horizontal directions (Fig.10). The grid structure consists of five columns and seven rows of points, with the middle column along the door's vertical centerline. Each column has seven grid points, ranging from 12" to 84" in height, and each row has five grid points. The purpose of these measurements was to see whether the readings by the door seals were higher, indicating that energy was leaking through the seals.

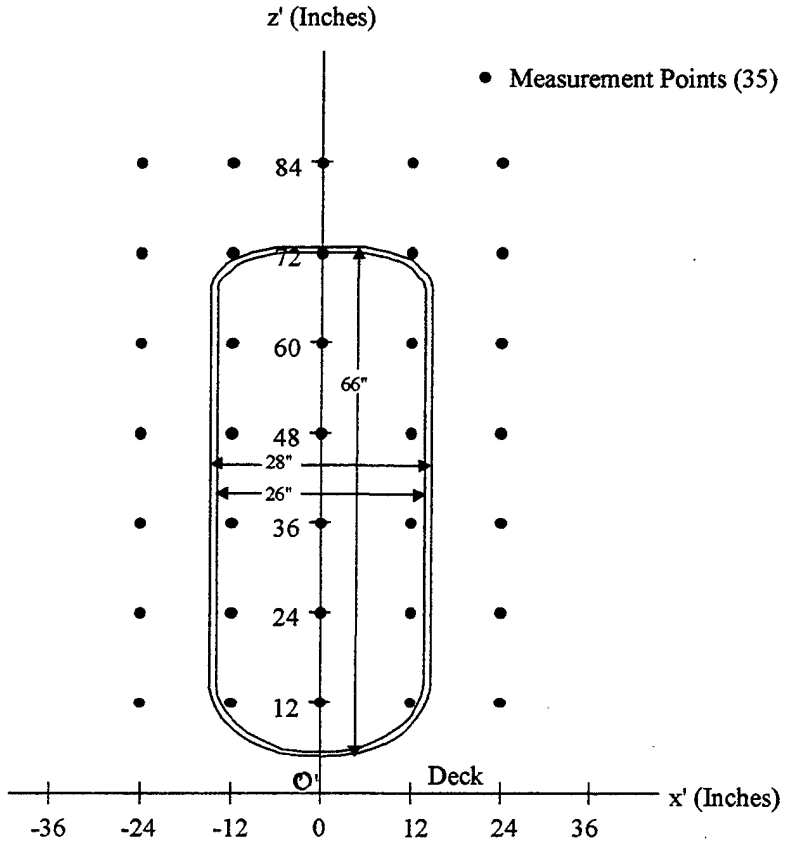

Fig.10. Grid of 35 measurement locations of effective propagation loss l_{SP} when the receiver is 9" inches from the closed door 1-28-1 in the corridor of compartment of $D_{1,2}$ at a height of 3' and the transmitter is in compartment $D_{1,3}$ at a height of 5' and a distance of 4' from 1-28-1. The local origin O' is located on the deck along the door's centerline.

The propagation loss is plotted in Fig.11 for the 5 grid points in the row that is 36" above the deck. These five curves are associated with grid points at the door's vertical centerline and at 12" and 24" to the left and right of the centerline. Clearly, l_{SP} varies with position and frequency, but the curves are roughly centered in a mildly wavy band that is roughly 10 dB wide. The band generally decreases as the frequency increases to 2 GHz; then it rises slightly. Except for one data point at 3 GHz along the centerline, $\alpha > 20$ dB, which implies a measurement error that is less than 0.915 dB by Table 1. Even the value of l_{SP} for the 3-GHz point is 5.5 dB above the noise floor. Consequently, the 10-dB fluctuations in the propagation loss for these points at each of the frequencies are not caused by measurement error.

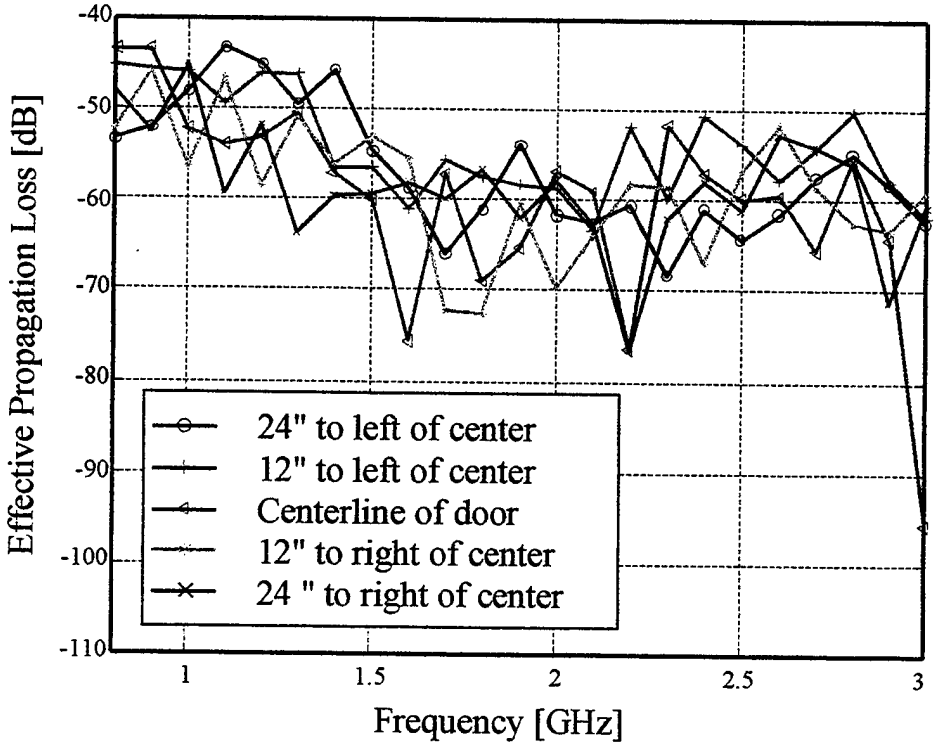

Fig.11. Five measurements of effective propagation loss when the receiver is 9" inches from closed door 1-28-1 in the corridor of compartment of $D_{1,2}$ at a height of 3' and the transmitter is in compartment $D_{1,3}$ at a height of 5' and a distance of 4' from 1-28-1.

Since RF spread spectrum communication systems over 902 MHz to 928 MHz are being tested for use during shipboard fires, consider the values at 900 MHz in Fig.11. The effective propagation loss is the same (approximately –45 dB) for the points closest to the door seal, the two points that are 12" on either side of the centerline. Since these two locations do not correspond to the smallest effective propagation loss for the five locations, one cannot argue that the transmitted energy is leaving $D_{1,3}$ via the door seals. It is unclear why such variations in the door readings were recorded. A likely cause is the multipath from the energy bouncing off the metallic surfaces which bound the passageway outside 1-28-1. In any event, the results are inconclusive.

Eleven of the remaining fifteen measurements of Class A1 were an attempt to isolate the different ways the energy could leave $D_{1,3}$ when both doors to it are closed. In all cases, the receiver was placed 29" from 1-28-1 in $D_{1,2}$ along the door's center at a height of 48". Since the door's watertight seal was a worn rubber grommet, various attempts were made to improve the seal such as removing the grommet, sanding the seal-door interface, and tightly packing the region about the door seal with steel wool. These efforts yielded little or no change in the received power. In addition, wires, holes, meshes, and nonmetallic sections penetrated the bulkhead of $D_{1,3}$. Attempts to make the exterior of this compartment electrically quiet were made by covering these locations with aluminum foil, steel wool, and metallic plates. Again, the results are inconclusive, perhaps because measurements were taken only at the one location.

The last four measurements of Class A1 provide a very limited look at the impact of the propagation environment on the polarizations of the transmitting and receiving antennas. The transmitter-receiver placement is the same as the preceding eleven measurements. The designations "V" and "H" in Fig.12 represent polarizations of the antennas, where the first letter and the second letter denote the polarizations of the transmitting antenna and the receiving antenna, respectively. For example, HV means that the transmitting antenna is horizontally polarized and the receiving antenna is vertically polarized. On scrutinizing Fig.12, one can see a general downward trend until 2 GHz, then a milder upward trend. Aside from these trends, no other observable pattern is discernible across the frequency band.

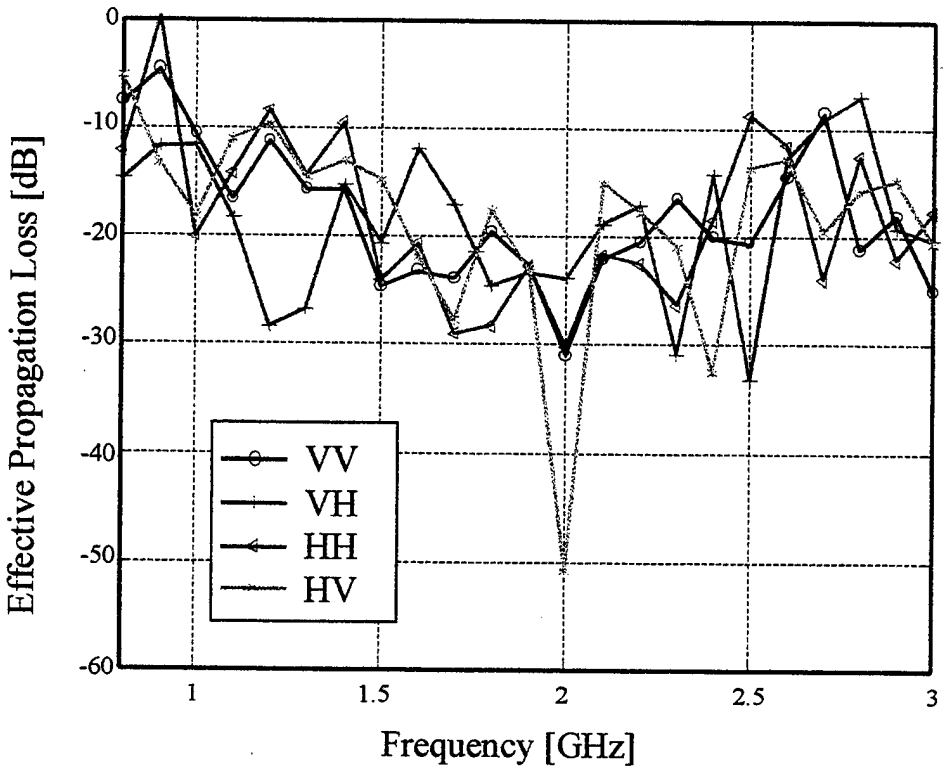

Fig.12. Effective propagation losses for different polarizations when the receiver is 29" inches from closed door 1-28-1 in the corridor of compartment of $D_{1,2}$ at a height of 4' and the transmitter is in compartment $D_{1,3}$ at a height of 5' and a distance of 4' from 1-28-1.

For the measurements along the slanted L-shaped passageway that is formed by the starboard passageway and the back of $D_{1,2}$ (Class A2), the received power exceeds the background noise level by 10 dBm to 30 dBm over the entire frequency band for most of the data. This variation in the power measurements depends on which doors were closed. In any case, significant energy is propagated along this passageway. It is suspected that the waveguide-like nature of the passageway directs the energy. However, since a distributed cable network that contains a leaky-wave communication line also runs overhead along the starboard passageway, surface-wave and coaxial-cable modes may be other means of propagation. For the cable network to run between adjacent compartments that comprise the passageway, it passes through the MCT, a cutout portion of the bulkhead over the connecting door that adjoins the compartments. Since it is possible that surface waves are induced on this cable, the MCT is a likely propagation conduit.

As the solid triangles in Fig.6 indicate, measurements were taken at several locations in $D_{1,2}$, $D_{1,4}$, and $D_{1,8}$. In particular, Fig.13 displays l_{SP} for the source in $D_{1,3}$ and for the receiving probe at the two locations of the MCT in $D_{1,4}$, one above door 1-28-3 which connects $D_{1,2}$ and $D_{1,4}$ (denoted $l_{SP,56}$) and the other above door 1-25-1 which connects $D_{1,4}$ and $D_{1,6}$ ($l_{SP,57}$). The distances between the source and the two receiver locations above doors 1-28-3 and 1-25-1 are 4.376 m and 3.974 m, which are respectively designated $R_{56} > R_{57}$. Clearly, the MCT above door 1-25-1 is closer to the source, because an adjacent bulkhead of $D_{1,4}$ is shared with $D_{1,4}$. In both instances, the door (1-28-1) between the source compartment $D_{1,3}$ and $D_{1,2}$ and the door (1-28-5) between $D_{1,2}$ and its foyer are open, and the door between the $D_{1,2}$ foyer and $D_{1,4}$ (1-28-3) is closed.

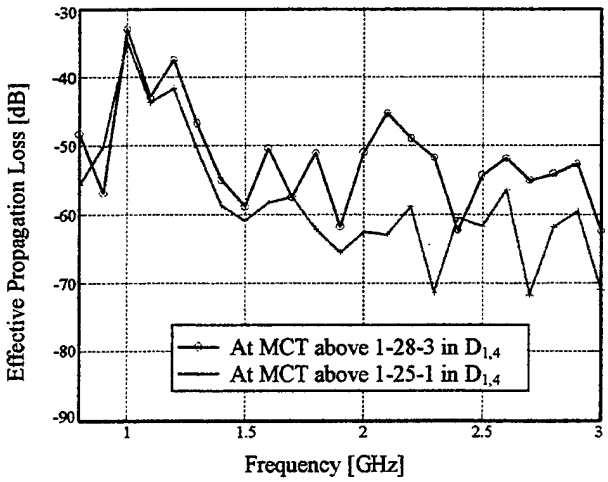

Fig.13. Effective propagation losses with the probe at the mask cable transits (MCTs) in $D_{1,4}$, one above door 1-28-3 and one above door 1-25-1. Both measurements are taken at a height of 7'.

From Fig.13, $l_{SP,56} > l_{SP,57}$ for all frequencies f except 900 MHz and 2500 MHz. Hence for the majority of frequencies, the energy appears to follow the corridor of $D_{1,2}$ through 1-28-5 into $D_{1,4}$, through 1-28-3, and finally through $D_{1,4}$ to 1-25-1. Even though $R_{56} > R_{57}$, the path to 1-25-1 through $D_{1,4}$ is a good 5 m longer than the path to 1-28-3, which accounts for the fact that the signal to 1-25-1 incurs more attenuation for most frequencies. On the other hand, since $l_{SP,56} < l_{SP,57}$ when f is 900 MHz or 2500 MHz, it is inferred that some energy must have followed another path, perhaps via $D_{1,7}$ to $D_{1,6}$ to $D_{1,4}$, via a venting structure from

$D_{1,3}$, or via some kind of surface wave between the common boundaries of $D_{1,3}$ and $D_{1,4}$ for these two frequencies. The last possibility seems least likely since the thick metallic bulkheads that comprise the boundary should reflect signals. Further measurements are required to determine why different results are obtained for 900 MHz and 2500 MHz and if they are special frequencies.

For Class A3, two propagation paths from the source in $D_{1,3}$ to the receiver in the forecastle between doors 1-15-1 and 1-15-3 are considered. The paths, one traversing along the starboard passageway and the other passing through the large central room, are given by

Path 1: $D_{1,3} \rightarrow D_{1,2} \rightarrow D_{1,4} \rightarrow D_{1,6} \rightarrow D_{1,8} \rightarrow D_{1,12}$ [Starboard Corridor];

Path 2: $D_{1,3} \rightarrow D_{1,2} \rightarrow D_{1,1} \rightarrow D_{1,12}$ [Central Room].

Since all the doors in $D_{1,3}$ and $D_{1,7}$ are closed except 1-28-1, it is we assumed that a significant amount of the energy leaving $D_{1,3}$ does so through 1-28-1. Moreover, the door (1-20-2) from $D_{1,1}$ to $D_{1,14}$ is closed and all doors along the starboard passageway (1-28-5, 1-28-3, 1-25-1, 1-22-1) are open to guide most of the energy along these two paths. When 1-15-1 is closed (open) and 1-15-3 is open (closed), the authors believe Path 1 (2) to be open and Path 2 (1) to be closed.

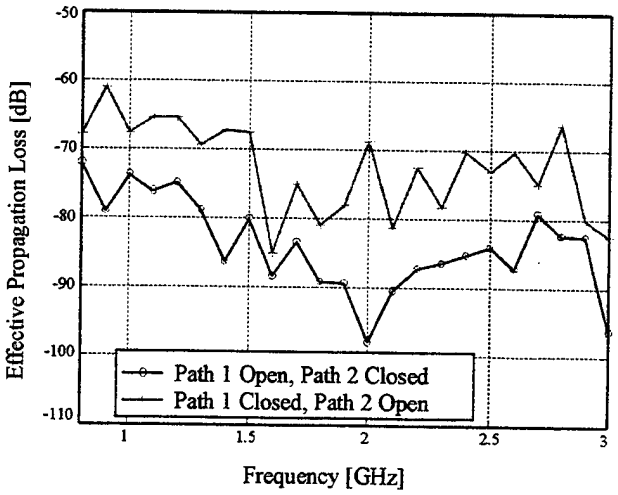

Fig. 14. Comparison of effective propagation losses for path along starboard corridor (Path 1) and for path through central-room (Path 2). The receiver is in the forecastle $D_{1,12}$ near door 1-15-1, and the transmitter is in $D_{1,3}$.

According to Fig.14, the path through the large central room (Path 2 Open) has better propagation than the corridor path at all frequencies, probably because the corridor path has more length due to its slanted-L shape and because the large central room acts more like free space. The received signal power from the starboard path is attenuated between 3 dB and 28 dB more than the received signal for the room path. The propagation losses are highly variable across the frequency band. For example, at 900 MHz, 1000 MHz, 1600 MHz, 2000 MHz, and 2900 MHz, the signal corresponding to the starboard path is further attenuated by 18 dB, 6 dB, 3 dB, 29 dB, and 3 dB, respectively. However, the received power level for the starboard path is significant, which is probably a result of the waveguide-like nature of the corridor and the surface-wave capability of the leaky-wave communication cable that runs along the corridor.

For Class A5, four measurements were taken to test inter-deck propagation. The transmitter was in compartment $D_{1,3}$ with door 1-28-1 closed and doors 1-28-3 and 1-28-5 open. The receiver was placed on the 01 Level above the foyer of $D_{1,2}$ and on the 2 Level below door 1-25-1 and on the bow side of door 2-25-1. The stairwell down to the 2 Level is accessed from an opening in the foyer of $D_{1,2}$. The stairwell to the 01 Level is reached by passing from the foyer of $D_{1,2}$ into $D_{1,4}$, by following the corridor until door 1-25-1, and then by turning aft to face the stairwell. A hatch at the top of this stairwell seals the 01 Level from the Main Deck. With door 2-25-1 and the hatch on the 01 Level open, the 01-Level measurement ($l_{SP,102}$) and the 2-Level measurement ($l_{SP,104}$) are compared to a Class-A1 measurement ($l_{SP,44}$) made in the foyer of $D_{1,2}$ (Fig. 15).

For 800 MHz $\leq f \leq$ 1300 MHz, $l_{SP,44} > l_{SP,104} > l_{SP,102}$. Hence propagation to the foyer of $D_{1,2}$ is better than propagation to 2 Level, which is better than propagation to the 01 Level. This makes sense because the path to the foyer is shorter than the path to the 2 Level, which is shorter than the path to the 01 Level. In particular, the differences in effective propagation loss at 900 MHz between the Main Deck and the 2 Level and the 01 Level are 15 dB and 20 dB, respectively, which are rather sizable differences. However, this pattern does not hold for the larger frequencies, where the three curves tend to oscillate. The reasons for the different behaviors are unclear; they could be the result of the complex structure of the ship or perhaps they may have something to do with the relative sizes of the corridor and the source's wavelength. The most that can be said is that these measurements easily exceed the background noise level, which strongly suggests that inter-deck propagation is feasible.

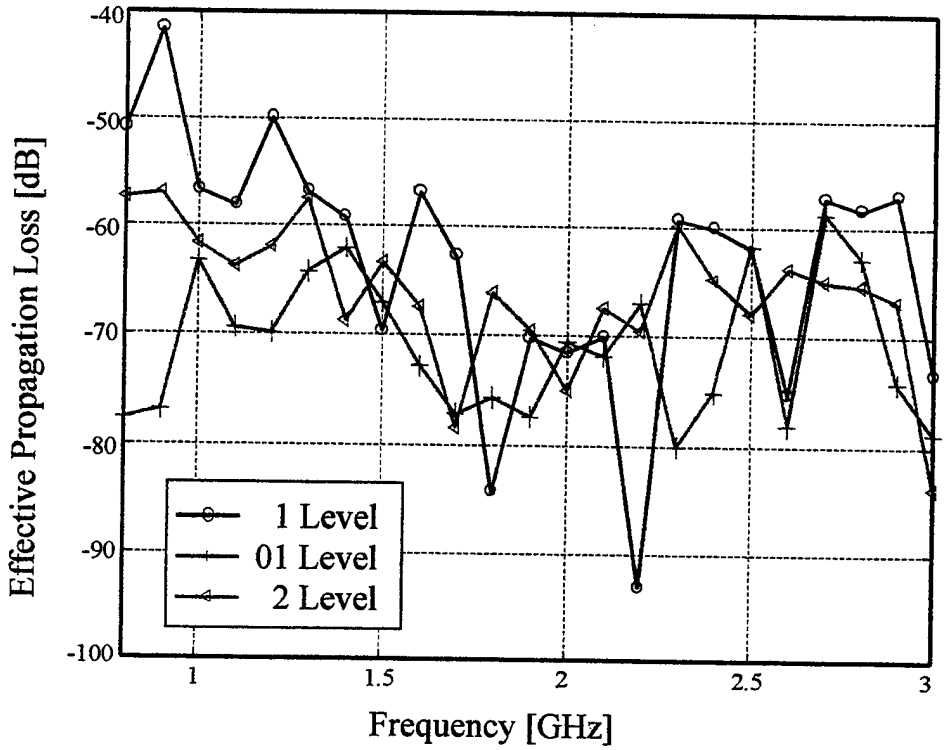

Fig. 15. Comparison of the effect of inter-deck propagation. The transmitter is in $D_{1,3}$, and the receiver is placed at three positions (one on each of Levels 01, 1, and 2) by the starboard stairwell at Frame 28.

6. Summary

The measurements taken on the ex-USS SHADWELL (23-25 February 1998) have provided an initial glimpse at the complex electromagnetic environment of the confined ship spaces aboard a naval vessel. This collection effort was a first attempt at obtaining some insight into RF propagation in this environment. A site survey was conducted, data were collected, and the data were processed and analyzed. As a consequence of equipment limitations, including the use of a spectrum analyzer instead of a network analyzer, no major conclusions were reached on what electromagnetic modes were actually propagated in the confined spaces of the SHADWELL. However a few inferences are drawn.

The fact that most measurements were well above the background noise level over the entire frequency interval (800 MHz to 3 GHz), even for many

closed-door configurations, strongly suggests that power levels are sufficient to ensure inter-deck and intra-deck communication when doors are closed for many operational situations. In addition, the measurements indicate that intra-deck propagation occurs along different paths such as through central-room compartments and along the starboard and port passageways. The data substantiates the observed good performance of wireless communication systems at 914 MHz and 2400 MHz that are being tested on the SHADWELL for use during emergency situations. Evidence of some of the suggested modes of propagation in confined ship spaces was observed, for example, the multipath effects caused by scatter from the steel structure of the SHADWELL. However, these measurements were not controlled well enough to separate the propagation modes. Clearly, more rigidly controlled testing is needed to gain a better understanding of the propagation modes in this environment and their relative impact on RF signals. Essentially, these measurements form the basis for planning further, more controlled tests with an improved measurement system.

Acknowledgments. The authors thank Mr. James Gagorik of the Office of Naval Research (ONR 33) and Dr. Frederick W. Williams of the Naval Technology Center for Safety and Survivability (NTCSS) for sponsoring this research. Further, we are indebted to Mr. Lawrence Cohen of the Radar Division of the Naval Research Laboratory (NRL 5300) for providing excellent background information and insightful comments.

References

[1] "Welcome Aboard NRL's Advanced Fire Research Vessel," Publication 0076-6180, Naval Research Laboratory, October 1996.

[2] H. W. Carhart and F. W. Williams, "The Ex-Shadwell-Full Scale Fire Research and Test Facility," NRL Memorandum Report 6074, 6 October 1987.

[3] T. M. Gilliland, "Radar Attenuation by Rocket Plumes," Report CPTR 81-7, Chemical Propulsion Information Agency, October 1981.

[4] B. R. Choquette, F. W. Williams, and T. T. Street, "The Effects of a Fire on Radio Wave Transmissions," NRL/MR/6180--98-8156, Naval Research Laboratory, 15 April 1998.

[5] D. L. Knepp and H. L. F. Houpis, "VHF/UHF Radar Scintillation Effects Observed by ALTAIR," in *The Effect of the Ionosphere on Radiowave Signals and System Performance* (Proceedings of Ionospheric Effects Symposium), eds. J. M. Goodman et al., 1-3 May 1990.

[6] T. T. Street, "Feasibility of Implementing a Network for Repair Locker #2 Area of Concern Using RF Communications: Emissions Testing," Letter Report 6180/0713.1, Naval Research Laboratory, 22 November 1995.

[7] L. S. Cohen and A. H. Light, "Investigation of AN/SRC-55 (XN-1) Hierarchical Yet Dynamically Reprogrammable Architecture (HYDRA) Electromagnetic Interference (EMI) to AN/SPS-40E," Letter Report 5332/002, Naval Research Laboratory, 14 January 1998.

[8] J. Perini and L. S. Cohen, "An Alternative Way to Stir the Fields in a Mode Stirred Chamber," submitted for publication in *IEEE Trans. on Electromagnetic Compat.*

[9] J. Lawton and F. J. Weinberg, *Electrical Aspects of Combustion*, Oxford: Clarendon Press, 1969.

[10] T. T. Street, "Wireless, Spread Spectrum, Low Level RF, DC Communications Network for Repair #2 and the Submarine Mockup Area on ex-USS SHADWELL," Letter Report 6180/0724.1, Naval Research Laboratory, 22 November 1995.

[11] T. T. Street and R. A. Robinson, "Wireless Communications Network RF Emission Survey," Letter Report 6180/0198, Naval Research Laboratory, 20 June 1997.

[12] E. L. Mokole, M. Parent, S. N. Samaddar, J. Valenzi, and E. Tomas, "Preliminary Report on Electromagnetic Propagation in an Enclosed Ship Environment," Letter Report 5340/193, Naval Research Laboratory, 30 October 1998.

[13] "Below-Decks Survey as Part of SEMCIP of USS OAK HILL (LSD 51)," Executive Summary, Contract N00178-95-C-3024, Eldyne, Inc, 1996.

[14] A. J. Poggio and E. K. Miller, "Techniques for Low-Frequency Problems," in *Antenna Handbook: Theory, Applications, and Design*, Y. T. Lo and S. W. Lee, eds., Ch. 3, p. 3-30, New York: Van Nostrand Reinhold, 1988.

[15] G. W. Collins, "TV and FM Broadcast Antennas," in *Antenna Handbook: Theory, Applications, and Design*, Y.T. Lo and S.W. Lee, eds., Ch. 27, p. 27-33, New York: Van Nostrand Reinhold, 1988.

EXAMINING THE PERFORMANCE BENEFITS OF ANTENNA DIVERSITY SYSTEMS IN PORTABLE WIRELESS ENVIRONMENTS

P. Irazoqui-Pastor[1] and J. T. Bernhard[2]
[1]Department of Electrical and Computer Engineering
University of New Hampshire
Durham, NH 03824
[2]Department of Electrical and Computer Engineering
University of Illinois at Urbana-Champaign
1406 W. Green St., Urbana, IL 61801

Abstract: As the commercial wireless spectrum has become crowded with more and more users, several research groups nationally and abroad have developed antenna diversity schemes for portable wireless devices to improve system performance. This research examines the possible performance benefits of a number of these diversity configurations using experimental rather than theoretical data to calculate the antenna system's correlation coefficient. The data, processed using an efficient numerical algorithm, includes the radiation patterns of each antenna as well as environment-specific incoming path distributions. This method of evaluation accounts for antenna coupling and chassis and user effects that may have a significant impact on diversity system performance that are not captured with theoretical analyses. This work addresses common portable communication devices, including voice handsets for Satellite Personal Communication Services (S-PCS) and laptop computers for Wireless Local Area Networks (WLAN). The associated antennas are external (e.g., monopoles) and internal (e.g., microstrip) and are arranged in a variety of diversity schemes. The possible costs and benefits of portable antenna diversity are discussed in light of the analysis results.

1. Introduction

As commercial wireless communication systems mature, the demand for higher quality and reliability is driving efforts to improve performance at every point in the signal path. Several groups have suggested antenna diversity in portable units to help mitigate the effects of multipath interference [1], [2], [3]. In these applications, however, traditional assumptions used to evaluate antenna diversity

configurations may no longer apply due to the small size of portable devices and proximity effects of the chassis and the user.

This work examines the effectiveness of spatial and pattern diversity schemes working in tandem using experimental rather than theoretical antenna data. This data captures the effects of the non-ideal portable environment that is lacking in idealized theoretical analyses. Processed with a numerically-efficient analysis and design tool [4], this data provides a more realistic measure of the potential benefits and drawbacks of a range of antenna diversity schemes.

Section 2 provides a brief description of antenna diversity systems and the theoretical background for the correlation coefficient calculation [5]. Section 3 details the specific system configurations used as examples, including the chassis, antennas, and antenna locations. Section 4 compares the results of correlation coefficient calculations using measured data from these configurations with calculations assuming ideal antenna patterns. Finally, Section 5 discusses the results as well as the evaluation and design of future antenna diversity systems in portable wireless environments.

2. Theoretical Development and Methods

There are four principle ways in which antennas are made to differ in diversity systems [5]. The first and most commonly used is frequency or spread spectrum diversity, where an antenna is made to transmit data at more than one frequency. This is commonly incorporated into many wireless applications and has been widely studied. Another diversity technique uses antennas with differing polarizations. A third technique, spatial diversity, is one in which the antennas are separated by some optimum distance. This distance is usually determined by factors including the wavelength of incoming signals and the anticipated angle of signal arrival. A pattern diversity system is one in which the antennas have different patterns to cover a desired volume in space. In this paper, we address spatial and pattern diversity on portable wireless devices.

In order to quantify the benefits of an antenna diversity system we calculate the correlation coefficient [5], [6], [7]. The correlation coefficient, ρ, is a mathematically obtained value between one and zero. It represents how much the signals from the antennas have in "common." Identical antennas receiving identical signals would have ρ equal to one, and signals from antennas having nothing in common would have ρ equal to zero. Since the objective in a diversity system is to have the nulls of one antenna not correspond to those of the other, the lower ρ the better. In general terms, the normalized cross-correlation $C_{mn}(\tau_1, \tau_2)$ for any two signals M and N, given in any two dimensions x and y, is given by (1)

$$C_{mn}(\tau_1,\tau_2)=\frac{\left|\int_{-\infty}^{\infty}\int_{-\infty}^{\infty}M(x,y)N^*(x-\tau_1,y-\tau_2)dxdy\right|^2}{\left|\int_{-\infty}^{\infty}\int_{-\infty}^{\infty}M(x,y)M^*(x-\tau_1,y-\tau_2)dxdy\right|\left|\int_{-\infty}^{\infty}\int_{-\infty}^{\infty}N(x,y)N^*(x-\tau_1,y-\tau_2)dxdy\right|} \quad (1)$$

where τ_1 and τ_2 are shift variables in the two dimensions. Shifting occurs along the axis representing the variable in the signal function. In the case of antenna patterns, this shifting takes place in degrees as one pattern is effectively rotated around the other. Rotation occurs by cycling τ_1 and τ_2 over the range of θ and ϕ. This can be done by physically turning one antenna on its axis, or more simply by mathematically rotating a calculated pattern about the other.

Research has shown [5], [6], [7] that the correlation coefficient between two antennas is a function of the antenna patterns, the separation between the antennas, and the incoming multipath wave distribution. Furthermore an equation for the incoming path distribution $P(\theta)$, (usually assumed omnidirectional in the azimuth [1], [2]) can be expressed in terms of three environment parameters as:

$$P(\theta)=\frac{1}{\sqrt{2\pi S^2}}e^{-\frac{(\theta-\theta_i)^2}{2S^2}} \quad (2)$$

where S is the standard deviation in the spread angle for incoming waves, θ is the angle of some single incoming beam, and θ_i is the direction of the principal incoming wave [1], [2].

Spatial diversity can be treated as a phase offset [4], [5], [6], [7] in the calculation of the correlation coefficient. It is represented theoretically as a function of the wave number k, the Cartesian components of the antenna separation vector D, and the angle of the incoming wave, as:

$$e^{-jk\sqrt{(D_x\sin(\theta)\cos(\phi))^2+(D_y\sin(\theta)\sin(\phi))^2+(D_z\cos(\theta))^2}} \quad (3)$$

To arrive at the final correlation coefficient, the spatial separation between the antennas accounted for in (3) and the distribution of incoming multipath waves given by (2) are included. The cross-correlation between the two patterns is

normalized by dividing it by the product of the auto-correlations for each individual pattern, thus:

$$\rho(\tau_1,\tau_2)=\frac{\left|\int_0^{2\pi}\int_0^{\pi}V(\theta,\phi)W^*(\theta-\tau_1,\phi-\tau_2)P(\theta)e^{-jk\sqrt{(D_x\sin(\theta)\cos(\phi))^2+(D_y\sin(\theta)\sin(\phi))^2+(D_z\cos(\theta))^2}}d\theta d\phi\right|^2}{\left|\int_0^{2\pi}\int_0^{\pi}V(\theta,\phi)V^*(\theta,\phi)P(\theta)d\theta d\phi\right|\left|\int_0^{2\pi}\int_0^{\pi}W(\theta,\phi)W^*(\theta,\phi)P(\theta)d\theta d\phi\right|} \quad (4)$$

To calculate the correlation coefficient, we implement a computationally-efficient algorithm called fast convolution that exploits the relationship between correlation and convolution [4], [8]. This method reduces the number of computations necessary by greater than one order of magnitude [9] compared to packaged cross-correlation functions. For any particular diversity configuration, τ_1 and τ_2 are fixed and represent the relative rotational position of one antenna with respect to the other. To aid in the design of diversity systems, τ_1, τ_2, and D can be varied to provide a normalized correlation coefficient plot for any orientation of one antenna with respect to the other.

3. Experimental Configurations

Three types of chassis are examined: the cellular phone, the palm-top, and the laptop. These represent the range in shape and size of most portable wireless devices today. Frequencies used include 1.622GHz for Satellite PCS, and 2.44GHz and 5.8GHz for spread-spectrum WLAN. We selected two different types of antennas, monopoles and microstrip patches, for their electromagnetic properties as well as their physical shape and the feasibility of incorporating them onto a specific chassis. The various antennas and chassis are combined to form three experimental configurations that provide insight into the possible benefits and limitations of antenna diversity systems in portable wireless devices.

The first configuration uses a cellular phone chassis at a frequency of 1.622 GHz for use in the Satellite PCS band. A monopole and a microstrip patch antenna are deployed on the chassis as shown in Figure 1. The patch antenna is a flip-up device that ordinarily rests flush with the back of the handset chassis. During satellite communication, it flips up to form a right angle with the chassis and aims directly upwards. The monopole is located on the top of the unit as with a traditional cellular phone. This allows the unit to receive signals incoming from directions near the horizon as well as supports in-building communication via transmission through windows. Options for spatial diversity are limited by the

size of the chassis and the wavelength of operation, but this antenna system would ideally provide a nearly isotropic reception pattern through pattern diversity.

The second configuration shown in Figure 2 includes a laptop equipped for operation in a 2.4 GHz LAN system with the display at a 90° from the keyboard. Again, a monopole and a microstrip patch are used. The monopole is located on a PCMCIA card that extends out from the side of the keyboard, and the microstrip patch is integrated into the back of the laptop display. The size of the chassis relative to the wavelength of operation supports effective spatial diversity.

In the third configuration, a laptop with the display at a 135° angle from the keyboard is equipped with two microstrip patch antennas operating in the 5.8 GHz WLAN band. One antenna is integrated into the back of the display as in the second configuration, and one is integrated into the side of the keyboard as shown in Figure 3. Both are oriented to receive vertically polarized waves.

For each configuration, the antenna's radiation characteristics in the azimuthal plane were measured in an anechoic chamber. A HP 8753C vector network analyzer served as the transmitter and receiver. For all measurements, the center of rotation was the center of the chassis under test. For each antenna, two patterns were measured: one with the second antenna open-circuited and one with the second antenna terminated in a 50Ω impedance. This was done to establish the effects of various diversity combining techniques on antenna patterns [10]. For instance, in a combined diversity system, the second antenna would appear terminated to the first, while in a switched diversity system, the second antenna would appear open-circuited to the first. The data collected from each measurement was interpolated to contain 1024 points/360° that was then used as input to the Matlab algorithm to calculate the experimental value of the normalized correlation coefficient. For comparison, free space theoretical patterns for each antenna were also sampled at 1024 points/360° to calculate a theoretical value of the normalized correlation coefficient.

4. Results

The measured azimuthal patterns for the three configurations are shown in Figures 4, 5, and 6, respectively. In our experiments, the patterns of each antenna varied in magnitude but not appreciably in shape when the second antenna was left open or terminated. This effect was most pronounced with the first configuration on the handset, due to the close proximity and coupling between the two antennas. While these variations will not affect the value of the normalized correlation coefficient, they will have an impact on the practical efficiency of each real-world system.

The normalized correlation coefficients calculated using both experimental and ideal theoretical data are presented in Table 1. These calculations all assume

an isotropic incoming distribution in the azimuthal plane when multipath signals are indistinguishable in time. Therefore, these calculations are as general as possible with respect to unpredictable and irreproducible environment and channel characteristics, and also are independent of diversity combining techniques. Table 1 also provides information on the relative displacements of the two antennas in each configuration.

Configuration	Frequency	Horizontal Displacement	Vertical Displacement	Theoretical Correlation	Measured Correlation
One	1.622GHz	2.5 cm	0 cm	0.749	0.853
Two	2.44GHz	8.5 cm	18.5 cm	0.256	0.101
Three	5.80GHz	34.6 cm	14 cm	0.080	0.067

Table 1: Calculated theoretical and measured correlation coefficients for the three diversity configurations.

The measured and theoretical correlation coefficients agree in general, with the discrepancies between the experimental and theoretical values being a result of the non-ideal operation environment presented by the chassis. The results for Configuration 1 indicate that the diversity gain of this system is poor in the azimuthal plane. While the diversity systems of Configuration 2 and Configuration 3 yield good correlation results, the results come at the cost of omnidirectional coverage in the plane of interest.

5. Discussion

In urban or indoor settings with a large number of reflective and diffractive surfaces, a greater variation in the angles of arrival translates to an increase in the benefits of pattern diversity. Generally, the benefits of pattern diversity increase as the incoming pattern distribution becomes more isotropic [11]. The ideal configuration for a pattern diversity system has the secondary antenna oriented so that there is minimal overlap between its pattern and that of the primary antenna. This might not be sufficient to achieve an omnidirectional reception pattern, but it will exhibit minimal amounts of signal loss as a result of multipath interference. In a real diversity system it is only important that the two antenna patterns have minimal overlap in the areas covered by the incoming path distribution.

We expect that spatial diversity is more effective than pattern diversity in scenarios such as open terrain environments where the multipath signals have similar angles of arrival and therefore a very narrow incoming path distribution. The direction of spatial separation, whether horizontal or vertical or some combination of the two, is only relevant in terms of the separation relative to the source. Therefore the effectiveness of a spatial diversity system is dependent on

the spatial separation in relation to the incoming path distribution. For scenarios limited to line of sight this may be constant but for more complicated incoming path distributions the effective separation between the antennas varies as a function of observer location or incoming signal angle. When the frequency is high, variations in the contribution of the spatial diversity term are more sensitive to variations in incoming angle. Additionally as the antenna separation is increased to more and more odd multiples of one half wavelength the variations in the spatial diversity term given by Equation 3 will be more numerous over the whole range of possible incoming path angles.

6. Conclusion

The design of pattern and spatial diversity systems is complicated by the tradeoff involved in choosing between antennas with pattern orientations that overlap minimally and those that cover the possible area of signal reception optimally. Given a specific application with its predetermined frequency and chassis parameters, four basic design elements are left to the engineer: First, choosing the right antenna types to give maximal coverage in the areas of interest. Second, positioning those antennas so as to maximize the benefits of spatial diversity given a predetermined incoming path distribution. Third, orienting the antennas so as to increase the effectiveness of a pattern diversity system. And fourth, spatially isolating the antennas from one another to allow for the greatest flexibility in diversity combining techniques.

This research has developed an algorithm to aid in the design and evaluation of both pattern and spatial diversity systems working separately or in tandem. The efficacy of an antenna diversity system is evaluated by calculating the normalized correlation between the signals from two antennas. This is done using exactly the same efficient discrete algorithm for theoretical, simulated, or idealized patterns. The tool developed incorporates two or three dimensional antenna patterns, three degrees of freedom in spatial and pattern diversity, and any specified incoming path distribution. The antenna patterns, spatial and pattern configurations, and incoming path distribution are defined by the user. The specific configurations of the spatial and pattern diversity system can be set to obtain the specific normalized correlation coefficient of a particular system. Additionally, multiple configuration variables (antenna spacing, patterns, or expected incoming distributions) can be left as variables so that the tool can be used for design to generate plots of the correlation coefficient as a function of these variables. The potential of this new tool has been demonstrated through evaluation of three integrated antenna diversity systems for common portable wireless chassis.

7. Acknowledgments

This work was supported in part by NSF Grant #CDA-9601602. The authors thank C. Short and E. Swanson for designing and fabricating antennas and performing measurements for the 5.8 GHz WLAN system. Rogers Corporation, Chandler, AZ, provided dielectric substrates.

8. References

[1] Y. Ebine and Y. Yamada, "A Vehicular-Mounted Vertical Space Diversity Antenna for a Land Mobile Radio," *IEEE Trans. Veh. Technol.*, vol. 40, no. 2, pp. 420-425, May 1991.

[2] Y. Yamada, K. Kagoshima, and K. Tsunekawa, "Diversity Antennas for Base and Mobile Stations in Land Mobile Communication Systems," *IEICE Trans.*, vol. E 74, no. 10, pp. 3202-3209, October 1991.

[3] J. S. Colburn, Y. Rahmat-Samii, M. A. Jensen, and G. J. Pottie, "Evaluation of Personal Communications Dual-Antenna Handset Diversity Performance," *IEEE Trans. Veh. Technol.*, vol. 47, no. 3, pp. 737-746, August 1998.

[4] P. Irazoqui-Pastor, E. Swanson, C. Short, and J. T. Bernhard, "An Analysis And Design Tool For Evaluation Of Integrated Antenna Diversity Systems In Portable Wireless Devices," *Proc. IEEE AP-S International Symp.*, vol. 3, pp. 2062-2065, 1999.

[5] W. C. Jakes, ed., *Microwave Mobile Communications*, IEEE Press, New York: 1974.

[6] T. Taga, "Analysis of Correlation Characteristics of Antenna Diversity in Land Mobile Radio Environments," *Electronics and Communications in Japan*, vol. 74, no. 8, pp. 101-115, 1991.

[7] R. G. Vaughan, "Pattern Translation and Rotation in Uncorrelated Source Distribution for Multiple Beam Antenna Design," *IEEE Trans. Antennas Propagat.*, vol. 46, no. 7, pp. 982-990, July 1998.

[8] A.V. Oppenheim and R.W. Schafer, *Discrete Time Signal Processing*, Upper Saddle River, NJ: Prentice Hall, 1989.

[9] P. Irazoqui-Pastor, "Evaluation of Integrated Antenna Diversity Systems," Master's thesis, University of New Hampshire, 1999.

[10] K. M. Coperich, "Numerical Analysis of Diversity Antenna Systems for Hand-held Communication Devices," Master's thesis, University of Illinois at Urbana-Champaign, 1996.

[11] D. Robbins and M. G. Amin, "Cellular Mobile Radio Communication Channels in View of Smart Antenna Systems," *Microwave Journal*, pp. 74, April 1998.

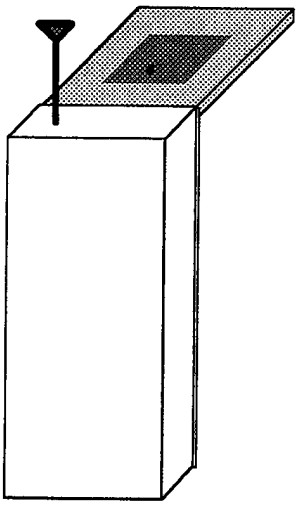

Figure 1: The first diversity configuration on a handset operating at 1.622 GHz with a monopole antenna and flip-up microstrip antenna.

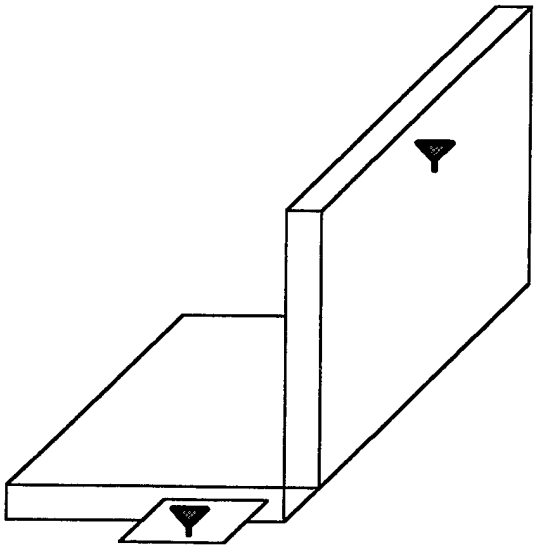

Figure 2: The second diversity configuration on a laptop computer operating at 2.44 GHz with a monopole antenna deployed from a PCMCIA card extended from the side of the keyboard and a microstrip antenna integrated into the back of the display. The angle of the display relative to the keyboard is 90^0.

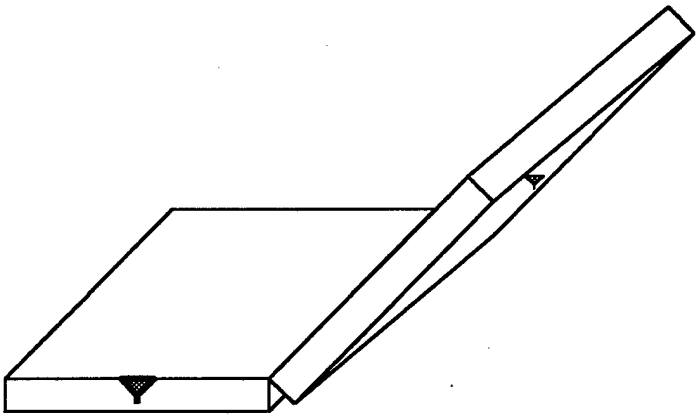

Figure 3: The third diversity configuration on a laptop computer operating at 5.8 GHz with a microstrip antenna integrated into side of the keyboard and a microstrip antenna integrated into the back of the display. The angle of the display relative to the keyboard is 135^0.

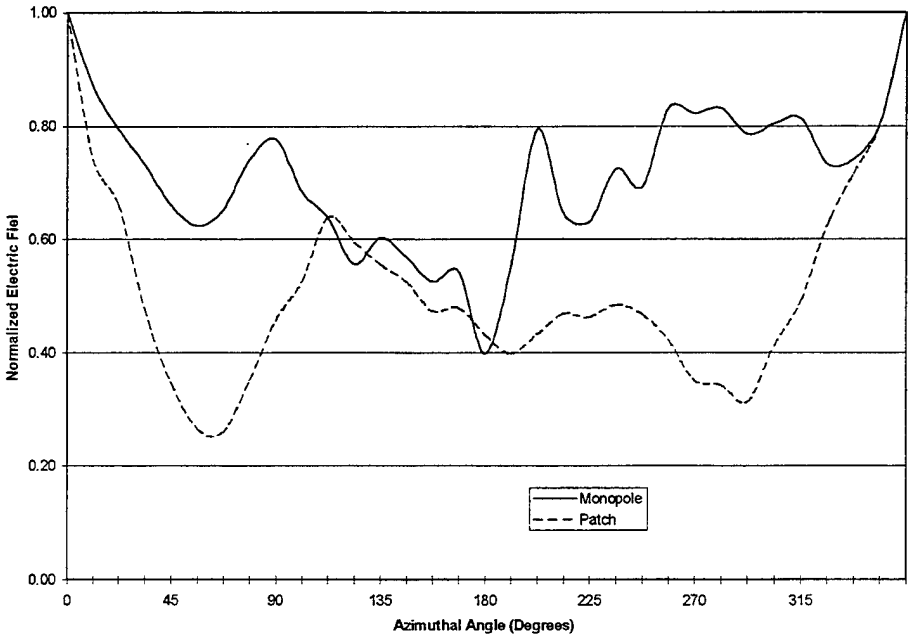

Figure 4: Measured normalized electric field radiation patterns for the two antennas of Configuration 1 in place on the handset chassis.

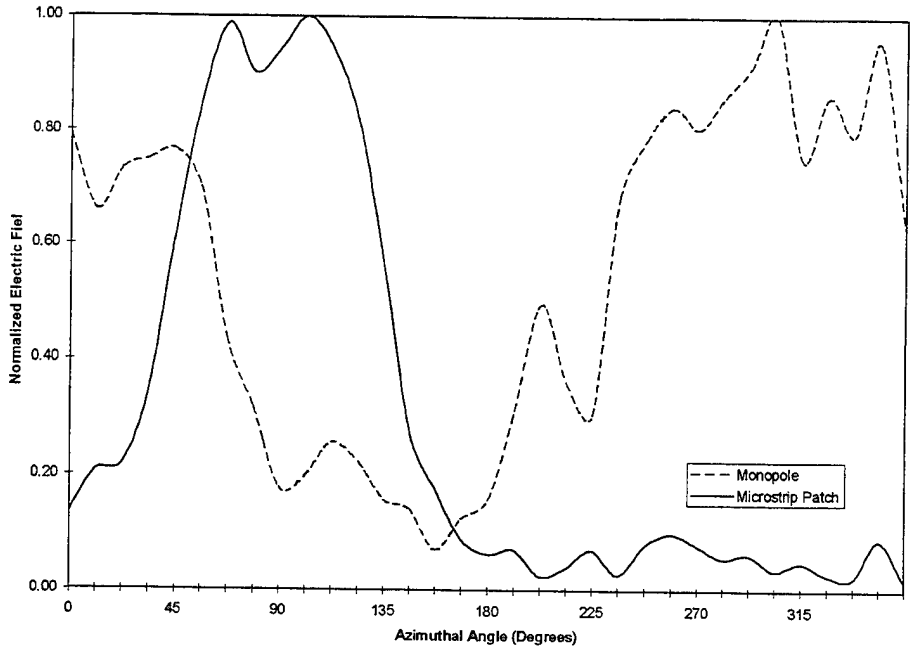

Figure 5: Measured normalized electric field radiation patterns for the two antennas of Configuration 2 in place on the laptop chassis.

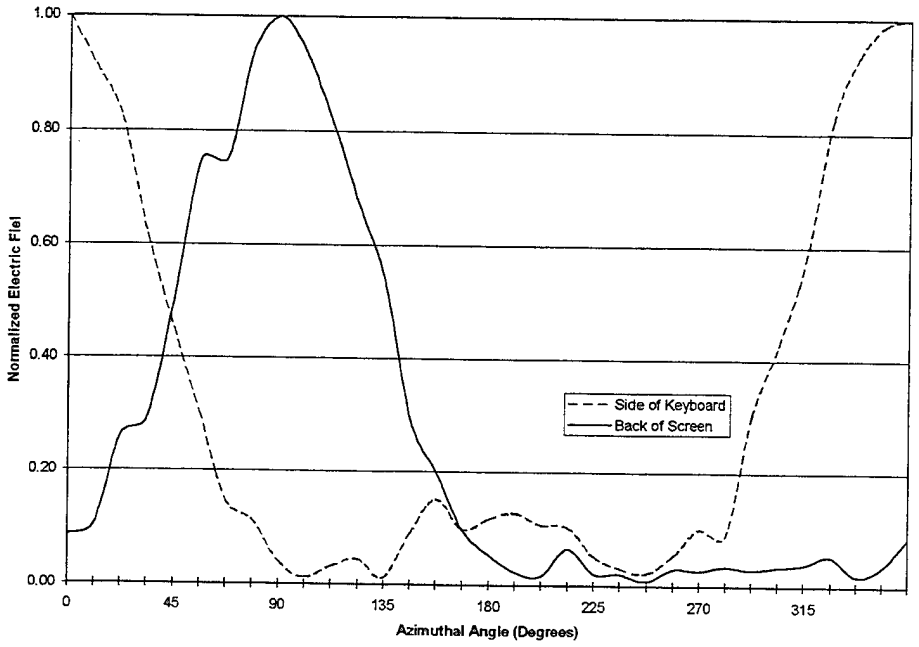

Figure 6: Measured normalized electric field radiation patterns for the two antennas of Configuration 3 in place on the laptop chassis.

The Circularly Polarized Cylindrical Patch

Zvonimir Sipus[1], Naftali Herscovici[2] and Davor Bonefacic[1]

[1]Faculty of Electrical Engineering and Computing
University of Zagreb, Unska 3, HR-10000 Zagreb, Croatia
[2]Cushcraft Corporation, Manchester, NH 03108, USA

Abstract The paper presents a new type of the antenna with a dipole-like radiation pattern and circular-polarization. The antenna is a cylindrical patch antenna fed by a coax line, with a special geometry with generates the circular polarization. The configuration was optimized so it would generate the minimum axial ratio in the azimuthal plane where the pattern is omnidirectional. The antenna proposed is a simple and inexpensive solution for any wireless communication systems where omnidirectional pattern and circular polarization are required.

INTRODUCTION

Antennas with a dipole-like pattern and circularly polarized are usually combination of a number of radiating elements. The most common configuration consists of four dipoles slanted 45° and located on the perimeter of a circle such that each dipole faces another dipole slanted in the opposite direction. When fed appropriately this array generates a dipole-like pattern with a circular polarization. The design of high-gain arrays based on this type of antenna would probably be quite complicated, and expensive.

This paper discusses the cylindrical-rectangular patch antenna as a new type of an antenna with circular-polarized dipole-like radiation pattern. The geometry of the antenna is shown in Figure 1. It is an almost square patch wrapped around a grounded dielectric cylinder. Both TM_{10} and TM_{01} modes are excited with shifted resonant frequency, similarly to the planar case [1], [2]. In this case, though, the circular polarization is achieved in the whole azimuthal plane, not only in a limited angular sector.

The main problem in designing such an antenna is that the radiation patterns due to the TM_{10} and TM_{01} modes have different phase characteristics which are important to synthesize in order to get circular polarization.

ANALYSIS

The analysis of the cylindrical patch antenna was performed using the moment method approach described in [3], [4]. A program for the computation of the input impedance and radiation pattern of cylindrical patch antennas was first developed [4]. The currents on the patch are ex-

panded into entire domain basis functions. Spectral-domain dyadic Green's function is calculated by using the general routine G1DMULT [5], which permits the analysis of patch antennas in multilayer structures. The algorithm divides the field problem in appropriate sub-problems by using equivalence, and determines the tangential field components at the interfaces between the layers of the structure (the spectral domain problem is modeled as a spatial domain problem with sources in the form of harmonic current tubes). The feed is modeled as a constant current distribution without considering its self-impedance. This analysis approach was previously tested in the design of both horizontal and vertical polarized cylindrical patch antennas [4].

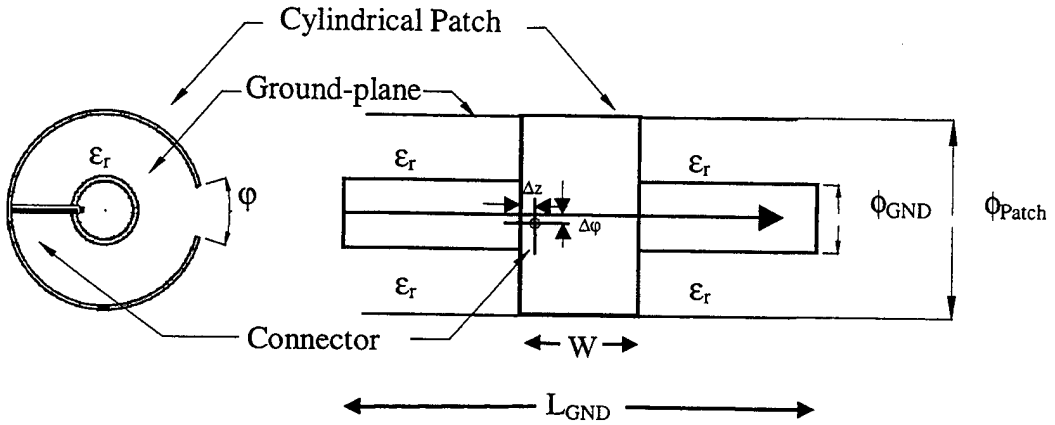

a. Axial cut

b. Longitudinal cut

Figure 1 - The geometry of the Circularly Polarized Omnidirectional Cylindrical Patch.

As mentioned above, the basis functions used are entire domain functions. During the design process, the phase of the coefficient of the fundamental TM_{01} and TM_{10} basis function are monitored. In the planar case, to obtain circular polarization, the phase differential between these two modes should be 90°. In the cylindrical case, considering the fact that the vertical mode has a different geometry than the horizontal mode, the optimum axial ratio (for the particular set of design parameters) was found for a phase differential of 50°. The synthesis process uses this information in the calculation of the patch dimensions. Finally, the antenna is optimized for axial ratio at 1.92 GHz.

DESIGN EXAMPLE

The parameters of the antenna are: the relative permittivity of the substrate, $\varepsilon_r = 4.2$, the diameter of the grounded cylinder, $\Phi_{GND} = 1.2$ cm, the diameter of the patch, $\Phi_{Patch} = 1.36$ cm, the width of the patch, W = 1.98 cm, the angular gap $\varphi = 25.8°$. The feed point is offset with respect to the z-axis and φ-axis: $\Delta z_{probe} = 1.9$ cm, $\Delta\varphi_{probe} = 18.9°$. The antenna was optimized for 1.92 GHz the

mid-frequency of the PCS band. Figure 2 shows the axial ratio pattern in the azimuthal plane of the antenna shown in Figure 1. From Figure 2 it can be seen that the axial ratio is lower than 6 dB in the whole azimuthal plane and no visible effect of the probe is noticed. Further improvement of the axial ratio could probably be achieved by increasing the dielectric permittivity, however the frequency bandwidth would be narrower. The lowest axial ratio is for $\varphi = 90^{\circ}$ and the highest axial ratio is for $\varphi=0°$. Figure 3 shows the copolarized and crosspolarized radiation patterns in the azimuthal plane. As expected the higher the crosspolarization level, the higher the

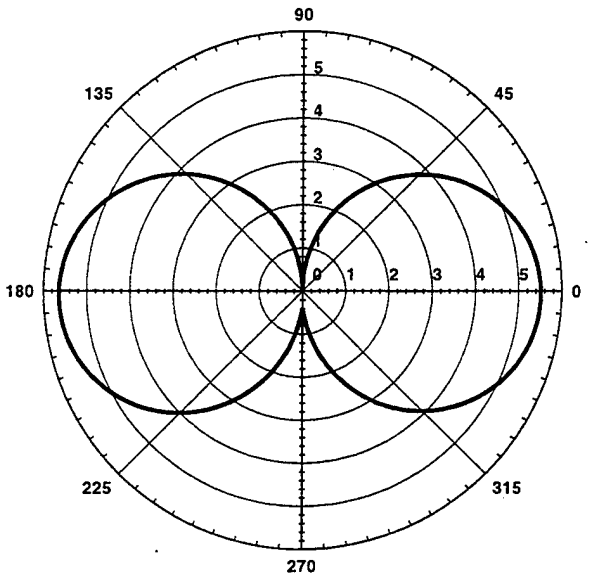

Figure 2 - The axial ratio in the azimuthal plane at 1.92 GHz

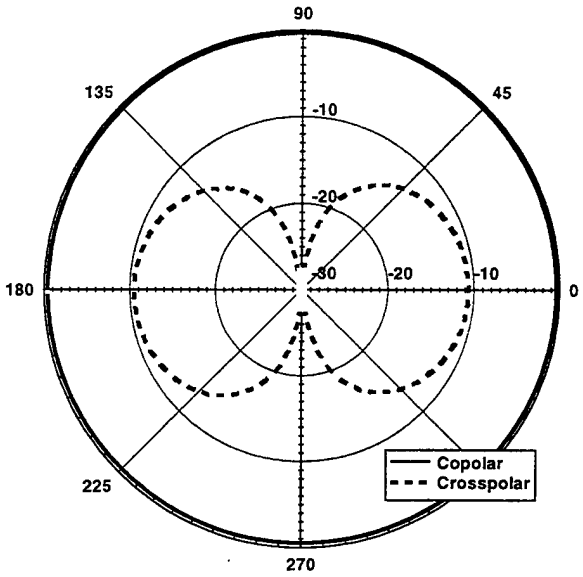

Figure 3 - The copolar and the crosspolar patterns at 1.92 GHz in the azimuthal plane

axial ratio is. The omnidirectionality is 0.2 dB, which is a result of the small diameter (in wavelengths) of the cylindrical patch. Figure 4 shows the axial ratio and the radiation pattern for two elevation planes ($\varphi = 90°$ and $\varphi =0°$). Here effect of the radiation of the probe is noticed towards the grazing angles where the axial ratio is high anyway. In the $\varphi =90°$ plane, the axial ratio is smaller than 3 dB from $\theta = 31°$ to $\theta = 112°$. This 81° elevation angular sector is reduced to 0° in the azimuthal angular sector of $\varphi = 57°$ to $\varphi = 125°$.

The frequency band of this particular antenna (defined as the frequency band over which an average degradation in the axial ratio of 2 dB occurs in the azimuthal plane) is approximately the same as the bandwidth of the planar version of the 'almost square' patch. For this particular design the bandwidth is less than 1%, and it can probably be improved if we use a dielectric substrate with a lower permittivity or a thicker dielectric.

CONCULSIONS AND FUTURE WORK

A new type of antenna was proposed. The antenna is circularly polarized and has a dipole-like pattern. The achievement of the circular polarization for this geometry is a definite challenge due to the different modal currents propagating in the vertical and circumferential planes. Since, (from the structural point of view) this radiating element is similar to the one proposed in [4], it can be very easily arrayed to obtain circularly polarized omnidirectional linear arrays.
The possibility of the design of omnidirectional cylindrical patches based on a planar geometry was demonstrated. The design of a wide-band element with similar characteristics as the one proposed is currently under consideration.

REFERENCES:

[1] W. Richards, Y. Lo, D. Harrison, "An improved theory for microstrip antennas and applications", *IEEE Transactions on Antennas and Propagation,* Vol. 29, pp. 38-46, Jan 1981.
[2] P. Sharma, K. Gupta: "Analysis and optimized design of single feed circularly polarized microstrip antennas", *IEEE Transactions on Antennas and Propagation,* Vol. 31, pp. 949-955, Nov. 1983.
[3] T. Habashy, Sami M. Ali, Jin Au Kong, "Input Impedance and Radiation Pattern of Cylindrical-Rectangular and Wraparound Microstrip Antennas", *IEEE Transactions on Antennas and Propagation,* Vol. 38, pp. 722-731, May 1990.
[4] Naftali Herscovici, Zvonimir Sipus and Per-Simon Kildal, "The Cylindrical Omnidirectional Patch Antenna," *The IEEE AP-S International Symposium, Montreal, July 1997.*
[5] Z. Sipus, P-S. Kildal, R. Leijon, M. Johansson: "An algorithm for calculating spectral domain Green's functions for planar, circular cylindrical and spherical multilayer structures," to be published in the ACES Journal.

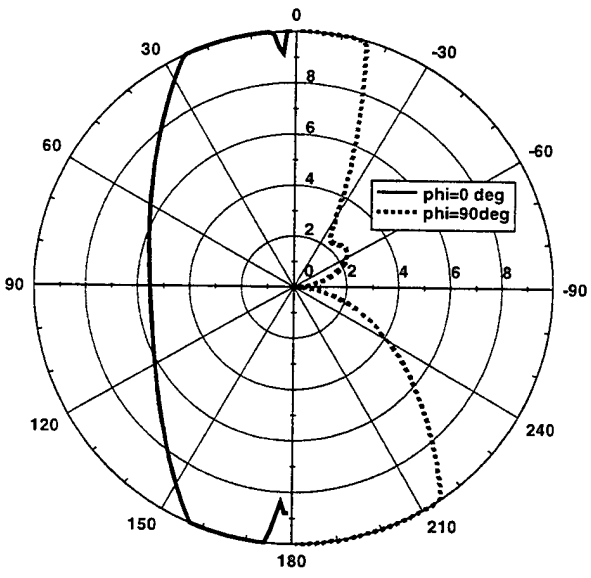

a.

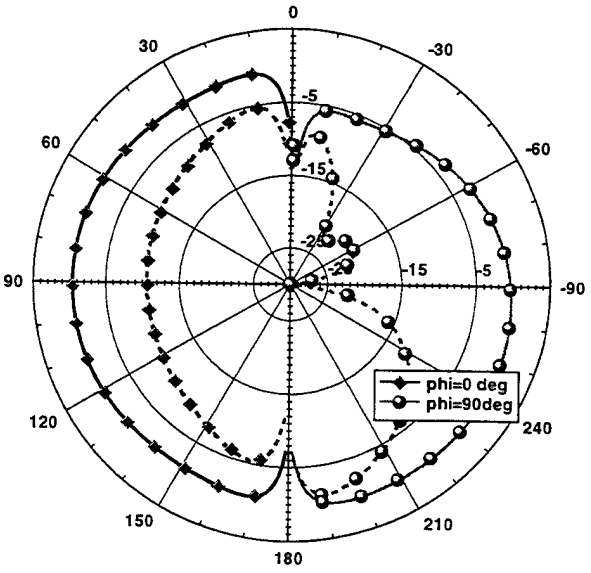

b.

Figure 4 – a. the axial ratio for $\varphi = 0°$ and $\varphi = 90°$, b. the elevation patterns for

STUDY OF BROADBAND DIELECTRIC RESONATOR ANTENNAS

A. A. Kishk, A. W. Glisson, G. P. Junker*

Department of Electrical Engineering
University of Mississippi, University, MS 38677

*501 W. Mariposa Ave., El Segundo, CA 90245

Abstract: A numerical study of a cylindrical dielectric resonator antenna on a conducting ground plane excited by a coaxial probe is presented. The numerical solution is based on the method of moments for a body of revolution coupled to a wire. We consider in this study dielectric resonators excited in the HEM_{11} and HEM_{12} modes for a split dielectric cylinder. This antenna shows a wideband performance of about 35%. Experimental measurements have verified this finding.

1. Introduction

Dielectric resonators are made of high dielectric constant materials. They have been used efficiently as microwave components in the design of filters because of their high quality factor. Therefore, many engineers have doubted their suitability for use as a radiator, thinking that they would no be efficient radiators and that they would have a very small radiation bandwidth. It has, however, been shown that some modes has a small radiation Q-factor [1]. The radiation efficiency has also been measured for the $HEM_{11\delta}$ mode of the cylindrical dielectric resonator with ϵ_r=38 and was found to be better than 98% [2]. Interest has continued to increase in dielectric resonator antennas (DRA's) [3] due to their small size, efficiency, and potential ability to perform multiple antenna tasks via simple mode coupling mechanisms. More attention and study needs to be given to this antenna to obtain a better understanding of its performance characteristics. Accurate analysis of the DRA must be performed numerically and is somewhat difficult. Such analyses, however, help in the physical understanding for the performance of this antenna and in determining optimal usage of the antenna. Many studies have concentrated on the cylindrical DRA structures [4], for which the TM and quasi- TM modes may be excited by having the dielectric

disk situated on a ground plane [5]. Little attention has been given to cylindrical DRA structures excited in the TE and quasi-TE modes, because they cannot be excited with the circular base is placed on a ground plane.

In this paper we briefly discuss some of the characteristics of the DRA's related to the $HEM_{11\delta}$ and the $HEM_{12\delta}$ modes compared to the more commonly studied $TM_{01\delta}$ mode and the $TE_{01\delta}$ mode. Some basics regarding their excitation mechanism are described, and empirical expressions are given to compute accurately the resonant frequency and the radiation Q-factor for the ideal case. To permit excitation of the $HEM_{12\delta}$ mode for a resonator situated on a ground plane, a split cylindrical DRA such as shown in Fig. 1 is considered. The $HEM_{11\delta}$ mode can also be excited in this configuration. Results are presented showing a broadband performance of the DRA excited in single mode operation, which reaches about 35%. Also, in some cases it is possible to have a dual band performance with the proper excitation of the DRA.

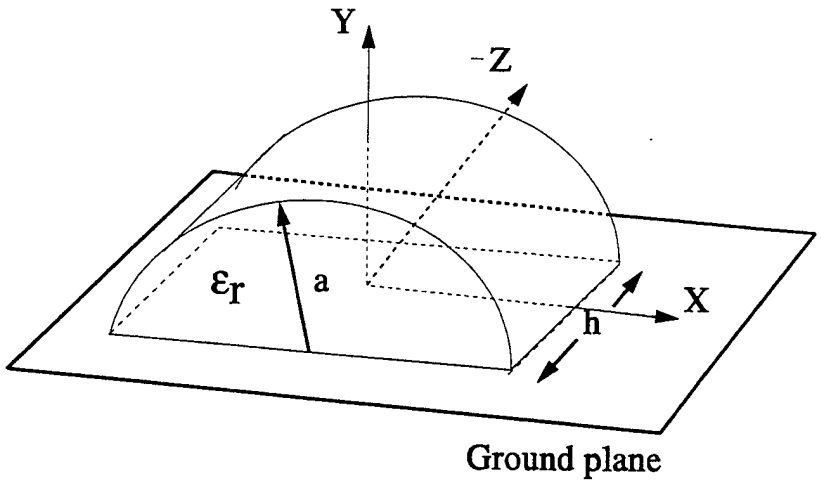

Fig. 1. Geometry of the split cylindrical DRA

2. Ideal Performance

To easily design a DRA for a particular use, one must have a reasonable idea of the resonant frequency, Q-factor, and mode of operation for various geometrical parameters associated with the DRA. The resonant frequency and the radiation Q-factor for a particular configuration may be computed numerically through a search

for the natural resonant frequencies (for a source free system) in the complex frequency plane as described in [6]. Once a natural frequency has been found, the mode associated with that natural frequency can be identified from its field distribution. The field distribution is also useful in determining an appropriate feed mechanism for the DRA.

For design purposes, however, this time consuming process would need to be repeated many times for different parameters until appropriate characteristics are achieved. It is desirable to have relatively accurate approximate methods to determine some of these characteristics quickly. Thus, we have computed the resonant frequencies and the radiation Q-factors for the first four modes $TM_{01\delta}$, $TE_{01\delta}$, $HEM_{11\delta}$ and the $HEM_{12\delta}$ modes for a cylindrical DRA as a function of different *a/h* (radius to height) ratios and for dielectric constants of 10, 22, and 38. Curve-fit equations are then obtained for the resonant frequencies and the Q-factors of these modes in terms of these parameters as

$$k_0 a = 2.920415\ \epsilon_r^{-0.465421} \times \left\{ 0.690841 + 0.319075\left(\frac{a}{h}\right) - 0.035494\left(\frac{a}{h}\right)^2 \right\} \quad (1)$$

and

$$Q = 0.012356\ \epsilon_r^{1.207086} \times \left\{ 5.2696\left(\frac{a}{h}\right) + 106.18807\left(\frac{a}{h}\right)^{0.624875} e^{-1.027195\left(\frac{a}{h}\right)} \right\} \quad (2)$$

for the $TE_{01\delta}$ mode,

$$k_0 a = 2.932566\,\epsilon_r^{-0.467715}\left\{1 - [0.075 - 0.05(\frac{a}{h})][\frac{\epsilon_r - 10}{28}]\right\} \times \left\{1.047542 + 0.377422(\frac{a}{h}) - 0.07112(\frac{a}{h})^2\right\} \quad (3)$$

and

$$Q = 0.008721\,\epsilon_r^{0.888413}\, e^{0.0397475\epsilon_r}\left\{1 - [0.3 - 0.2(\frac{a}{h})][\frac{38 - \epsilon_r}{28}]\right\} \times \left\{9.498196(\frac{a}{h}) + 2058.33(\frac{a}{h})^{4.322261}\, e^{-3.50099(\frac{a}{h})}\right\} \quad (4)$$

for the $TM_{01\delta}$ mode,

$$k_0 a = 2.734956\ \epsilon_r^{-0.436076} \times \left\{0.54318 + 0.589025(\frac{a}{h}) - 0.049591\,(\frac{a}{h})^2\right\} \quad (5)$$

and

$$Q = 0.012604\,\epsilon_r^{1.201971} \times \left\{2.134757(\frac{a}{h}) + 228.0429(\frac{a}{h})e^{-2.046468(\frac{a}{h}) + 0.110953(\frac{a}{h})^2}\right\} \quad (6)$$

for the $HEM_{11\delta}$ mode, and

$$k_0 a = 3.114093\,\epsilon_r^{-0.494406}\left\{1.189612 - (0.041212 - 3.408916\,e^{-2.624985(\frac{a}{h})})(\frac{a}{h}) + 1.548193\log(\frac{a}{h})\right\} \tag{7}$$

and

$$Q = (0.369661 + 0.02334\epsilon_r + 0.001051\epsilon^2)\left\{1 - 0.3(\frac{38-\epsilon_r}{28})^2[2.92 - (\frac{a}{h})]^{0.8}\right\} \times \left\{41.29139(\frac{a}{h})^{-2} - 110.8862(\frac{a}{h})^{-1} + (\frac{a}{h})(15.58616 + 334.2778\,e^{-1.070847(\frac{a}{h}) - 0.084812(\frac{a}{h})^2})\right\} \tag{8}$$

for the $HEM_{12\delta}$ mode.

The actual results for the resonant frequencies and Q factors obtained from the numerical search in the complex frequency plane and results computed using the above expressions are given in Figs. 2 to 5. In these figures the symbols represent the values obtained directly from the numerical search and the lines represent results predicted from the above expressions. It can be seen that the results predicted using the expressions agree reasonably well with the results obtained from the numerical search. It should be noted that the scales for graphs are the same for each of the different modes, so that comparisons can be fairly easily made between the different modes.

From the figures it is clear that the rates of change in the resonant frequency of the $TE_{01\delta}$ and $HEM_{12\delta}$ modes with respect to *a/h* is lower than those for the modes $TM_{01\delta}$ and $HEM_{11\delta}$. This provides an indication of the possibility of better wideband

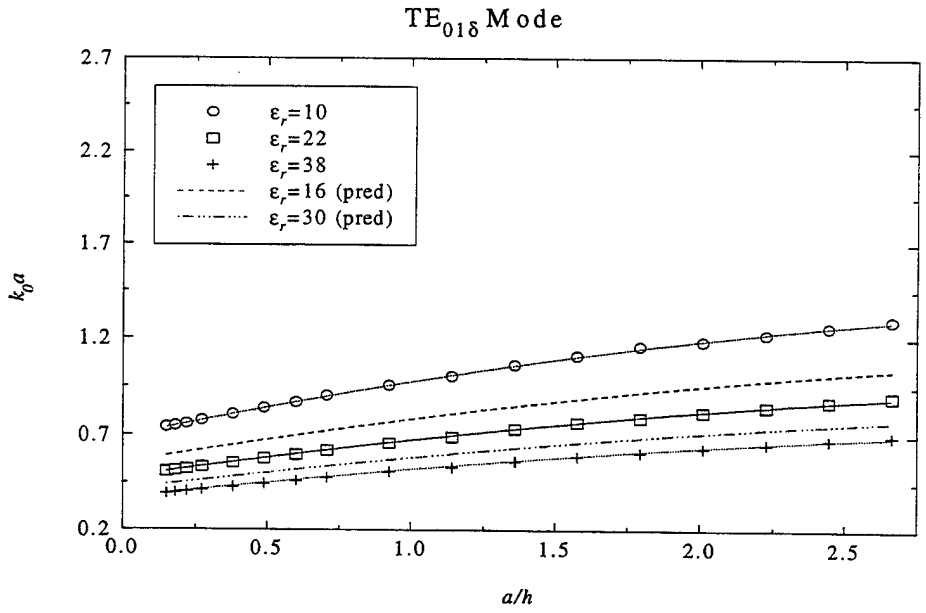

Fig. 2a. Normalized resonant frequency for the $TE_{01\delta}$ mode

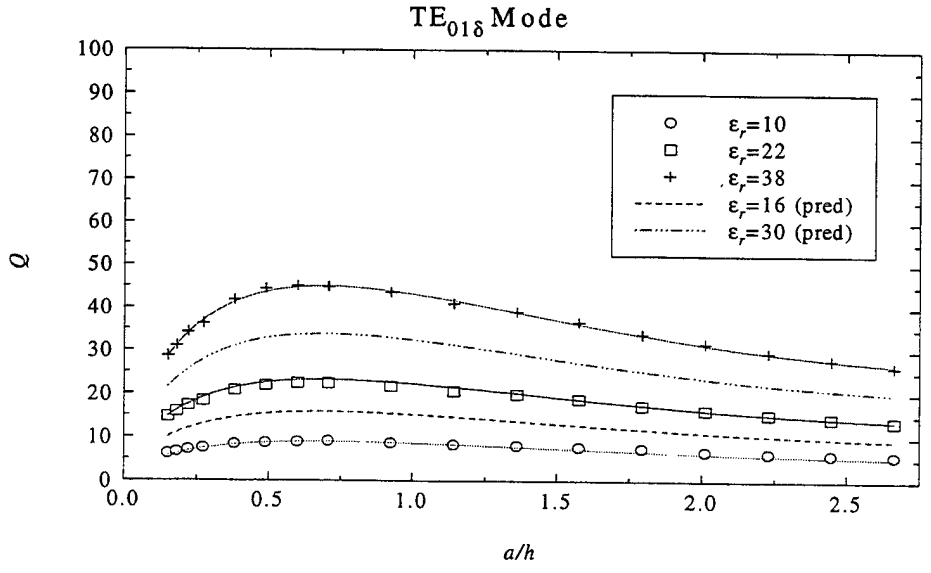

Fig. 2b. Radiation Q-factor for the $TE_{01\delta}$ mode

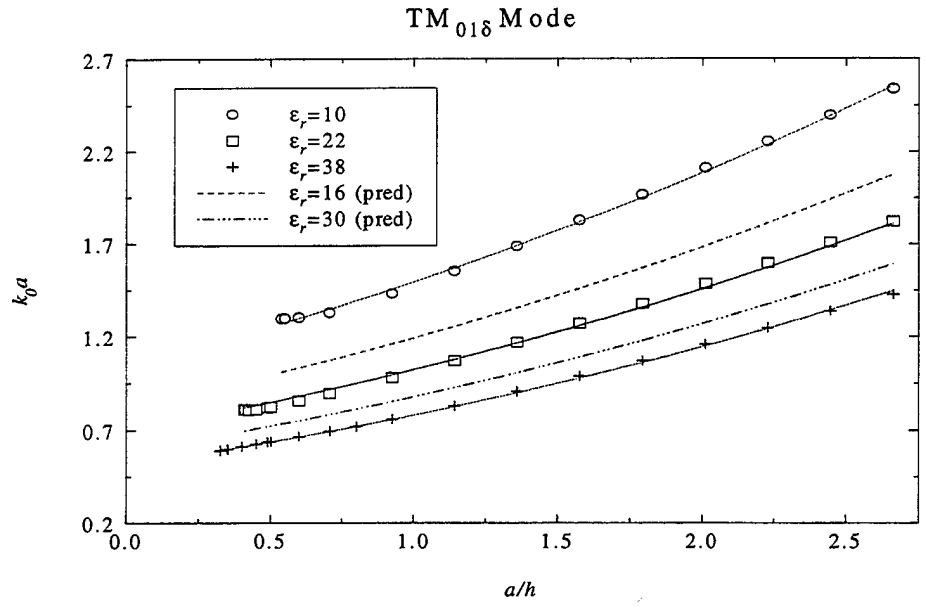

Fig. 3a. Normalized resonant frequency for the $TM_{01\delta}$ mode

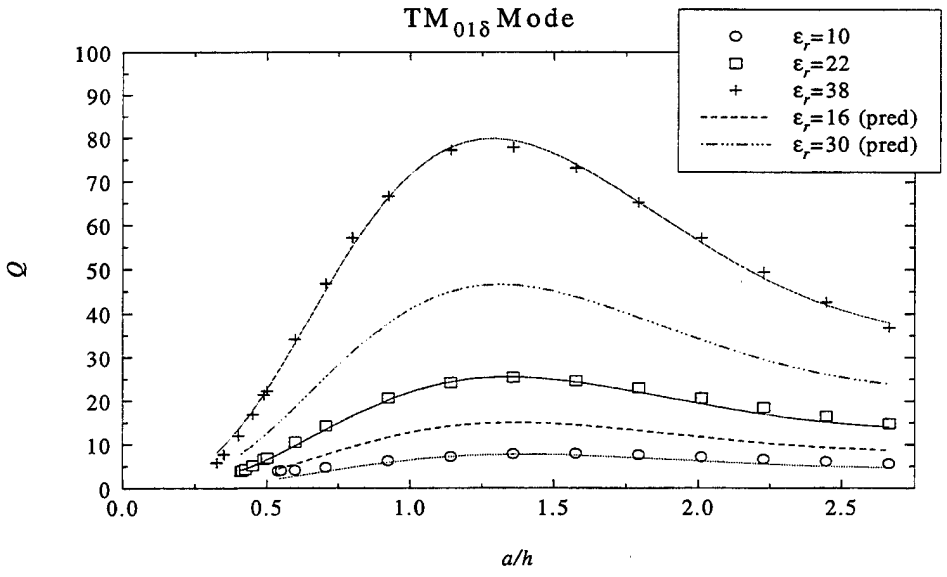

Fig.3b. Radiation Q-factor for the $TM_{01\delta}$ mode

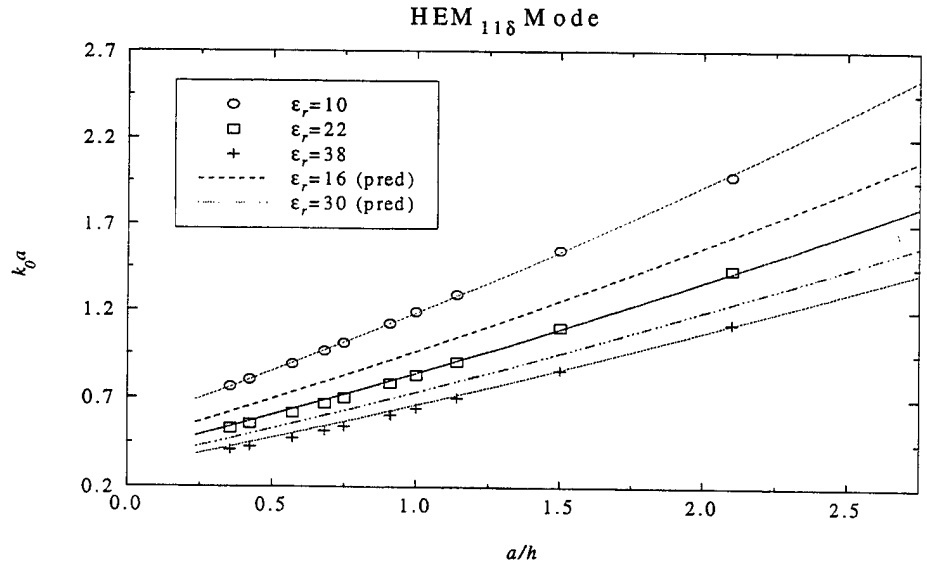

Fig. 4a. Normalized resonant frequency for the $HEM_{11\delta}$ mode

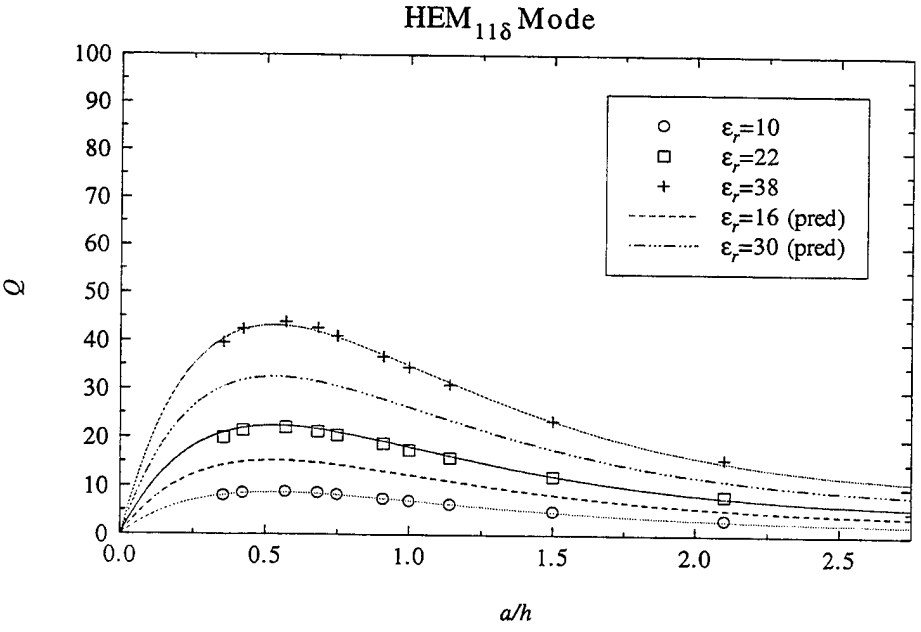

Fig. 4b. Radiation Q-factor for the $HEM_{11\delta}$ mode

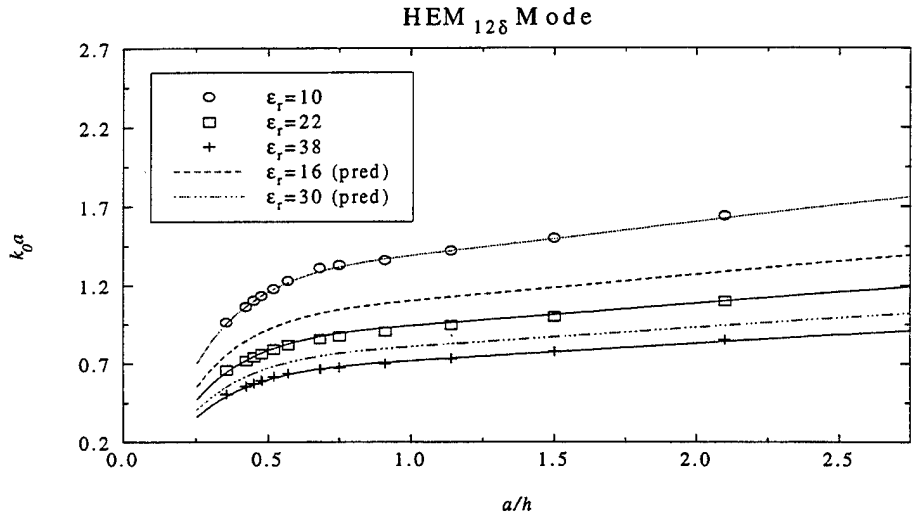

Fig. 5a. Normalized resonant frequency for the $HEM_{12\delta}$ mode

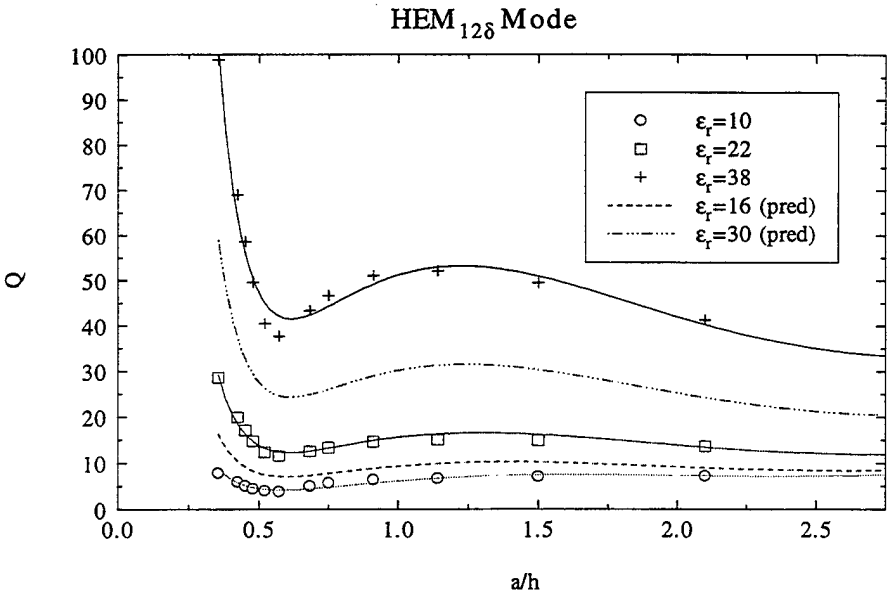

Fig.5b. Radiation Q-factor for the $HEM_{12\delta}$ mode

performance for the $TE_{01\delta}$ and $HEM_{12\delta}$ modes than for those of the $TM_{01\delta}$ and $HEM_{11\delta}$ type. To excite these modes properly, knowledge of the near field distribution for each mode permits one to choose the excitation mechanism appropriately. An electric current excitation can be chosen as a probe along the high density electric field lines or a magnetic current excitation can be chosen along the high density magnetic field lines by using narrow slots in the ground plane. The ideal far field patterns for the $HEM_{11\delta}$ and $HEM_{12\delta}$ modes are given in Figs. 6 and 7, respectively. In these and other radiation pattern plots that appear subsequently, the angular variation shown on the polar plots represents the standard spherical coordinate angles θ for y-z plane plots and φ for x-y plane plots. These far field radiation patterns are obtained based on the assumption that only the desired mode is radiating. Thus, they can be used as a reference for comparison with the actual radiation patterns that are obtained where more than one mode could be excited and contributing to the radiation patterns.

3. Numerical Results

Excitation of the $HEM_{11\delta}$ mode for the split cylindrical dielectric resonator antenna of Fig. 1 will result in a broadside radiation pattern. This broadside radiation pattern is similar to the radiation pattern of a narrow slot in a ground plane. The $HEM_{11\delta}$ mode mode can be excited by a monopole displaced along the z-axis from the position of z_f=0 (see Fig. 8). Here, we have restricted the orientation and position of

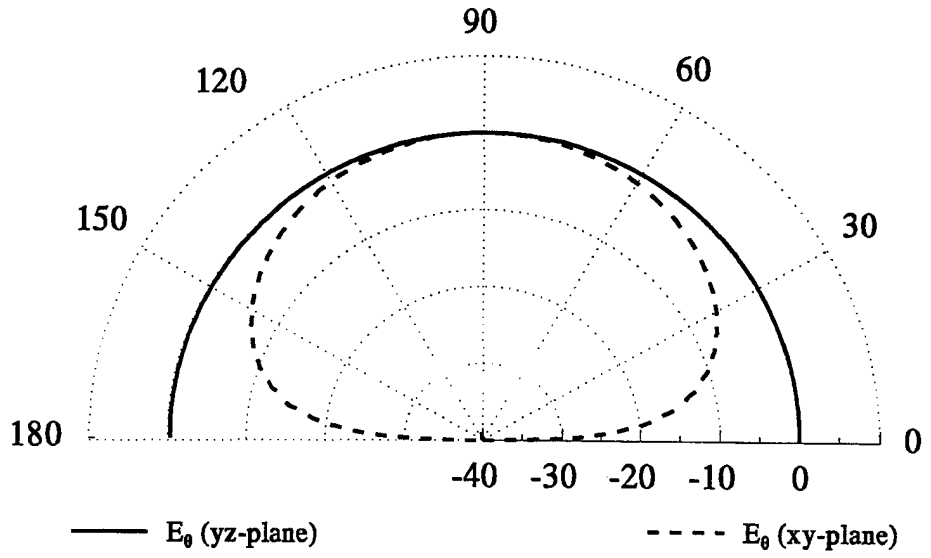

Fig. 6. Radiation patterns of the $HEM_{11\delta}$ mode

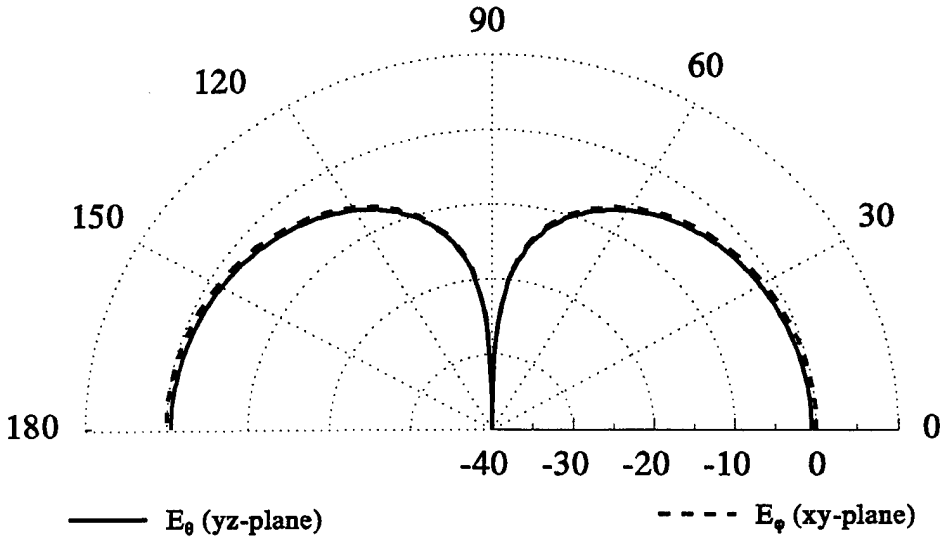

Fig. 7. Radiation patterns of the $HEM_{12\delta}$ mode

the monopole to be along the y-direction on the z-axis, where the DRA is the tallest, to allow for the largest possible variations of the monopole length as shown in Fig. 8. Fig. 9 shows the return loss of the split resonator with a_1=2.25 cm, h=3.9 cm, a_w= 0.0118 cm, z_f= 15.8 mm and ϵ_r = 12 with different wire lengths. Changing the wire length changes the return loss and shows that an optimum length of l_w=18 mm produces a bandwidth of about 22% (-10 dB return loss). Samples of the radiation patterns are computed at different frequencies as shown in Fig. 10. The radiation patterns show that the $HEM_{11\delta}$ mode is excited efficiently within this band, as the radiations patterns are very similar over the frequency range from 1.5 GHz to 1.9 GHz. When the excitation monopole is located at z_f=11.85 mm, i.e., closer to the center of the DRA, the bandwidth seems even wider than before, but a different monopole length (l_w=15.75 mm) is required as shown in Fig. 11. However, one observes in Fig. 12 that for this case the radiation pattern at f=1.9 GHz has deteriorated to be significantly changed from that of the $HEM_{11\delta}$ mode because other modes have started to contribute to the radiation pattern. When the monopole is placed even closer to the DRA center with z_f=3.95 mm, the matching bandwidth does not change much, as shown in Fig. 13, but the radiation patterns deteriorate even further at f=1.7 GHz and f=1.9 GHz as shown in Fig. 14. When the monopole is located at the DRA center with z_f=0.0 a very wide matching bandwidth is obtained as shown in Fig 15. This bandwidth is about 35%. From the radiation patterns in

Fig. 16, however, we can see that the radiating mode in this case is the $HEM_{12\delta}$ mode between the frequency range of 1.7 GHz to 2.3 GHz.

4. Dual-band Antennas

To obtain a dual band antenna, we must excite either two different modes having similar far field patterns with the required frequency separation or have two resonators of different sizes and materials operating at the same mode but at a different frequency. The latter approach will make the antenna large in size. A different possible approach is to make the two resonators together as if one resonator is loading the other. In this case, the design process is more difficult and requires many trials to reach to the required characteristics. Here we present an example of a dielectric resonator with h_2=22.8 mm, a_2=14.15 mm, and ϵ_2=36.0 that is inserted inside a dielectric resonator with h_1=39.5 mm, a_1=24.5 mm, and ϵ_1=12.0. The system is excited by a monopole located inside the smaller cylinder as illustrated in Fig. 17. The return loss of this antenna with different monopole lengths is shown in Fig. 18, where it can be seen that we have achieved multi-frequency operation. Figs. 19 and 20 show the radiation patterns at different frequencies and show that we have 3 different bands. The middle band is due to the excitation of the $HEM_{12\delta}$ mode and the other two bands are influenced by the $HEM_{11\delta}$ mode. The lower band appears to be due to the large DRA, while the upper band appears to be due to the smaller DRA.

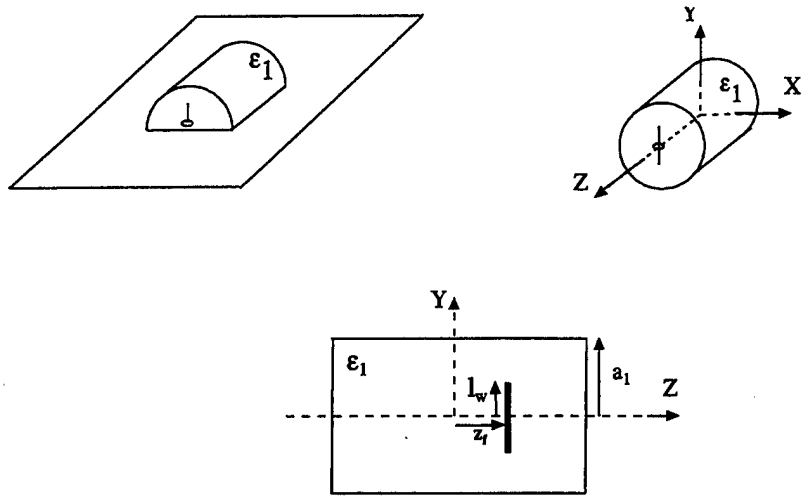

Fig. 8. Geometry for the split DRA with vertical dipole located on the z-axis: 3-D and cross-section views

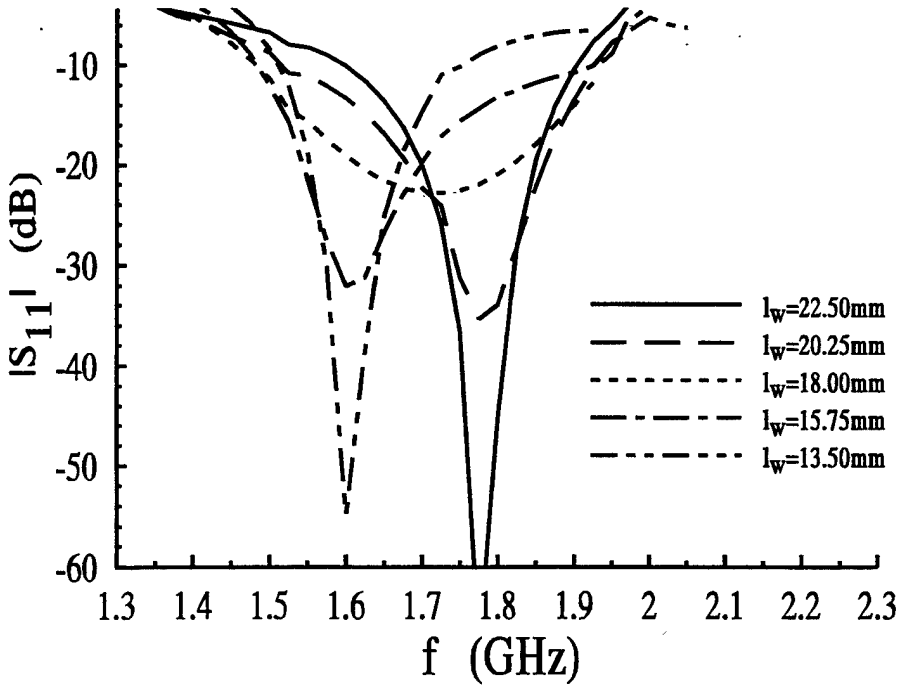

Fig. 9. Return loss versus frequency with z_f=15.8 mm

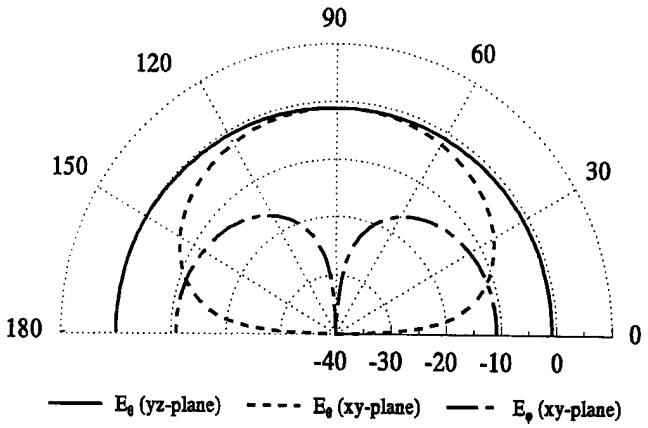

f = 1.5 GHz

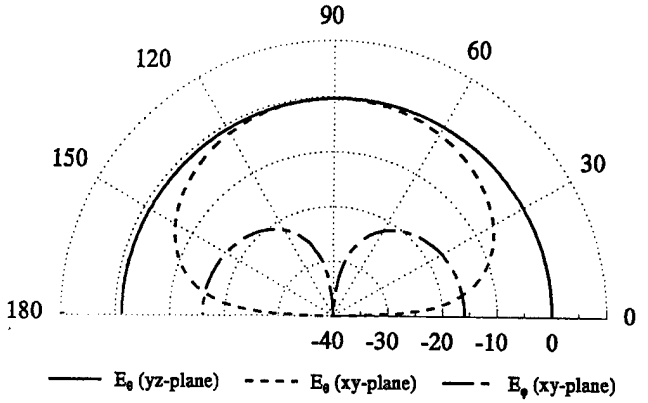

f = 1.7 GHz

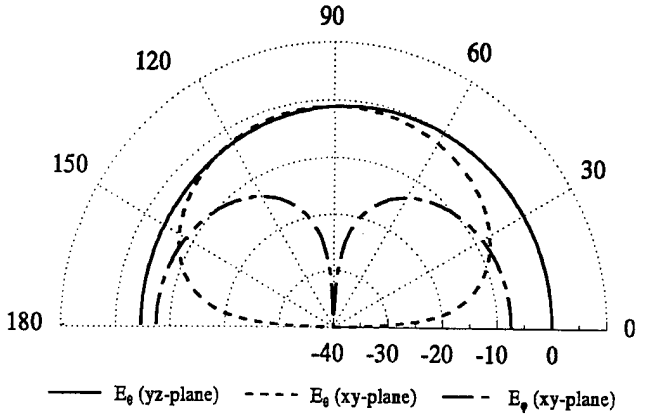

f = 1.9 Ghz

Fig. 10. Radiation patterns with z_f=15.8 mm and l_w=18 mm

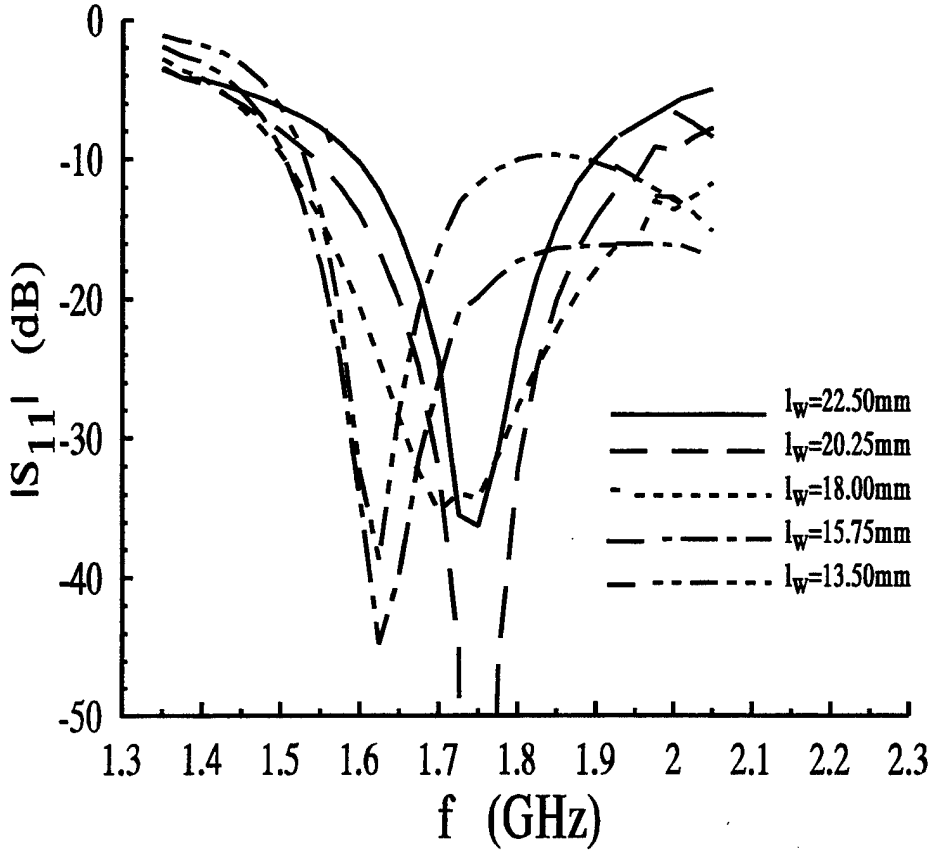

Fig. 11. Return loss versus frequency with z_f=11.85 mm

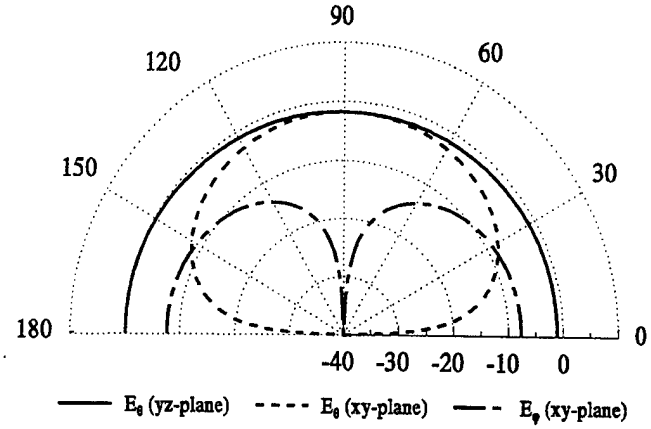

f = 1.5 GHz

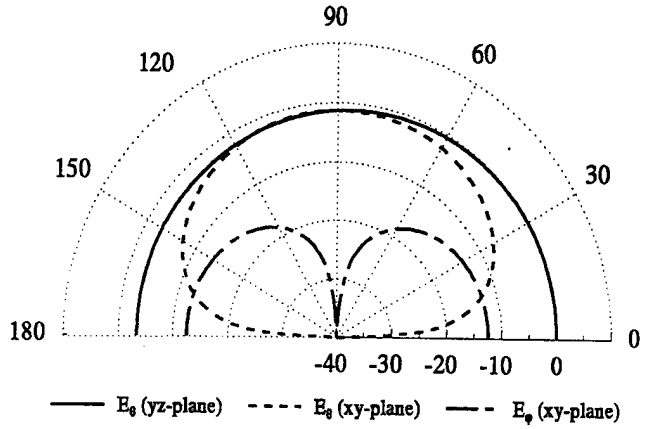

f = 1.7 GHz

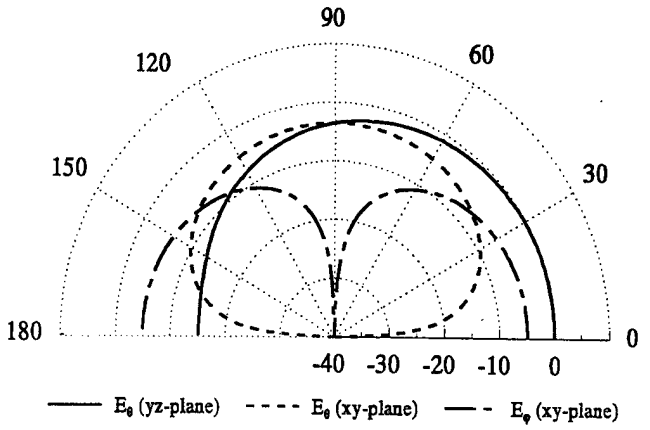

f = 1.9 GHz

Fig. 12. Radiation patterns with z_f=11.85 mm and l_w=15.75 mm

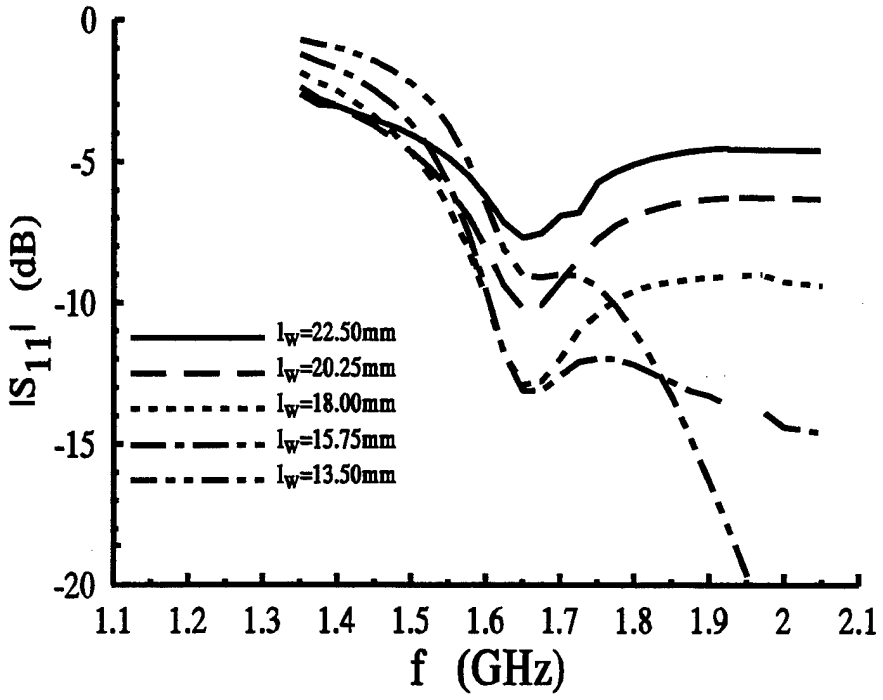

Fig. 13. Return loss versus frequency with z_f=3.95 mm

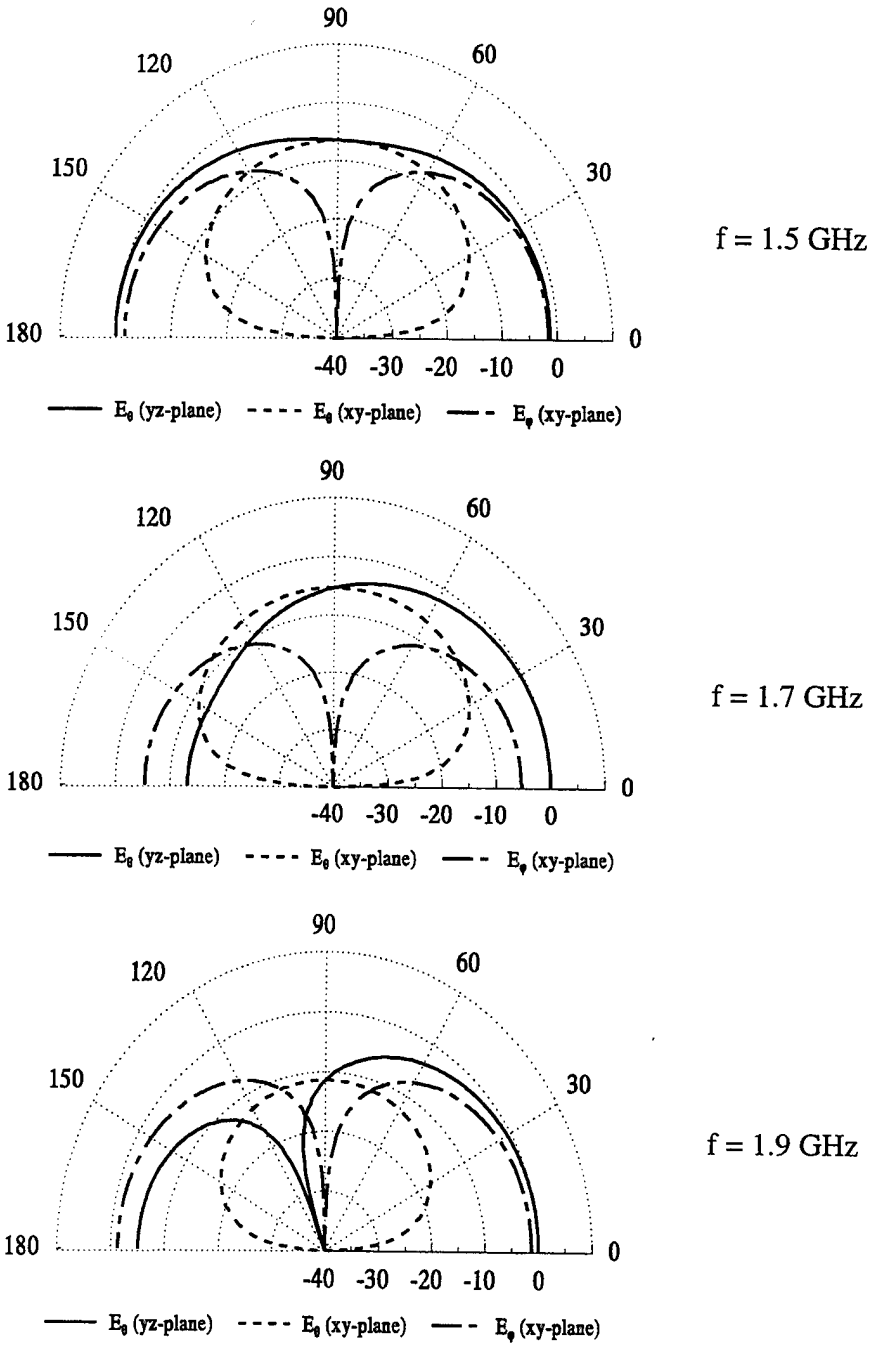

Fig. 14. Radiation patterns with z_f=3.95 mm and l_w=15.75 mm

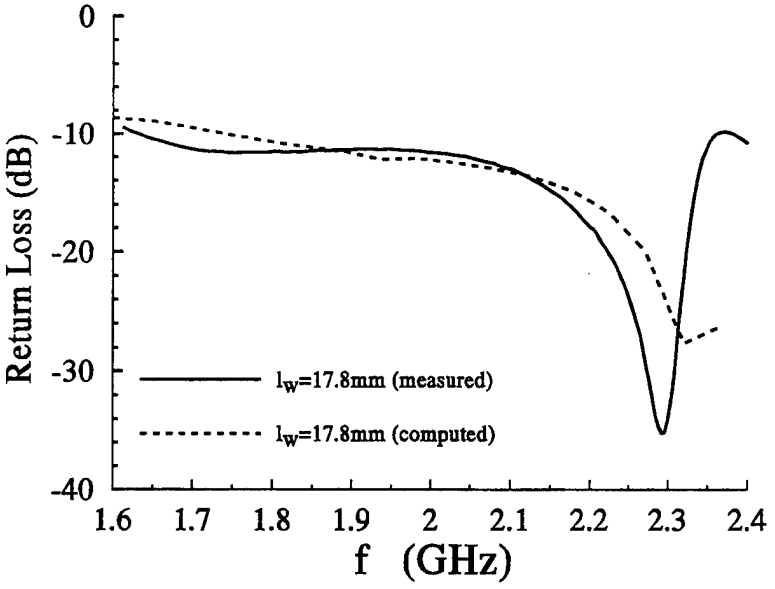

(a)

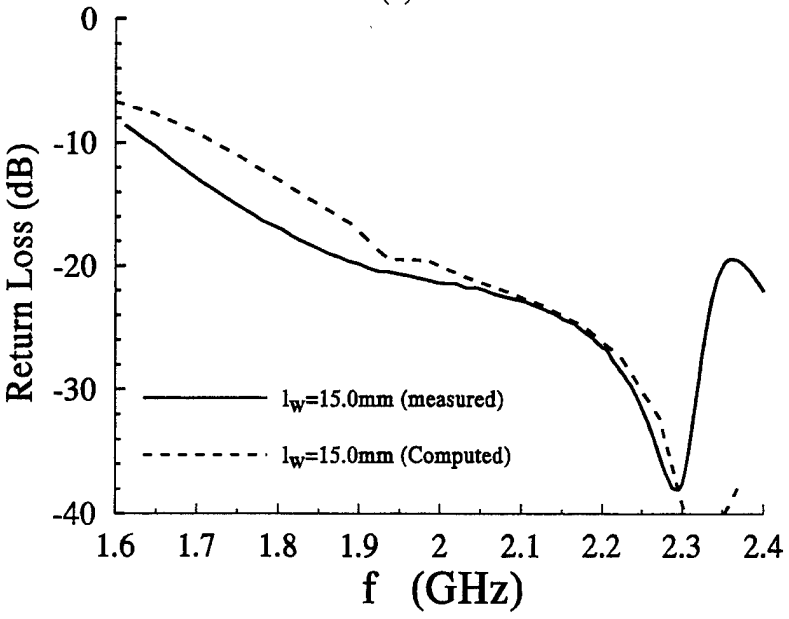

(b)

Fig. 15. Return loss versus frequency with z_f=0.0 mm and (a) l_w=17.8 mm or (b) l_w=15.0

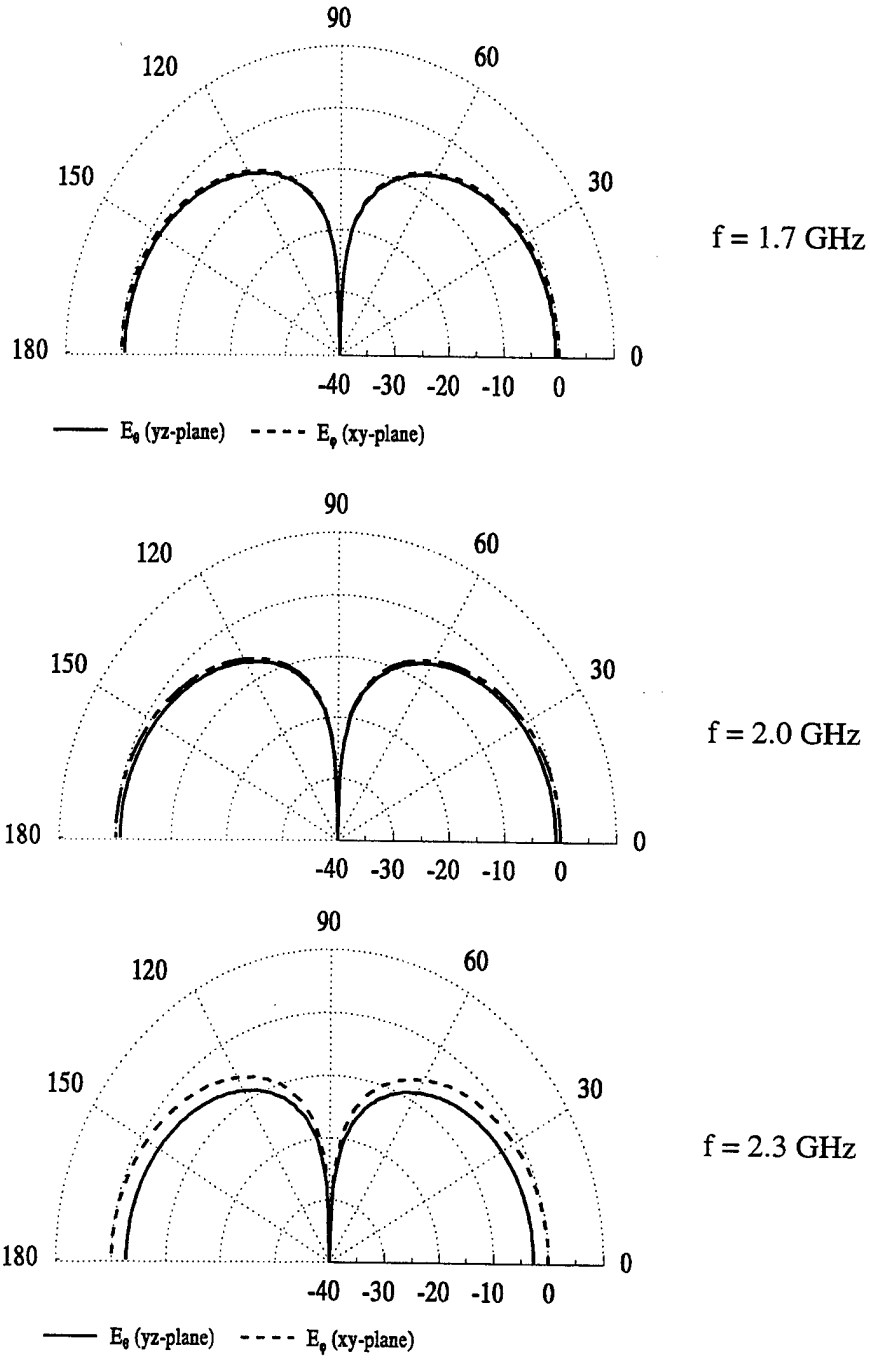

Fig. 16. Radiation patterns with z_f=0.0 mm and l_w=15.0 mm

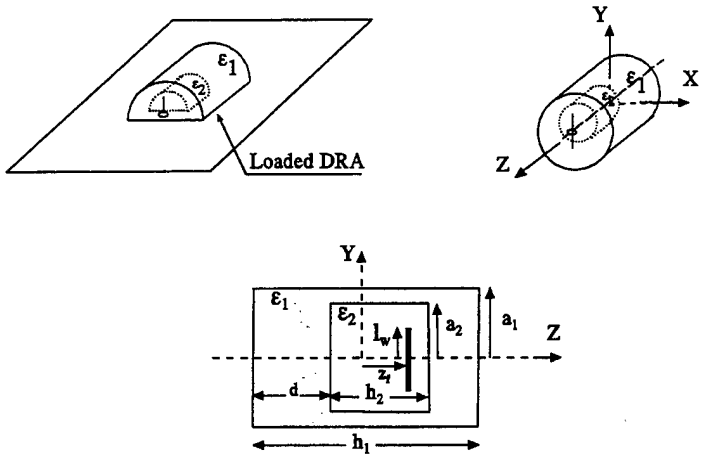

Fig. 17. Geometry for the loaded split DRA with vertical dipole located on the z-axis: 3-D and cross-section views

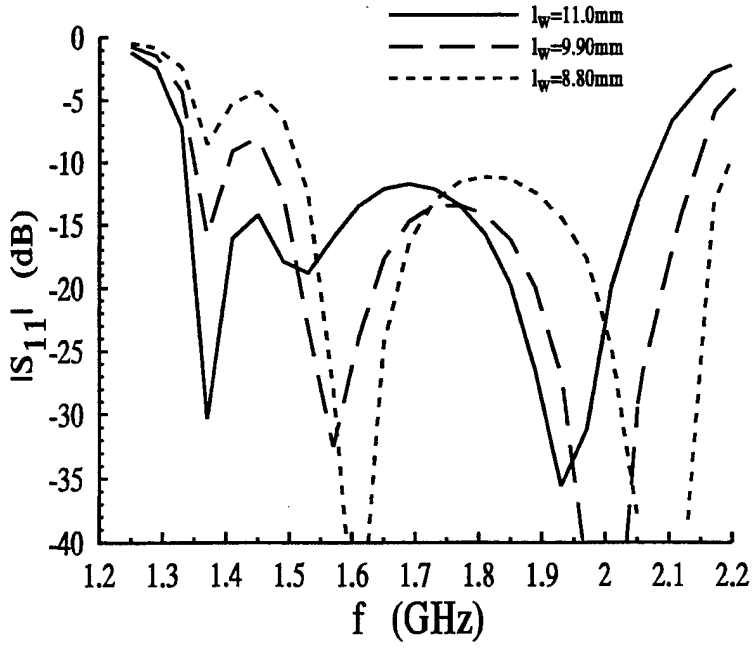

Fig. 18. Return loss versus frequency for the loaded split cylinder with the probe in the inner cylinder at $z_f = 4$ mm

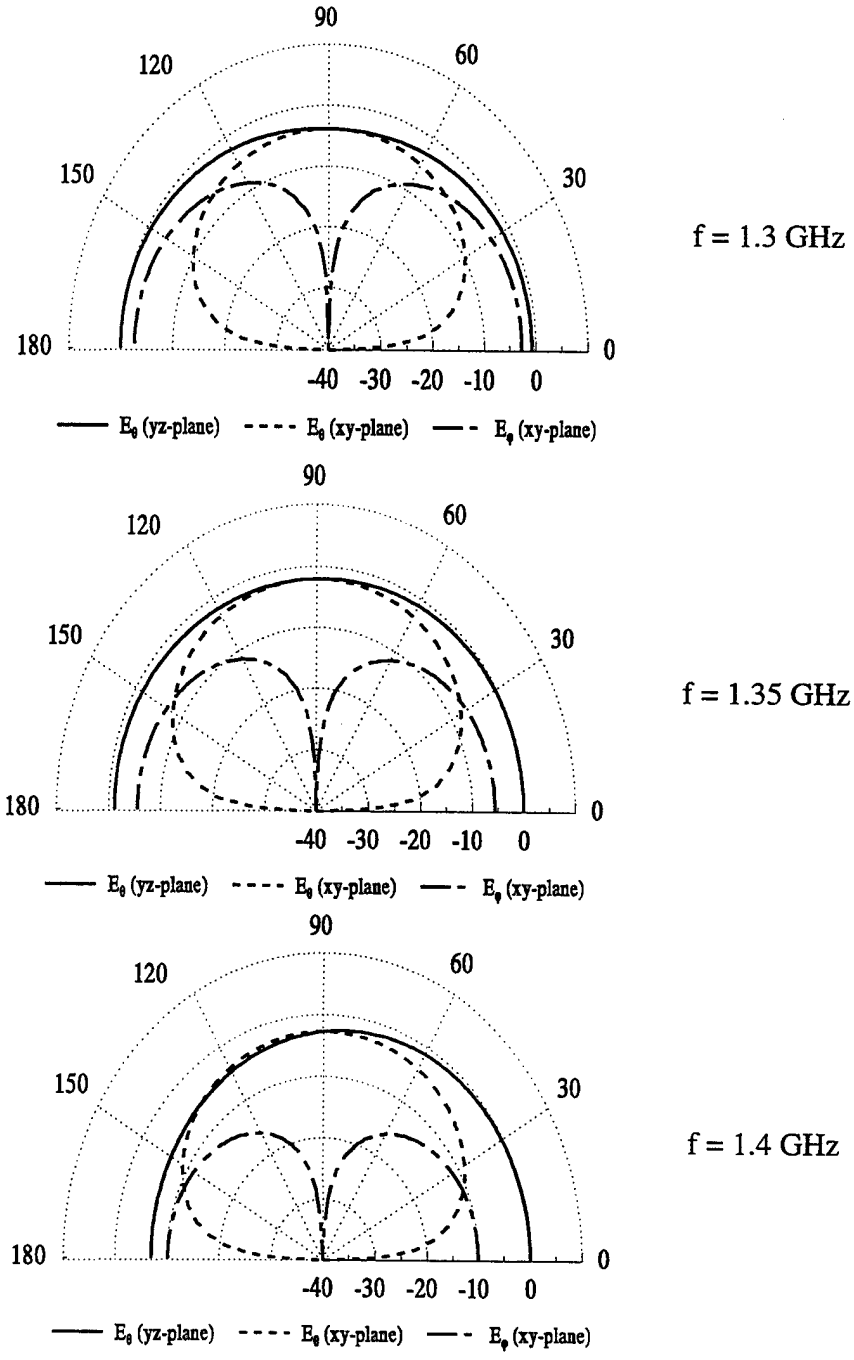

Fig. 19. Radiation patterns for the loaded split DRA with z_f=4 mm and l_w=11 mm around f=1.35 GHz

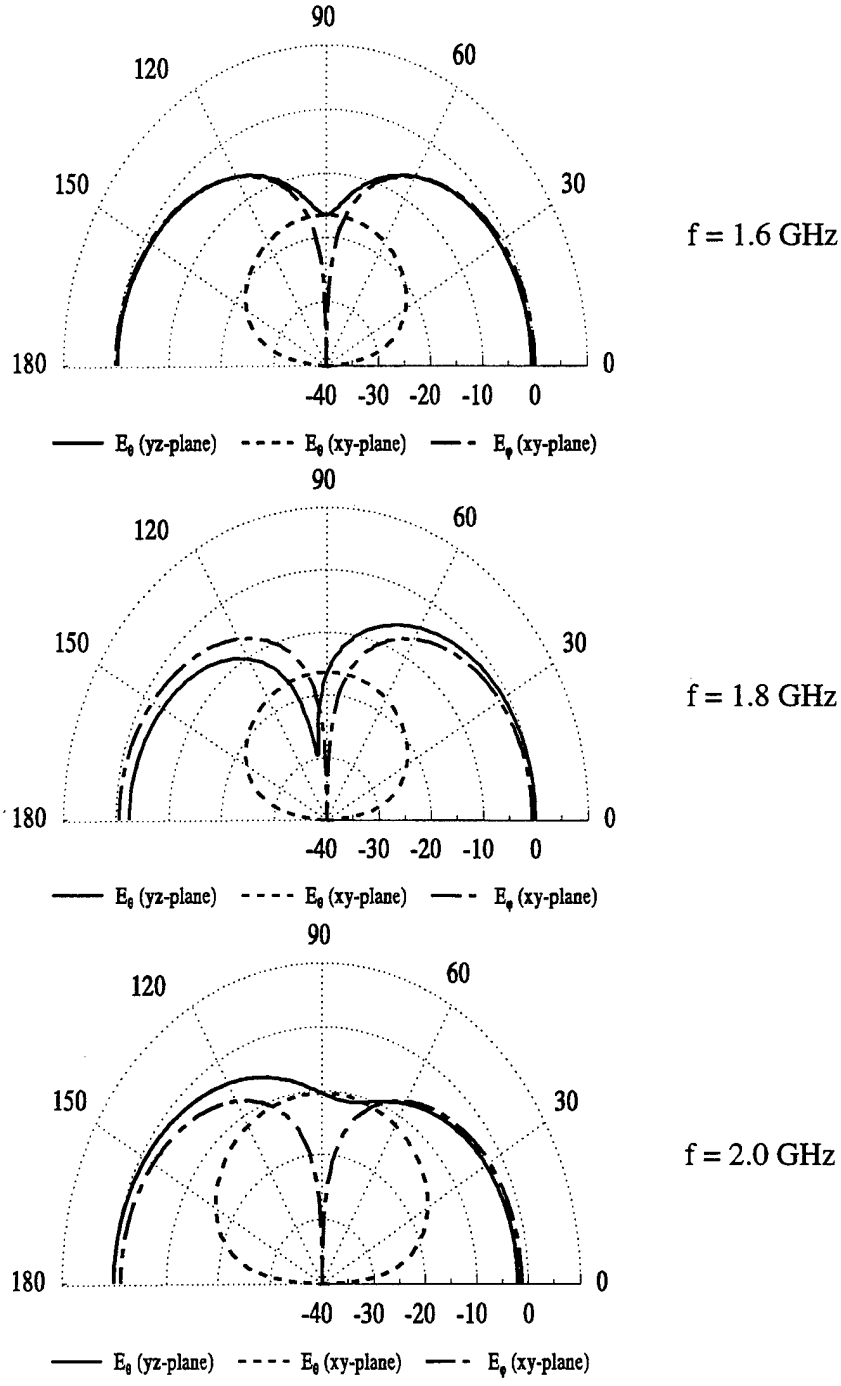

Fig. 20. Radiation patterns for the loaded split DRA with z_f=4 mm and l_w=11 mm around f=1.8 GHz

5. Acknowledgement

This work was partially supported by The Army Research Office under grant No. DAAG55-98-0308.

6. References

[1] D. Kajfez and P. Guillon, (Ed.), *Dielectric Resonators.* Norwood, MA: Artech House, 1986.

[2] R. K. Mongia, A. Ittipiboon, and M. Cuhaci, "Measurement of Radiation Efficiency of Dielectric Resonator Antennas," *IEEE Microwave and Guided Letters*, vol. 4, no. 3, pp. 80-82, 1994.

[3] G. P. Junker, A. A. Kishk, and A. W. Glisson, "Input Impedance of Dielectric Resonator Antennas Excited by a Coaxial Probe," *IEEE Trans Antennas Propagat.*, vol. AP-42, pp. 960-966, July 1994.

[4] A. A. Kishk, M. R. Zunoubi, D. Kajfez, "A Numerical Study of a Dielectric Disk Antenna above a Grounded Dielectric Substrate," *IEEE Trans. Antennas Propagat.*, vol. AP-41, pp. 813-821, June 1993.

[5] G. P. Junker, A. A. Kishk, A. W. Glisson, "Input Impedance of Aperture Coupled Dielectric Resonator Antenna," *IEEE Trans. on Antennas and Propagation*, vol. AP-44, no. 5, pp. 600-607, May 1996.

[6] A. W .Glisson, D. Kajfez, and J. James, "Evaluation of Modes in Dielectric Resonators Using a Surface Integral Equation Formulation," *IEEE Trans. Microwave Theory Tech.*, vol. MTT-31, pp. 1023-1029, December 1983.

ELECTRICAL TUNING OF INTEGRATED MOBILE PHONE ANTENNAS

Juha-Pekka Louhos and Ilkka Pankinaho
Nokia Mobile Phones
P.O.Box 86, FIN-24101 Salo
Finland

Abstract: The development of small integrated antennas plays a significant role in the progress of the future wireless mobile terminals, which will continuously decrease in size. Since the obtainable impedance bandwidth of electrically small antennas is proportional to the changes in the antenna volume new impedance matching techniques are needed in order to fulfill the broadband operation.

This paper describes the enhancement of impedance bandwidth electrically by changing the reactive loading of the resonator either by means of a PIN diode or a varactor diode. In the PIN diode implementation the resonance is switched between the transmit and receive bands whereas in the varactor based design the tuning is continuous. Due to the biasing limitations of the mobile phone, the DC current in the PIN diode implementations is restricted to 10 mA and the DC voltage in the varactor implementations to 3V.

The tuning effect is achieved by placing a tunable capacitive load either in the short-circuit or the open-end of a PIFA. Structures are implemented both on the E-GSM and GSM1800 systems. In addition to the obtained -10 dB bandwidth also the effects of the tuning on radiation efficiency and radiation properties are discussed.

1. Implementation techniques for a tunable PIFA

The tunable matching of mobile phone antennas is based on the changing of their resonance properties by an external reactive circuit. In this case, the word "matching" may be slightly misleading, because the matching circuit is not necessarily located between the radiating element and the feeding line, as in the usual RF design. Still, the use of the matching expression may be reasonable,

because as the variable reactive load tunes the resonant frequency it obviously simultaneously also improves the matching in the vicinity of the resonance.

In theory, the load can be either capacitive or inductive and, as to the λ/4-structures, the reactive load can be placed either in series or parallel to the original antenna. The series connection can be achieved by placing the load between the short-circuit and the ground, and the parallel connection by loading the antenna between the ground plane and the radiating element. Due to the space limitations of the mobile phone antennas, the parallel inductive or series capacitive loading is not very advisable, because it shifts the resonant frequency upwards. The reactive tuning makes it possible to enhance the impedance bandwidth of a narrowband antenna over as large a frequency range as desired. In practical mobile phone antenna design, however, the feed point of the antenna is usually placed on a particular point on the radiating patch, which sets limits on the achievable tuning range. In addition to the fixed feed point, the tunability of a resonator type antenna depends on several other factors, such as the available bias, used tuning component, coupling of the resonator at zero bias and the characteristics of the antenna input impedance. Figure 1 shows some possible tuning techniques based on the capacitive loading of a λ/4-resonator antenna.

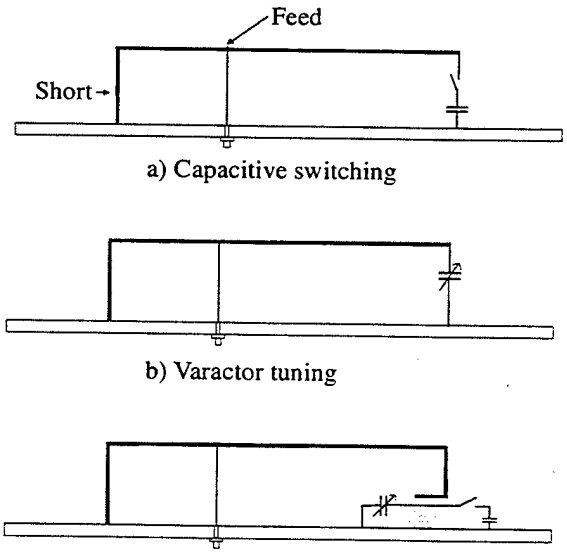

Figure 1. *Tuning with a capacitive load.*

In case a), the tuning is executed by adding a switchable capacitive load to the open end of the PIFA. In case b), the same kind of tuning is achieved by using a

voltage-controlled capacitance diode. In case c), the implementation is based on the capacitively loaded PIFA structure. The total capacitive load depends on the capacitances of the folded open-end and the floated ground plate. The idea of this technique is to change the capacitance of the floated ground structure either by a varactor or a switched capacitance and thus affect the total capacitance value of the open-end.

The resonance properties can also be manipulated by modifying the electrical properties of the short-circuit. The tuning can be achieved either by inserting additional shorting posts or by modifying the properties of the original short circuit by a series connected capacitive circuit, as shown in Figure 2.

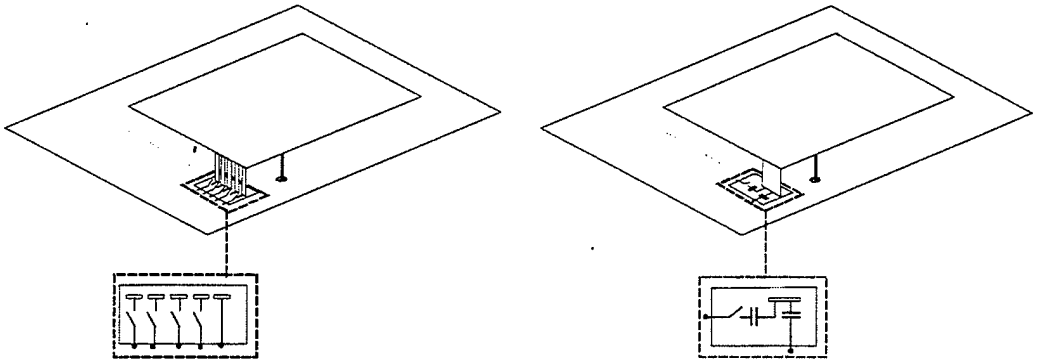

Figure 2. *Frequency tuning by changing the properties of the short circuit.*

In case a), the inductivity of the short-circuit is reduced by increasing the number of the shorting posts with use of switches. In case b), the same effect is achieved by a capacitive switching method. The biggest difference between these two methods is that when the switch is activated to the low impedance state, the resonance frequency shifts upwards in case a) and, on the contrary, downwards in case b).

2. Characteristics of PIN and varactor diodes

2.1 Characteristics of PIN diodes

A PIN diode is a semiconductor component in which an intrinsic I-region of thickness d is sandwiched between highly doped P and N type layers. The

semiconductor material is usually silicon, but gallium arsenide can be also used. PIN diodes are used as switches or attenuators for signals at radio and microwave frequencies. The sketch of a PIN diode is shown in Figure 3.

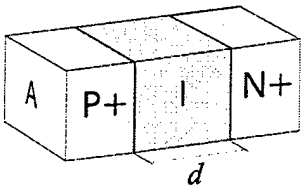

Figure 3. *Physical structure of a PIN diode [1].*

The most important property of the PIN diode is that it can, under certain circumstances, behave as an almost pure resistance at high frequencies. The value of the resistance is dependent on the resistivity of the intrinsic region and the applied bias current. The intrinsic region has a high resistance R_0 at zero bias. In forward bias, the junction resistance depends on the conductivity of the I layer. An increase in the applied forward bias reduces the injection of carriers from the P+ and N+ regions. This phenomenon reduces the specific resistance to a level below the one obtained from doping alone, thus inducing a lower junction resistance. The resulting forward resistance for radio frequencies R_f can be approximated. Together with N+ and P+ regions, the I region, forms a junction capacitance C_j. (See e.g. [1].)

The dielectric relaxation frequency f_{dr} is the frequency above which the junction capacitance becomes independent of bias and is expressed as [2]

$$f_{dr} = \frac{1}{2\pi R_j C_j} = \frac{1}{\tau}, \qquad (2.1)$$

where R_j is the junction resistance which can be approximated, depending on the bias and τ is the carrier lifetime which is the reciprocal of f_{dr}. In order to fulfill the requirement of the bias independent junction capacitance, the f_{dr} property of a PIN diode should be chosen so that it remains well below the operating frequency range with the maximum forward operation bias. In [3], the minimum requirement for f_{dr} is determined with respect to the RF signal as

$$f_{dr} \leq \frac{f_{RF}}{10}. \qquad (2.2)$$

In datasheet values, the carrier lifetime is usually measured with 10 mA forward bias and, depending on the structure of the diode, the corresponding carrier lifetime is between 5 ns – 3000 ns. The carrier lifetime requirement is determined according to the lowest operation frequency. In order to fulfill the previous requirement of τ in mobile phone antenna applications above 900MHz, the carrier lifetime of a PIN diode should be over 11 ns. The amount of the required forward bias depends on the carrier lifetime and thus on the structure of the PIN diode. A PIN diode with lower carrier lifetime characteristics can be saturated (i.e., taken to the point of minimum resistance) by a much lower current than a diode with a much higher τ. In the zero bias, on the other hand, the distortion becomes lower when the width of the I layer increases. The distortion decreases when the frequency of the signal increases as a consequence of the increased distance to the dielectric relaxation frequency [4].

Although the electronic behaviour of the PIN diode can be theoretically modelled only by the parallel connection of the junction resistance R_j and the junction capacitance C_j, modelling of this kind is not sufficient in practice. In commercial products, the diode is always placed into a certain package whose parasitics can have significant effects on the operation properties. The package introduces additional reactive elements in the form of package inductance L_p , package capacitance C_p and the series resistance R_s. The equivalent circuit for a PIN diode at high frequency, meaning that the requirement for the f_{dr} has been met, is shown in Figure 4. [3].

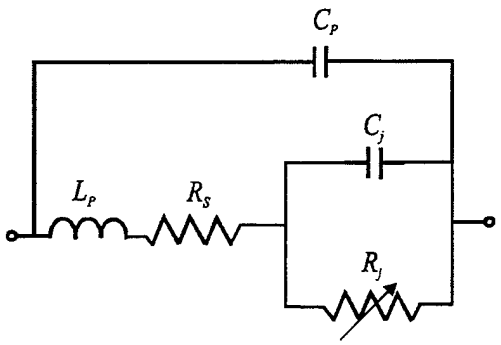

Figure 4 *PIN diode equivalent circuit.*

In antenna applications, the PIN diode is used as a switch having either a very high or a low impedance, depending on the control current. In the simplest case, the switching circuit is configured by using only one series or shunt diode. In

series connection, the insertion loss *IL* defines the loss of signal attributed to the diode when a switch is on, whereas the isolation *IS* defines the amount of RF leakage between the input and the output when a switch is off. In the shunt configurations, the behaviour is just the opposite.

The impedance Z_d of a PIN diode is written according to Figure 4. as

$$Z_d(f)=\frac{\frac{1}{j\omega C_p}\left(j\omega L_p+R_s+\frac{R_J}{1+j\omega R_j C_j}\right)}{\frac{1}{j\omega C_p}+j\omega L_p+R_s+\frac{R_j}{1+j\omega R_j C_j}}, \qquad (2.3)$$

where $\omega=2\pi f$.

If the diode with impedance Z_d is connected in series with a transmission line with impedance Z_0, then the resulting equation for the attenuation in dBs between the input and the output ports of the diode can be written as [2]

$$20\log\left|\frac{U_{in}}{U_{out}}\right|=20\log\left|1+\frac{Z_d}{2Z_0}\right|. \qquad (2.4)$$

In practice, the parasitic package capacitance C_p (0.08pF - 0.12pF) has a quite minimal effect on the switching performance and can be neglected. Based on this assumption, the insertion loss of a series-connected PIN diode can be approximated by

$$IL_{series}(f)=10\log\left(\left(1+\frac{R_s+R_j}{2Z_0}\right)^2+\left(\frac{\pi f L_p}{Z_0}\right)^2\right) \qquad (2.5)$$

and the isolation by

$$IS_{series}(f)=10\log\left(1+\left(\frac{\pi f L_p-1/4\pi f C_j}{Z_0}\right)^2\right). \qquad (2.6)$$

According to Equations (2.5) and (2.6), a good switching performance, i.e., a low insertion loss and a high isolation, with the series-connected PIN diode is achieved by a low junction resistance, a low package inductance and a small junction capacitance. The small junction capacitance refers either to the use of a bulk type PIN diode or a strongly reverse-biased epi diode. However, the requirement of a low junction resistance in this case means that the amount of needed forward bias current increases, which is not a desired feature in the mobile phone applications.

Due to the package parasitics, the insertion loss and isolation characteristics decrease as the operation frequency increases. The typical effects of the package inductance and the package capacitance are shown in Figure 5.

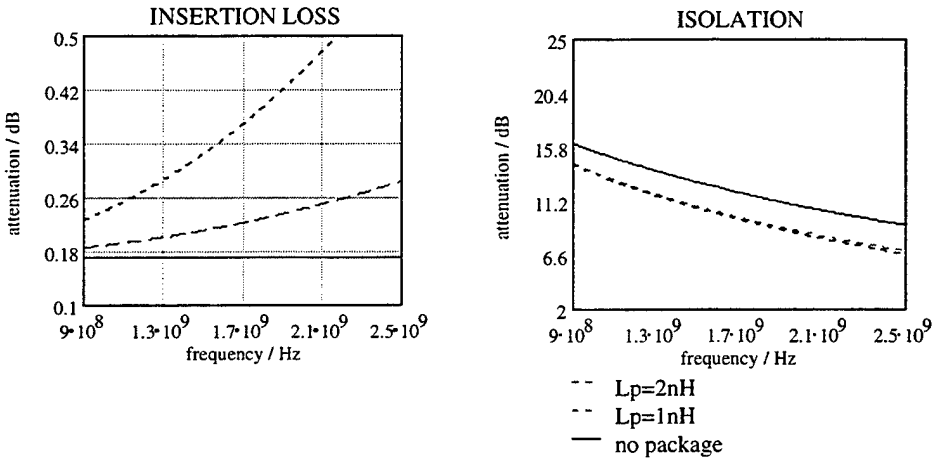

Figure 5. *Effects of the package parasitics on the insertion loss and isolation characteristics of a series-connected PIN diode (R_s = 1Ω, R_{jON} = 1Ω, R_{jOFF} = 1000Ω, C_j = 0.25 pF, C_p= 0.08 pF, Z_0= 50 Ω).*

2.2 Characteristics of varactor diodes

The operation of a varactor diode is based on the reverse-biased pn junction. An increase in the reverse bias widens the depletion region between the p- and n-type substrates, and the junction capacitance is reduced. The junction capacitance C_j for a reverse-biased pn junction as a function of the applied reverse dc voltage V is given by

$$C_j(V) = C_{j0}\left(1 - \frac{V}{\Phi_{bi}}\right)^{-M}, \quad (2.7)$$

where C_{j0} is the junction capacitance at zero bias, Φ_{bi} the contact potential (silicon 0.7V and GaAs 1.3V) and M a coefficient depending on the junction doping profile [5]. Both C_{j0} and M are dependent on the doping characteristics of the pn junction. For the abrubt type varactor M=0.5, but in hyperabrupt type varactor M varies with the applied reverse bias between 0.5 and 5. If the range of the applied bias is sufficiently narrow, the voltage dependency of M may be ignored, and it may be replaced by an average value over that range.

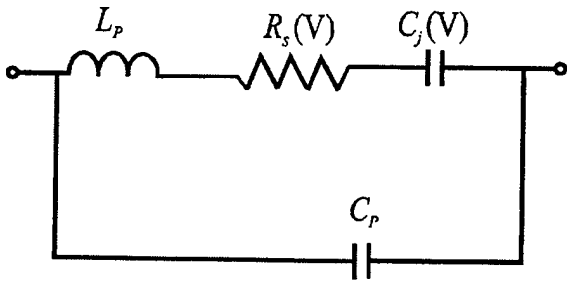

Figure 6. *Varactor diode equivalent circuit.*

The equivalent circuit of the diode is modelled by a voltage dependent junction capacitance $C_j(V)$ and the series resistance R_S (V), associated with the ohmic contact and the finite thickness of the epitaxial layer. Since the depletion region expands as the bias is increased, the undepleted region becomes smaller which decreases the resistance of the structure. The series resistance should be as low as possible in order to keep the losses associated with the diode low. As the operation is based on the reverse-biased pn-junction, it can be assumed that the junction resistance will be very large and may therefore be ignored. In commercial products, the diode is usually installed in a package. Due to the package material, the geometry and the bonding wires the package always has some kind of package inductance L_p and package capacitance C_p, that have an influence on the performance of the diode. L_p and C_p are assumed to be constant with the bias voltage.

According to Figure 6., the impedance of a varactor diode can be written as

$$Z_d(\omega,V)=\frac{\frac{1}{j\omega C_p}(R_s(V)+j(\omega L_p-\frac{1}{\omega C_j(V)}))}{R_s(V)+j(\omega L_p-\frac{1}{\omega C_j(V)}-\frac{1}{\omega C_p})}, \qquad (2.8)$$

where $\omega=2\pi f$.

The disadvantage of this model is that it fails to take into account the non-linearities of the junction. The parameters for this circuit have to be taken straight from the manufacturers' datasheet curves. Usually, the effect of the package capacitance on the characteristics of the diode is negligible and can be ignored. By this supposition, Equation (2.8) simplifies to

$$Z_d(\omega,V)=R_s(V)+j(\omega L_p-\frac{1}{\omega C_j(V)}). \qquad (2.9)$$

Since the operation of a varactor diode is based on the reverse-biased pn junction the operation frequency range should be below a particular frequency, whereas for a PIN diode switch it is just vice versa. For a varactor diode, this cut-off frequency f_{coff} is defined by the diode series resistance $R_s(V)$ and the junction capacitance $C_j(V)$ as

$$f_{coff}(V)=\frac{1}{2\pi R_s(V)C_j(V)}. \qquad (2.10)$$

Since both R_s and C_j decrease as a function of the increased reverse bias, the cut-off frequency is usually defined according to the zero bias values of these parameters

In order to keep the diode impedance constantly in the capacitive operating mode, the series resonance frequency of the diode should in all circumstances remain clearly above the operating frequency range. In the series resonance condition, the reactive part of the impedance equals zero, and the resonant frequency can be solved from Equation (2.9) and written as

$$f_r=\frac{1}{2\pi\sqrt{L_pC_j(V)}}. \qquad (2.11)$$

Since the junction capacitance decreases as a function of the applied reverse bias, the criterion for the capacitive operating mode is met, provided that the f_r exceeds the highest operating frequency at the zero bias level.

In low-loss designs such as antenna applications, f_{coff} is usually much higher (> $10 f_r$) than the series resonance frequency f_r of the packed diode, which means that in case the series resonance frequency requirement is fulfilled, the cut-off frequency requirement is also fulfilled. It must be emphasized that the cut-off frequency mainly defines the energy dissipation of the varactor, while the f_r defines the frequency above which the operation of the varactor becomes inductive due to the effect of the package inductance.

In mobile phone applications the temperature of the environment can vary within a rather large range. This can have a significant effect on the properties of the varactor-based tuning circuit, because the capacitance of the diode tends to increase as the temperature increases. The capacitance of a hyperabrupt diode is more sensitive to temperature in comparison to the abrupt diode.

3. Measurement analysis

3.1 Brief theory of the quality factor analysis

Small antennas are always resonators. The quality factor Q of a resonator describes its ability to store electromagnetic energy and is defined as

$$Q = 2\pi f_r \frac{W}{P_l}, \tag{3.1}$$

where W describes the stored energy and P_l is the loss power.

The total loss power of a resonator circuit is divided into two parts, depending on the source of the loss [6]. One of these parts represents the internal losses of the resonator (Q_u) and the other part takes into account the effects caused by the external loading (Q_e). The total power loss (Q_l) of the resonator is expressed by

$$\frac{1}{Q_l} = \frac{1}{Q_u} + \frac{1}{Q_e} . \tag{3.2}$$

The internal losses takes into account the dielectric, conductor and radiation losses and thus the unloaded quality factor can be written by using the respective Q-values in the following way:

$$\frac{1}{Q_u}=\frac{1}{Q_r}+\frac{1}{Q_d}+\frac{1}{Q_c}\,. \tag{3.3}$$

In practice, Q_l is determined from the reflection coefficient measurements by the ratio between the resonant frequency f_r and the corresponding half-power bandwidth B_{hp} [6]

$$Q_l=\frac{f_r}{B_{hp}}. \tag{3.4}$$

The half-power bandwidth is determined according to the frequency points in which the power reflection coefficient is

$$|\rho|^2=\frac{1+|\rho_{\min}|^2}{2}. \tag{3.5}$$

The unloaded quality factor can be calculated from Q_l and the reflection coefficient at the resonant frequency $\rho(f_r)$ according to [6] by

$$Q_u=\frac{2Q_l}{1\pm|\rho(f_r)|}, \tag{3.6}$$

in which the plus sign is used in the undercoupled case and the minus sign in the overcoupled case.

By assuming the external losses equal for both the original and tuned antenna structures the differencies in the measured loaded quality factors between these two implementations can be regarded as a consequence of the tuning circuit losses. Based on the previous assumption the unloaded Q for the tuned structure can be written as

$$\frac{1}{Q_{utuned}}=\frac{1}{Q_{uorig}}+\frac{1}{Q_{sw}}=\frac{1}{Q_r}+\frac{1}{Q_d}+\frac{1}{Q_c}+\frac{1}{Q_{sw}}, \tag{3.7}$$

where Q_{utuned} is the unloaded Q-factor of the tuned resonator, Q_{uorig} is the unloaded Q-factor of the original resonator and Q_{sw} is the switch quality factor taking into account the losses induced by the tuning circuitry.

3.2 Measurement of the radiation efficiency by the Wheeler method

The radiation efficiency η_r of an antenna describes the ratio between the total radiated power P_r and the total input power P_{in}. Due to the inverse proportionality between the particular resonator loss and the quality factor the calculation of the radiation efficiency can be based also on the Q-values.

$$\eta_r = \frac{P_r}{P_{in}} = \frac{Q_u}{Q_r}, \tag{3.8}$$

In the Wheeler method, the Q-value of the electrically small antenna is measured both in the free space and in the situation where the antenna is placed under a radiation shield . The effect of the shield is to remove that part of the power that is radiated without changing the current distribution in the antenna, leaving thus the losses inside the antenna the same [7]. In other words, in the free space the resonator losses are formed by the sum of the radiation resistance R_s and loss resistance R_l whereas in the conductive shield the only loss is assumed to be caused by the R_l term. By defining now the unloaded quality factors in both circumstances the radiation efficiency can be calculated by the following equation

$$\eta_r = 1 - \frac{Q_u}{Q_w} = \frac{Q_w - Q_u}{Q_w}, \tag{3.9}$$

where Q_u is the unloaded quality factor in the free space and Q_w the corresponding quality factor with the radiation shield.

By comparing now the Equations (3.7) and (3.8) the radiation quality factor can be solved from

$$Q_r = \frac{Q_u}{\eta_r} = \frac{Q_u Q_w}{Q_w - Q_u} \tag{3.10}$$

4. Practical implementations and results

4.1 Capacitively loaded short circuit

The properties of the capacitively loaded short circuit, shown in Figure 2b, were studied both in 900 MHz and 1800 MHz bands. The main reason for choosing the capacitive loading instead of the inductively loaded short circuit structure, illustrated in Figure 2a, was partly the required number of components and partly the current consumption of the switching device. The bandwidth targets were chosen either according to the E-GSM900 or the GSM1800 system. In the E-GSM, the frequency band requirement for the downlink is 880 - 915 MHz and for the uplink 925-960 MHz. Corresponding bands for the GSM1800 are 1710 - 1780 MHz and 1805 - 1880 MHz. The aim was to cover the frequency bands of these systems by PIN diode solutions, and then to compare the radiation properties of these implementations to other antenna solutions. Both implementations were based on the PIFA structure illustrated in Figure 7. The location of the short-circuit on the PCB was constant despite the frequency band.

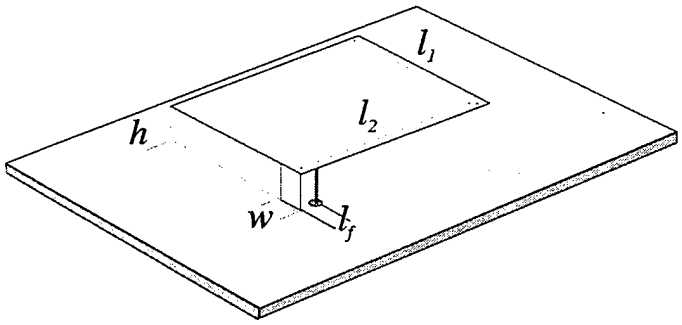

Figure 7. *Structure of the prototype PIFAs.*

The basic idea of the capacitive loading is to influence the original resonance properties of the antenna by changing the inductivity of the antenna short-circuit. During these implementations, the capacitive loading was placed in series with the short-circuit. The series capacitive load reduces the inductance of the short-circuit, inducing an increase in the antenna resonance frequency. Since in the mobile phone systems the transmitting (Tx) band is usually located at lower frequencies than the receiving (Rx) band, capacitive loading of this type is usable only when the original resonance of the antenna is ≤ Tx centre frequency.

4.1.1 Implementation by a PIN Diode

The aim of this implementation is to find a switching solution that only tunes the resonance properties of the antenna between the Tx and the Rx bands. Since the switching from "off" to "on" by the PIN diode requires a some sort of dc-biasing current, the first requirement for the implementation is that the uplink (Tx) operation should be achieved in the on-state and the downlink (Rx) operation in the off-state. Another requirement concerns the impedance bandwidth properties of the original antenna. The bandwidth of the original antenna should cover at least the Rx band. The broader is the original antenna bandwidth, the smaller is the change required in the inductance of the short-circuit, and thus also in the capacitive loading.

The switching performance is attained by a PIN diode D_1. The short-circuit of the antenna is connected by a chip capacitor C_1 directly to the ground, whereas another ground connection is executed by the PIN diode and chip capacitor C_2. The Rx resonance frequency depends mainly on the value of C_1 (the PIN diode switched off) and the Tx-resonance on the total capacitance defined by the parallel connection of C_1 ,C_2 and the forward-biased PIN diode. The configurations of the switching circuit and the corresponding pad layout are shown in Figure 8.

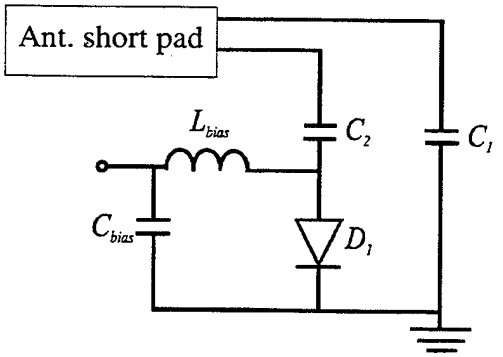

Figure 8. *Switching circuit and the corresponding pad layout.*

The frequency change between the on-state and the off-state depends on the C_2 $/C_1$ -ratio. The higher the ratio is, the larger is also the change in the antenna resonances between the on- and off- states. The required capacitance ratio is defined according to Rx (off) and Tx (on) requirements. Due to the inductance of the PIN diode package, the C_2 has to be chosen so that the PIN diode -switched

connection remains capacitive within the operating frequency range. If C_2 exceeds this particular value, the PIN diode -switched connection becomes inductive and the switching effect is just opposite to what is desired, since now the switching circuit is more capacitive in the on-state than in the off-state, that is, the on-state corresponds to Rx.

The 900 MHz implementation was based on the 760 MHz PIFA with the following dimensions: h= 5 mm, l_1 = 30 mm, l_2 = 65 mm and w = 4 mm. The 1800 MHz implementation was based on the 1600 MHz PIFA with the following dimensions: h = 5 mm, l_1 = 20 mm, l_2 = 30 mm and w = 4 mm. The measured reflection coefficients for both the conventional and the switched structures are shown in Figures 9. and 10. More detailed information on the resonance properties are given in Table 4.1. The component information for both implementations can be found in Table 4.2.

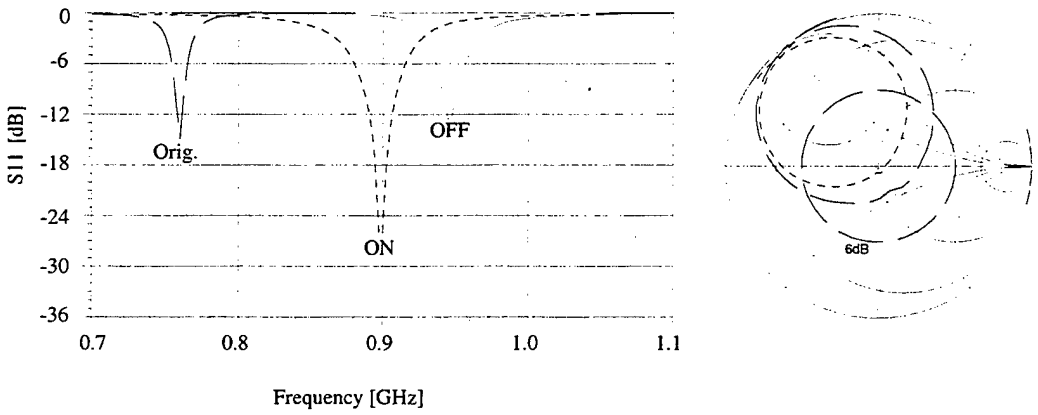

Figure 9. *Measured reflection coefficients for the 900 MHz implementation.*

The radiation efficiency measurements are based on the Wheeler method introduced in Section 3.2. The radiation quality factor Q_r is calculated according to Equation (3.10) and the antenna switch quality factor Q_{sw} according to the changes in the unloaded quality factors in the Wheeler cap measurements. The antenna switch quality factor contains the losses of both the discrete components and the pad layout. (See e.g. Figure 8.)

Table 4.1 *More detailed information on the resonant properties of the 900 MHz and 1800 MHz implementations.*

The 900 MHz implementation	Orig.	ON-state	OFF-state
Resonance frequency f_r [MHz]	760	899	946
Bandwidth BW (L_{retn} = 6 dB) [MHz]	12	30	20
Antenna switch quality factor Q_{sw}	-	126.9	209.3
Radiation efficiency (Wheeler) η_r [%]	82	70	73
Radiation quality factor Q_r	102.4	42.7	52.4
The 1800 MHz implementation	Orig.	ON-state	OFF-state
Resonance frequency f_r [MHz]	1575	1745	1840
Bandwidth BW (L_{retn} = 6 dB) [MHz]	60	85	84
Antenna switch quality factor Q_{sw}	-	106.5	174.8
Radiation efficiency (Wheeler) η_r [%]	93	69	80
Radiation quality factor Q_r	31.7	38.7	31.1

As seen in Figure 9., the measured bandwidth (L_{retn} = 6dB) of the original 760 MHz PIFA was only about 12 MHz. This means that the antenna fails to have the bandwidth properties required of the antenna itself. The bandwidth of the original antenna should be over 35 MHz before the E-GSM band can be covered by the aid of a PIN diode. In the 1800 MHz implementation, the bandwidth of the original antenna was also insufficient, since theGSM1800 system requirement for both the Tx and Rx is 75 MHz. In the switched versions, however, the impedance bandwidth requirements were nearly fulfilled, partly because of the slightly higher frequencies and partly because of the losses of the switching circuit.

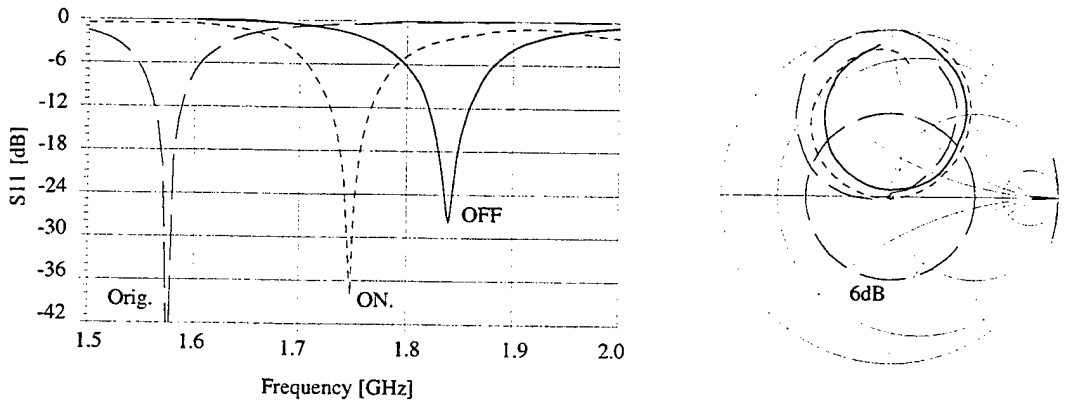

Figure 10. *Measured reflection coefficients for the 1800 MHz.*

Table 4.2 *Component information.*

PIN diode:	Siemens BAR 64
- package inductance L_p	1.4 nH
- package capacitance C_p	0.08 pF
- junction capacitance C_j	0.45 pF
- junction resistance R_j (I_{dc}=10 mA)	2.1 Ω
Switching current I_{dc}(off) / I_{dc}(on)	0 / 10 mA
Capacitors C_1 / C_2 :	
- 900 MHz implementation	8.2 pF / 5.6 pF
-1800 MHz implementation	2.2 pF / 1.2 pF

The same switching effect can be obtained by several capacitance ratios C_2/C_1. During the implementation process, the main problem was how to achieve a good radiation efficiency in the on-state. In the various implementations carried out during this work, the radiation efficiency of the antenna, according to both the Wheeler method and the radiation measurements, seemed to increase when the resonance of the original antenna was lowered. The restricting factor on the E-GSM implementation was found to be the series inductance formed with the PIN diode package inductance L_p and the capacitance C_2. The lower original antenna resonance made it possible to use smaller capacitance values which induced an increase in the series resonance frequency of the PIN diode and C_2 connection. For instance, in the first phase the E-GSM operation was executed by a 850 MHz PIFA (l_2 = 58 mm). The Tx-operation was achieved by a capacitance C_2 = 12 pF, giving only a 20% radiation efficiency for the on-state. The off-state was executed by C_1 = 6.8 pF, giving a radiation efficiency of 60%. Due to the weaker radiation efficiency properties, the original antenna resonance was lowered to 760 MHz by increasing the l_2 to 65 mm. Consequently, the Tx-operation could be achieved by a smaller on-capacitance value C_2 = 8.2 pF, which increased the series resonance of the PIN diode and the C_2 connection from 1030 MHz to 1240 MHz. By this change, the radiation efficiency of the Tx increased to 77 %.

4.2 CAPACITIVELY LOADED OPEN END

The following implementations concern the capacitive loading of the open-end of a completely short-circuited PIFA. The dimensions of the original 1.85 GHz PIFA are: $w = l_1$ = 25 mm, l_2 = 36 mm and h = 5 mm. The capacitive loading is executed by using either the capacitor plate structure introduced in Section 1 or

alternatively an inductive post connection between the radiating edge and the floated ground. The sketches of both structures are shown in Figure 11.

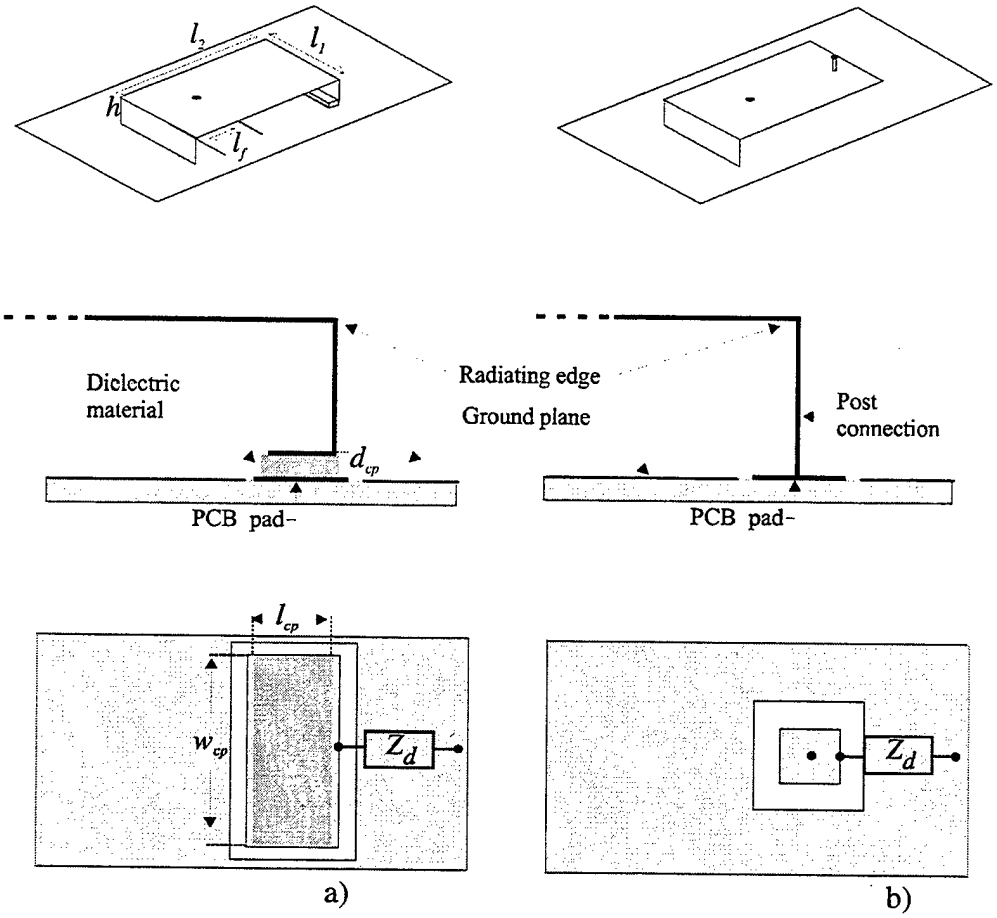

Figure 11. *Capacitive loading of the open end a) by a capacitor plate and b) by a post connection.*

The connection between the PCB pad and the ground is controlled either by a PIN diode -switched capacitance or a varactor. The equivalent circuit for the whole connection is given in Figure 12. The Z_{con} describes the impedance between the radiating edge (*1*) and the PCB pad having a plate capacitance $C_{pad.}$. The impedance of the switching or tuning circuit is included in the impedance Z_d. The upper PCB surface, enclosing the PCB pad, was only grounded from the "l_{cp}" edges and not from the "w_{cp}" edges, which may induce an additional

coupling between the pad and the ground surface. The coupling is modelled by a series capacitance C_s and a series inductance L_s.

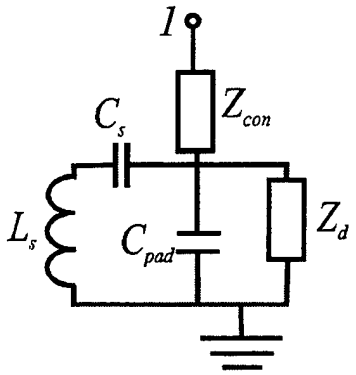

Figure 12. *Model for the capacitively loaded open-end.*

The effect of the switching or tuning capacitance on the antenna resonance properties mainly depends on the ratio between the C_{pad} and the capacitive reactance of Z_d. In the switched case, the change in the antenna resonance properties between the on-state and the off-state mainly depends on the value of the capacitive reactance of Z_d. The lower the capacitive reactance of Z_d is, the larger becomes the shift in the resonances. In the varactor- tuned case, the obtainable tuning depends both on the varactor zero bias capacitance and on its capacitance ratio. The lowest obtainable resonance is defined by the varactor zero bias capacitance, and the highest resonance by the available dc-biasing voltage.

4.2.1 PIN Diode -Switched Parallel Plate Capacitor

The aim of the following implementation was to achieve the same switching effect on E-GSM as was achieved in Section 4.1.1. The dimensions of the air-filled capacitor plate structure were l_{cp} = 5 mm, w_{cp} = 25 mm and d_{cp} = 0.5 mm, corresponding to a capacitance of 2.2 pF. The dimensions of the antenna open-end pad were equal to the capacitor plate structure. According to the dimensions of the original 1.85GHz PIFA, the Rx-operation requires an open-end capacitance of 2.4pF. In the Tx, the requirement is 2.7 pF, which means that the needed change is only about 0.3 pF. In order to achieve such a small difference between the on- and off-states the value of the switched capacitance should be about the same order as the value of the pad capacitance C_{pad}.

The switching is based on a PIN diode similar to the one used in the previous short-circuit implementations. The configuration of the switching circuit is shown in Figure 13. The switching to Tx is executed by capacitance C_1 = 1.2 pF. The measured reflection coefficients are shown in Figure 14., and the more detailed numerical information is given in Table 4.3.

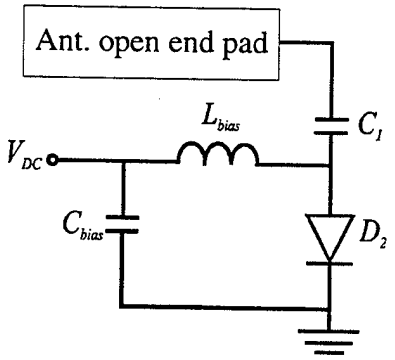

Figure 13. *Circuit configuration for the PIN diode (BAR64) -switched capacitor structure.*

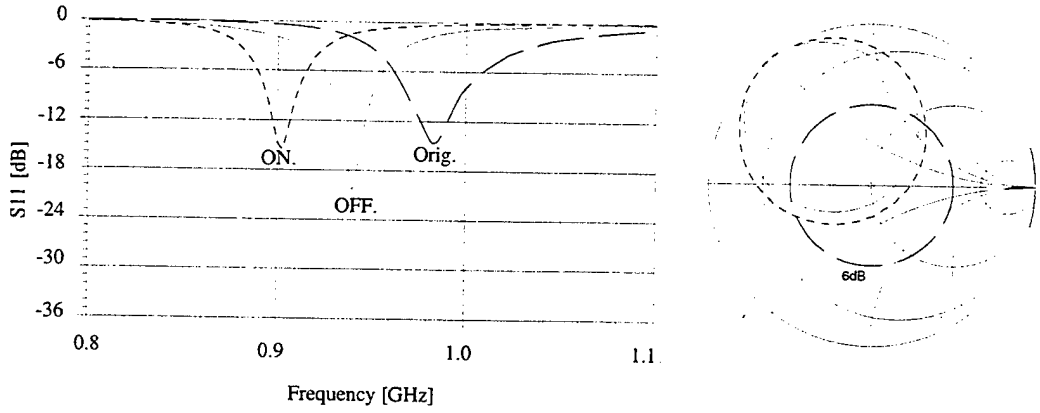

Figure 14. *Measured reflection coefficients for the PIN diode (BAR-64)-switched parallel plate capacitor structure (feeding distance l_f = 8 mm)*

Table 4.3 *More detailed information about the resonance properties of the PIN diode switched capacitor plate structure.*

	Orig.	ON-state	OFF-state
Resonance frequency f_r [MHz]	985	903	938
Bandwidth BW (L_{retn} = 6 dB) [MHz]	48	27	32
Radiation efficiency (Wheeler) η_r [%]	70	39	51
Radiation quality factor Q_r	39.6	113.8	71.9

4.2.2 Varactor Tuned Parallel Plate Capacitor

The basic behaviour of the varactor-tuned parallel plate capacitor is similar to the previous implementation. The aim is to cover the whole E-GSM band by shifting the antenna resonance continuously between 880 MHz and 960 MHz, with the maximum available dc-voltage, 3 V. Due to the basic behaviour of the varactor capacitance, the corresponding state for the on–switched PIN diode is now defined by the varactor zero bias capacitance. According to the manufacturer's datasheets [8], the zero bias capacitance of the SMV1234 varactor is about 10 pF. If it is assumed that the effect of the package parasitics and biasing circuits is similar both for the previous PIN diode implementation and the corresponding varactor tuning circuit structure illustrated in Figure 15., it can be seen quite easily that C_l equates the zero bias capacitance of the used varactor.

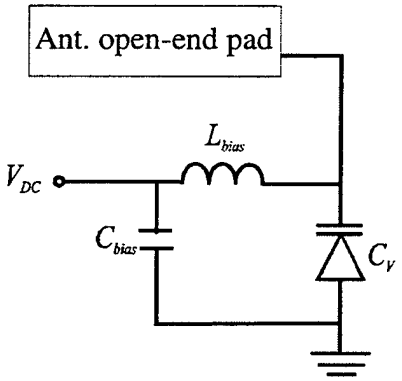

Figure 15. *Varactor tuning circuit for the open-end.*

Because of the higher capacitance the resonant frequency of the previous capacitor plate loaded PIFA decreases lower than the E-GSM Tx-band. Since the aim was to achieve the 880 MHz resonance by the zero bias operation, the capacitance of the antenna capacitor plate was slightly reduced by narrowing the

dimension l_{cp} from the original 5 mm to 3.5 mm, decreasing the parallel plate capacitance to a value of 1.6 pF.

The measured reflection coefficients for the bias voltages of 0 V – 6 V are shown in Figure 16. The voltage range has been doubled from 3 V only to prove that the tunability, when related to the obtained matching levels, is not nearly as sensitive to the capacitance change as was the situation in the short-end tuned cases. According to this implementation, the E-GSM frequency range could be covered by a DC-voltage range of 0 V – 2 V. As the reverse bias increases, the resonance approaches the previously measured $Z_d = 0$ resonance (the expression "Orig.") and the tuning effect, when compared to the applied dc-voltage becomes narrower.

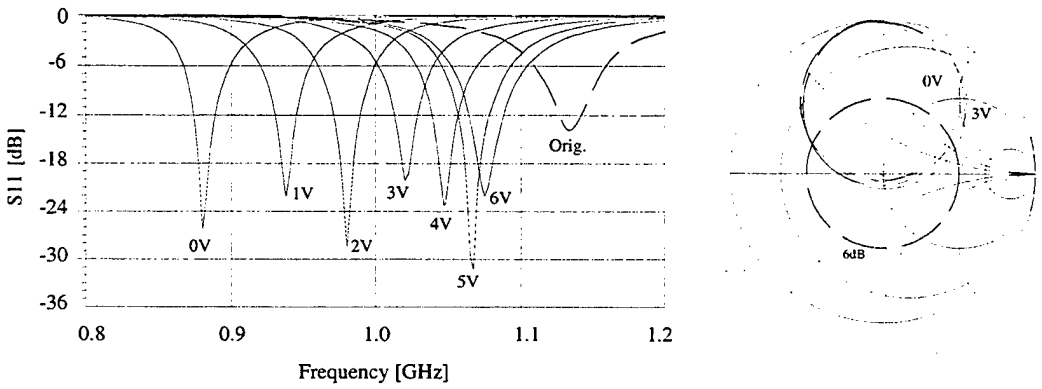

Figure 16. *Measured reflection coefficients for the varactor (Alpha SMV1234-011) -tuned 1.85 GHz PIFA loaded with a parallel plate capacitor structure (feeding distance l_f = 12 mm).*

Table 4.4 *More detailed information on the resonant properties of the previous varactor -tuned PIFA*

	Orig.	0 V	1 V	3 V
Resonance frequency f_r [MHz]	1 135	881	937	1 020
Bandwidth BW (L_{retn} = 6 dB) [MHz]	50	32	34	40
Antenna switch quality factor Q_{sw}	-	60.0	96.7	134.4
Radiation efficiency (Wheeler) η_r[%]	76	19	40	50
Radiation quality factor Q_r	39.6	176.3	82	65.2

4.2.3 Varactor Tuned Post Connection

The only difference between the following implementation and the previously shown varactor-tuned capacitor plate structure can be detected in the connection between the radiating edge and the PCB. The loading effect is achieved by replacing the capacitor plate structure by a single post connection, placed in the centre of the radiating edge, as shown previously in Figure 11.b. Due to the post connection a dc-block capacitance C_{dc} has been added between the varactor (SMV1234) and the open-end pad, as illustrated in Figure 17. It must be emphazised that the connection between the PCB pad and the radiating edge is no more capacitive but inductive. The capacitive operation is achieved by choosing an adequately small value for the C_{dc}. In the first phase, the C_{dc} was 1 pF, which provided a tuning from 1 120 MHz to 1 200 MHz with a 0 – 3V bias. Since the aim was to achieve tuning of E-GSM, the C_{dc} was increased to 2.2 pF, which dropped the zero bias resonance to 875 MHz. As a consequence, the whole E-GSM band could be covered by a 1.5 V bias. The measured reflection coefficients, both for the tuned structure and the original antenna, containing the post connection between the radiating edge and the open-end pad, are shown in Figure 18. If compared to the results of the corresponding capacitor plate-loaded PIFA in Table 4.4, the post structure seems to offer similar tuning properties with a slightly better radiation efficiency.

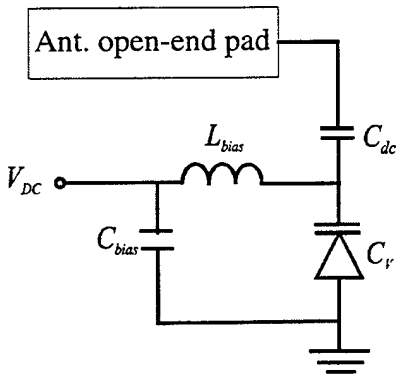

Figure 17. *The circuit configuration for the varactor-tuned post connection.*

Table 4.5 *More detailed information on the resonant properties.*

	Orig.	0 V	1 V	2 V
Resonance frequency f_r [MHz]	1 550	880	937	970
Bandwidth BW (L_{retn} = 6 dB) [MHz]	97	33	38	40
Antenna switch quality factor Q_{sw}	-	80.9	101.2	107.8
Radiation efficiency (Wheeler) η_r[%]	89	41	48	55
Radiation quality factor Q_r	21.1	78.8	68.5	53.6

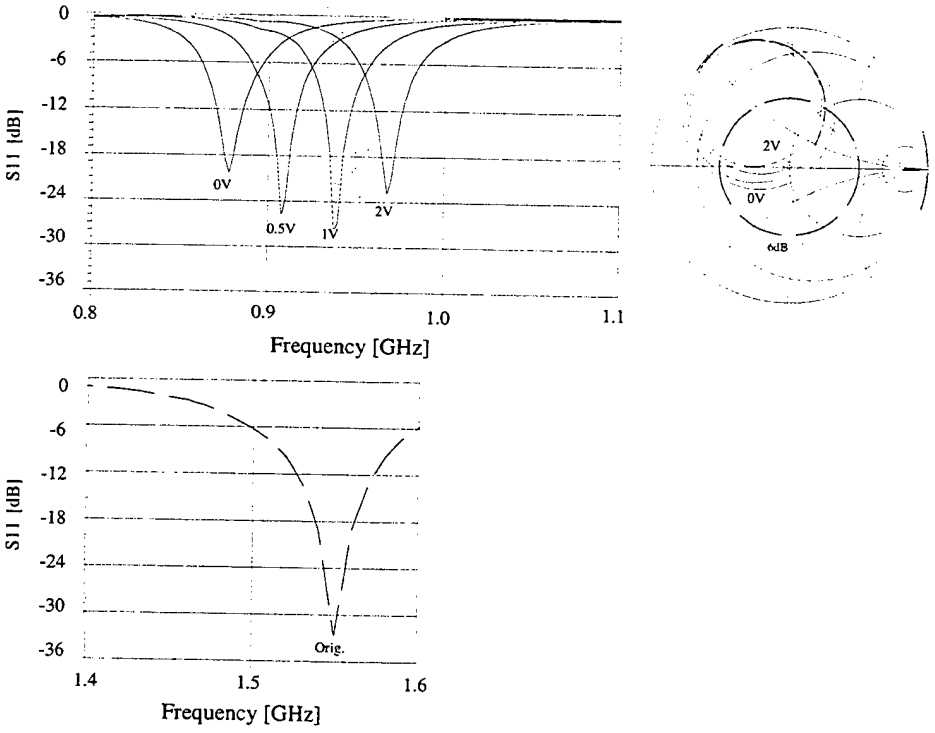

Figure 18. *Measured reflection coefficients for the varactor (Alpha SMV1234-011) -tuned 1.85 GHz PIFA with a post connection (feeding distance l_f = 10 mm).*

4.3 Radiation pattern measurement results

The measurements for the radiation pattern were conducted in an anechoic chamber. The measurements were conducted on the same biasing levels, i.e., at the same resonant frequencies as in Table 5.1. Due to the uncertainties in the absolute power levels, the measurements were analyzed merely by comparing the changes between the average power levels of both the E- and the H-planes between the tuned and the original antennas. According to several consecutive measurements with the same test structure, the variations in measured average radiated power levels were about ± 1 dB. The uncertainties are mainly caused by the variations of the field in the anechoic chamber and by the differencies in the antenna set-up from one measurement to another. The uncertainty of the measurements also depends on the properties of the reference horn and the measurement cables. Another factor that may increase the uncertainty is the implementation of the dc-biasing for the tuned antenna structure. During these measurements, the biasing of the tuning circuit was executed by mounting an approximately 1-meter long cable between the antenna switch pad on the rotation table and the dc-voltage source on the chamber floor. The uncertainties caused both by the feeding and biasing cables were minimized by assembling ferrites around these cables.

Although the determination of radiation efficiency from the radiation pattern actually requires 3D measurements, the measured average radiated powers of both the copolarized E- and H-planes were compared to the Wheeler method -based radiation efficiency calculations. The aim of this test was simply to find out if there was any correlation between these two different measurements. The comparison was made solely with the short-end tuned prototypes. The average radiated power of the tuned antenna was normalised in relation to the original antenna. The results of this analysis are shown in Table 4.6.

According to Table 4.6, the correspondence between the E- and H-plane radiation properties and the Wheeler method -based radiation efficiency calculations seems to be quite satisfactory for the GSM1800 implementation, but, on the E-GSM, the difference between these two values is likely to increase especially on the H-plane.

Table 4.6 *Comparison between the measured E- and H-plane average radiation powers and the Wheeler method -based radiation efficiency of the short-circuit tuned prototypes.*

	E-plane (copolar)		H-plane (copolar)		
State:	Avg. [dB]	Avg. [mag]	Avg. [dB]	Avg. [mag]	Wheeler
E-GSM implementation by a PIN diode / Table 4.1					
Original	0.0	1.00	0.0	1.00	0.82
OFF	-1.0	0.79	1.6	1.45	0.73
ON	-0.8	0.83	0.9	1.23	0.70
GSM1800 implementation by a PIN diode / Table 4.1					
Original	0.0	1.00	0.0	1.00	0.93
OFF	-1.4	0.72	-1.3	0.74	0.80
ON	-1.6	0.69	-1.7	0.68	0.69

4.3.1 Tuning and its effects to the crosspolarization levels

The loading of the resonator antenna by a switching or tuning component also has an influence on the crosspolarization levels. According to [9], the predicted increase in the crosspolarization level, when the patch is loaded, can be attributed to two mechanisms: the physical positioning and the loading effect of the diode. The positioning of the diode induces discontinuities to the current distribution of the original antenna. In [9], the level of crosspolarization was found to increase when the varactor diode was located nearer the radiating edge. The loading effect is related to the current consumption of the diode. The higher the current consumption of the diode is, the greater will also be the increase in the crosspolarization levels. However, the prototypes of this thesis are based on PIFA structures of different kinds, and therefore no reliable comparison can be made between the crosspolarization levels between different loading positions. The crosspolarization levels can only be compared between the loaded and the original antennas as a function of the applied bias. The changes in the crosspolarization levels were analyzed by comparing the average radiation powers between the copolarized and the crosspolarized radiation patterns. The crosspolarization levels were found to increase simultaneously with the increased loading effect of the tuning circuit.

5. Conclusions

The impedance bandwidth was enhanced by shifting the antenna resonance capacitively either by using a PIN diode switch or, continuously, by a varactor diode. The impedance bandwidth requirements were achieved with all prototypes, i.e., the available biasing (PIN diode: I_{dc}< 10 mA, varactor: $V_{dc} \leq$ 3V) was not a limiting factor during these implementations. Instead, the most constricting factor on the achievable impedance bandwidth of the short-circuit tuned prototypes was the positioning of the probe feed. It must be emphasized that the PIN diode switched versions of the studied antennas did not fulfill the bandwidth requirements for Tx- and Rx-bands. Two prototype antennas concentrating on the short-circuit tuning in the E-GSM and the GSM1800 system were presented. The achieved radiation efficiency on Tx-band of the E-GSM PIN diode implementation was about 70%. By comparing the changes in the required antenna switching quality factors it can be seen that the required Q-values in the E-GSM implementations are higher than those in the corresponding GSM1800 designs. Based on this , the losses are likely to increase simultaneously when the operation frequency increases.

Series resonance behaviour was found to be the restricting factor in obtaining a good on-state radiation efficiency in the PIN diode implementation. Based on the difficulties in the E-GSM & PIN diode design, at least some rule of thumb in the designing might be to implement the tuning circuit in such a way that these kinds of additional series resonances would not occur near the desired operating frequency range.

It must be emphasized that the capacitive series loading is not a proper solution from the point of view of antenna miniaturization, since the original antenna is required to resonate even at lower frequencies than the desired operation band. A more advisable technique, in the antenna miniaturization point of view, would be the use of a series inductive loading. At least in theory, an operation similar to the series capacitive loading, but in the inductive form, could be achieved, for instance, by replacing the capacitance C_1 in the PIN diode based implementation (see Figure 8.) by an inductance.

The second part of the experimental investigations concentrated on the capacitive tuning on the open-end of a completely short-circuited 1.85 GHz PIFA. The aim was to achieve the E-GSM operation by placing a capacitively tuned load on the open-end. The first observation conserning all the open-end tuned prototypes was that the matching was not as sensitive to the changes in the loading capacitance

as it had been in the short-circuit tuned cases. For instance, the resonant frequency of the varactor-tuned capacitor plate implementation could be shifted from about 880 MHz to 1 080 MHz without causing any significant effects on the matching of L_{retn} = 20 dB. The E-GSM operation, for instance, was achieved already by a 1.5 V bias. From the radiation point of view, however, the results turned out to be less promising. Whereas the assumption before these practical implementations, based on several results reported in the literature, was that the radiation efficiency on the open-end tuned implementation should be considerably higher than in the short-circuit tuned case, it was impossible to make a similar conclusion on the basis of the practical measurements. Despite the used tuning technique, the radiation efficiency remained below 50% and was in some circumstances even lower than in the corresponding short-circuit design.

However the weaker radiation properties of the open-end tuned prototypes cannot be explained by the tuning losses alone. A more reasonable or actually a self-evident explanation for such a weak radiation efficiency of the open-end tuned prototypes is the antenna miniaturization.

In addition to the radiation efficiency measurements based on the Wheeler method and conducted during the prototype implementation process, the radiation properties of each prototype were measured in an anechoic chamber. The purpose of these radiation measurements was, first of all, to compare the results to the radiation efficiency measurements of the Wheeler method and, secondly, to detect the changes induced by the tuning on the crosspolarization levels of the original antenna. Although the measured radiation properties were analyzed only by comparing the average radiation power levels of E- and H-planes between the original and the tuned antenna structures, there seemed to be a quite good correlation between the measured average radiation powers and the Wheeler method based radiation efficiency, especially in the E-plane.

- An important factor which also significantly influences the selection of different switching or tuning devices is their distortion properties. It must be pointed out that in the mobile phone applications, distortion is one of the main factors which may restrict the usage of such switching or tuning circuitry. Therefore, the distortion properties should equally be analyzed with such the other properties as the impedance bandwidth and the radiation characteristics. Naturally, it can be suggested without any practical distortion tests that the distortion produced, for instance, by a varactor is higher than the distortion produced by a PIN diode. However, the distortion is also dependent on several other factors, such as the circuit design and the component selection.

6. References

[1] Siemens, Discrete & RF Semiconductors, "Carrier Lifetime and Forward Resistance in RF PIN diodes", *Application Note No. 034*, Siemens AG, München, 1997, 4 p.

[2] Alpha Industries, Inc., G. Hiller, "Design with PIN Diodes", *Application Notes*, 1998.

[3] Hewlett Packard, "Applications of PIN Diodes", *Application Note 922*, 1998.

[4] Hewlett Packard, "A Low Distortion PIN Diode Switch Using Surface Mount Devices", *Application Note 1049,* 1998.

[5] A. Lehto, A. Räisänen, *RF- ja Mikroaaltotekniikka (RF and Microwave Engineering, in Finnish*), Espoo: Otatieto Oy, 1994, 250 p.

[6] E. Nyfors, P. Vainikainen, *Industrial Microwave Sensors*, Norwood: Artech House, 1989, 351 p.

[7] H. R. Virani, "Electrically Small Antennas", *Journal of the Institution of Electronic and Radio Engineers,* Vol. 58, No. 6, pp. 266 – 274, September-December 1988.

[8] Alpha Industries, Inc., *Discrete Semiconductors for RF/Microwave Applications - Catalogue*, Section 2: Varactor Diodes, 1998.

[9] R.B. Waterhouse, N. V. Shuley: "Full Characterization of Varactor-Loaded, Probe-Fed, Rectangular, Microstrip Patch Antennas," *IEE Proc.–Microwave. Antennas Propagation.,* Vol. 141, No. 5, pp. 367-372, October 1994.

ARRAY ANTENNA DESIGN FOR BASE STATION APPLICATIONS

Björn Johannisson and Anders Derneryd

Ericsson Microwave Systems AB
SE-431 84 Mölndal, Sweden

E-mail: Bjorn.Johannisson@ericsson.com, Anders.Derneryd@ericsson.com

Abstract: Adaptive antenna systems represent an area in which considerable development efforts and field trials are being conducted to increase capacity in mobile communication networks. Ericsson has developed array antennas for use in the 900, 1800 and 1900 MHz frequency bands. With the use of an efficient grid of microstrip patch elements connected to beam-forming Butler matrices these antennas yield high antenna gain and excellent spatial efficiency. In this paper design considerations and solutions for these array antennas are presented together with measured results.

1. Introduction

The continuing growth in the number of mobile communication users leads many operators to an increasing need for larger capacity in their networks. Several options are available for them, such as more frequency spectrum, frequency-hopping techniques, microcell solutions and adaptive antenna systems.

An example of more spectrum allocation is the introduction of frequency bands at 1800 and 1900 MHz in addition to the 800 and 900 MHz bands that have been used for a longer time. Due to the larger path loss at higher frequencies, mobile communication networks at 1800 and 1900 MHz require more base-stations or higher levels of radiated power for the same coverage. The possibility of increased antenna gain through the use of array antennas is therefore of particular interest at these higher frequencies. As a result there exists both capacity and coverage arguments for introducing adaptive antenna systems into the mobile communication networks.

Given a limited frequency spectrum the alternative to adaptive antennas will be a denser network of base-station sites. A drawback of this kind of dense network is the cost involved in finding new locations for the antennas and base-station cabinets. Another aspect associated with adding numerous base-stations is the risk of being perceived as an aesthetic eyesore, due to the large quantities of associated antenna installations. Indeed, in many regions, the general public demand is for fewer installations.

Ericsson has vast experience of array antenna products which, thanks to a superior design practice and the integration of antenna and electronic components, make attractive system solutions. Product examples found in commercial and defense applications include Maxite active antennas, the MINI-LINK family, Erieye airborne early-warning radar and Arthur artillery hunting radar.

2. Adaptive Antenna Configurations

In order to evaluate the performance of adaptive antenna systems a number of field trial activities have been performed in GSM and TDMA (IS-136) systems. These trials have been performed in live networks together with Mannesmann Mobilfunk GmbH (GSM) and AT&T Wireless Services (TDMA) in order to evaluate the performance of the adaptive systems. The results show considerably increased capacity when using adaptive antenna systems [1,2].

It has also been shown that large increases in capacity can be achieved by only replacing a limited number of existing installations with adaptive systems [3,4]. In this way new site locations can be avoided. An example of an adaptive antenna installation at an existing site is shown in figure 1.

The basic principle in the adaptive antennas is to use an array antenna with a horizontal extension that makes it possible to create narrow antenna beams in the azimuth plane. These narrow beams can be directed toward targeted mobile terminals and will reduce both uplink and downlink interference levels in the network, which will increase network capacity.

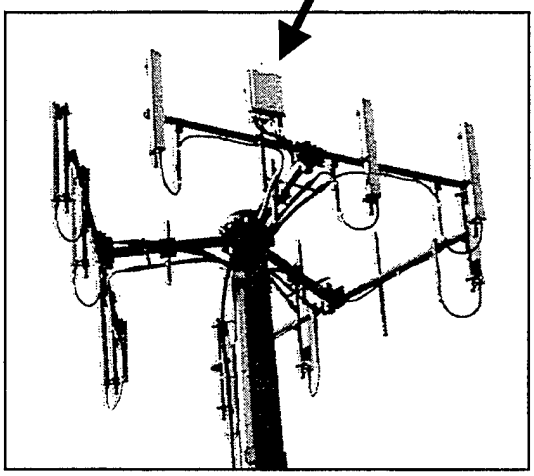

Figure 1. Adaptive antenna installation at an existing site.

Using dual polarized antennas makes polarization diversity schemes possible and only a single antenna unit is needed in each direction from a base-station. This will help minimizing the installation and aesthetic problems at the sites.

Scanning a narrow beam requires changing the phase front along the antenna elements, correspond to different angular beam directions. To avoid the need for phase requirements on feeder cables, it is an advantage to perform RF beam-forming within the antenna unit instead of having it done in the base-station cabinet. In the antenna phase coherence is easily achieved and no advanced calibration procedures need to take place. One example of a passive beam-forming network is the Butler matrix, which generates a set of simultaneous orthogonal beams from a single array antenna and minimizes beam-forming loss. A crossover gain drop between the orthogonal beams must be considered in the system design. Ideally, gain at the crossover point using a Butler matrix is 3.9 dB less than beam peak gain.

3. Array Antennas

Two-dimensional antenna arrays for use in adaptive antenna systems have been developed and manufactured by Ericsson for the 900, 1800 and 1900 MHz frequency bands. The adaptive array antenna transmits and receives radio-frequency signals in directed narrow beams. Figure 2 shows a principal block diagram of an array composed of a dual-polarized multibeam antenna with four azimuth beams in each of two orthogonal polarizations.

The orientation of the polarization is slant linear ±45°. Each column in the array has a vertical feed network that combines the power from dual polarized radiating elements into two ports. The Butler matrices do horizontal beam-forming and combine the radiating element signals to beam ports for each polarization, giving four beams with +45° and four beams with -45° polarization.

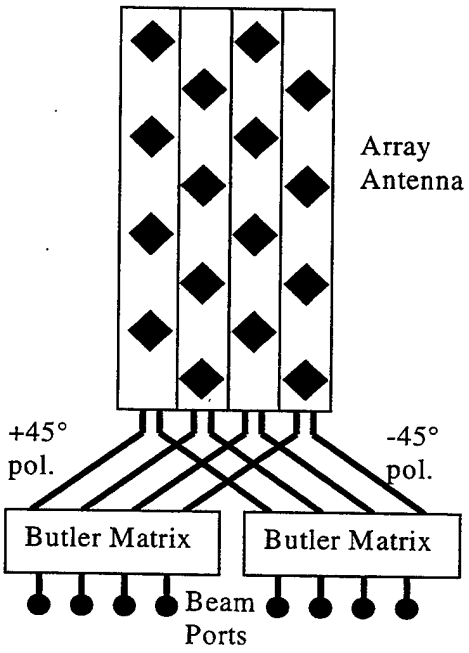

Figure 2. Block diagram of dual polarized, four column adaptive antenna.

The columns are spaced half a wavelength apart with radiating elements positioned in a triangular grid. The radiating elements are dual polarized aperture-coupled microstrip patches. As the same array antenna is used both to transmit and receive it must work over the entire system frequency band, which for the mobile communication systems considered here is in the order of 10%.

To facilitate the required bandwidth a rather broadband design of aperture-coupled patches and feed networks is needed. For the microstrip patch design it involves locating the patches about 1/10 of a wavelength above the aperture ground plane. The dielectric between the patch and the ground plane is primarily air. In front of the antenna a radome is located to protect it from the environment

The antennas described in this paper use Butler matrices to form horizontal beams. A Butler matrix has an equal number of antenna ports and beam ports. For each polarization, a separate Butler matrix is connected to the columns of microstrip patches. By interleaving the beams of both polarizations, where every other beam has opposite polarization, crossover depth between adjacent beams is significantly reduced. This can be seen in figure 3 where measured radiation patterns for a GSM 900 array are presented. A more detailed presentation of individual beams from an adaptive array antenna can be found in [5].

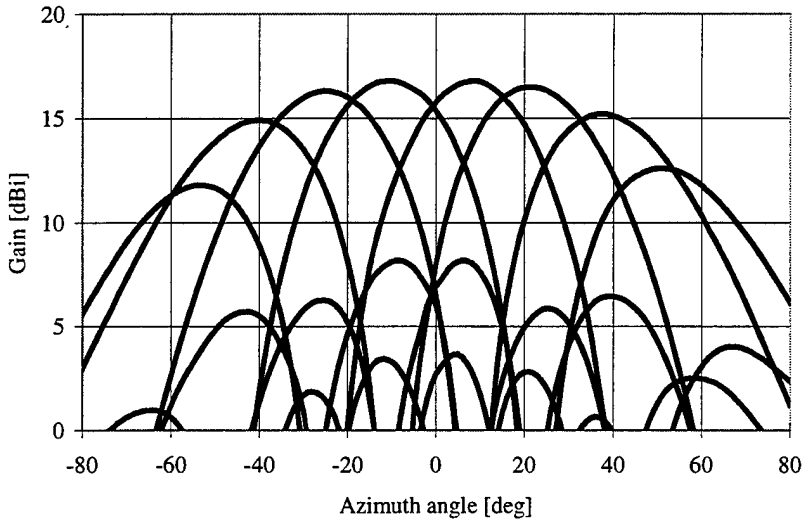

Figure 3. Measured radiation pattern for a dual polarized array having eight interleaved beams.

4. Element Grid

In order to minimize feed network losses and coupling effects between radiating elements a sparse grid of elements is advantageous. On the other hand, grating lobes must be avoided for remained beam pattern control at all beam positions.

Figure 4 shows an effective element pattern layout in which the radiating element positions have been optimized to avoid grating lobes even at the outermost beams.

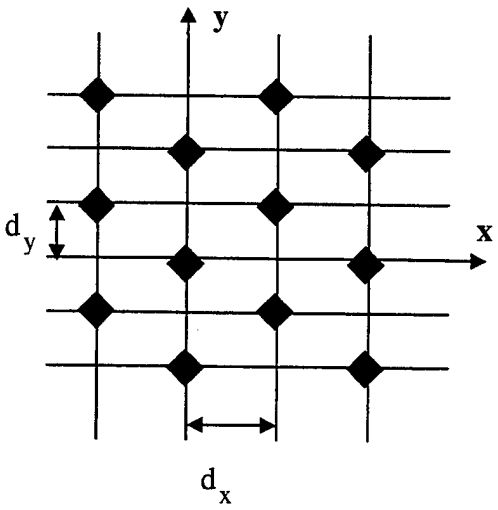

Figure 4. Radiating element layout

A corresponding beam space is illustrated Figure 5. The element spacing d_x and d_y must not be greater than 0.5 wavelengths along x- or y-axis to avoid generating grating lobes for any scan angle in one dimension.

By using a triangular grid grating lobes only come close to the visible space for the outermost beam positions, where achieved gain is not as critical as for the center beams.

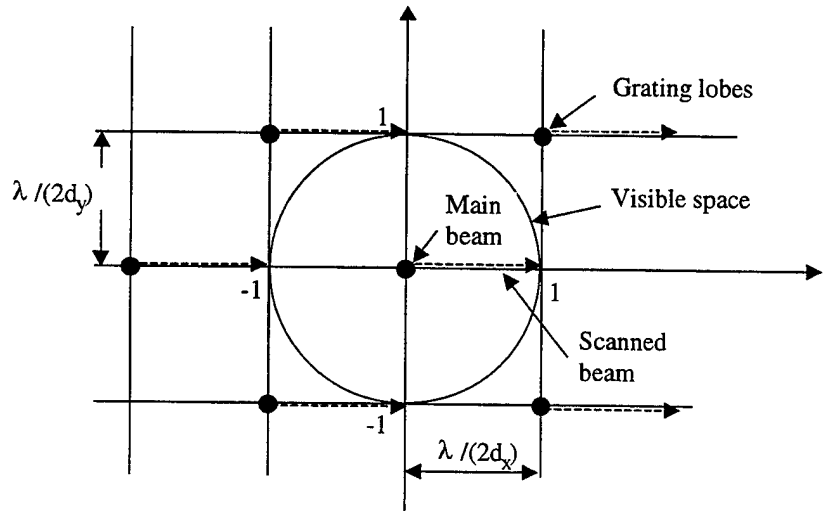

Figure 5. Beam space for array antenna.

5. Sector Coverage Antenna

In GSM as well as TDMA systems, base-stations must occasionally transmit a control channel simultaneously over the entire sector region. To satisfy this requirement, a separate sector antenna function has been introduced as part of the adaptive antenna system. An effective solution uses an additional column of radiating elements next to the array antenna columns. For best results, the deviation between the sector antenna radiation pattern and the array antenna multibeam envelope must be as small as possible.

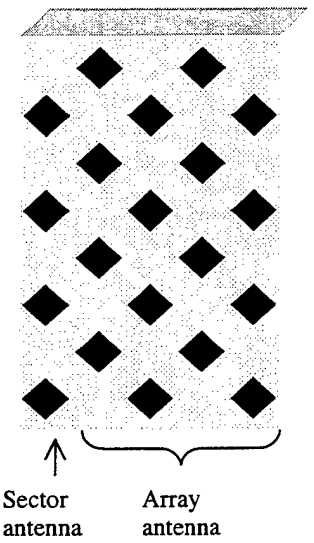

Figure 6. Sector antenna adjacent to array antenna.

By putting the sector antenna next to the array antenna, as shown in figure 6, the two antennas are still in principle functionally separated, even if they are mechanically one unit with a common radome. The advantage of using one mechanical unit is the smaller aesthetic impact and the simpler installation procedure. For a proper behavior it is important to ensure that the mutual coupling effects between the two antennas does not distort the antenna patterns.

The resulting measured pattern for a sector beam next to the GSM 900 array beams can be seen in figure 7. The relative level of the sector beam pattern has been adjusted for easier visual evaluation of similarity between the sector pattern and the array antenna envelope.

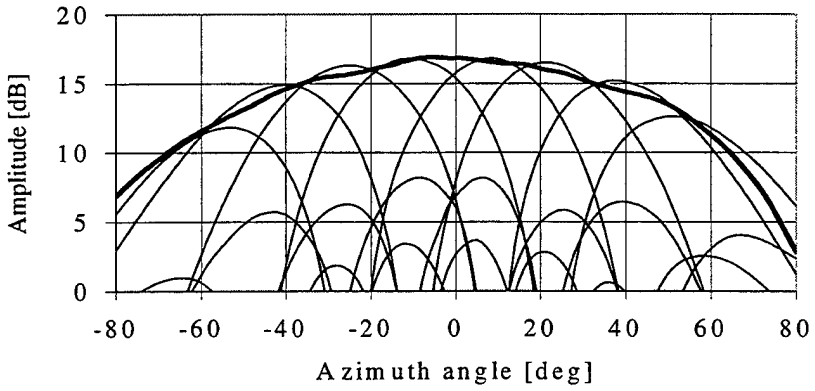

Figure 7. Sector antenna beam together with array beam patterns.

6. Antenna Performance

The antennas described in this paper, figure 8 showing one example, have high antenna gain and good spatial efficiency over a large frequency bandwidth.

The large antenna gain achieved with these arrays can be exploited for better coverage in the mobile communication system, besides increased capacity. The amount of antenna gain offered for the tested antennas are shown in table 1. The increase in antenna gain can be exploited to offer greater coverage. As an example the gain of the GSM 900 array, which is less than one meter high is comparable to that of a traditional, two-meter sector antenna.

Return loss for one polarization in an array is presented in figure 9, where the bold line corresponds to the sector beam port while the other lines are array beam ports.

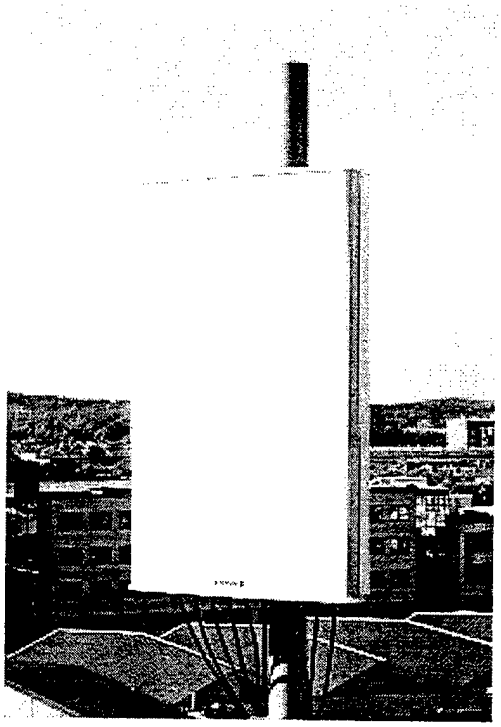

Figure 8. Adaptive antenna array

Table 1. Dimensions and measured antenna gain for different tested arrays.

	Frequency	Dimensions	Antenna Gain
GSM 900	880 - 960 MHz	0.8 m x 0.9 m	> 16.5 dBi
GSM 1800	1710 - 1880 MHz	1.25 m x 0.5 m	> 22.0 dBi
TDMA 1900	1850 - 1990 MHz	0.65 m x 0.44 m*	> 17.5 dBi

* including sector antenna column

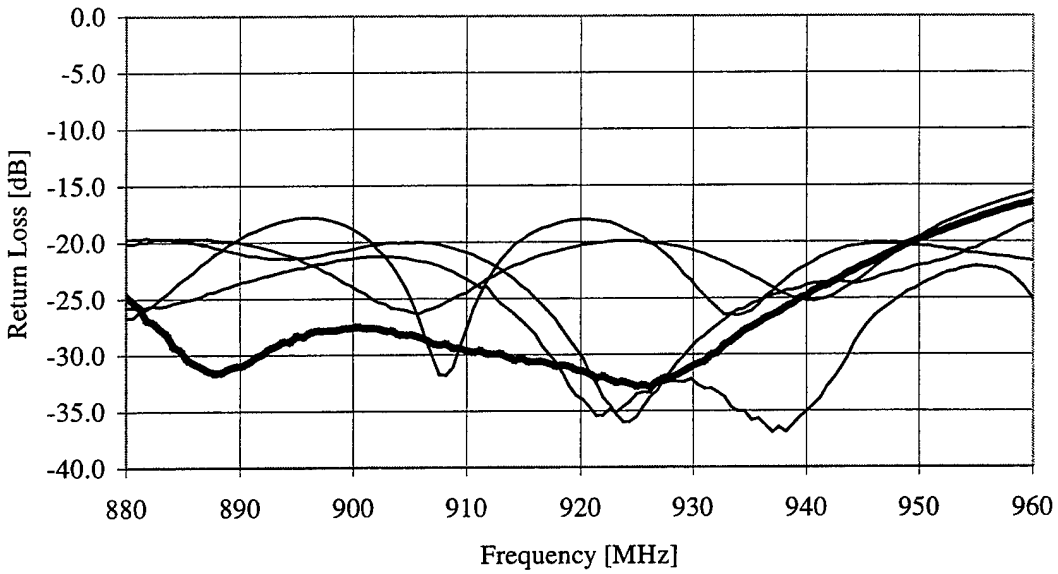

Figure 9. Return loss of one polarization side of an adaptive array antenna. Bold line corresponds to sector port and the other curves are array beam ports.

7. Future trends of base-station adaptive antennas

Mobile communication base-station cabinets have traditionally been attached to passive antennas in a mast. To derive sufficient power radiation from these antennas, it has been necessary to use amplifiers with high output power and low-loss feeder cables.

Although high-power amplifiers are relatively efficient, the overall power efficiency of a traditional base-station is low, since a lot of heat is generated at the base-station cabinets. Consequently, air conditioners must be installed, further reducing the total efficiency of the base-station. Moreover, even when low-loss feeder cables are used, a considerable amount of power is lost in transit to the antenna as well as in the antenna power-combining/power-distribution network. A future introduction of adaptive antennas, which employ distributed power amplifiers along the antenna array close to the radiating elements, can greatly improve overall power efficiency.

8. Conclusions

A way to achieve higher capacity is to use adaptive antenna systems. Ericsson and cooperating operators have tested such antenna systems in live GSM and TDMA networks, proving that adaptive antenna systems enable operators to increase the capacity of their mobile communication networks.

The antennas used in these field trials are dual polarized two-dimensional array antennas with eight simultaneous beams. Beam-forming is performed with Butler matrices giving orthogonal beams. Interleaved beams of different polarizations reduce the cross-over depths and give high spatial efficiency. Loss is also reduced by the introduction of a sparse element grid. The high measured antenna gain in the described array antennas will also give large coverage from a compact antenna installation.

The sector coverage beam needed in mobile communication systems is introduced as a separate column next to the array antenna located under the same radome. Simpler installation and better aesthetic impact are achieved with this solution.

REFERENCES

[1] S Andersson, U Forssén, J Karlsson, T Witzschel, P Fisher and A Krug, "Ericsson/Mannesmann GSM field-trials with adaptive antennas", *Proc. 47th IEEE Vehicular Technology Conference*, Phoenix, AZ, May 1997.

[2] Bo Hagerman et. al. "Ericsson-AT&T Wireless Services Joint Adaptive Antenna Multi-Site Field Trial for TDMA (IS-136) Systems", *Proc. Sixth Annual Smart Antenna Workshop*, Stanford, CA, July 1999.

[3] F Kronestedt and S Andersson, "Migration of Adaptive Antennas into Existing Networks", *Proc. 48th IEEE Vehicular Technology Conference*, Ottawa, Canada, pp. 1670-1674, May 1998.

[4] H Aroudaki and K Bandelow, "Effects of introducing adaptive antennas into existing GSM networks", *Proc. 49th IEEE Vehicular Technology Conference*, Houston, TX, pp. 670-674, May 1999.

[5] B Johannisson, "Adaptive Base Station Antennas for Mobile Communication Systems", *Proc. IEEE AP-S Conference on Antennas and Propagation for Wireless Communications*, Waltham, MA, pp. 49-52, November 1998.

A CIRCUALR COAXIAL ORTHOGONAL MODE JUNCTION DIPLEXER AND POTENTIAL BENEFIT OF INCOPORATED WITH RIDGES AND T-SEPTA IN ITS INNER CONDUCTOR

Henry Z. Zhang

CSIRO Telecommunications & Industrial Physics
PO Box 76, Epping, NSW 1710, Australia
e-mail: henry.zhang@tip.csiro.au

Abstract: A circular coaxial Orthogonal Mode Junction (OMJ), comprising a circular coaxial waveguide and four side-coupled rectangular waveguides, is proposed as a basic structure for separating multiple bands from a wideband dielectric cone-loaded feed horn. The proposed OMJ diplexer is analysed using the Boundary-Contour Mode-Matching (BCMM) method in conjunction with the mode-matching method and verified using the finite-element method. The possibility of incorporating the ridges and T-septa in the OMJ diplexer's inner conductor to enhance its bandwidth is also discussed. Further, the paper presents some interesting results for a coaxial waveguide with two ridges and two T-septa placed in its inner conductor.

1. Introduction

The dielectric-cone-loaded, hybrid-mode feed horn has been shown to operate over very wide bandwidth [1] and found application in dual-band feed systems [2]. To fully exploit this type of feed for multi-band applications, some means of separating these multiple bands is necessary. To this end, the coaxial Orthogonal Mode Junction (OMJ) shown in Fig.1 is proposed as a basic structure for separating multiple bands from the horn. The coaxial OMJ, comprising a coaxial waveguide with four side-coupled rectangular waveguides, couples the incoming dual-polarised signals from the coaxial waveguide to four rectangular waveguides. These dual-polarised signals from the opposite pairs of rectangular waveguides are later re-combined in a circular waveguide using a circular OMJ (without the core). The desired dual-polarised signals in the circular waveguide can then be easily extracted by using an orthogonal mode transducer, as shown in Fig. 2. By a series of such coaxial OMJ structures, a number of bands can be separated from the horn. Furthermore, the highest band can propagate in the inner circular waveguide that makes up the core of the coaxial waveguide.

To date, coaxial OMJ structures of the type shown in Fig. 1 have largely been designed experimentally as the theoretical analysis of such as structure is a formidable problem. However, experimental design alone is not only extremely time consuming but also a difficult means of fully exploring all the design possibilities. To both shorten the design cycle and to maximise the bandwidth potential of the structure, a rigorous theoretical method capable for computer optimisation is outlined in section 2 of this paper.

The previous analysis has shown that the bandwidth of a circular coaxial waveguide can be significantly enhanced by incorporated with four ridges or four T-septa in its inner conductor [3,4]. This indicates that the bandwidth of the proposed OMJ diplexer would also be increased by incorporated with ridges and T-septa in its inner conductor.

As an extension, this paper also presents a new structure, a coaxial waveguide with two ridges and two T-septa symmetrically placed in its inner conductor. The new asymmetric structure is proposed for the applications that require significantly broader bandwidth in one channel. Section 4 and 5 will present the formulation and numerical analysis results for this asymmetric structure.

2. Formulation for Coaxial OMJ

The coaxial OMJ structure to be analysed is shown in Fig. 1, where the orthogonal polarised incoming waves are coupled to the corresponding pair of rectangular waveguides. The influence of the opposite pair of waveguides can be ignored if the narrow dimension of the rectangular waveguide is small comparing with the diameter of the coaxial waveguide's outer surface. Therefore, we only need to analyse the junction of a coaxial waveguide with two side-coupled rectangular waveguides.

Similar to the resonator method [5] used in analysing the T-junction structure, the coaxial OMJ is decomposed into four short-circuited waveguides that form a resonator region V, as shown in Fig. 3. As the structure is symmetric with respect to the x axis, only half of it needs to be considered, as illustrated in Fig. 4. The Hertzian potential for TE and TM modes in region I to V are defined as follows

Region I and II:

$$\psi^{Ih} = \sum_{m_{c1}=1}^{M_{c1}} \sum_{m_{r1}=1}^{M_{r1}} A^{Ih}_{m_{c1}m_{r1}} f^{Ih}_{2m_{c1}-1}\left(k^{Ih}_{\rho m_{c1}m_{r1}}\rho\right)\cos\left(2m_{c1}-1\right)\phi \times \left[F^{Ih}_{m_{c1}m_{r1}} e^{-jk^{Ih}_{zm_{c1}m_{r1}}(z\mp c/2)} - B^{Ih}_{m_{c1}m_{r1}} e^{jk^{Ih}_{zm_{c1}m_{r1}}(z\mp c/2)}\right] \quad (1.1)$$

$$\psi^{Ie} = \sum_{n_{c1}=1}^{N_{c1}} \sum_{n_{r1}=1}^{N_{r1}} A^{Ie}_{n_{c1}n_{r1}} f^{Ie}_{2n_{c1}-1}\left(k^{Ie}_{\rho n_{c1}n_{r1}}\rho\right)\sin\left(2n_{c1}-1\right)\phi \times \left[F^{Ie}_{n_{c1}n_{r1}} e^{-jk^{Ie}_{zn_{c1}n_{r1}}(z\mp c/2)} - B^{Ie}_{n_{c1}n_{r1}} e^{jk^{Ir}_{zn_{c1}n_{r1}}(z\mp c/2)}\right] \quad (1.2)$$

Region III and IV:

$$\psi^{IIIh} = \sum_{m_{z3}=0}^{M_{z3}} \sum_{m_{y3}=1}^{M_{y3}} A^{IIIh}_{m_{z3}m_{y3}} \cos\frac{2m_{y3}\pi}{d}\left(y+\frac{d}{2}\right)\sin\frac{m_{z3}\pi}{c}\left(z+\frac{c}{2}\right)\times \left[F^{IIIh}_{m_{z3}m_{y3}} e^{-jk^{IIIh}_{xm_{z3}m_{y3}}(x\mp x_0)} - B^{IIIh}_{m_{z3}m_{y3}} e^{jk^{IIIh}_{xm_{z3}m_{y3}}(x\mp x_0)}\right] \quad (1.3)$$

$$\psi^{IIIe} = \sum_{n_{z3}=1}^{N_{z3}} \sum_{n_{y3}=1}^{N_{y3}} A^{IIIe}_{n_{z3}n_{y3}} \sin\frac{2n_{y3}\pi}{d}\left(y+\frac{d}{2}\right)\cos\frac{n_{z3}\pi}{c}\left(z+\frac{c}{2}\right)\times \left[F^{IIIe}_{n_{z3}n_{y3}} e^{-jk^{IIIe}_{xn_{z3}n_{y3}}(x\mp x_0)} - B^{IIIe}_{n_{z3}n_{y3}} e^{jk^{IIIe}_{xn_{z3}n_{y3}}(x\mp x_0)}\right] \quad (1.4)$$

where

$$f^{Ih}_{2n-1}\left(k_\rho\rho\right) = J'_{2n-1}\left(k^{IIh}_\rho a\right)Y_{2n-1}\left(k^{Ih}_\rho\rho\right)/Y'_{2n-1}\left(k^{Ih}_\rho a\right) - J_{2n-1}\left(k^{Ih}_\rho\rho\right)$$

$$f^{Ie}_{2n-1}\left(k_\rho\rho\right) = J_{2n-1}\left(k^{Ie}_\rho a\right)Y_{2n-1}\left(k^{Ie}_\rho\rho\right)/Y_{2n-1}\left(k^{Ie}_\rho a\right) - J_{2n-1}\left(k^{Ie}_\rho\rho\right)$$

$$\left(k^{Ih}_{\rho m_{c1}m_{r1}}\right)^2 = \omega^2\mu_0\varepsilon_0 - \left(k^{Ih}_{zm_{c1}m_{r1}}\right)^2; \qquad \left(k^{Ie}_{\rho n_{c1}n_{r1}}\right)^2 = \omega^2\mu_0\varepsilon_0 - \left(k^{Ie}_{zn_{c1}n_{r1}}\right)^2$$

$$\left(k^{IIIh}_{xm_{z3}m_{y3}}\right)^2 = \omega^2\mu_0\varepsilon_0 - \left(2m_{y3}\pi/d\right)^2 - \left(m_{z3}\pi/c\right)^2$$

$$\left(k^{IIIe}_{xn_{z3}n_{y3}}\right)^2 = \omega^2\mu_0\varepsilon_0 - \left(2n_{y3}\pi/d\right)^2 - \left(n_{z3}\pi/c\right)^2$$

with

$$(m_{y3} = 0,1,2,3,\ldots;\ m_{z3} = 1,2,3,\ldots)$$

$$(n_{y3} = 1,2,3,\ldots\ldots;\ n_{z3} = 1,2,3,\ldots)$$

The negative sign in the propagation elements in equations (1.1) to (1.4) represent the potential in region I and III. The positive sign represent those in region II and IV. J and Y are the Bessel and Neumann functions, respectively; A_{ij} is normalisation factor; F_{ij} and B_{ij} are forward and backward wave coefficients, respectively.

Region V is a resonator and its potential for TE and TM modes are given as:

$$\psi^{VIh} = \sum_{i_{c1}=1}^{I_{c1}} \sum_{i_{r1}=1}^{I_{r1}} C^{Ih}_{i_{c1}i_{r1}} f^{Ih}_{2i_{c1}-1}\left(k^{Ih}_{\rho i_{c1}i_{r1}}\rho\right)\cos(2i_{c1}-1)\phi \sin\left[k^{Ih}_{zi_{c1}i_{r1}}(z+c/2)\right] \tag{1.5}$$

$$+ \sum_{i_{c2}=1}^{I_{c2}} \sum_{i_{r2}=1}^{I_{r2}} C^{IIh}_{i_{c2}i_{r2}} f^{IIh}_{2i_{c2}-1}\left(k^{IIh}_{\rho i_{c2}i_{r2}}\rho\right)\cos(2i_{c2}-1)\phi \sin\left[k^{IIh}_{zi_{c2}i_{r2}}(z-c/2)\right]$$

$$+ \sum_{i_{c3}=1}^{I_{c3}} \sum_{i_{r3}=1}^{I_{r3}} C^{IIIh}_{i_{c3}i_{r3}} f^{IIIh}_{2i_{c3}-1}\left(k^{IIIh}_{\rho i_{c3}i_{r3}}\rho\right)\cos(2i_{c3}-1)\phi \sin\left[\frac{i_{r3}\pi}{c}(z+c/2)\right]$$

$$+ \sum_{i_{c4}=1}^{I_{c4}} \sum_{i_{r4}=1}^{I_{r4}} C^{IVh}_{i_{c4}i_{r4}} f^{IVh}_{2i_{c4}-1}\left(k^{IVh}_{\rho i_{c4}i_{r4}}\rho\right)\cos(2i_{c4}-1)\phi \sin\left[\frac{i_{r4}\pi}{c}(z+c/2)\right]$$

$$\psi^{VIe} = \sum_{i_{c1}=1}^{I_{c1}} \sum_{i_{r1}=1}^{I_{r1}} C^{Ie}_{i_{c1}i_{r1}} f^{Ie}_{2i_{c1}-1}\left(k^{Ie}_{\rho i_{c1}i_{r1}}\rho\right)\sin(2i_{c1}-1)\phi \cos\left[k^{Ie}_{zi_{c1}i_{r1}}(z+c/2)\right] \tag{1.6}$$

$$+ \sum_{i_{c2}=1}^{I_{c2}} \sum_{i_{r2}=1}^{I_{r2}} C^{IIe}_{i_{c2}i_{r2}} f^{IIe}_{2i_{c2}-1}\left(k^{IIe}_{\rho i_{c2}i_{r2}}\rho\right)\sin(2i_{c2}-1)\phi \cos\left[k^{IIe}_{zi_{c2}i_{r2}}(z-c/2)\right]$$

$$+ \sum_{i_{c3}=1}^{I_{c3}} \sum_{i_{r3}=1}^{I_{r3}} C^{IIIe}_{i_{c3}i_{r3}} f^{IIIe}_{2i_{c3}-1}\left(k^{IIIe}_{\rho i_{c3}i_{r3}}\rho\right)\sin(2i_{c3}-1)\phi \cos\left[\frac{i_{r3}\pi}{c}(z+c/2)\right]$$

$$+ \sum_{i_{c4}=1}^{I_{c4}} \sum_{i_{r4}=1}^{I_{r4}} C^{IVe}_{i_{c4}i_{r4}} f^{IVe}_{2i_{c4}-1}\left(k^{IVe}_{\rho i_{c4}i_{r4}}\rho\right)\sin(2i_{c4}-1)\phi \cos\left[\frac{i_{r4}\pi}{c}(z+c/2)\right]$$

where

$$f^{IIIh}_{2n-1}\left(k^{IIIh}_{\rho}\right) = f^{IVh}_{2n-1}\left(k^{Vh}_{\rho}\right) = J'_{2n-1}\left(k^{IIIh}_{\rho}a\right)Y_{2n-1}\left(k^{IIIh}_{\rho}\rho\right)/Y'_{2n-1}\left(k^{IIIh}_{\rho}a\right) - J_{2n-1}\left(k^{IIIh}_{\rho}\rho\right)$$

$$f^{IIIe}_{2n-1}\left(k^{IIIe}_{\rho}\right) = f^{IVe}_{2n-1}\left(k^{Ve}_{\rho}\right) = J_{2n-1}\left(k^{IIIe}_{\rho}a\right)Y_{2n-1}\left(k^{IIIe}_{\rho}\rho\right)/Y_{2n-1}\left(k^{IIIe}_{\rho}a\right) - J_{2n-1}\left(k^{IIIe}_{\rho}\rho\right)$$

$$\left(k^{IIIh}_{\rho i_{c3}i_{r3}}\right)^2 = \omega^2\mu_0\varepsilon_0 - (i_{r3}\pi/c)^2 \qquad (i_{r3} = 1,2,3,.....)$$

$$\left(k^{IIIe}_{\rho j_{c3}j_{r3}}\right)^2 = \omega^2\mu_0\varepsilon_0 - (j_{r3}\pi/c)^2 \qquad (j_{r3} = 1,2,3,.....)$$

Matching the tangential fields at the corresponding apertures gives 16 equations. As the equations for describing the fields in the short-circuited waveguides III and IV is not satisfy the boundary condition at the outer conductor surfaces, a boundary-contour integration is taken to force them to satisfy the boundary conditions. This combination of a boundary-contour integration with mode matching at the moon shape, as shown in Fig. 4, is known as the boundary-contour mode-matching method [6-8]. The 16 equations are further reduced to 8 equations after eliminating the unknown coefficients related to region V. The remaining equations are associated with the forward and backward coefficients in

regions I to IV. Re-arranging these eight equations yields a scattering matrix of the corresponding four-port block discontinuity directly.

The scattering matrix of the matching irises can be easily obtained by using the mode-matching method [9]. The performance of the entire OMJ structure with matching irises and transition steps can then be obtained by cascading the matrices obtained using the BCMM and mode-matching methods.

The circular OMJ structure (without core) can obtained using the formulas given above by replacing f^h and f^e with a Bessel function.

3. Numerical Results for Coaxial OMJ

The convergence of the BCMM method has been examined. Good convergence was observed when the number of modes is equal to or greater than 5×5 TE + 5×5 TM. All the subsequent results were obtained using 5×5 TE + 5×5 TM. The results for the coaxial OMJ structure with matching irises and transition steps obtained using the BCMM and mode-matching method are tabulated in Table 1, and compared with those obtained using the finite-element method [10]. The table shows a good agreement between these results.

The proposed method is significantly faster than the finite-element method. It enables us to design an OMJ structure by using computer optimisation. Fig. 5 shows the results for the design of a coaxial OMJ structure. Its good return loss in the desired band was obtained by computer optimisation. Fig. 6 illustrates one more example of OMJ diplexer design. Both coaxial OMJ and circular OMJ (used for re-combining the signals from four rectangular waveguides to a circular waveguide) have good return loss after the optimisation. A pair of coaxial and circular OMJ structures makes up a complete diplexer for diplexing signals from the dielectric-cone-loaded horn.

4. Formulation for Coaxial Waveguide with Ridges and T-septa

The circular coaxial waveguide with four ridges or four T-septa symmetrically placed in the inner conductor is shown in Fig. 7(a) and 7(b). The detailed formulation for analysing the cutoff and bandwidth characteristics of these structures can be found in [3,4]. The newly proposed combined ridge and T-septum waveguide structure is shown in Fig. 7(c). As the structure is symmetric with respect to the x and y axes, only one quarter of it is needed for analysis, as shown in Figure 7(d). This quarter is divided into three regions, as shown in the

same figure. The Hertzian potential for the modes with respect to the z axis can be expressed as follows:

$$\psi_h^I = \sum_{m=0}^{M} A_m f^I_{m\pi/\varphi_2}(k_t\rho)\cos[(m\pi/\varphi_2)(\phi-\alpha_3)] \tag{2.1}$$

$$\psi_h^{II} = \sum_{n=0}^{N} \left[B_n^a f^{IIa}_{n\pi/\varphi_1}(k_t\rho) + B_n^b f^{IIb}_{n\pi/\varphi_1}(k_t\rho)\right]\cos[(n\pi/\varphi_1)(\phi-\alpha_3)] \tag{2.2}$$

$$\psi_h^{III} = \sum_{p=1}^{P} C_p f^{III}_{2p-1}(k_t\rho)\begin{Bmatrix}\cos\\ \sin\end{Bmatrix}[(2p-1)\phi] \tag{2.3}$$

where

$$f^I_{m\pi/\varphi_2}(k_t\rho) = J'_{m\pi/\varphi_2}(k_t a)Y_{m\pi/\varphi_2}(k_t\rho) - J_{m\pi/\varphi_2}(k_t\rho)Y'_{m\pi/\varphi_2}(k_t a)$$

$$f^{IIa}_{n\pi/\varphi_1}(k_t\rho) = J_{n\pi/\varphi_1}(k_t\rho), \qquad f^{IIb}_{n\pi/\varphi_1}(k_t\rho) = Y_{n\pi/\varphi_1}(k_t\rho)$$

$$f^{III}_{2p-1}(k_t\rho) = J'_{2p-1}(k_t d)Y_{2p-1}(k_t\rho) - J_{2p-1}(k_t\rho)Y'_{2p-1}(k_t d).$$

The *cos* and *sin* functions within the curly bracket represent electric and magnetic symmetry with respect to the y axis, respectively, J and Y are Bessel functions of the first and second kinds, A_m, B_n and C_p are the unknown amplitude coefficients, and k_t is the transverse wavenumber with respect to the z axis.

The H and E fields in each region can be derived from these potential. Matching the tangential fields over the common apertures, and taking the inner products with appropriate basic functions gives a matrix equation. The eigenvalues k_t can be obtained by finding the roots of this matrix equation.

5. Numerical Results for Coaxial Waveguide with Ridges and T-septa

Using the formulations given in section 4, we analyse the bandwidth characteristics of the combined ridged and T-septum coaxial waveguide structure, and compare with those of the T-septum only coaxial waveguide structures. Fig. 8 shows the variation of bandwidth ($\lambda_{c11}/\lambda_{c31}$) as a function φ_1, with *(d-c)/d* as a parameter. The figure shows that the bandwidth of the combined ridge and T-septum structure with polarisation in the direction of T-septum is significantly broader than that of the corresponding T-septum structure. Fig. 9 shows that the bandwidth of the structure with polarisation in the direction of T-septum reduces (ridge increases) with the increase in width ($2\alpha_3$) of the ridge. This indicates that the bandwidth of one polarisation can be transferred to the other by changing the width of the ridge.

The computational results obtained from the mode-matching method have been verified using the finite-element method [10]. As shown in Table 2, the agreement of the results obtained using these two methods is excellent.

6. Conclusion

A coaxial Orthogonal Mode Junction (OMJ) structure is proposed for separating multi-band signals from the dielectric-cone-loaded dual-band feed horn. The proposed structure is analysed using the boundary contour mode-matching and mode-matching method. The results obtained using these methods show a good agreement with those obtained using the finite-element method. The proposed method is significantly faster than the finite-element method, while allows the diplexer to be designed by computer optimisation.

A circular coaxial waveguide with two T-septa and two ridges symmetrically placed in the inner conductor is proposed and analysed using the mode-matching method. The results show that the bandwidth of the proposed structure with electric field polarised in the direction of the T-septum is significantly broader than that of the corresponding structure with four T-septa symmetrically placed in the inner conductor. The improvement in the bandwidth of the new structure with the polarisation in the direction of T-septum is at the expense of the polarisation in the direction of ridge. Using this structure in the design of a dual-channel diplexer, the bandwidth of one channel can be transferred to the other, resulting in a significant improvement in the bandwidth of one channel. This interesting characteristic would be useful in some specified antenna applications.

7. Future Works

It has been shown that a circular coaxial OMJ can be used as a basic structure for separating multiple bands from a coaxial waveguide. However, it suffers from the limited bandwidth of the coaxial waveguide structure. The proposal of ridged and T-septum coaxial waveguide is aimed at enhancing the bandwidth of the coaxial waveguide structure. It was designed to couple the signals from the broadband horn to itself, as shown in Fig. 10. However, the launching of desired mode in the ridged or T-septum coaxial waveguide has to be relied on empirical method. This is not only time consuming, but also difficult to achieve the required specifications in many situations.

Incorporation of ridges or T-septum into the coaxial OMJ's inner conductor would be a nature convergence of these two separated projects. As the bandwidth of the coaxial waveguide can be enhanced by incorporated with ridges or T-septa

in its inner conductor. We predict that the bandwidth of the coaxial OMJ would be increased by incorporated with ridges or T-septa in its inner conductor, as shown in Fig. 11. We are going to develop a numerical method for analysing this ridged or T-septum coaxial OMJ structure. The results will be reported when they are available.

Acknowledgments

The author thanks Mr. Kieran J. Greene for his contributions and useful discussions on this work, and Dr. Graeme L. James for his encouragement and criticism regarding this paper.

References

[1] P. R. Clark and G. L. James, "Ultra-wideband hybrid-mode feeds", *Electron. Lett.*, 1995, Vol.31, No. 23, pp. 1968-1969.

[2] G. L. James, P. R. Clark and K. J. Greene, "Design of waveguide dual-band feed systems", *Fifth Australian Symposium on Antennas*, Feb. 1996.

[3] H. Z. Zhang and G. L. James, "Characteristics of quad-ridged waveguides for dual-band horn applications", *IEE Proc. Microwave, Antennas and propagation,* Vol. 145, No. 3, June 1998, pp. 225-228.

[4] H. Z. Zhang "Bandwidth and cutoff characteristics of a circular coaxial waveguide with four T-septa symmetrically placed in the inner conductor", *IEE Proc. Microwave, Antennas and Propagation,* Vol. 145, No. 4, Aug. 1998, pp. 366-368.

[5] E. Kuhn, "Exact calculation and some applications of the equivalent networks of open E-plane T-junction", *Colloquium on Microwave Communications 1974,* Vol. MT, pp. 363-372.

[6] G. G. Gentili and A. Melloni, "Analysis of the X-junction between two rectangular waveguides and a circular waveguide", *IEEE Microwave and Guided Wave Let.* Vol. 7, No. 8, Aug. 1997, pp. 245-247.

[7] J. M. Reiter and F. Arndt, "Rigorous analysis of arbitrarily shaped H- and E-plane discontinuities in rectangular waveguides by a full-wave boundary contour mode-matching method", *IEEE Trans. Microwave Theory and Tech.,* Vol. 43, No. 4, April 1995, pp. 796-801.

[8] J. M. Reiter and F. Arndt, "A boundary contour mode-matching method for the rigorous analysis of cascaded arbitrarily shaped H-plane discontinuities in rectangular waveguides", Vol. *I* Vol. *IEEE Microwave and Guided Wave Let.* Vol. 2, No. 10, Oct. 1992, pp. 403-405.

[9] J. Uher, J. Bornemann and U. Rosenberg, Waveguide Components for Antenna Feed Systems: Theory and CAD, Artech House, Boston London.

[10] High Frequency Structure Simulator User's manual, Ansoft Corporation.

Table 1

Comparison of the normalised cutoff wavelength (λ_{c11}/d) of TE_{11} mode obtained using two different methods. c/d = 5/6, (b-c)/d = 1/30, $\alpha_1 = 60°$ and $\alpha_2 = \alpha_3 = 10°$.

Polarisation	T-septum	T-septum	ridge	ridge
a/c	1/3	1/2	1/3	1/2
Mode-matching	11.017	9.901	6.939	6.481
Finite-element	10.988	9.875	6.908	6.455

Table 2

Comparison of the results obtained using BCMM and finite-element method for the circular coaxial OMJ connected with matching irises and step transitions. *f = 0.45* GHz. (dimensions in mm). The values given in the table are in dB.

Method	S_{11}	S_{12}	S_{13}	S_{22}	Models
BCMM	-3.24	-9.05	-6.99	-3.43	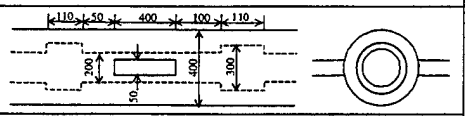
HFSS	-2.97	-9.43	-7.21	-3.27	
BCMM	-9.18	-3.70	-6.44	-9.18	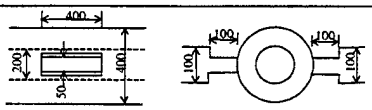
HFSS	-9.22	-3.70	-6.43	-9.19	
BCMM	-1.92	-12.89	-8.18	-2.02	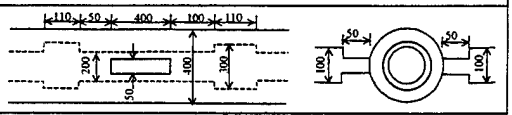
HFSS	-1.75	-13.43	-8.42	-1.91	
BCMM	-2.07	-12.85	-7.85	-1.55	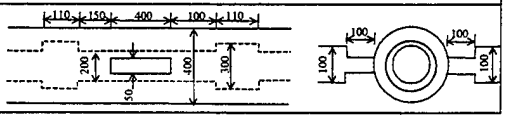
HFSS	-2.03	-13.02	-7.95	-1.48	

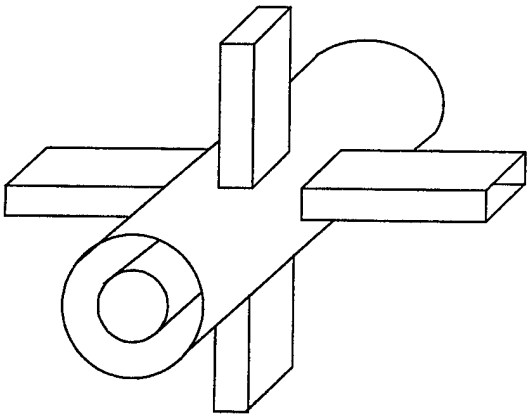

Fig. 1 A basic structure for the design of OMJ diplexer.

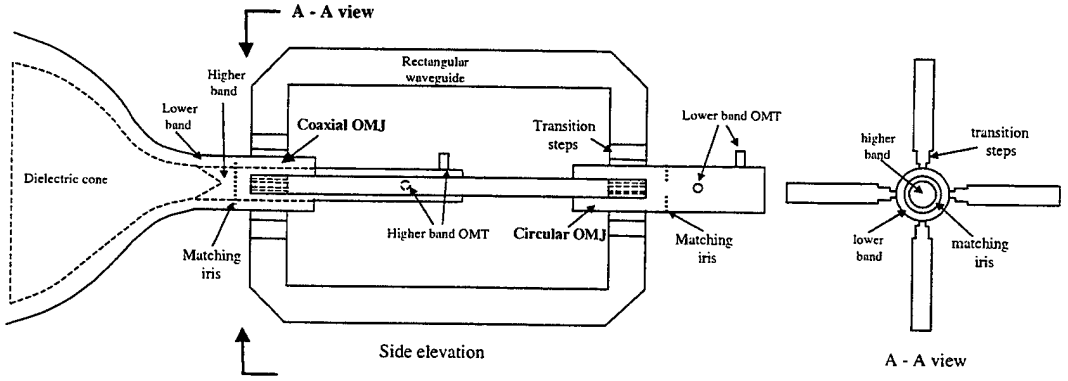

Fig. 2 A diplexer using a coaxial and a circular OMJ structures for diplexing signals from a dielectric-cone-loaded horn.

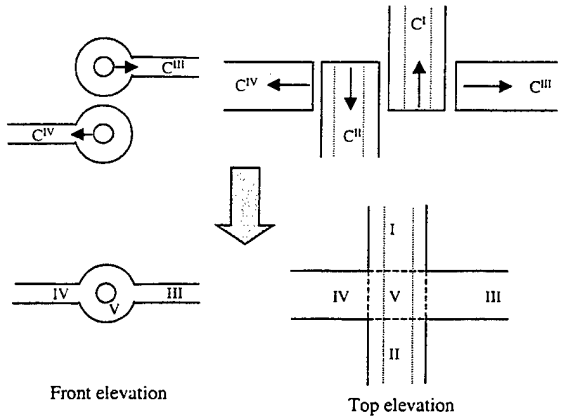

Fig. 3 Decomposition of a coaxial OMJ.

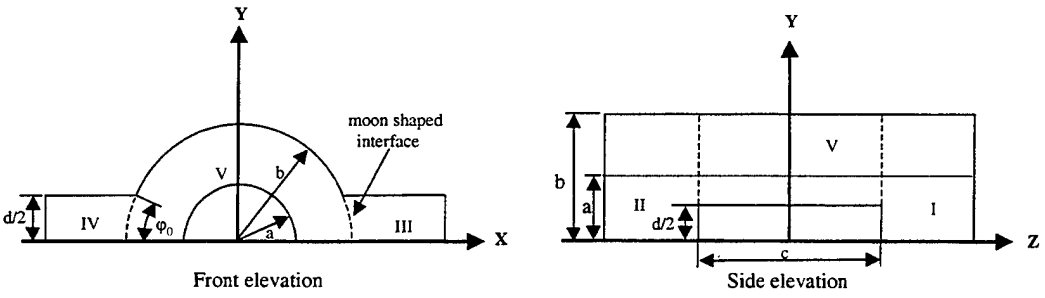

Fig. 4 Detail of a circular coaxial waveguide with two side-coupled rectangular waveguides.

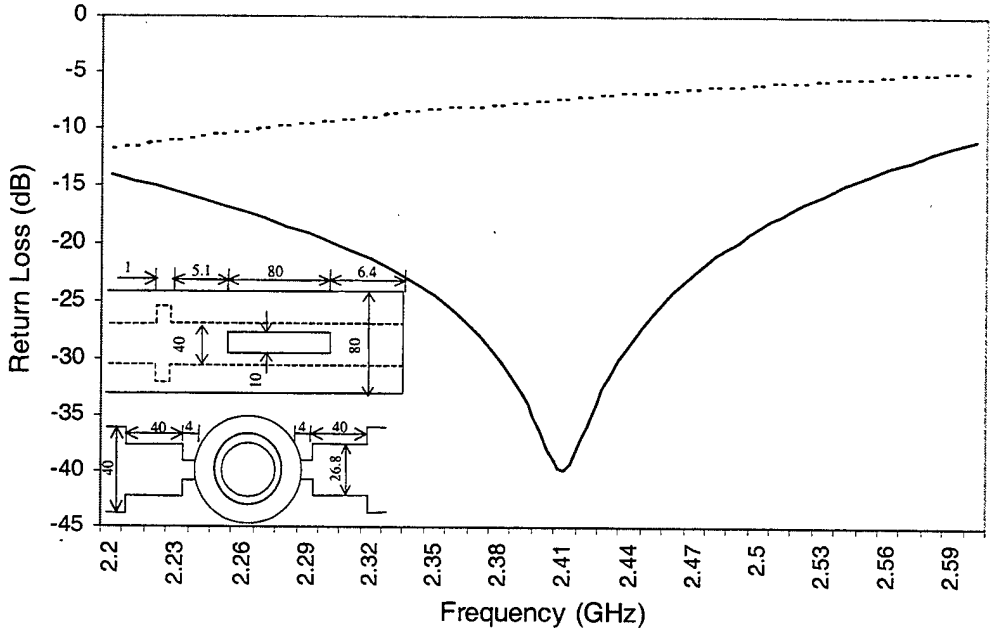

Fig. 5 Return loss of an OMJ structure before (dashed line) and after (solid line) optimisation.

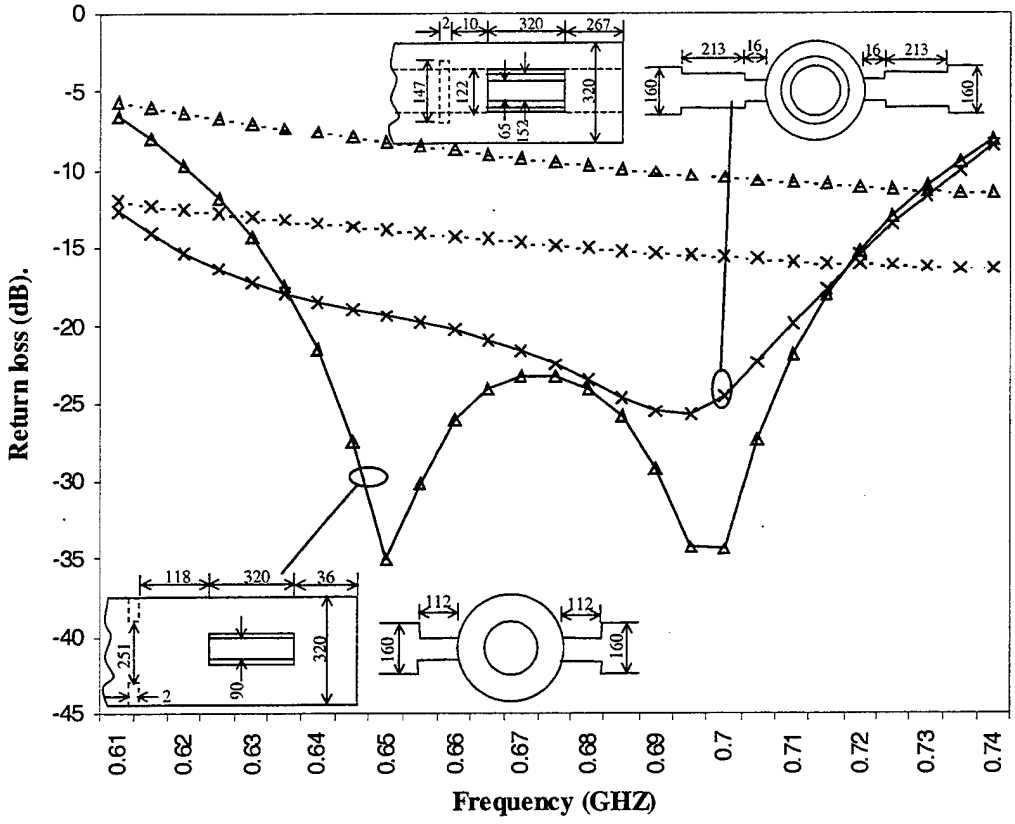

Fig. 6 A design example of using a circular and circular coaxial OMJ structures for diplexing the lower band from a dielectric-cone-loaded horn. The solid and dash lines are for those before and after optimisation, respectively.

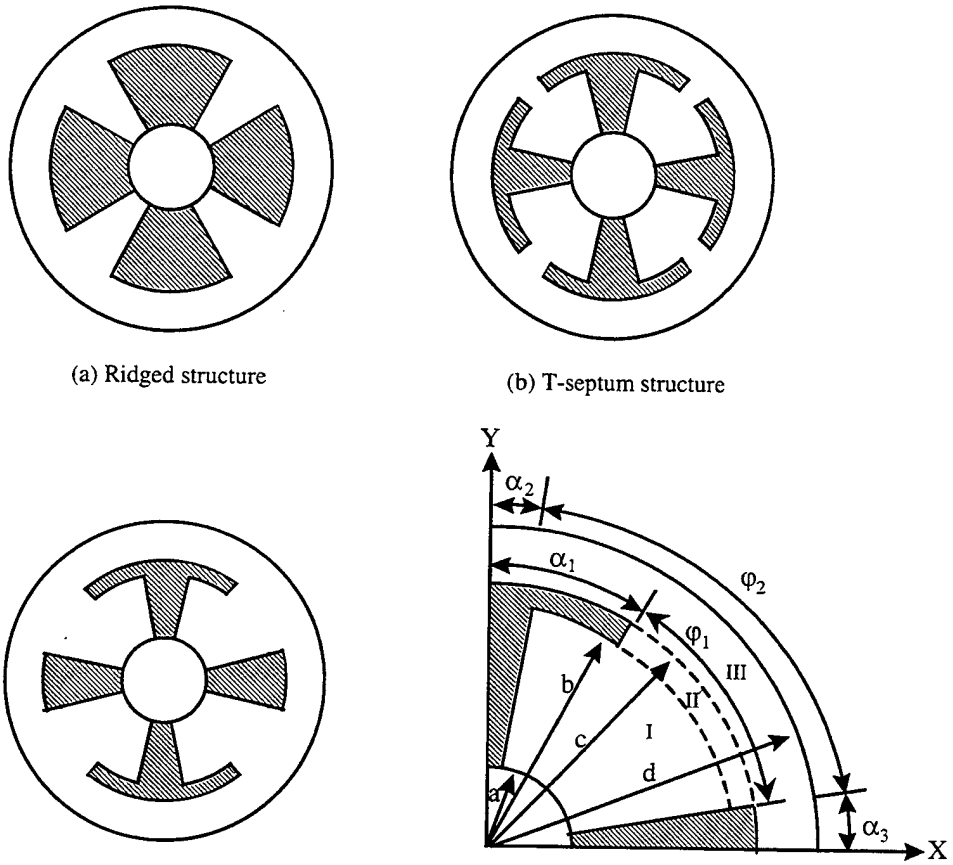

(a) Ridged structure

(b) T-septum structure

(c) Combined ridge and T-septum structure

(d) One quarter of combined ridge and T-septum structure

Fig. 7 Coaxial waveguides with ridges and T-septa placed in its inner conductor.

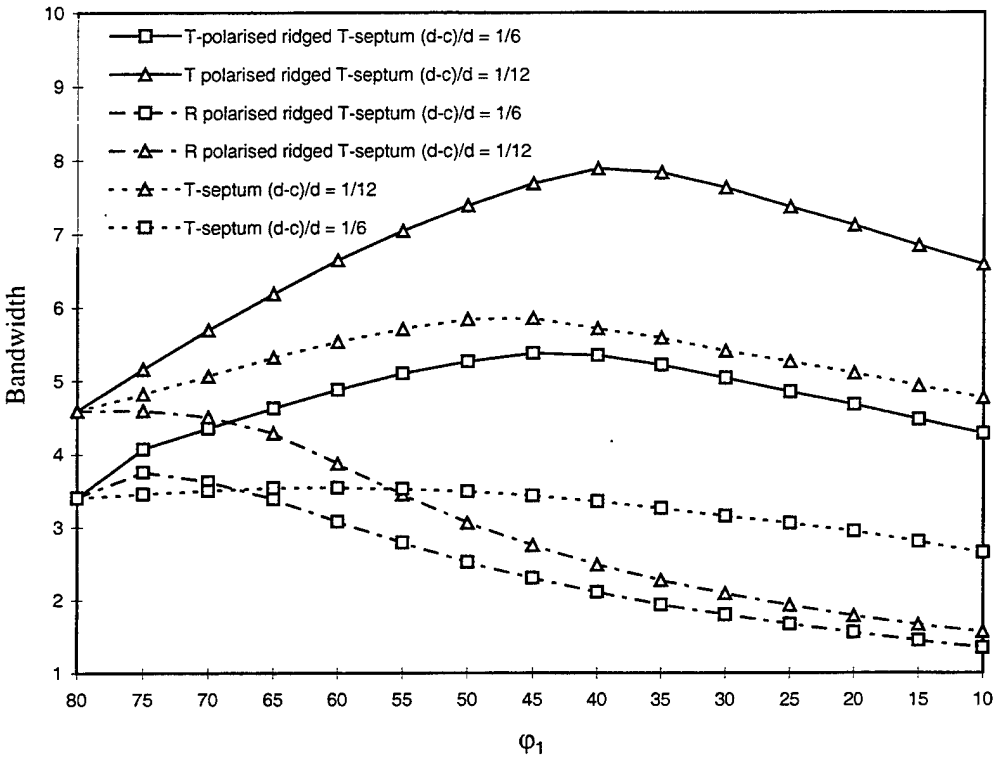

Fig. 8 Variation of bandwidth of the combined ridge and T-septum and T-septum waveguides as a function of φ_1. *a/d = 1/3*, $\alpha_2 = \alpha_3 = 5°$, *(c-b)/d = 1/30.*

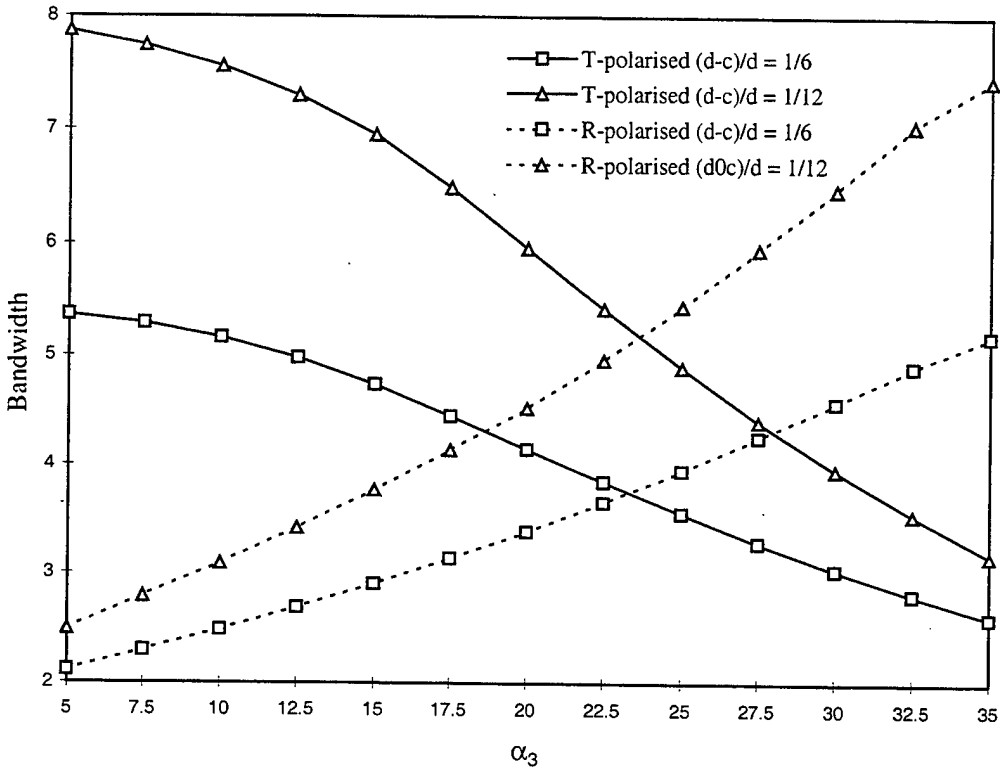

Fig. 9 Variation of bandwidth of the combined ridge and T-septum waveguide as a function of α_3. *a/d = 1/3*, $\alpha_2 = 5°$, $\varphi_1 = 40°$, *(c-b)/d = 1/30.*

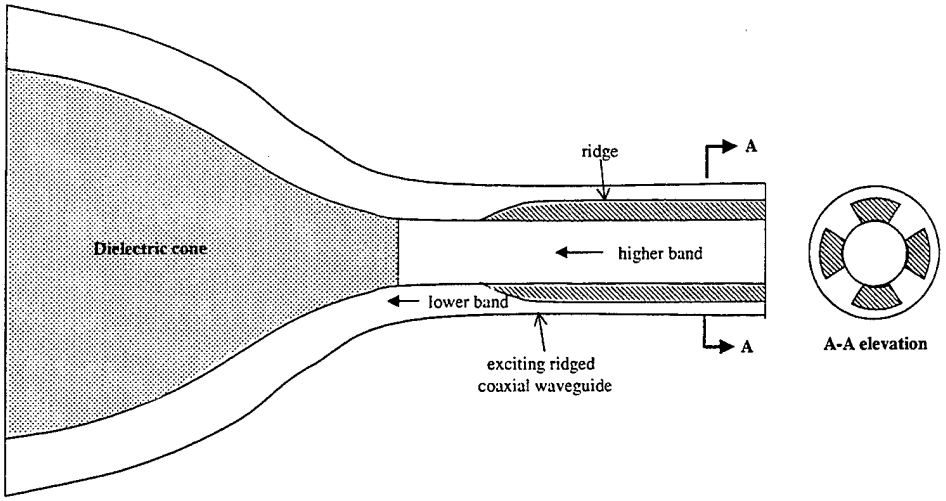

Fig. 10 Dielectric-cone-loaded horn with ridged coaxial waveguide.

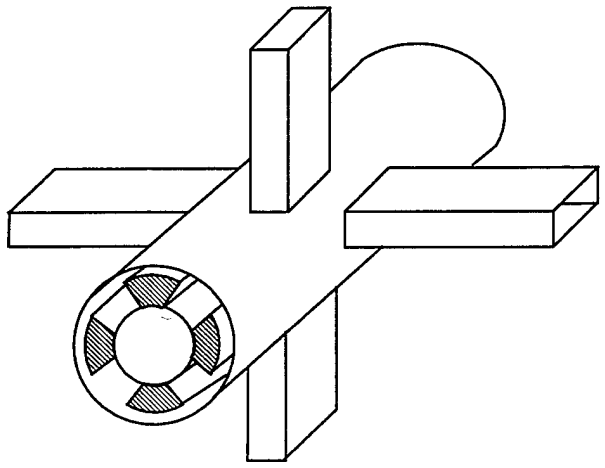

Fig. 11 Ridged coaxial OMJ structure for enhancing the bandwidth.

VHF or UHF GROUNDED VERTICAL DIPOLE

Valentin Trainotti, Senior Member IEEE, Juan Skora.
CITEFA
Buenos Aires, Argentina

Abstract: Dipole antennas are the oldest radiating systems since they were used for the first time by Hertz during the laboratory experience proving the existence of electromagnetic waves existence in the late nineteen century (1885-1888).

Dipole antennas were the backbone of thousands of radiating systems used in electronics for many years, specially in radio communications in high and very high frequencies, due to their radiation high efficiency properties. Dipoles are balanced systems and for this reason a balanced transmission lines was used during many years to feed them. Coaxial lines are very popular nowadays for a lot of reasons and dipoles in these cases are fed by means of a balun or a balanced-unbalanced device, installed close to the dipole input. In the case of a vertical dipole using a metallic skirt attached near the dipole middle is possible to avoid the balanced device. Dipole feeding points are connected one to the grounded coaxial shield and the other to the coaxial hot point directly, connecting at the same time any static potential at the electronic system. This problem could be unimportant for powerful transmitting systems but could be dangerous with sensitive receivers or preamplifiers.

The proposal here is to use an entirely grounded dipole where both coaxial line conductors are statically connected at ground potential to avoid high static potential problems and at the same time a low dipole input impedance as a function of frequency. The dipole is made up of a piece of metal tube close to half wavelength and a metallic skirt is placed around it in its lower part and connected directly very close to the dipole middle. Feeding point in the metallic skirt and dipole physical dimensions are carefully chosen to match the transmission line characteristic impedance. This technique permits at the same time reasonable impedance matching over the bandwidth around the operation frequency.

Practical results obtained on several models in the HF, VHF and UHF bands show the impedance and radiation property measurements.

1. INTRODUCTION.

Dipole antennas have been used for many years, starting with the Hertz experiences (1885-1888) during the electromagnetic wave radiation validation. Dipole radiation efficiency is very high specially in the VHF and UHF spectrum making it one of the more popular antenna for a lot of applications. At the same time it is a very simple mechanical structure. From the electric point of view this is a symmetrical structure and for this reason it must be fed by a symmetric transmission line or by a coaxial line through a balun. The radiated wave is linearly polarized and depending on the applications, horizontal or vertical polarization is used. In both cases the possibility exists of having an entirely grounded dipole using the quarter wave transmission line technique generally in parallel with the principal or feeding transmission line. This technique is generally used for horizontally polarized dipoles or the dipole parallel to the metallic ground plane. Figure 1 shows some classical examples of dipole grounding where a secondary line or a balun is used as a grounding system and at the same time, in some cases, for impedance compensation. This technique has been used successfully during a long time in several applications. Nevertheless, for vertically polarized dipoles, grounding is generally more difficult to make, and, in a lot of cases, the hot coaxial center conductor is connected directly to the upper dipole part without any protection for static problems.

2. DIRECT FED CYLINDRICAL SKIRT GROUNDED DIPOLE.

This kind of dipole uses an entirely metallic structure of about half wavelength with close to one quarter wavelength skirt placed in one of the dipole sides. This skirt is made like a wire cage or with a solid tube according to the operational frequency. The feed point is placed directly between the dipole metallic part and the skirt in order to use a standard coaxial line without any other device and it is chosen theoretically during the design obtaining the best match to the 50 ohms transmission line characteristic impedance at the operation band center frequency. Dipole metallic structure is connected directly to ground in the case of HF or VHF vertically polarized antennas or to the metallic skin structures in the case of installations in vehicles, planes, satellites, or ships. This possibility permits a permanent ground connection avoiding static discharges because the hot coaxial center conductor is connected directly to ground for static or direct current potentials.

Figure 2 shows a typical grounded dipole sketch. Input impedance is a function of the dipole length, the dipole structure diameter, and the skirt diameter. In the latter

case the skirt diameter is affected by the skirt physical characteristics i.e. if the skirt is a solid tube or if it is made up of a wire cage. Wire cages have a physical diameter but the effective diameter depends on the physical cage diameter and the number and diameter of cage wires. As the number of wires is increased the effective cage diameter approaches the physical diameter. This result is affected by the antenna metallic support because it is placed within the cage axis. A case of theoretical input impedance as a function of $H/\lambda o$ can be seen in figure 3.
Figure 4 shows theoretical input impedance values of a dipole model as a function of the distance from the skirt-dipole connection and for a fixed skirt diameter. At the same time input impedance as a function of skirt physical diameter can be seen. From this analysis an input close to 50 ohms impedance and practically resistive values are obtained for a chosen operation frequency. Impedance with practically resistive values are obtained by modifying the skirt diameter and the feeding point position in order that reactive values be close to zero. This possibility generally could not be the optimum bandwidth for the radiating system but the optimum for a narrow band device.

For a low power communication systems a standing wave ratio lower than 2 is considered adequate. From this standard a very good antenna bandwidth can be achieved. (Maximum reflection loss = 0.50 dB).

Input impedance values show two resistance and reactance peaks. Between them there is a zone of low impedance when analyzed as a function of frequency. This behavior permits a wider band of operation compared to a very low VSWR close to the zero reactance operation, but this depends on the maximum VSWR tolerated value.

3. INPUT IMPEDANCE.

Several models have been designed and measured in HF, VHF and UHF bands. In the HF band antenna input impedance has been measured using a General Radio model 1606 impedance bridge with a Boonton 102-D digital frequency generator and an Icom IC-726 transceiver used as a signal detector. The impedance bridge was placed at a distance from the antenna feeding point by means of a coaxial transmission line piece, in order not to disturb the near field, so neither the instrumentation nor the operator could affect the actual antenna impedance.

The dipole model for the 10 meter band (28-30 MHz) was designed and constructed with an aluminum tube representing a mechanical as well as an electrical structure. The skirt was made up by 4 copper wires symmetrically

placed all around the central tube and connected to it at its middle. The four wires are connected to the hot coaxial wire at the proper distance below the antenna middle in order to obtain an input impedance value as closely as possible to the characteristic transmission line impedance.

Figure 5 shows the impedance obtained for an HF grounded vertical dipole designed for the 10 meter band (28-30 MHz) during skirt-support separation (Ss) modifications. Values obtained can be compares with the previuos calculations, and it can be point out that experimental values have less excursion than theoretically predicted. Optimum values are seen plotted on a maximum VSWR=2 Smith chart. The obtained bandwidth is around 3.6 MHz or 12.3 percent for a standing wave ratio lower than 2.

For higher frequencies antenna input impedance has been measured using a Hewlett Packard model HP8410A network analyzer and a model HP8620C sweep generator.

The 50 MHz dipole model has been constructed using an aluminum tube like mechanical as well as electrical structure, very similar to the HF model, using a four wire cylindrical cage.

Figure 6 shows the grounded dipole input impedance of a 6 meter band (50-54 MHz) radio beacon. The resulting antenna bandwidth for a standing wave ratio lower than 2 gives a bandwidth around 5.5 MHz or 10.4 %. This value permits the possibility of changing frequencies within the operation band with a very low radiation efficiency loss. Designs for the HF 10 meter band and for the VHF 6 meter band are intended use the soil or the home concrete roof as its ground plane. For higher frequencies the antenna design could be for a vertical dipole in free space i.e. at several wavelengths over ground in order to obtain an omnidirectional vertical polarized antenna or over a vehicle metallic skin intended for mobile or space communication use.

Impedance values for a 2 meter band vertical dipole model (144-148 MHz) were measured over a metallic ground plane and in free space. Very low difference in the input impedance were computed. This shows the small ground plane influence on the dipole characteristics. The results reflect a typical dipole behavior because displacement currents are making loops around the dipole and only a few lines are intercepting the ground plane. For both cases input impedance results are shown in figure 7. In free space measured impedance in the antenna feeding points are shown as a wider band case (VSWR lower than 2) and a

narrower band case of input impedance for the ground plane model. In the first case 12 MHz bandwidth has been obtained (9%) and 9 MHz in the second (7%).

Another model was designed and measured for a frequency of 400 MHz. Input impedance measured results can be seen in figure 8 where the dipole, like in the 2 meter band, was placed in free space and over a metallic ground plane.
Taking into account a standing wave ratio of 2.0, like a maximum VSWR, a 44 MHz bandwidth has been measured in free space (11 %). Center frequency with minimum VSWR around 1.23 is 398 MHz. Placing the dipole over a metallic ground plane produces a center frequency of 391 MHz, VSWR 1.17 and bandwidth of 40 MHz (10%).
Nevertheless in the 400 MHz model, an additional portion of spectrum could be covered at higher frequencies with a VSWR lower than 2 and with a 50 MHz additional bandwidth (12%) with a 515 MHz center frequency and a VSWR 1.14. In the metallic ground plane case this additional bandwidth has a center frequency at 595 MHz with a VSWR of 1.2 and bandwidth is 34 MHz (8.5%).
These results are due to the dipole behavior as a function of frequency where the input resistance and reactance have several maximums and minimums from the first one, close to half a wavelength. This additional low VSWR behavior at higher frequencies can be useful for several applications specially for wide band communications. In the case of a higher frequency dipole these impedance variations are lower than in the thinner low frequency dipoles and wider bandwidth can be achieved, specially when both useful spectrum portions can be both unified within a Smith chart region with a VSWR lower than 2.

Of course, dipole broadbanding would be an additional work for the near future where dipole dimensions will be analyzed accordingly in order to maximize the frequency bandwidth for a maximum of 2 VSWR.

4. RADIATION PATTERNS.

Radiation pattern measurements in the HF bands is a difficult task, for this reason radiation patterns have been measured in an anechoic chamber within the UHF region by means of a Scientific Atlanta model 1783 receiver and a model 2151 signal generator.
Figure 9 shows a grounded vertical dipole radiation pattern in the 400 MHz band in the horizontal and vertical plane. In the vertical plane some pattern distorsions can be seen possibly due to the interaction between dipole and the coaxial transmission line and very good omnidirectionality in the horizontal plane where this interaction is minimum. In the same figure when a vertical dipole is placed

over a metallic ground plane its vertical radiation pattern can be seen. In this latter case the transmission line inteaction is almost negligible and the limited ground plane size diffraction effect can be clearly seen giving lobes in the ground plane's rear part.
The measured gain in an anechoic chamber for this dipole in free space is very close to 2 dBi in the radiation pattern maximum using a three antenna method.

5. CONCLUSIONS.

A grounded dipolar radiating structure has been designed, constructed and measured showing electromagnetics results very similar than the traditional vertical series fed dipole.

This type of grounded structure could be useful to avoid static effects for high velocity vehicles or in environments where they are bombarded by high energy particles in vacuum while mantaining the radiation characteristics.

A reasonable bandwith close to 10% in each measured model and band can be easily achieved without any special tuning device making this dipole a simple and practical structure to be implemented.

6. AKNOWLEDGEMENTS.

The authors would like to express they gratitude to the CITEFA Authorities and to the Antenna and Propagation Division Personnel for their support during this development and specially to Pablo Perez for his mechanical work. Thanks to Lucas Gonzalez (ENCOTEK) of Richardson, TX for his comments on the written version.

7. BIBLIOGRAPHY.

7.1. Reich, H. "VERY HIGH FREQUENCY TECHNIQUES", Mc. Graw Hill, N.Y. 1947.

7.2. Kraus, J. D. "ANTENNAS ", Mc. Graw Hill, N.Y. 1950.

7.3. Wolff, E.A. "ANTENNA ANALYSIS", John Wiley & Sons, Inc. N.Y. 1966.

7.4. Trainotti, V. "MF DIGITAL AM STATION ANTENNAS", *IEEE Trans. On Broadcasting*, Vol. 45, N° 1, pp. 30-77, March 1999.

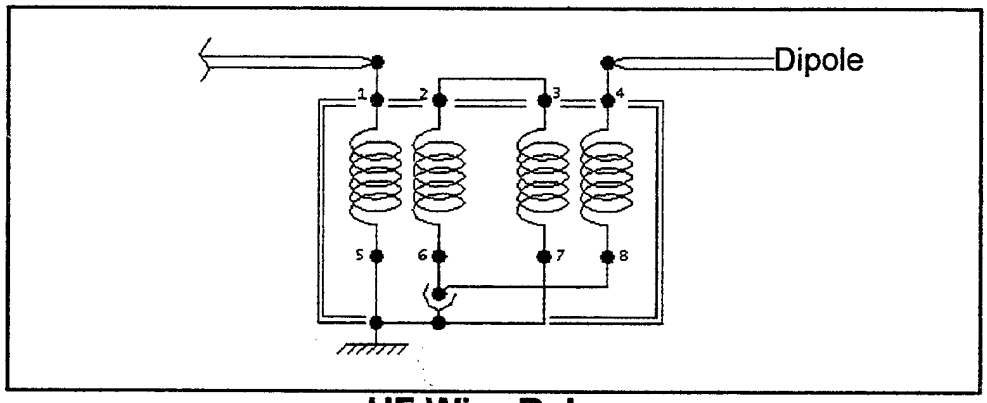

HF Wire Balun

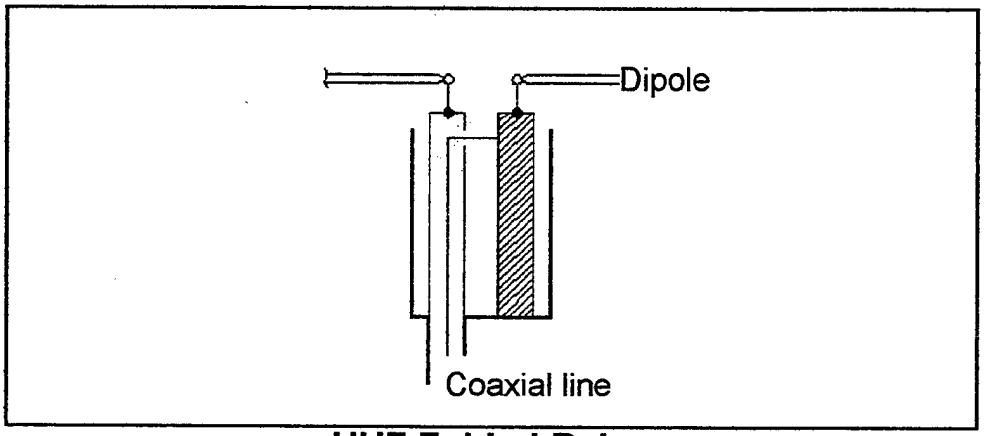

UHF Folded Balun

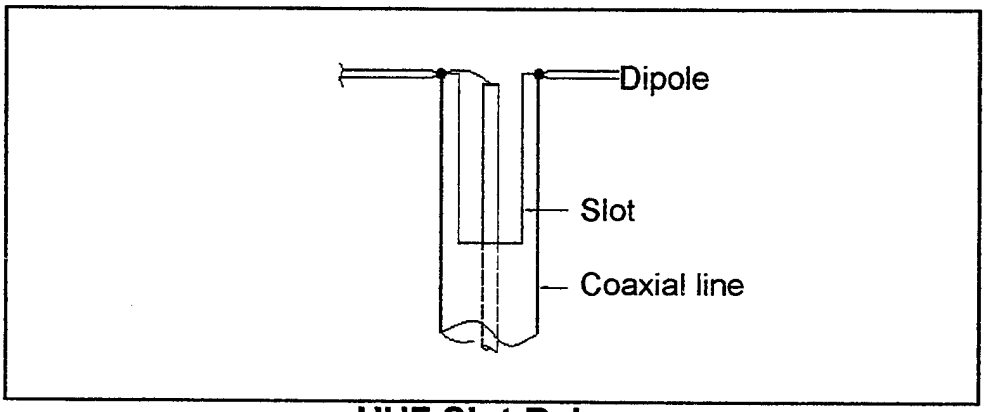

UHF Slot Balun

Figure1: Some classical dipole grounding.

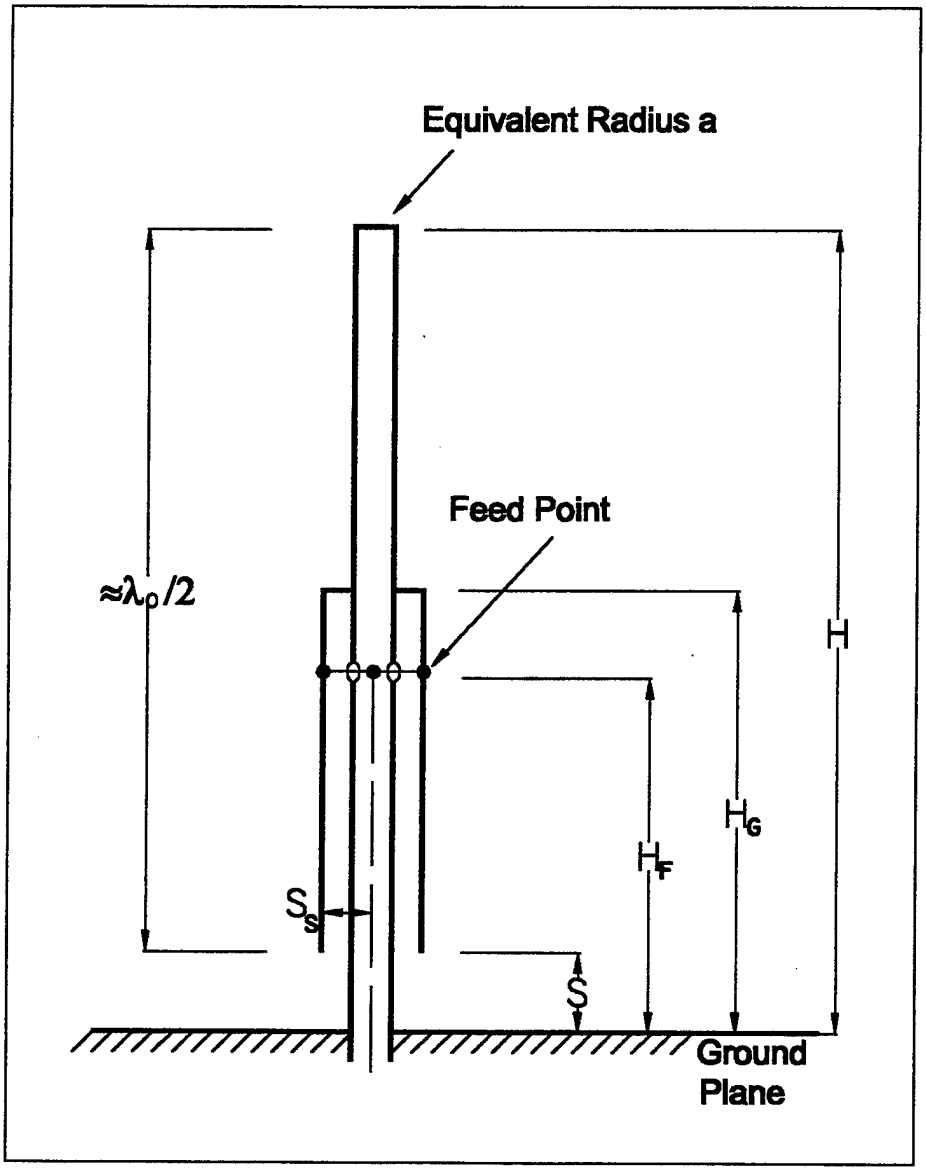

Figure 2: Grounded vertical dipole sketch.

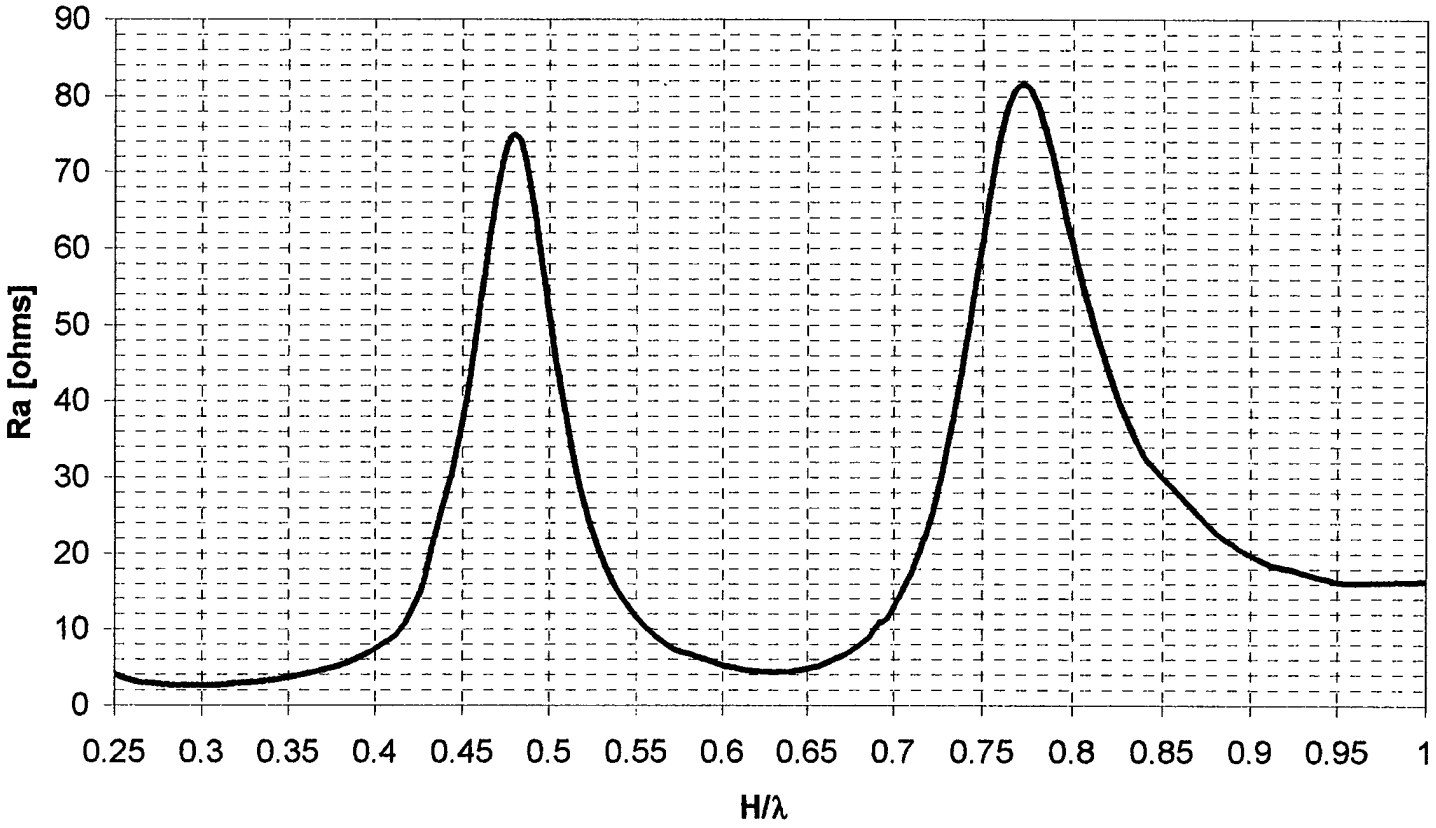

Figure 3a: Grounded vertical dipole input resistance as a function of H/λ. H=0.5017 λ_o, H_G=0.2473 λ_o, H_F=0.1908 λ_o, S=0.0106 λ_o, S_S=0.0099 λ_o.

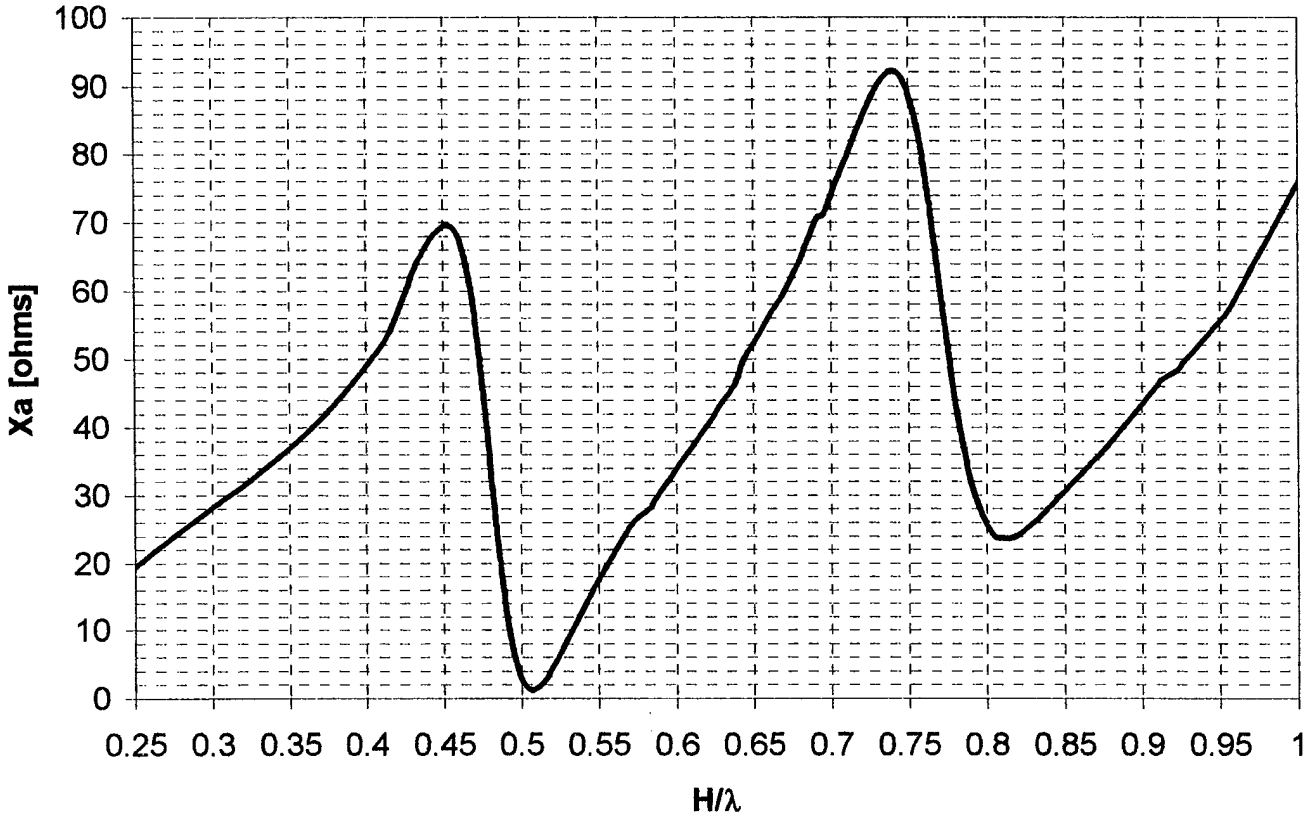

Figure 3b: Grounded vertical dipole input reactance as a function of H/λ. $H=0.5017\ \lambda_o$, $H_G=0.2473\ \lambda_o$, $H_F=0.1908\ \lambda_o$, $S=0.0106\ \lambda_o$, $S_S=0.0099\ \lambda_o$.

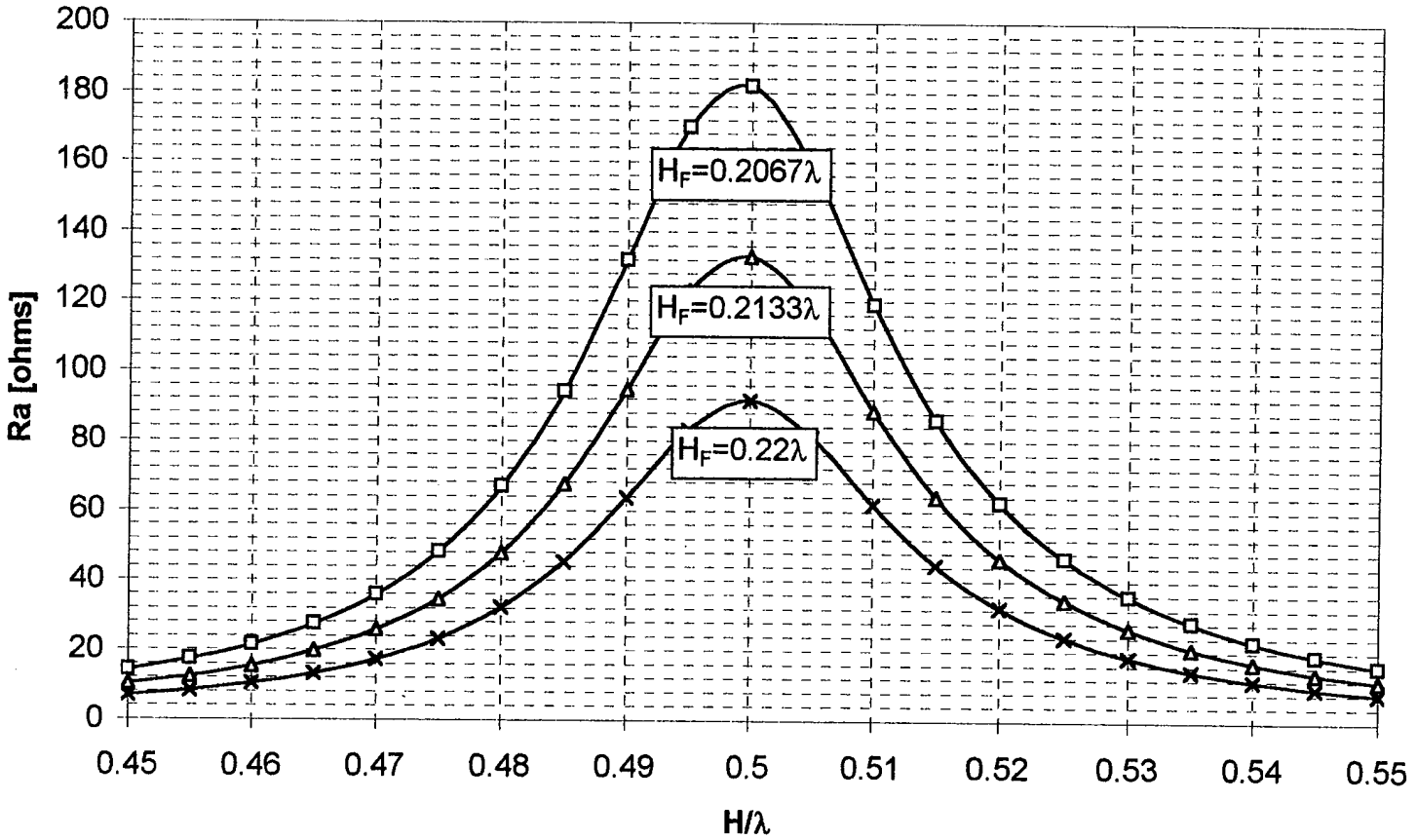

Figure 4a: Grounded vertical dipole input resistance as a function of feeding position for H=0.5 λ_o, H_G=0.25 λ_o, S=0.01 λ_o, S_S=0.0066 λ_o.

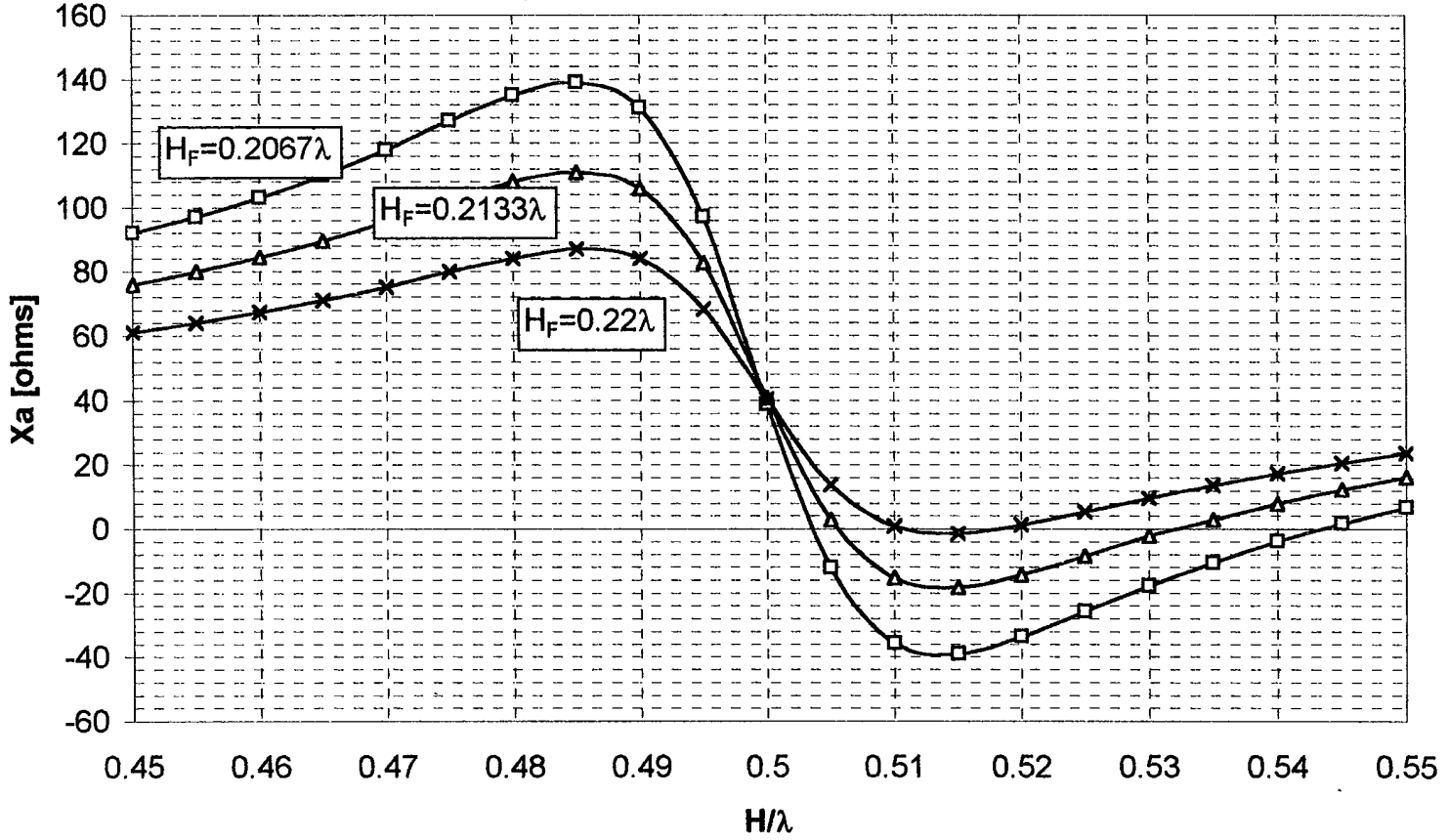

Figure 4b: Grounded vertical dipole input reactance as a function of feeding position for H=0.5 λ_o, H_G=0.25 λ_o, S=0.01 λ_o, S_S=0.0066 λ_o.

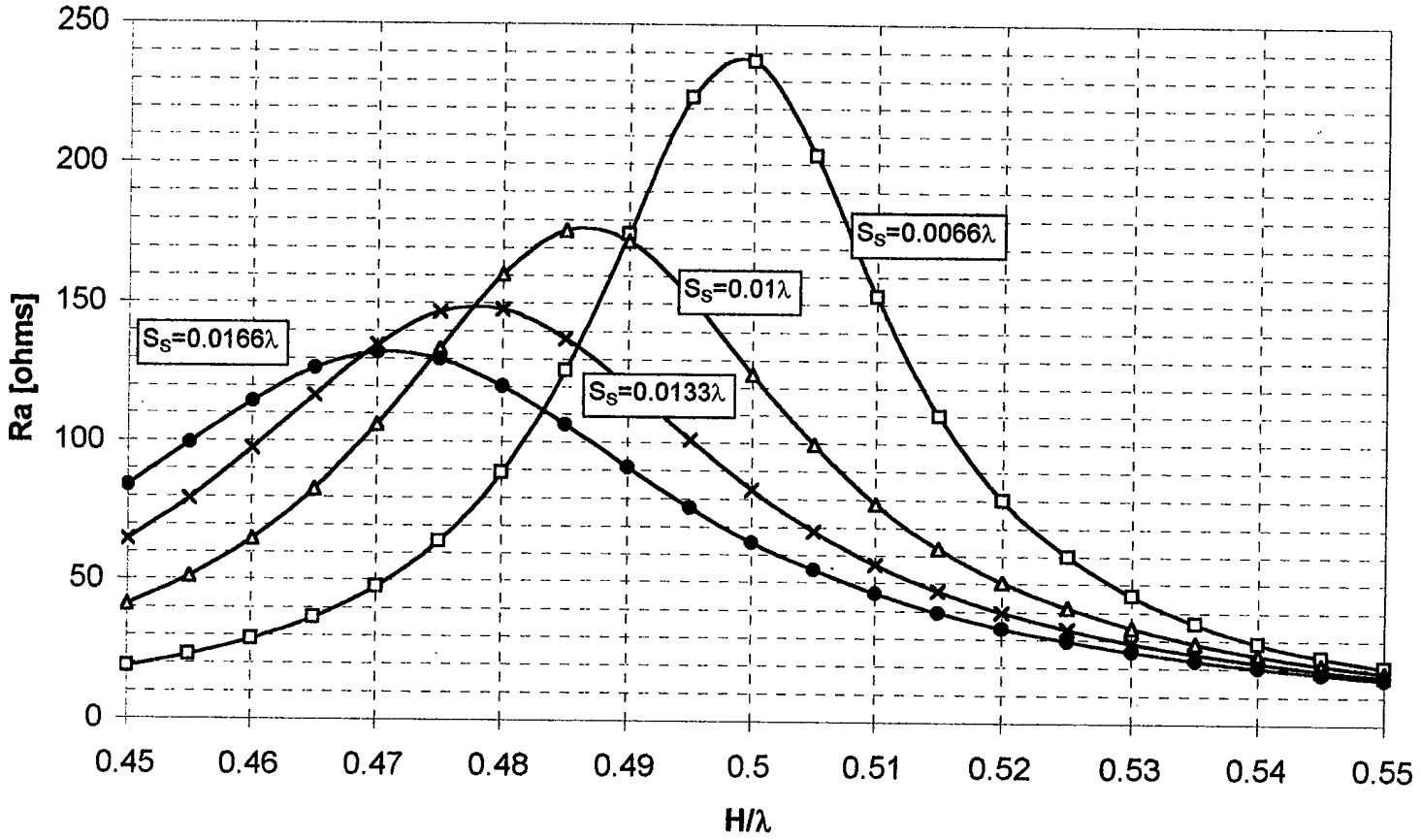

Figure 4c: Grounded vertical dipole input resistance as a function of skirt radius for H=0.5 λ_o, H_G=0.25 λ_o, H_F=0.2 λ_o, S=0.01 λ_o, a=0.0033 λ_o.

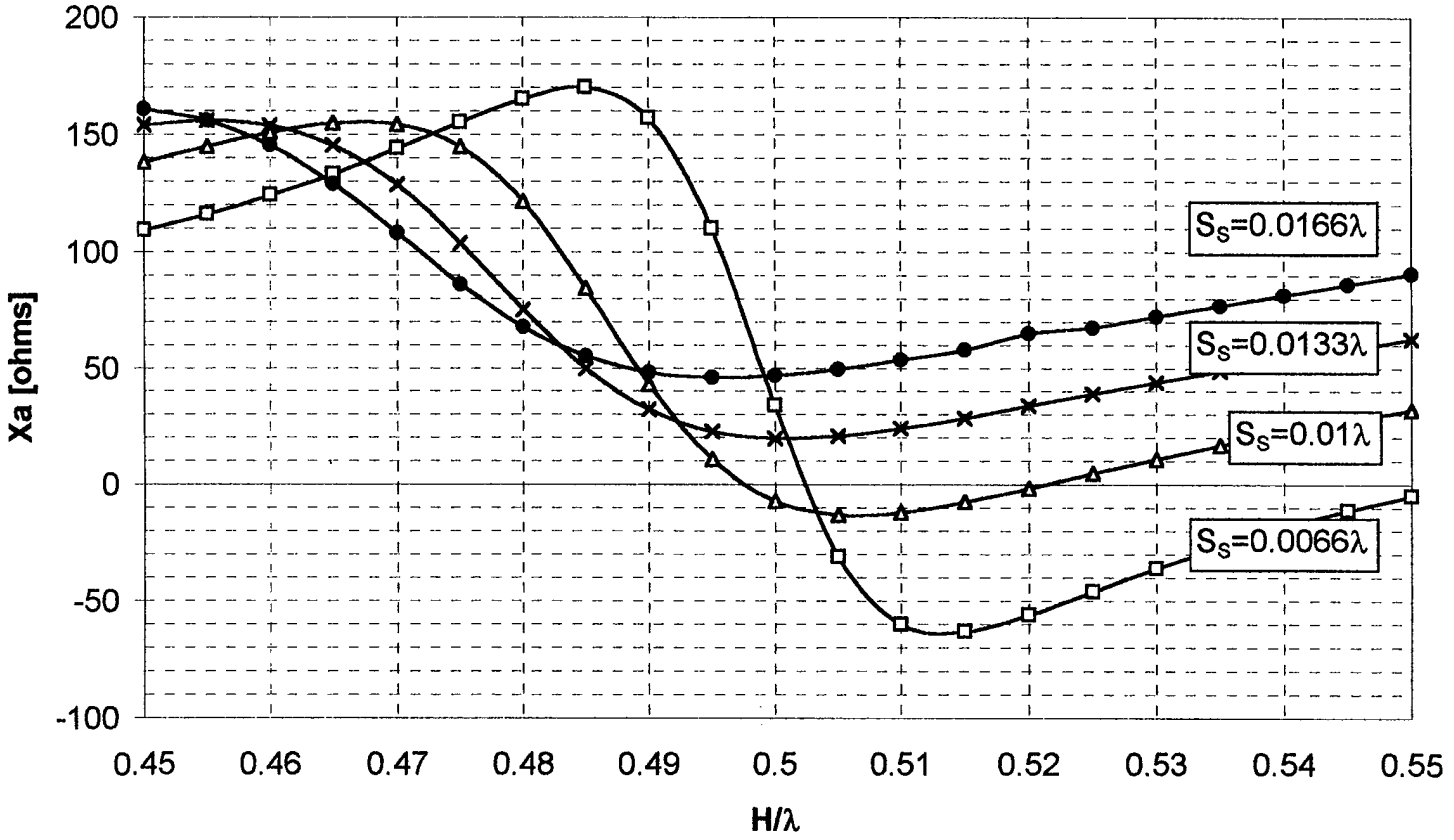

Figure 4d: Grounded vertical dipole input reactance as a function of skirt radius for $H=0.5\ \lambda_o$, $H_G=0.25\ \lambda_o$, $H_F=0.2\ \lambda_o$, $S=0.01\ \lambda_o$, $a=0.0033\ \lambda_o$.

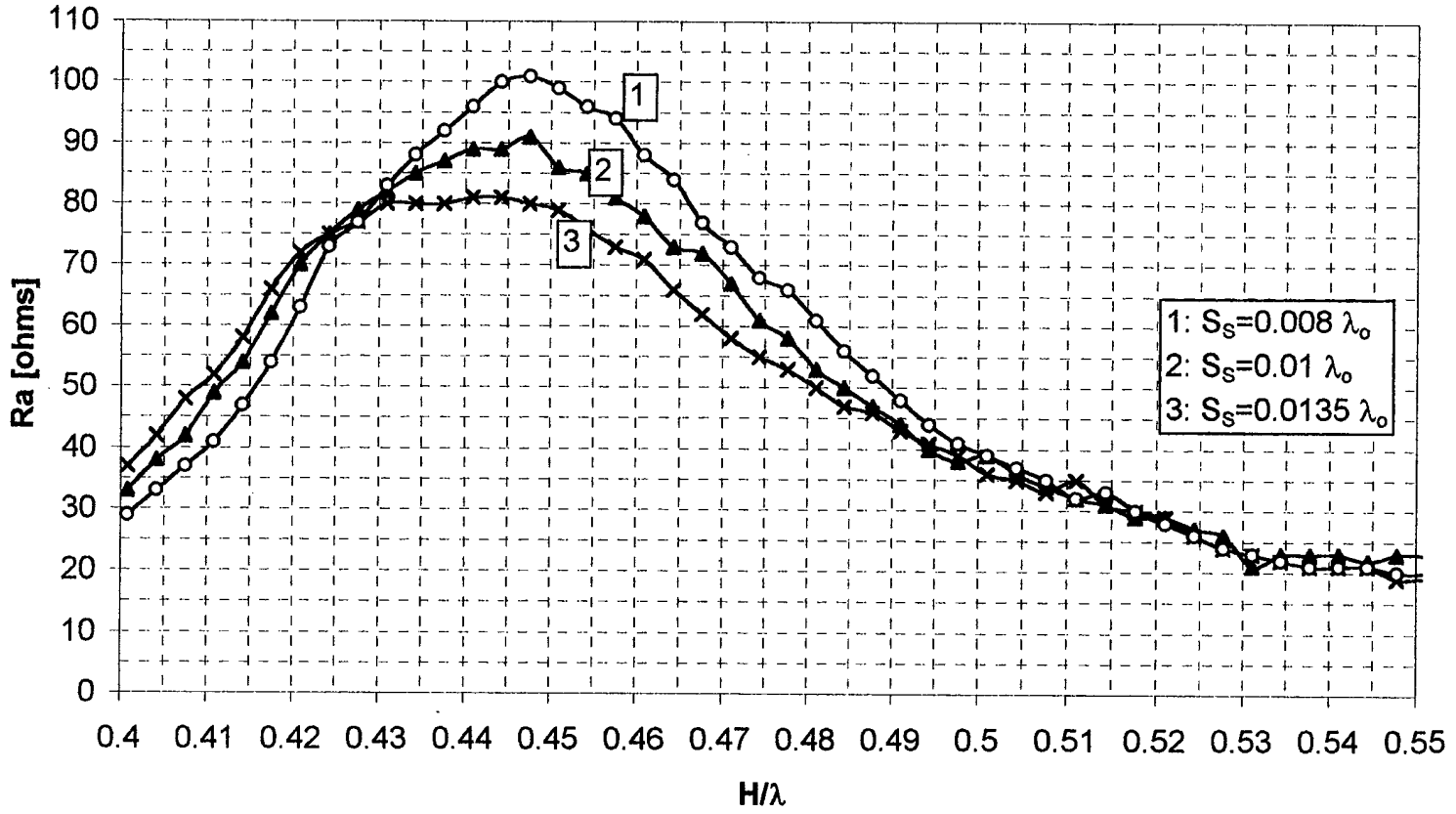

Figure 5a: 10 meter grounded vertical dipole model measured input resistance as a function of skirt radius for H=0.501 λ_o, H_G=0.251 λ_o, H_F=0.2 λ_o, S=0.01 λ_o, f_o=30 MHz.

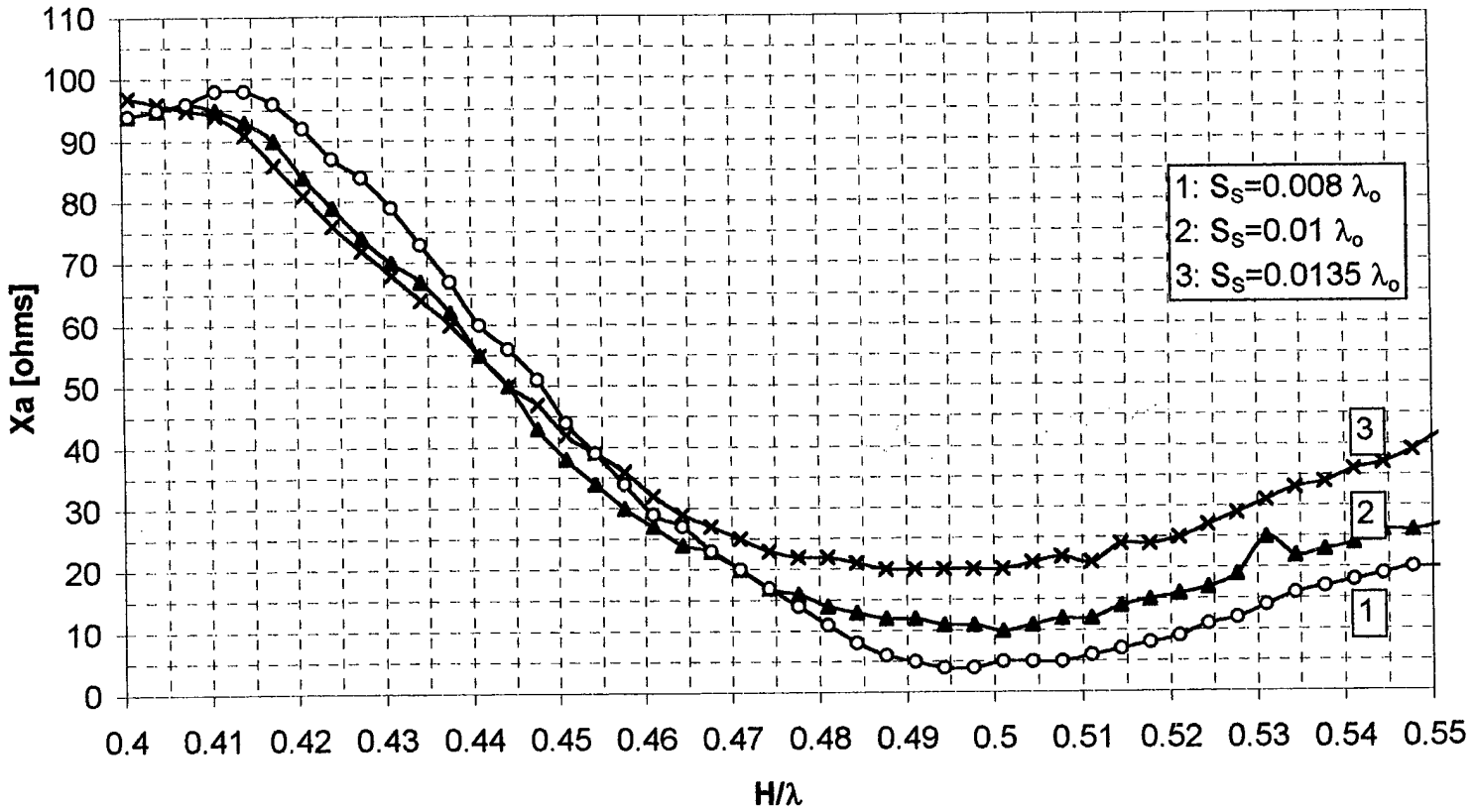

Figure 5b: 10 meter grounded vertical dipole model measured input reactance as a function of skirt radius for H=0.501 λ_o, H_G=0.251 λ_o, H_F=0.2 λ_o, S=0.01 λ_o, f_o=30 MHz.

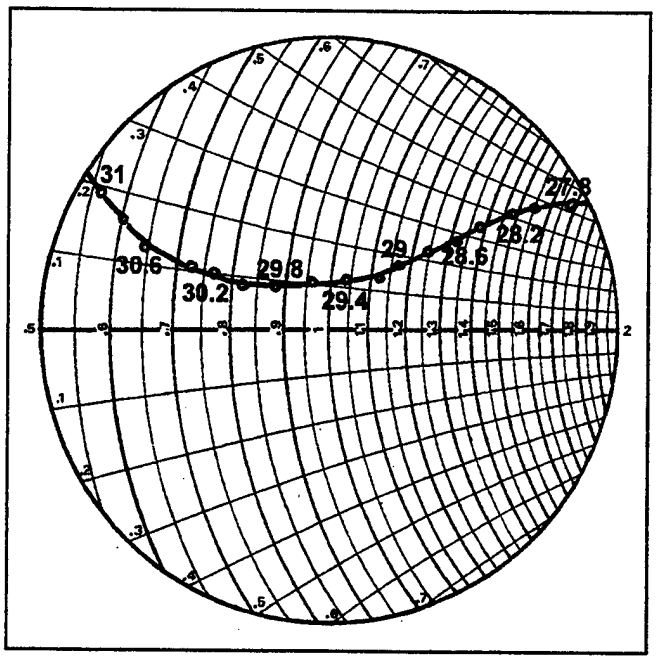

Figure 5c: 10 meter band grounded vertical dipole measured impedance.

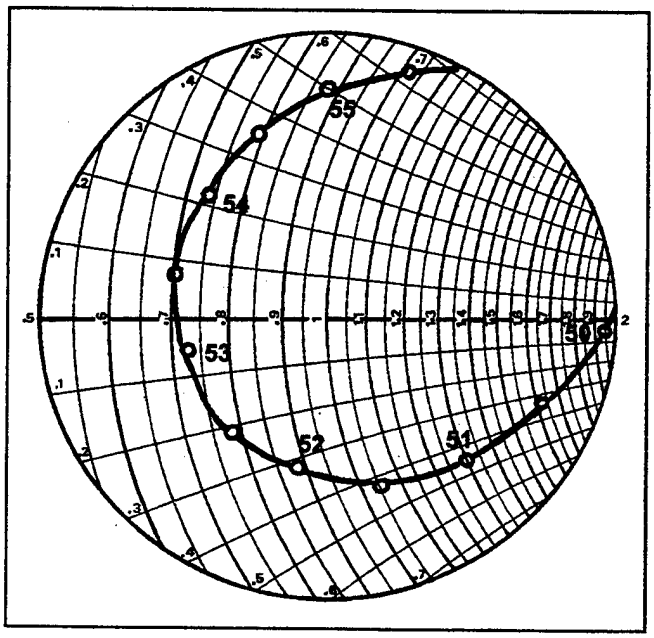

Figure 6: 6 meter band grounded vertical dipole measured impedance.

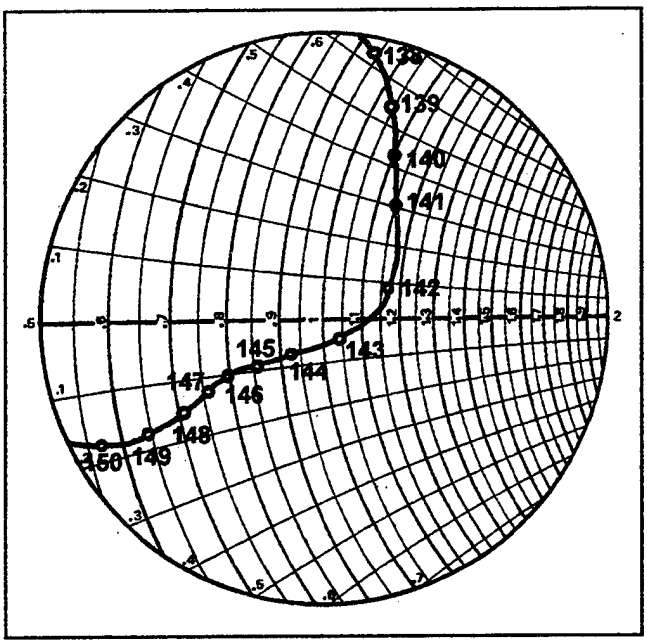

Figure 7a: 2 meter band grounded vertical dipole measured impedance, in free space.

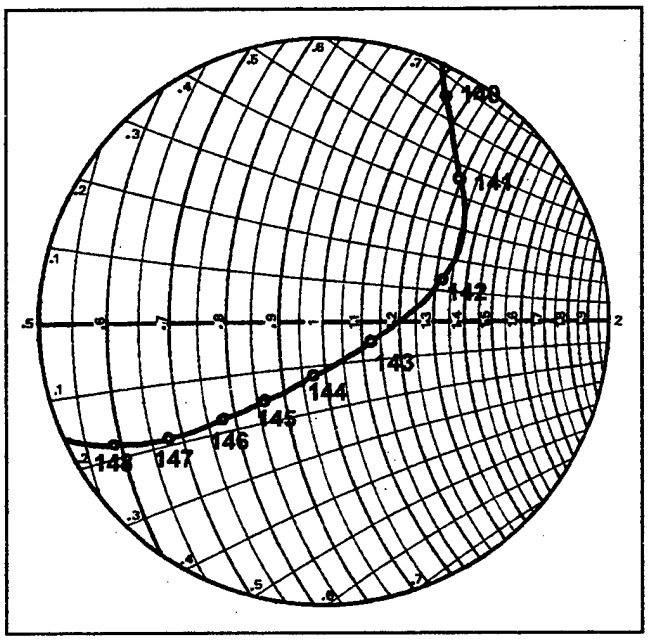

Figure 7b: 2 meter band grounded vertical dipole measured impedance, over a metallic ground plane.

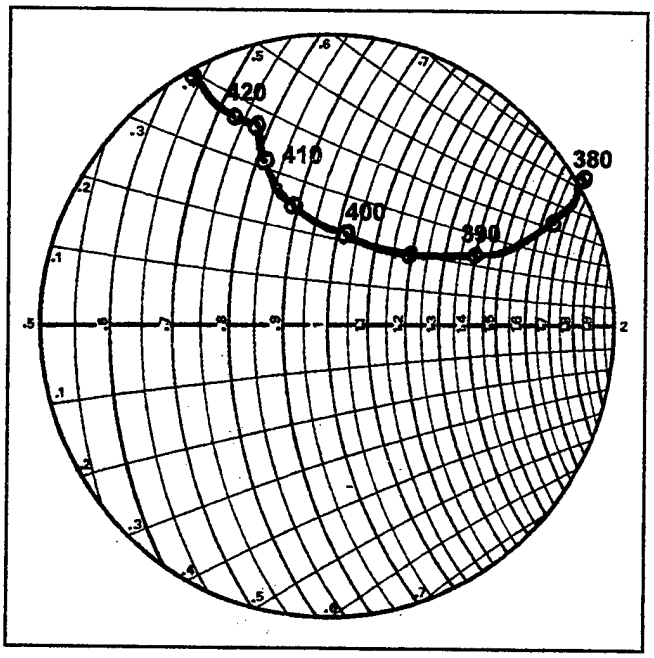

Figure 8a: 400 MHz band grounded vertical dipole measured impedance, in free space.

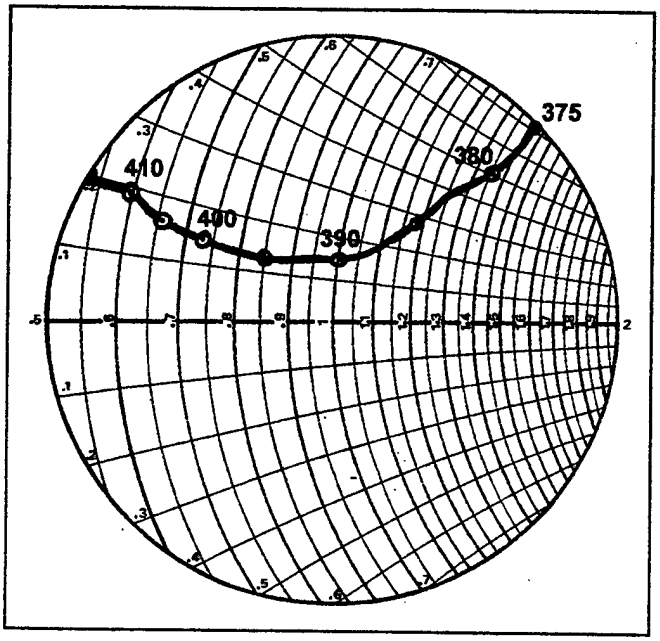

Figure 8b: 400 MHz band grounded vertical dipole measured impedance, over a metallic ground plane.

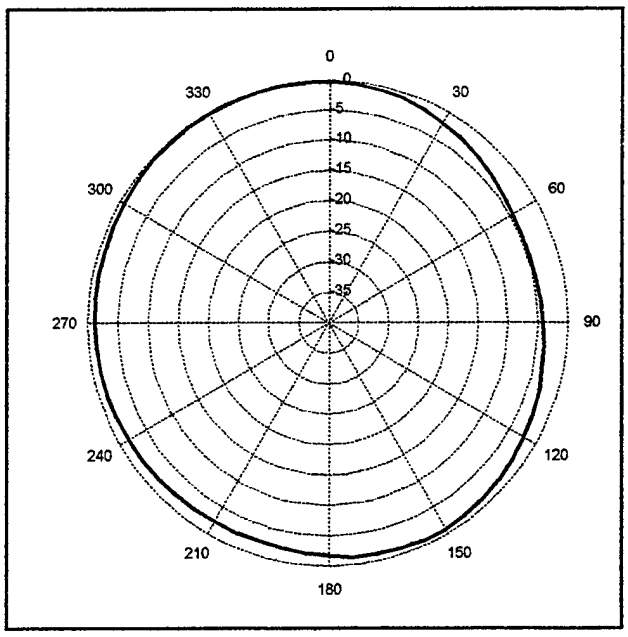

Figure 9a: 400 MHz grounded vertical dipole measured azimuthal radiation pattern.

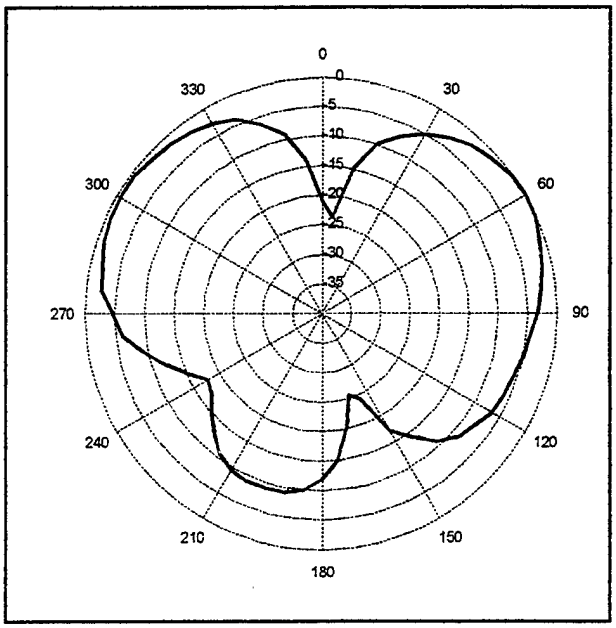

Figure 9b: 400 MHz grounded vertical dipole measured elevation radiation pattern.

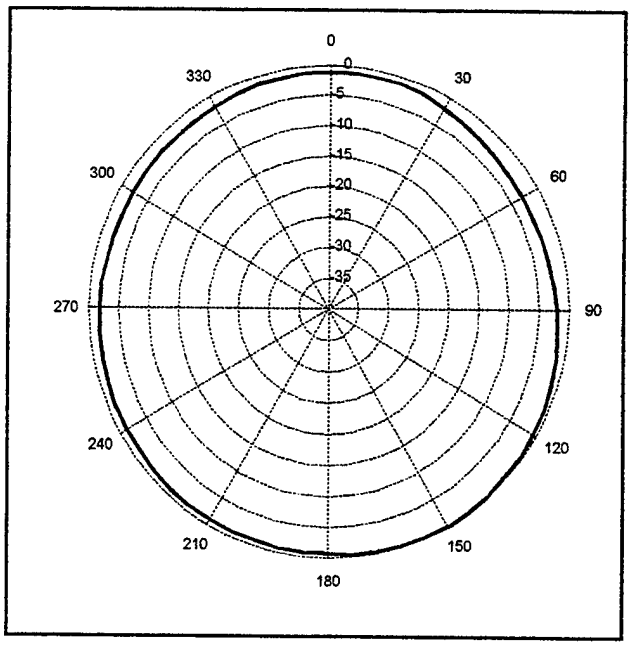

Figure 9c: 400 MHz grounded vertical dipole placed over metallic ground plane measured azimuthal radiation pattern.

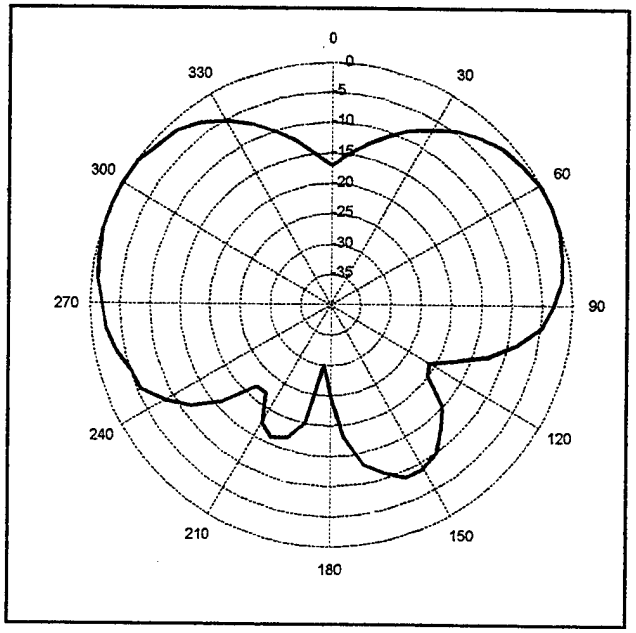

Figure 9d: 400 MHz grounded vertical dipole placed over metallic ground plane measured elevation radiation pattern.

Noise Contribution Analysis for the Arecibo Gregorian Radio Telescope

Germán Cortés-Medellín,
Vertex Antenna Systems, LLC
Santa Clara, CA
cortes@tiw.com

Paul F. Goldsmith, Lynn Baker, M.M. Davis D.B. Campbell
National Astronomy and Ionosphere Center
Cornell University
goldsmit@astrosun.tn.cornell.edu

Abstract

We have analyzed the performance of the Arecibo radio telescope with the new Gregorian corrector by a technique based on electromagnetic field ray tracing. We have obtained both, the aperture field distribution and the far field radiation pattern of this antenna. We have developed a noise temperature analysis technique based on the classification of ray trajectories and ray temperature assignments according to the final surface interaction. We have obtained the noise temperature perceived by the feed as a function of zenith angle. Based on this analysis, we have optimized the design of a surface shield or skirt, to be placed around the rim of the tertiary, that reduces significantly the total noise temperature.

1. Introduction

In a radio telescope, minimizing any contribution to the system noise temperature is of great importance when detecting faint signals in the sky, since the integration time to obtain a given signal to noise ratio varies as the square of the system noise temperature.

The Arecibo radio telescope, with its 305-meter spherical reflector, has the largest collecting area of any radio or radar antenna on the Earth, (see Figure 1-1). Suspended 137 meters above the dish is a dome containing the instrument's Gregorian corrector system. The dome is six stories high and weighs 75 tons. The dome is supported from a triangular platform, which is held in position by eighteen steel cables, strung from three reinforced concrete towers. The network of cables maintains the platform position within a fraction of a centimeter under normal wind conditions. In order to reduce the noise contribution due to spill over the rim of the primary reflector during beam scanning off zenith, a ground screen 18.8 meters high was placed around the edge of the primary reflector, with the appropriate angle to redirect the spill over radiation back to the sky along a path

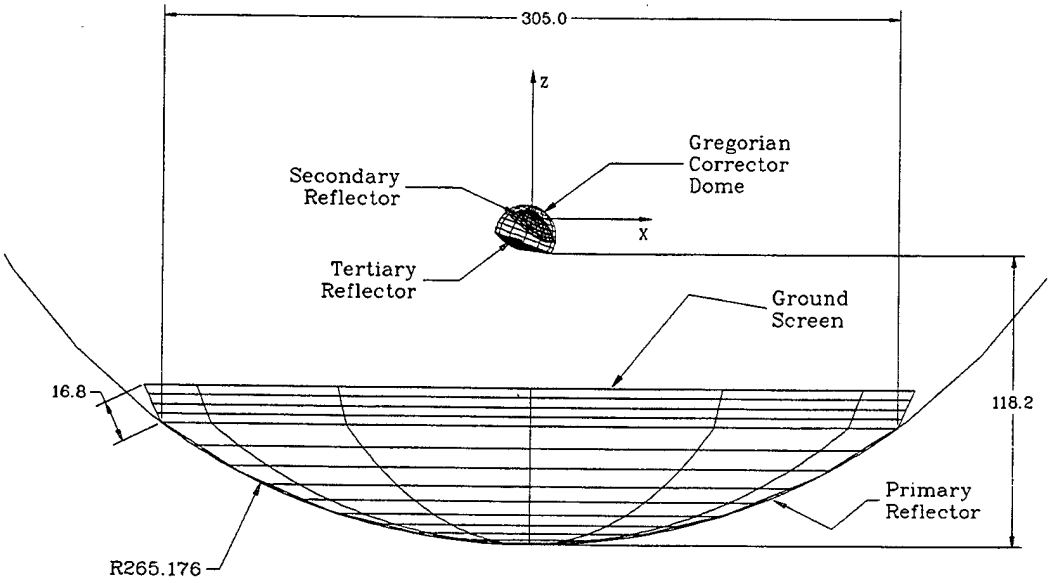

Figure 1-1. Arecibo radio telescope geometry

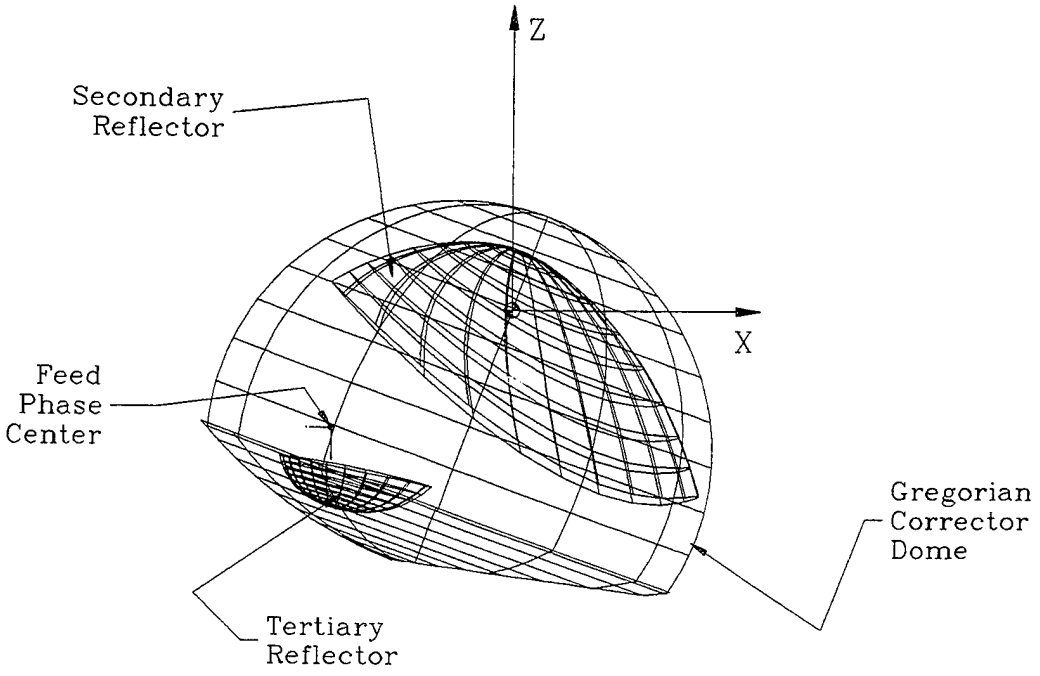

Figure 1-2. Gregorian Corrector system

The Gregorian corrector system became operational last year. It consists of two shaped reflectors [1], shown in Figure 1-2, designed to eliminate the spherical aberration of the primary reflector, and focus all radiation to a single focal point, (the feed phase center in Figure 1-2). At the same time, the corrector system controls the aperture illumination, redistributing the energy so there is nearly uniform aperture illumination, combined with relatively little spillover past the outer rim of the primary reflector, [2].

A simulation tool was developed that permits to obtain a "map" of the noise contributions of the Gregorian corrector system. Using a ray tracing and classification scheme, it is possible to follow rays starting from the feed horn through the reflector geometry until they leave the system or are stopped inside the dome enclosing the Gregorian reflectors. The simulation tool permits assigning independent surface temperatures to any of the reflectors, as well as to any structural elements within the dome.

Based on this simulation tool, the present work presents the results in noise temperature reduction by optimizing the orientation and size of a simulated reflector shield or "skirt" placed around the tertiary mirror.

2. Simulation and Antenna Performance

The antenna parameters are calculated from the aperture field distribution, which is obtained by an electromagnetic field ray tracing technique [3]. This technique transports the field wave front, with information about, main radius of curvature, principal directions of the wave front, and field amplitude, phase and polarization, from the feed phase center through out the aperture plane.

An example of a typical ray trace scan of the Arecibo radio telescope is shown in Figure 2-1, indicating the main components of the Gregorian corrector as well as the main ray trajectories.

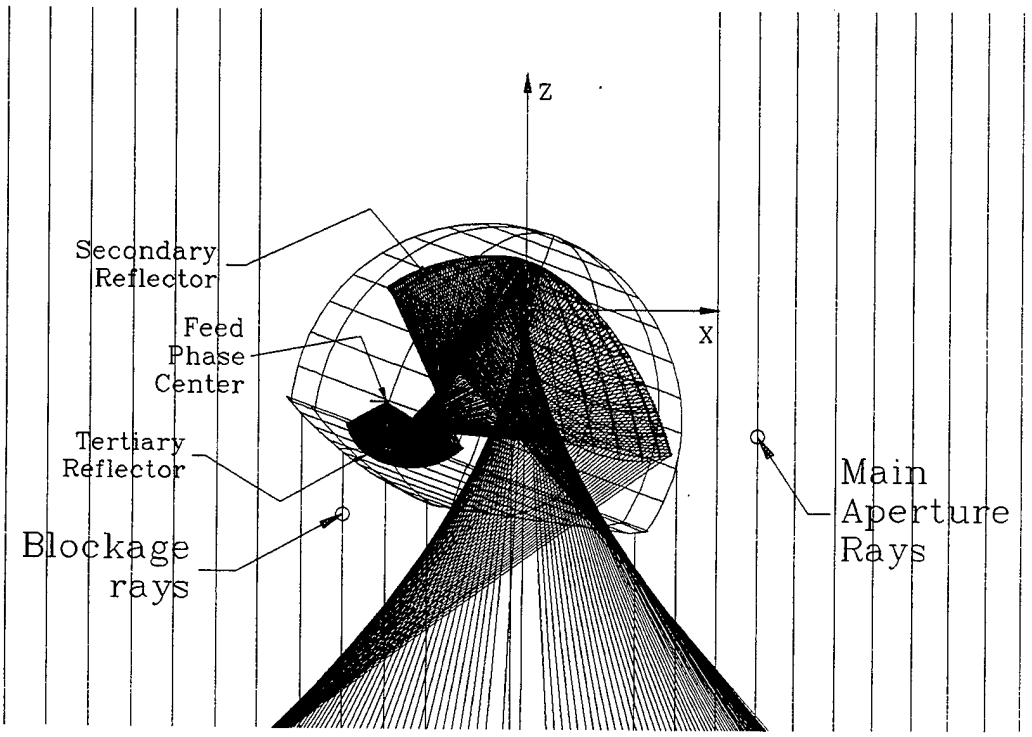

Figure 2-1. Ray Tracing of the Gregorian Corrector system

In Table 2-1 we present the calculated antenna performance at a wavelength of 3.0 cm, assuming perfect surface accuracy. The feed is assumed to have a $\cos^N(\theta)$ power pattern with a –12 dB taper at the edge of the tertiary reflector.

Table 2-1 Antenna performance at 3 cm

Wavelength	3.0	cm
Frequency	9.99	GHz
Gain	87.1	dB
HPBW	29.5x33.6	arcs
Aperture Phase RMS	0.00055	λ
Strehl ratio	99.995	%
Polarization Efficiency	99.7	%
Aperture Efficiency	92.9	%
Beam Efficiency	79.1	%
Noise Temp	16.9	K

Figure 2-2 shows the aperture illumination with its characteristic offset elliptical shape, equivalent to an unobstructed circular aperture of 220 meters in diameter. The minor semi axis of the ellipse is oriented along the main x-axis of the antenna to allow for larger zenith scan angles before spill over occurs, when compared to a circular illumination. Furthermore, included in the shape of the mirrors, there is a provision to optimize aperture illumination by redirecting the fields away from the blockage portion of the aperture, as well as to increase the edge taper for noise reduction.

The far field radiation pattern is presented in Figure 2-3. The main beam is of elliptical cross section with HPBW of 29.5x33.6 arcs. The calculated value of beam efficiency[1] is 79.1 %.

[1] This includes the beam energy above –10 dB.

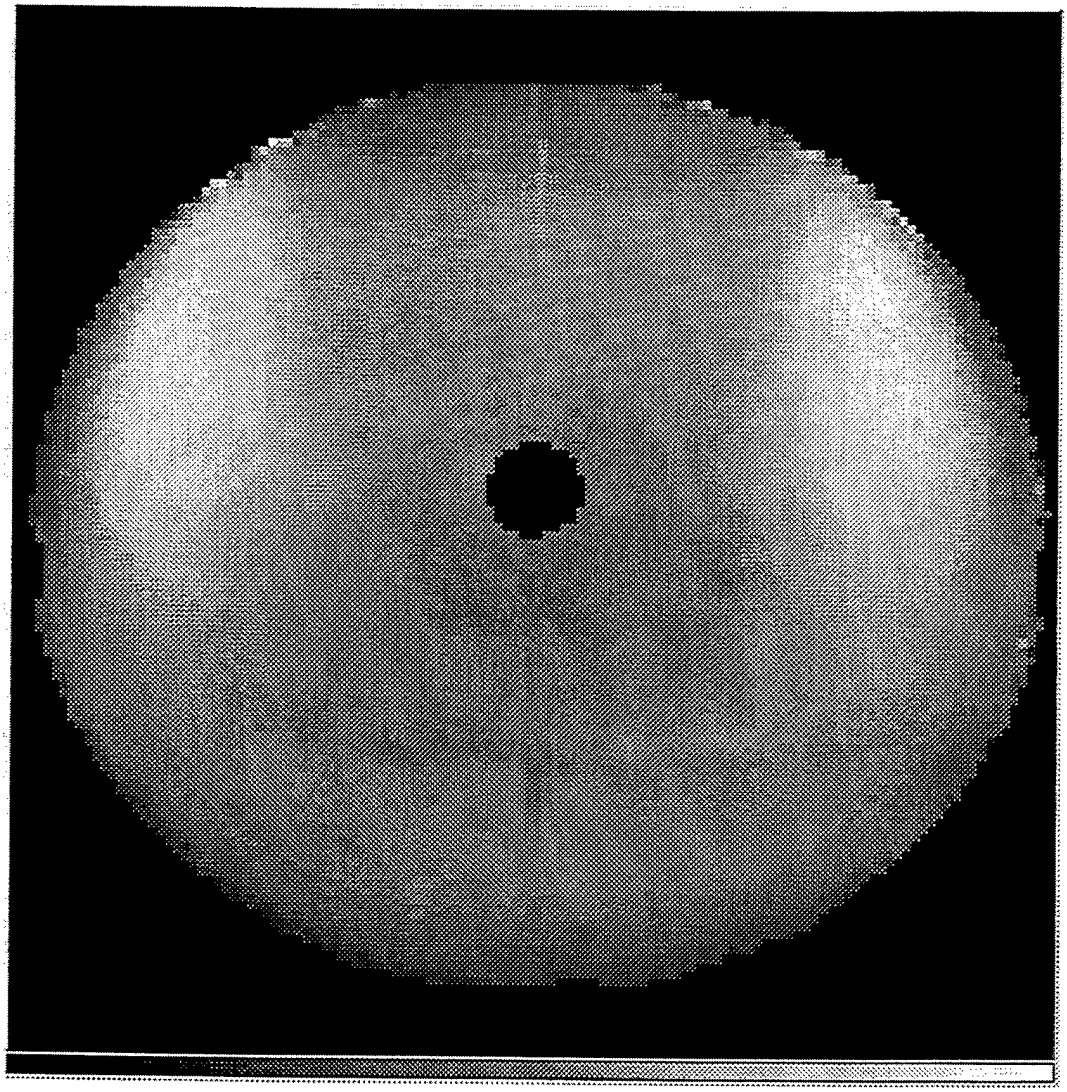

Figure 2-2 Aperture Field Distribution

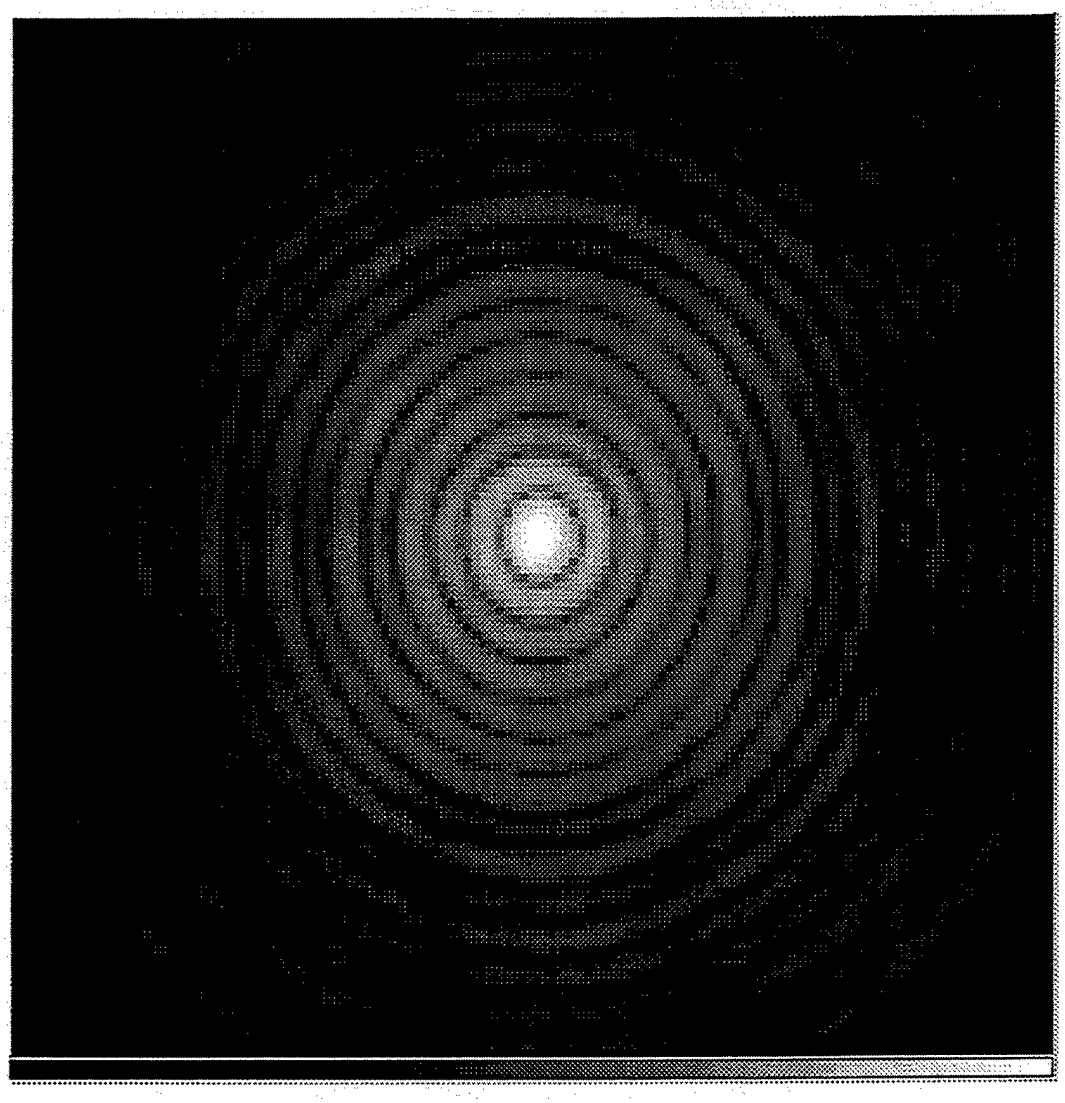

Figure 2-3 Far field radiation pattern

3. Ray Classification Scheme

The ray classification scheme is based on the number of surface interactions that a given ray suffers along his trajectory. The set of rays that reach the aperture in phase, with a number of interactions equal to the number of optical surfaces in the system, corresponds to the main aperture rays (see Figure 2-1).

The Arecibo radio telescope is a three reflector system, including the Gregorian corrector. Therefore, rays with a number of surface interactions different from 3, correspond to blockage, scatter, and stray rays.

Figure 3-1 shows an example of a single scan of the main aperture rays with three surface interactions. Likewise, Figure 3-2 shows an example of ray trajectories with 4 surface interactions corresponding to blockage with the lower cap of the Gregorian dome, and stray rays with 1, 2, and 5 surface interactions, respectively.

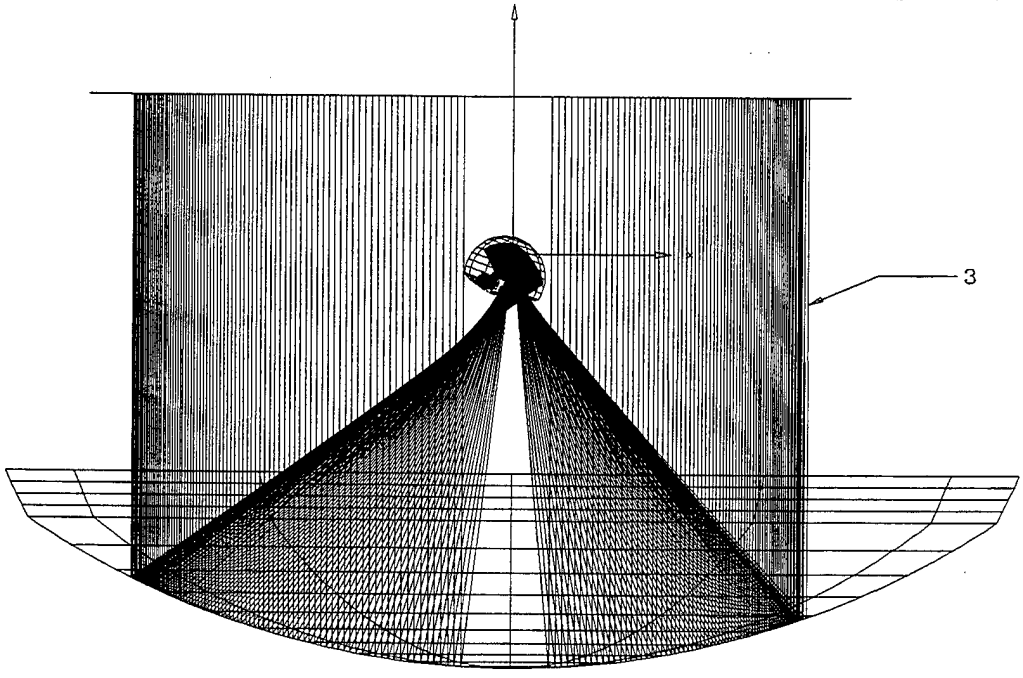

Figure 3-1 Main aperture ray trajectories with three surface interactions

Figure 3-3 shows in more detail these trajectories inside the Gregorian dome enclosure. A common characteristic of these rays is that they depart with trajectories very near to the feed axis; some of them may reach the aperture after

an additional number of surface interactions, while others are absorbed inside the dome, or by the lower portion of it.

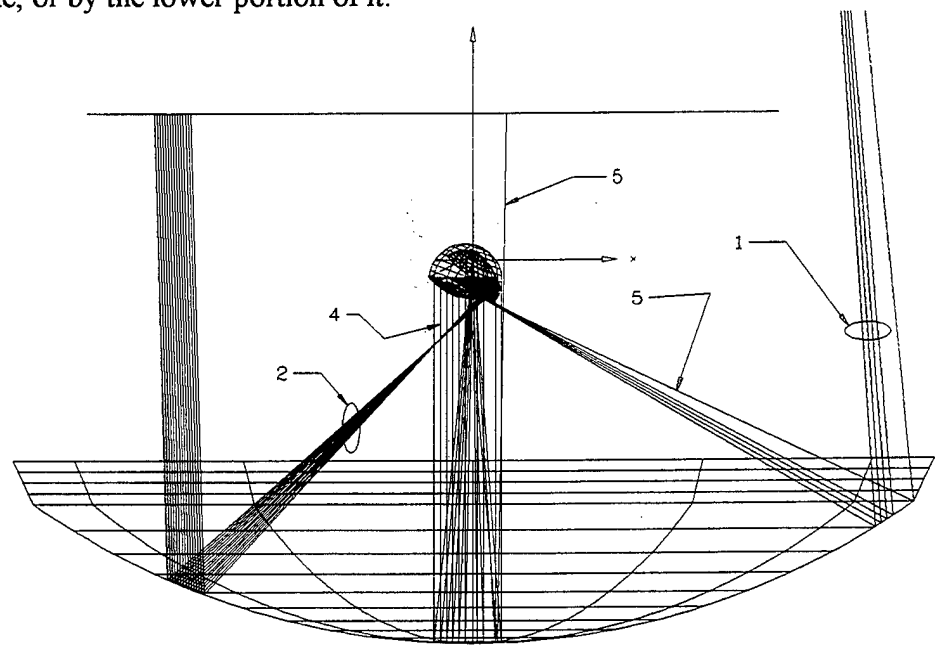

Figure 3-2 Example of ray trajectories with 1, 2, 4 and 5 surface interactions

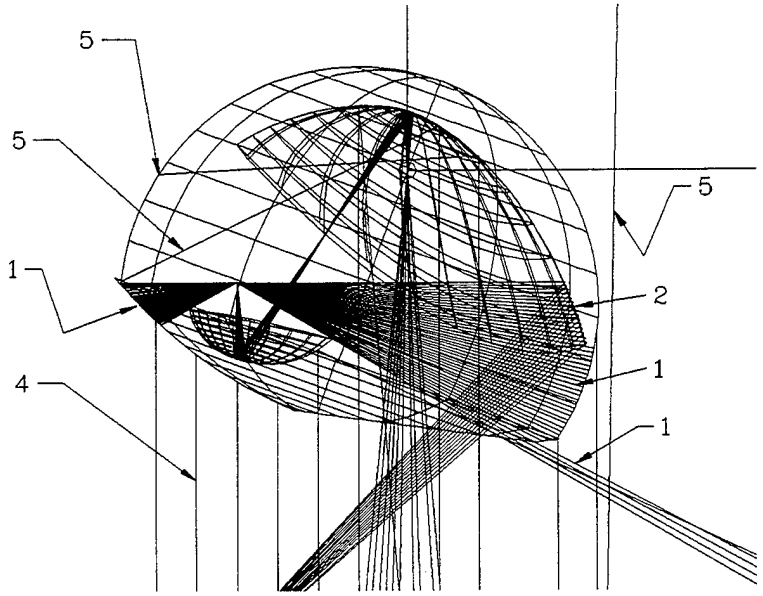

Figure 3-3 Detail inside the Gregorian dome of ray trajectories with 1, 2, 4 and 5 surface interactions

4. Ray Classification and Noise Temperature

By observing Figure 3-3, we notice that those rays that are trapped inside the dome, or are blocked by it, are terminated at the temperature of the dome. Likewise, those ray trajectories reaching the aperture will be terminated at the sky temperature. Consequently, the feed will "see" a noise temperature contribution from a given direction according to the termination temperature of that ray trajectory. Therefore, by assigning a given physical temperature to each reflector or surface, the feed noise temperature can be obtained by the integral of the apparent scene temperature surrounding the feed weighted by the feed radiation pattern, i.e., [4]

$$T_F = \frac{\iint_{4\pi} T_{AP}(\theta,\phi) P_n(\theta,\phi) d\Omega}{\iint_{4\pi} P_n(\theta,\phi) d\Omega} \qquad (4.1)$$

Where:

- T_F: The noise temperature perceived by the feed
- T_{AP}: Apparent noise temperature distribution surrounding the feed
- P_n: Feed radiation pattern

In this calculation we are ignoring diffraction contributions, such as the wide-angle radiation pattern of the antenna.

For the purposes of noise temperature calculations, the antenna may be viewed as composed of perfect reflectors and perfect black bodies, (i.e., the dome), at a given temperature. Rays that are stopped by any surface sense the surface temperature and add that contribution to the integral.

In this simulation, ray trajectories are terminated in any of three different types of terminating surfaces: black body surfaces, the aperture plane, and a stop-sphere. The aperture plane defines the *sky temperature*, i.e., rays reaching the aperture plane are assigned the *sky temperature*. The stop-sphere is a spherical surface that surrounds the antenna workspace, defining the ray-tracing boundary. For the purpose of noise calculation, the stop-sphere is a two-temperature surface; its lower hemisphere defines the *ground temperature*, while the upper hemisphere is at the same temperature as the aperture plane. Out of bound rays intersecting the

temperature, whereas, rays with a positive z-direction component, are assigned the sky temperature.

For the following and all subsequent analysis, the Ground Temperature is 300K, the sky temperature is 4K assuming a perfect atmosphere, and the dome is considered as a black body at 300K. Also, the feed radiation pattern is azimuthally symmetric with a $\cos^N(\theta)$ distribution for off axis angles from 0° to 90°, and is zero for angles larger than 90°.

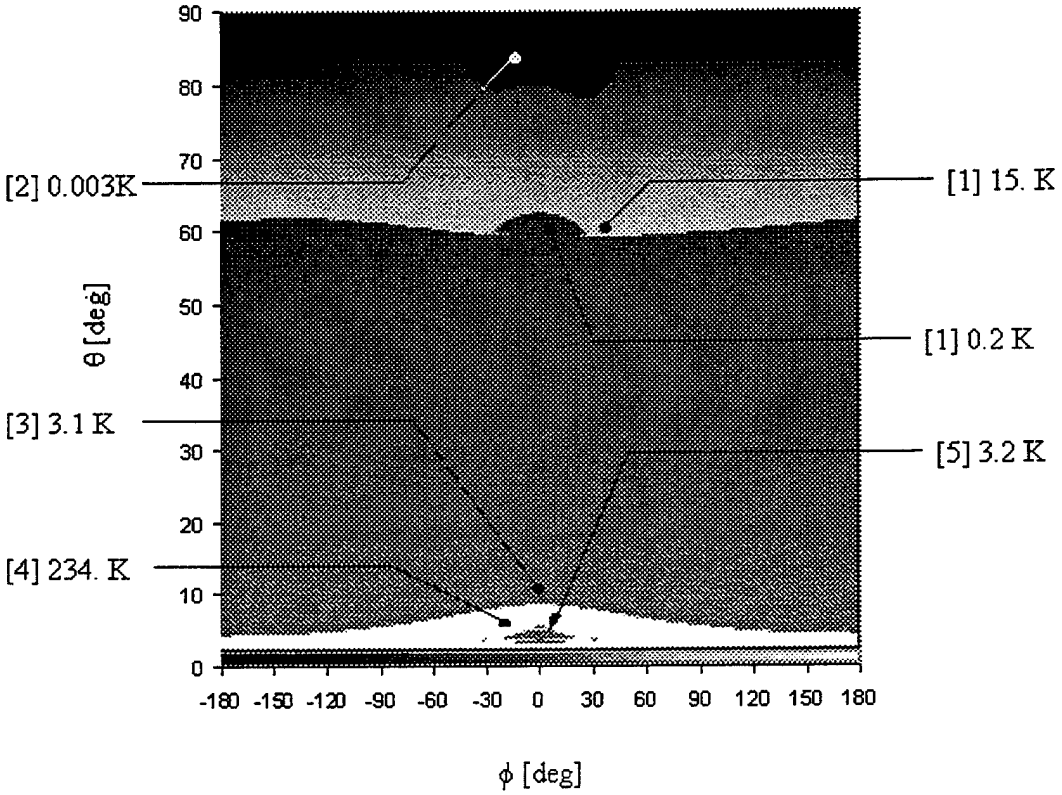

Figure 4-1. Noise Temperature map in the feed coordinate system

Figure 4-1 shows the resultant noise temperature scan map in the feed (θ, ϕ) coordinate system, where the angle θ, is with respect to the feed z-axis, and ϕ is the azimuthal angle. In the map six regions can be easily identified, these correspond to rays with different number of surface interactions. The following nomenclature was used in the map: the number of surface interactions is indicated by in square brackets; the temperature indicated is the no-normalized noise contribution to the integral in Equation 4.1, i.e., the product of the actual

terminating surface temperature in that direction times the feed radiation pattern. Hence, rays with one surface interaction can be found at two different terminating temperatures, 15K at the inside of the dome and 0.2 K at the sky, respectively. Evidence of these can be corroborated in previous Figures 3-2 and 3-3. Likewise, there is a white area between ($0 \leq\theta \leq 6°$), corresponding to four surface interactions and a temperature of 234K. Those are the rays blocked by the lower cap of the dome.

In the middle of this band, near $\phi=0$, there is a region of rays with multiple surface interactions, dominated by 5 interactions at 3.2K. The region from $\theta=6°$ to $\theta=60°$ corresponds to the main aperture rays, with three surface interactions and 3.1K at the signaled point. Finally, there is a small region in the top of the map, with very low temperature contribution, i.e., rays with two surface interactions and 0.003K. This corresponds to rays that hit the lower portion of the secondary reflector, right in Figure 3-3, and then hit the main reflector to be redirected to the sky.

The region from $\theta=60°$ to $\theta=90°$ corresponds almost exclusively to the rays blocked by the inside of the dome, and which contribute significantly to the noise temperature.

5. Noise Temperature vs. Zenith Angle

The triangular frame that support structure allows the rotation of the Gregorian dome around the center of the main reflector for beam scanning angles, with respect to the zenith, from $\theta= 0°$ to $20°$ as shown in Figure 5-1, and a full 360° rotation in azimuth. Additional scanning is provided by the diurnal rotation of the Earth.

Figure 5-2 shows the noise temperature seen by the feed as a function of zenith angle from 0° to 20°. The noise temperature starts at 16.9K and increases to 17.3K around $\theta= 5°$, and stays steady until $\theta= 18°$, where it begins to increase again, reaching 19.8K at $\theta=20°$. Note that the receiver noise temperature is not included in this calculation.

The reason of these temperature increases can be better understood by observing the composite mosaic of single scan ray tracing presented in Figure 5-3. The first picture in the mosaic, with a zenith angle of $\theta=0°$, shows a set of rays bouncing off the main reflector towards the sky, at the left side of the primary dish. This set of rays can be observed also in Figure 3-2 and 3-3, and corresponds to rays with one single surface interaction therefore raising the noise temperature.

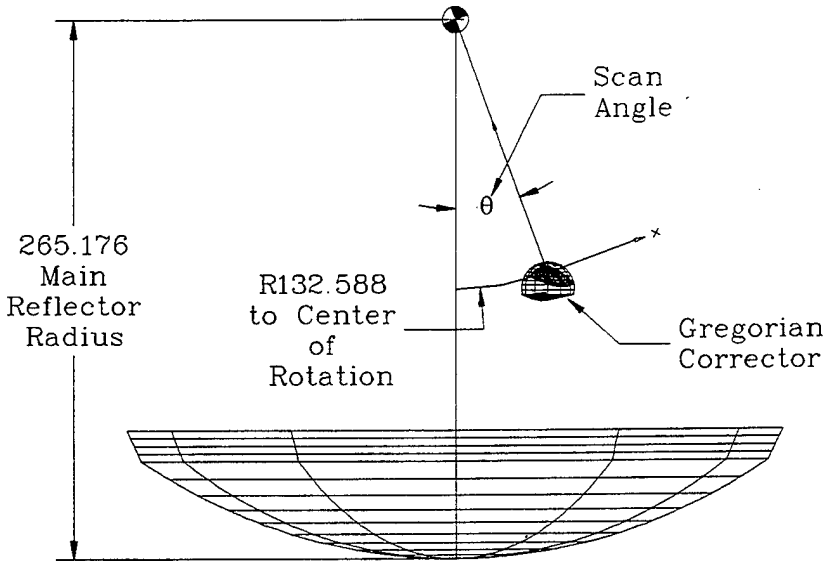

Figure 5-1 General geometry of a sky scan for the Arecibo radio telescope.

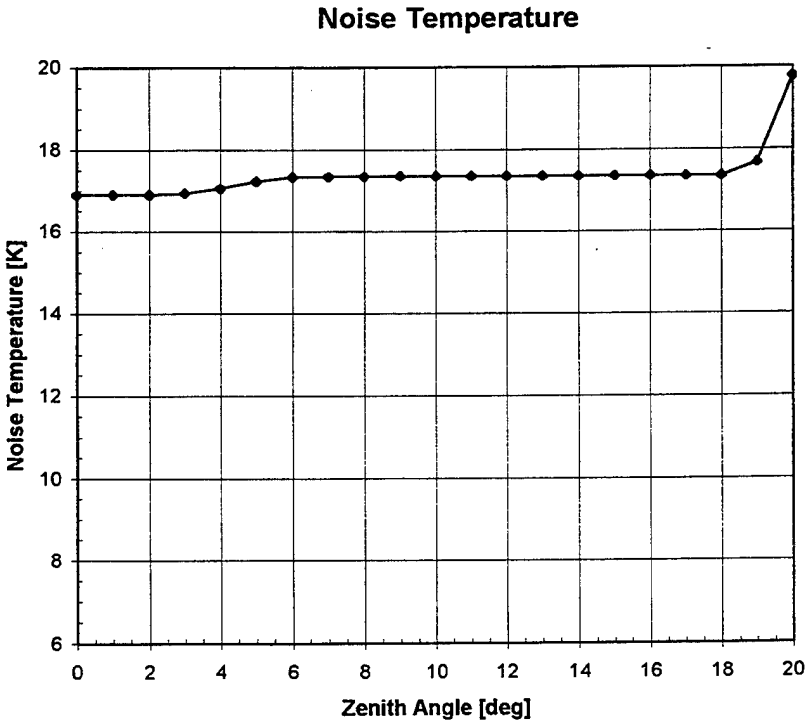

Figure 5-2 Noise temperature vs. Zenith angle.

As the zenith angle increases, i.e., θ=2° to 4°, this set of rays reaches the ground screen and are beginning to be reflected back to the dome structure, on which they are terminated, since in this simulation is considered as a black body at 300K. Finally, as the zenith angle increases, these rays spill over the ground screen and hit the ground for angles from θ=6° to 8°. There are no further changes until the zenith angle reaches 15°. Although, there is not a change in noise temperature, part of the main aperture rays begin to bounce off the ground screen passing under the Gregorian platform towards the sky. Finally, at about θ=18°, the main aperture rays begin to spill over the ground screen, therefore, rising the noise temperature. This behavior has already been verified by measurements in 1.4 –1.7 GHz range

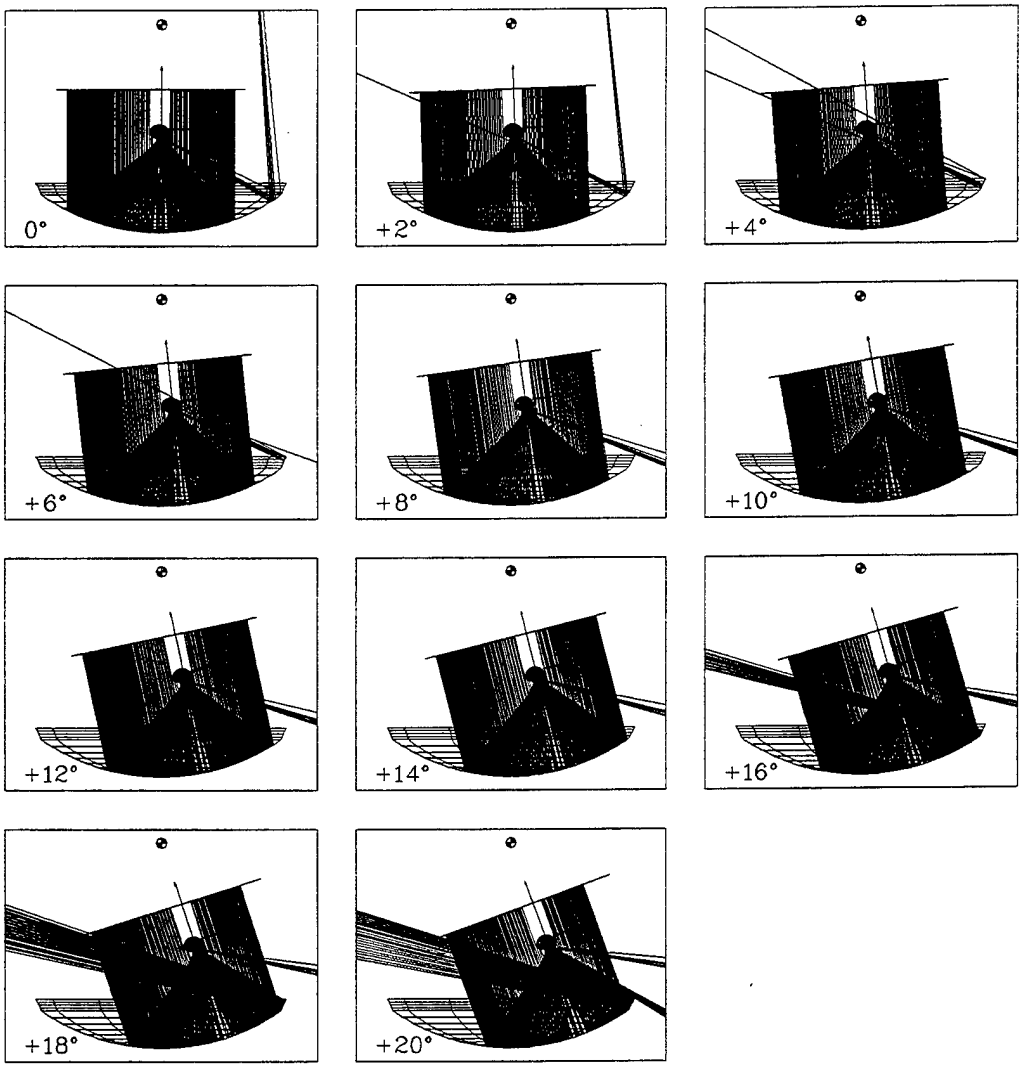

Figure 5-3 Ray tracing samples at various Zenith angles.

6. Noise Temperature Reduction Scheme

By observing Figure 4-1, we notice that the set of rays with a single surface interaction which are absorbed by the inner walls of the dome structure, make an important contribution to the noise temperature from feed angles ranging from 60° to 90° as seen also in Figure 3-3. Therefore, a reduction of the noise temperature can be accomplished by surrounding the tertiary reflector with a shield or skirt, with the appropriate angle to reflect these rays onto the sky. The height of this shield must be different at both sides of the tertiary mirror in order to avoid any obstruction to the main aperture ray trajectories (see Figure 2-1).

In Figure 6-1, we show an example of two separate shields with different heights and inclination angles that were used to obtain the appropriate ray deflection angles.

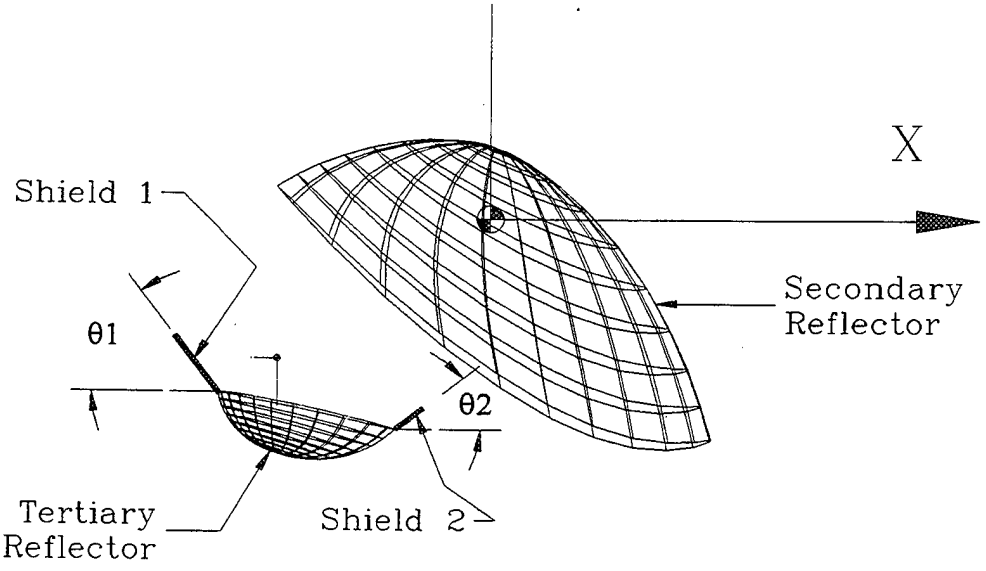

Figure 6-1 Differential shield height and inclination for Noise reduction

We first obtained the optimum inclination angle of Shield No.1, by itself, by generating a noise temperature scan as a function of inclination angle, which is presented in Figure 6-2. This figure indicates that the optimum angle lies between 65° and 75°. In the same manner, we obtain the appropriate deflection angle for Shield No.2, with the inclination angle of Shield No.1 fixed at 70°. The noise temperature scan obtained is presented in Figure 6-3. The inclination angle chosen for Shield No.2 is 35°.

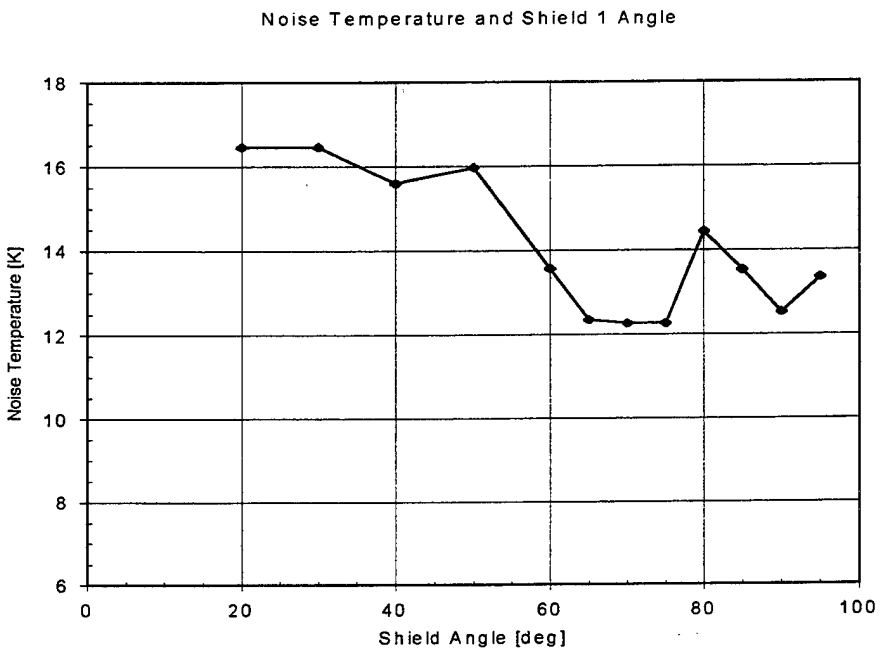

Figure 6-2 Feed noise temperature vs. inclination angle of Shield No. 1

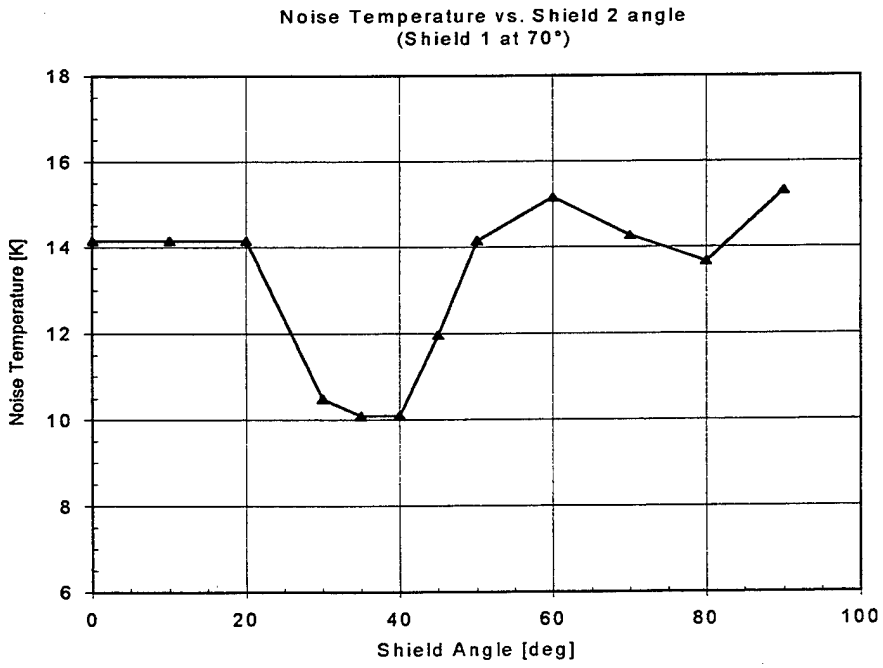

Figure 6-3 Feed noise temperature vs. inclination angle of Shield No. 2.

With the information obtained from both shields, i.e., inclination angle and length, we generate a linear interpolating surface in the shape of a truncated cone, shown in Figure 6-4

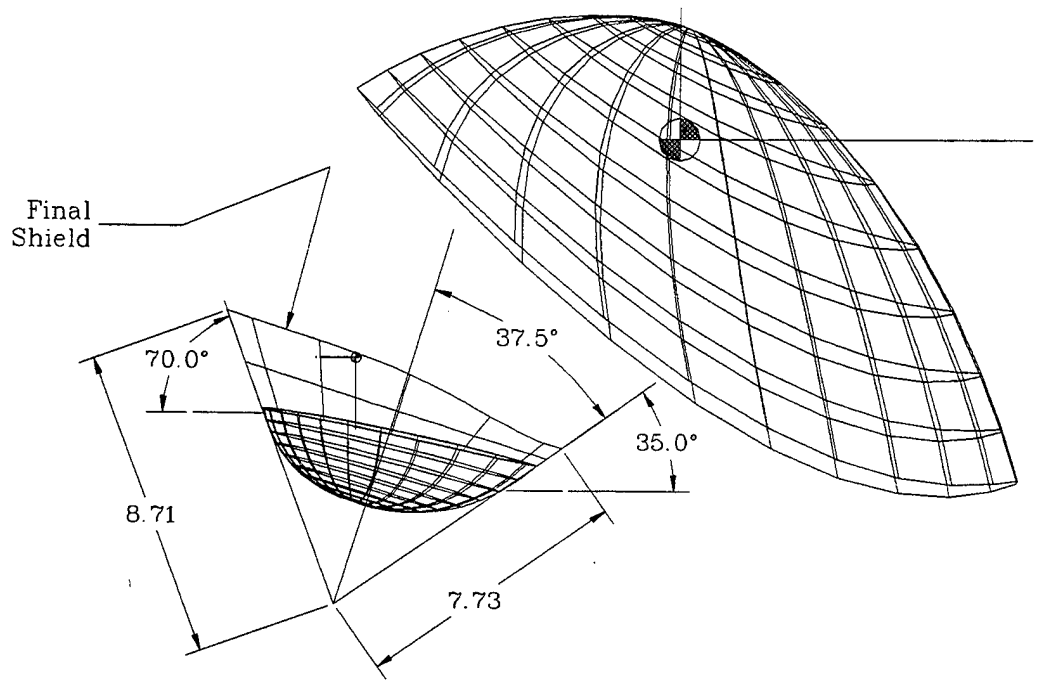

Figure 6-4. Final shield geometry (dimensions in meters)

With the tertiary shield in place, the noise temperature was changed form 16.9K to 8.6K at 0° zenith angle. Figure 6-5 presents the noise temperature map obtained at a zenith angle of 0° with the tertiary conical shield in place. Most of the rays in the map with angles between θ_{Feed}=60° to 90°, that would have been terminated inside of the dome are now reflected back to the sky, hence reducing the overall noise temperature. The map also shows some new features; one of these is as small spot marked as A, with a temperature of 1.6K, where the linear interpolation design of shield is not adequate. Another feature is the horizontal stripes marked as B, with a temperature of 14K, which are simply an artifact due to a finite separation, in the simulation, between the shield and the tertiary edge in some portions of the tertiary boundary.

Additionally, with the shield in place, there is no variation in noise temperature as a function of azimuth angle, as shown in Figure 6-6, until about θ_{Zenith}=18°, at which angle the noise temperature increases due to the same mechanism as in the previous scan, with no tertiary shield

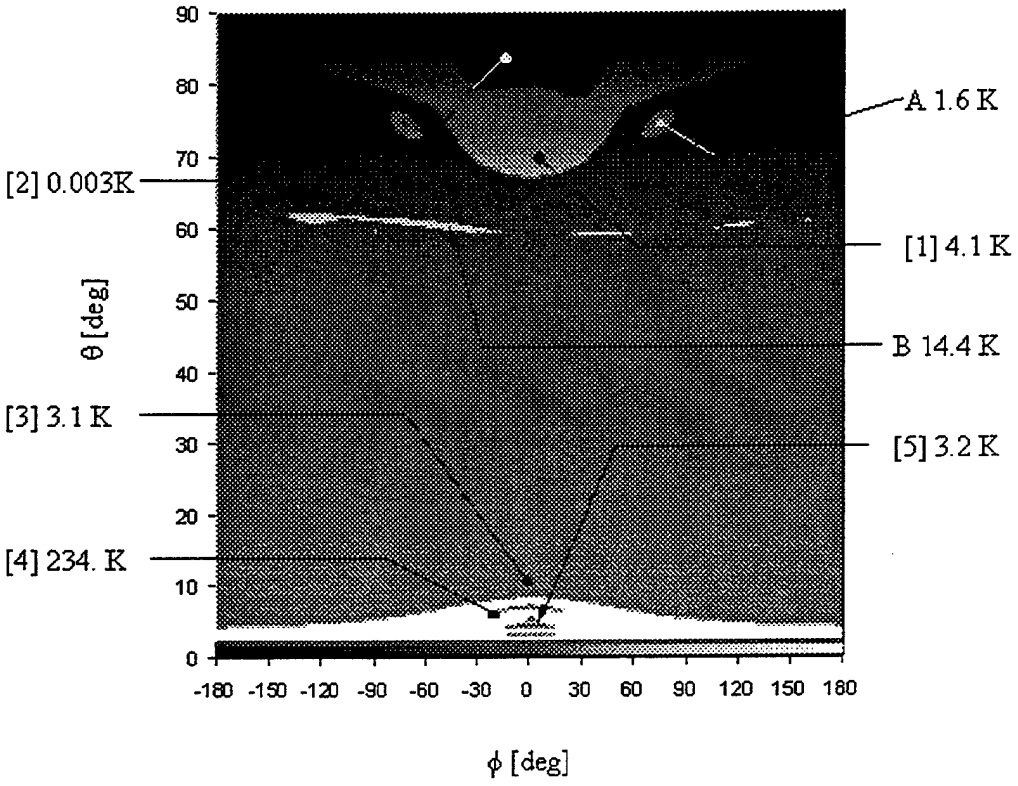

Figure 6-5. Noise Temperature map with tertiary shield

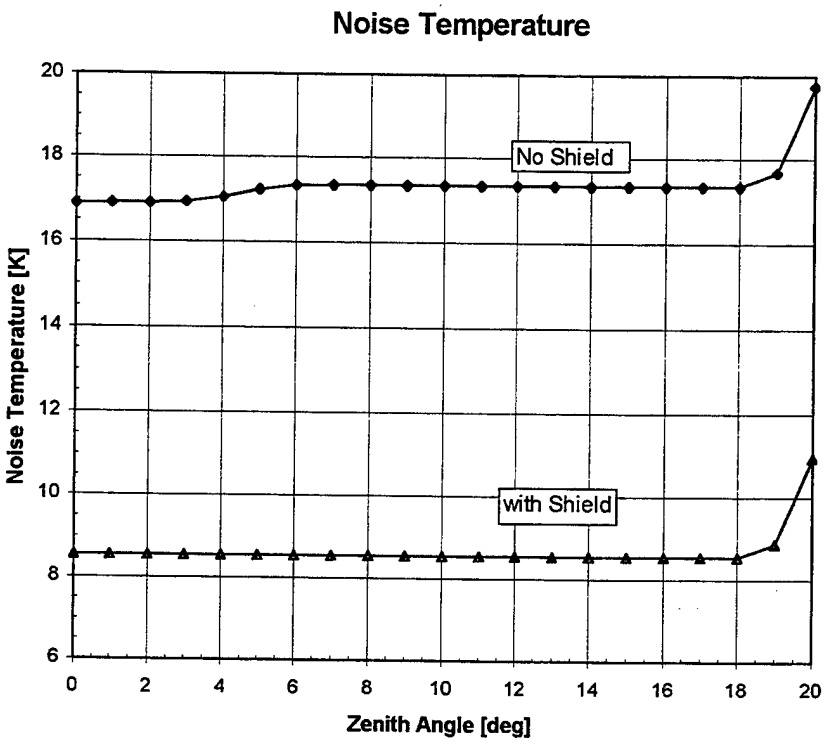

Figure 6-6. Noise Temperature vs. zenith angle with tertiary shield

7. Conclusions

We have analyzed the performance of the Arecibo radio telescope with Gregorian corrector system using a technique based on electromagnetic field ray tracing. We have obtained both the aperture field distribution and the far field radiation pattern of this antenna. We have developed a noise temperature analysis technique based on the classification of ray trajectories and ray temperature assignments according to the final surface interaction. We have obtained noise temperature maps in the feed coordinate system, which, in conjunction with the ray classification scheme, help to diagnose problematic noise temperature contributions of the antenna. We also have obtained the noise temperature perceived by the feed as a function of zenith angle. Based on this analysis, we have optimized the design of a shield or skirt, to be placed around the rim of the tertiary, which redirects the feed spill over to the sky reducing the total noise temperature from an initial value of 16.9K to 8.3K. This technique should allow further improvement of this already very high sensitivity system for radio and radar astronomy.

References

[1] P. S. Kildal, L. Baker, and T. Hagfors, "Development of a Dual-Reflector Feed for the Arecibo Radio Telescope: An Overview", *IEEE Trans. Antennas and Propagation,* Vol. 33, pp. 12-17, Oct. 1991.

[2] P.F. Goldsmith, "The Second Arecibo Upgrade", *IEEE Potentials,* vol. 15, pp. 38-43, Aug/Sep. 1996.

[3] G. Cortés Medellín, *Analysis of Segmented Reflector antenna for a Large Millimeter wave Radio Telescope".* Ph.D. dissertation, ch. 3, May. 1993.

[4] F. T. Ulaby, R. K. Moore, A. K. Fung, *Microwave Remote Sensing, Active and Passive.* Vol-1, pp. 204-207, Addison-Wesley Publishing Company, 1981

METHODS OF MOMENT ANALYSIS OF ELECTRICALLY LARGE SQUARE AND RECTANGULAR LOOP ANTENNA WITH NON-UNIFORM CURRENT

C.P. Lim, L.W. Li, and M.S. Leong
Communications and Microwave Division
Department of Electrical Engineering
National University of Singapore
10 Kent Ridge Crescent, Singapore 119260

Abstract: This paper firstly presents a method of moments analysis which obtains the non-uniform current distribution in closed form, and their resulted radiated patterns in both near and far zones, of square and rectangular loop antennas with electrically larger perimeter. An oblique incident field in its general form is considered in the formulation of the non-uniform current distributions. In the Galerkin's method of moments (MoM) analysis, the Fourier cosine series is considered as the full-domain basis function series. As a result, the current distributions along the square and rectangular loops are expressed analytically in terms of the azimuth angle for various sizes of large loops. Finally, an alternative vector analysis of the electromagnetic (EM) fields radiated from thin rectangular loop antennas of arbitrary length $2a$ and width $2b$ is introduced. This method which employs the dyadic Green's function (DGF) in the derivation of the EM radiated fields makes the analysis general, compact and straightforward. Both near- and far zones are considered so that the EM radiated fields are expressed in terms of the vector wave eigenfunctions. Not only the exact solution of the EM fields in the near and far zones are derived by the use of the spherical Bessel and Hankel functions of the first kind respectively, but also the regions between b and $\sqrt{a^2+b^2}$ which are defined as intermediate zones are characterized by both the spherical Bessel and Hankel functions of the first kind. Validity of the numerical results is discussed and clarified.

1 Introduction

Thin circular loop antennas carrying different forms of the currents and their radiation characteristics have been investigated by many researchers over the last several decades. The recognized contributions to the field are made by many researchers, e.g., [1-19], to the authors' best knowledge. The radiation characteristics of the circular loop antennas can also be readily found from antenna text books [20,21]. However, literature on polygonal loop antennas located in free-space is limited [22-24]. In the past, it has been cited that "theoretical analysis seems to be unsuccessful" for rectangular loop and therefore application of the rectangular loop antenna has received less attention [24]. In past, the rectangular loop antennas were modeled as a dipole [23] and the presentation was extremely complicated as compare to the analysis demonstrated here. For [22], only experimental techniques and measurements were presented.In [20,21], only approximated current distribution is used to show the radiation patterns in far zone. For the near-zone field, none has been reported in the literature due to the difficulty in evaluating integrals analytically. Therefore, this paper aims to present the formulations of the accurate current distributions using Galerkin's MoM and the EM fields in both near, far and intermediate zones using DGF for the square and rectangular loop antennas.

2 General Formulation of Current Distributions

Fig. 1 shows the geometry of a thin rectangular loop antenna located at $z = 0$ and fed at $\phi_i = 0$ with the delta-function generator $V_0\delta(\phi)$.

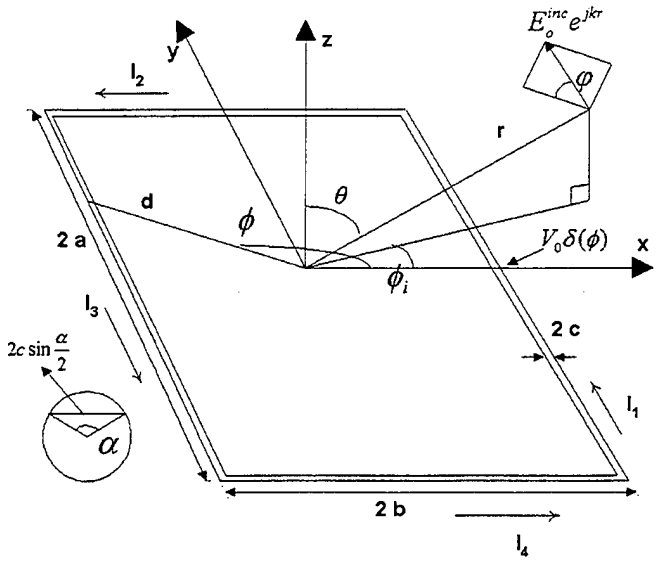

Figure 1: Geometry of a thin rectangular loop antenna.

The loop current satisfies the integral equation [1,5,10,25] as follows:

$$dE_\phi^{inc}(d,\phi) = \frac{j\eta_o}{4\pi}\sum_{t=1}^{4}\int_{\text{region t}} K_t(\phi-\phi')I_t(\phi')\,d\phi' \tag{1}$$

where E_ϕ^{inc} denotes the incident field, d stands for the distance between origin and side of the loop and $\eta_o = 120\pi\Omega$ is the free-space wave impedance. The current $I_t(\phi)$ can be expressed by

$$I_t(\phi) = \sum_{m=0}^{\infty}(2-\delta_{m0})I_m^t\cos(m\phi) \tag{2}$$

where t takes the form of integers of 1 to 4 for square and rectangular loop, δ_{m0} denotes the Kronecker symbol and I_m^t stands for the series expansion coefficients. The integral kernel in (1) is represented by the following Fourier series expansion

$$K_t(\phi-\phi') = \sum_{m=0}^{\infty}(2-\delta_{m0})g_m^t\cos m(\phi-\phi') \tag{3}$$

$$g_m^t = \int_{\text{region t}}\left(\frac{k_0 d}{2}(N_{m+1}^t + N_{m-1}^t) - \frac{m^2}{k_0 d}N_m^t\right)d\phi' \tag{4}$$

$$d = \left\{\begin{bmatrix} \frac{a}{|\cos\phi'|}, & \text{for region 1 \& 3} \\ \frac{b}{|\sin\phi'|}, & \text{for region 2 \& 4}\end{bmatrix}\right. \tag{5}$$

$$N_m^t = \frac{(2-\delta_{m0})}{4\pi^2}\int_{\text{region t}}\int_{-\pi}^{\pi} \cdot\frac{\cos m(\phi-\phi')\exp(-jk_0r')}{r'}\,d\alpha\,d\phi' \tag{6}$$

$$r' = \left\{ \begin{bmatrix} \sqrt{(\frac{a}{|\cos\phi'|})^2 + 4c^2 \sin\frac{\alpha}{2}}, & \text{for region 1 \& 3} \\ \sqrt{(\frac{b}{|\sin\phi'|})^2 + 4c^2 \sin\frac{\alpha}{2}}, & \text{for region 2 \& 4} \end{bmatrix} \right\} \tag{7}$$

$$\begin{bmatrix} \text{region 1} \\ \text{region 2} \\ \text{region 3} \\ \text{region 4} \end{bmatrix} \Longrightarrow \begin{bmatrix} -\phi_0 < \phi' \leq \phi_0 \\ \phi_0 < \phi' \leq \pi - \phi_0 \\ \pi - \phi_0 < \phi' \leq \pi + \phi_0 \\ \pi + \phi_0 < \phi' \leq 2\pi - \phi_0 \end{bmatrix} \tag{8}$$

and

$$\phi_0 = \tan^{-1}\frac{b}{a}. \tag{9}$$

The incident field E_ϕ^{inc} at the angle ϕ is given by

$$\begin{aligned} E_\phi^{inc} &= E_0^{inc}[\cos\psi\cos(\phi - \phi_i) + \sin\psi\sin(\phi - \phi_i)\cos\theta] \\ &\quad \cdot e^{jk_0 d\cos(\phi - \phi_i)\sin\theta}. \end{aligned} \tag{10}$$

It can also be expressed in terms of the Fourier series as follows:

$$E_\phi^{inc} = \sum_{m=-\infty}^{\infty}\sum_{t=1}^{4} f_m^t e^{-jm\phi} \tag{11}$$

where

$$\begin{aligned} f_m^t &= \frac{1}{2\pi}\int_{\text{region t}} E_0^{inc}\left\{ j^{m-1}\cos\psi e^{jm\phi_0} J_m'(k_0 d\sin\theta) \right. \\ &\quad \left. + j^m \sin\psi\cos\theta e^{jm\phi_0}\frac{m J_m(k_0 d\sin\theta)}{k_0 d\sin\theta} \right\} d\phi'. \end{aligned} \tag{12}$$

To obtain maximum electric and magnetic responses, the loop orientation is made at $\psi = 0$, $\theta = \frac{\pi}{2}$, and $\phi_0 = 0$ which simplifies f_m^t and I_m^t to

$$f_m^t = \frac{1}{2\pi}\int_{\text{region t}} \frac{j^{m-1}}{2}\left\{ J_{m-1}(k_0 d) - J_{m+1}(k_0 d) \right\} d\phi' \tag{13}$$

and

$$I_m^t = -j\frac{V(0) + 2\pi f_m^t}{g_m^t \pi \eta_o}. \tag{14}$$

3 General Formulation of EM Radiated Fields

The detailed formulation of the EM radiated fields of circular loop antennas has been shown in [19, (1)-(7)]. In view of this, the authors will not repeat the procedure. The near, far and intermediate zones defined in this paper are depicted in Fig. 2. With the current distribution given in (2), we can obtain the EM fields expressions for the four zones as follows:

$$\begin{bmatrix} E_r^0 \\ E_r^1 \\ E_r^2 \\ E_r^3 \end{bmatrix} = -\frac{\eta_0 k_0^2}{4\pi}\sum_{n=1}^{\infty}\sum_{m=0}^{n} D_{mn} P_n^m(\cos\theta) \begin{matrix} \cos \\ \sin \end{matrix} (m\phi)$$

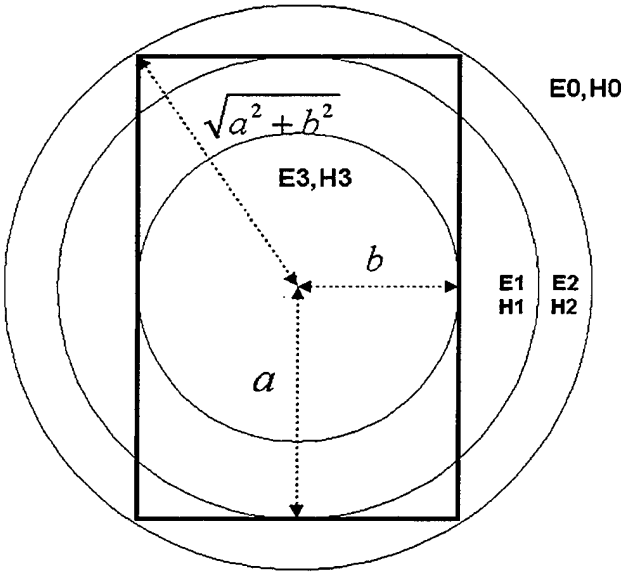

Figure 2: Intermediate zones.

$$\cdot \frac{n(n+1)}{k_0 r}\left\{ j_n(k_0 r)\begin{bmatrix} 0 \\ (\Phi_{e_{omn}}^{N,r,1>} + \Phi_{e_{mn}}^{N,\phi,1>}) \\ (\Phi_{e_{omn}}^{N,r,2>} + \Phi_{e_{mn}}^{N,\phi,2>}) \\ (\Phi_{e_{omn}}^{N,r>} + \Phi_{e_{omn}}^{N,\phi>}) \end{bmatrix} \right.$$

$$\left. + h_n^{(1)}(k_0 r)\begin{bmatrix} (\Phi_{e_{omn}}^{N,r<} + \Phi_{e_{mn}}^{N,\phi<}) \\ (\Phi_{e_{omn}}^{N,r,1<} + \Phi_{e_{mn}}^{N,\phi,1<}) \\ (\Phi_{e_{omn}}^{N,r,2<} + \Phi_{e_{omn}}^{N,\phi,2<}) \\ 0 \end{bmatrix} \right\}. \tag{15a}$$

$$\begin{bmatrix} E_\theta^0 \\ E_\theta^1 \\ E_\theta^2 \\ E_\theta^3 \end{bmatrix} = -\frac{\eta_0 k_0^2}{4\pi} \sum_{n=1}^{\infty} \sum_{m=0}^{n} \mp D_{mn} \frac{m}{\sin\theta} P_n^m(\cos\theta)$$

$$\cdot \begin{matrix} \sin \\ \cos \end{matrix} (m\phi) \left\{ j_n(k_0 r)\begin{bmatrix} 0 \\ \Phi_{e_{omn}}^{M,1>} \\ \Phi_{e_{omn}}^{M,2>} \\ \Phi_{e_{omn}}^{M>} \end{bmatrix} \right.$$

$$\left. + h_n^{(1)}(k_0 r)\begin{bmatrix} \Phi_{e_{omn}}^{M<} \\ \Phi_{e_{omn}}^{M,1<} \\ \Phi_{e_{omn}}^{M,2<} \\ 0 \end{bmatrix} \right\}$$

$$+ D_{mn} \frac{dP_n^m(\cos\theta)}{d\theta} \begin{matrix} \cos \\ \sin \end{matrix} (m\phi)$$

$$\cdot \left\{ \frac{d[rj_n(k_0r)]}{k_0rdr} \begin{bmatrix} 0 \\ (\Phi_{e_{mn}}^{N,r,1>} + \Phi_{e_{mn}}^{N,\phi,1>}) \\ (\Phi_{e_{o_{mn}}}^{N,r,2>} + \Phi_{e_{o_{mn}}}^{N,\phi,2>}) \\ (\Phi_{e_{o_{mn}}}^{N,r>} + \Phi_{e_{o_{mn}}}^{N,\phi>}) \end{bmatrix} \right.$$

$$\left. + \frac{d[rh_n^{(1)}(k_0r)]}{k_0rdr} \begin{bmatrix} (\Phi_{e_{o_{mn}}}^{N,r<} + \Phi_{e_{o_{mn}}}^{N,\phi<}) \\ (\Phi_{e_{mn}}^{N,r,1<} + \Phi_{e_{mn}}^{N,\phi,1<}) \\ (\Phi_{e_{o_{mn}}}^{N,r,2<} + \Phi_{e_{o_{mn}}}^{N,\phi,2<}) \\ 0 \end{bmatrix} \right\} \tag{15b}$$

$$\begin{bmatrix} E_\phi^0 \\ E_\phi^1 \\ E_\phi^2 \\ E_\phi^3 \end{bmatrix} = -\frac{\eta_0 k_0^2}{4\pi} \sum_{n=1}^{\infty} \sum_{m=0}^{n} -D_{mn} \frac{dP_n^m(\cos\theta)}{d\theta}$$

$$\cdot \begin{matrix} \cos \\ \sin \end{matrix} (m\phi) \left\{ j_n(k_0r) \begin{bmatrix} 0 \\ \Phi_{e_{mn}}^{M,1>} \\ \Phi_{e_{o_{mn}}}^{M,2>} \\ \Phi_{e_{o_{mn}}}^{M>} \end{bmatrix} \right.$$

$$\left. + h_n^{(1)}(k_0r) \begin{bmatrix} \Phi_{e_{o_{mn}}}^{M<} \\ \Phi_{e_{mn}}^{M,1<} \\ \Phi_{e_{o_{mn}}}^{M,2<} \\ 0 \end{bmatrix} \right\}$$

$$\mp D_{mn} \frac{m}{\sin\theta} P_n^m(\cos\theta) \begin{matrix} \sin \\ \cos \end{matrix} (m\phi)$$

$$\cdot \left\{ \frac{d[rj_n(k_0r)]}{k_0rdr} \begin{bmatrix} 0 \\ (\Phi_{e_{mn}}^{N,r,1>} + \Phi_{e_{mn}}^{N,\phi,1>}) \\ (\Phi_{e_{o_{mn}}}^{N,r,2>} + \Phi_{e_{o_{mn}}}^{N,\phi,2>}) \\ (\Phi_{e_{o_{mn}}}^{N,r>} + \Phi_{e_{o_{mn}}}^{N,\phi>}) \end{bmatrix} \right.$$

$$\left. + \frac{d[rh_n^{(1)}(k_0r)]}{k_0rdr} \begin{bmatrix} (\Phi_{e_{o_{mn}}}^{N,r<} + \Phi_{e_{mn}}^{N,\phi<}) \\ (\Phi_{e_{mn}}^{N,r,1<} + \Phi_{e_{mn}}^{N,\phi,1<}) \\ (\Phi_{e_{o_{mn}}}^{N,r,2<} + \Phi_{e_{o_{mn}}}^{N,\phi,2<}) \\ 0 \end{bmatrix} \right\}. \tag{15c}$$

and

$$\begin{bmatrix} H_r^0 \\ H_r^1 \\ H_r^2 \\ H_r^3 \end{bmatrix} = \frac{ik_0^2}{4\pi} \sum_{n=1}^{\infty} \sum_{m=0}^{n} D_{mn} P_n^m(\cos\theta) \begin{matrix} \cos \\ \sin \end{matrix} (m\phi)$$

$$\cdot \frac{n(n+1)}{k_0r} \left\{ j_n(k_0r) \begin{bmatrix} 0 \\ \Phi_{e_{mn}}^{M,1>} \\ \Phi_{e_{o_{mn}}}^{M,2>} \\ \Phi_{e_{o_{mn}}}^{M>} \end{bmatrix} \right.$$

$$+h_n^{(1)}(k_0 r)\begin{bmatrix} \Phi_{e_{mn}}^{M<} \\ \Phi_{e_{mn}}^{M,1<} \\ \Phi_{e_{o^{mn}}}^{M,2<} \\ 0 \end{bmatrix}\Bigg\} \tag{16a}$$

$$\begin{bmatrix} H_\theta^0 \\ H_\theta^1 \\ H_\theta^2 \\ H_\theta^3 \end{bmatrix} = \frac{ik_0^2}{4\pi}\sum_{n=1}^{\infty}\sum_{m=0}^{n} D_{mn}\frac{m}{\sin\theta}P_n^m(\cos\theta)\begin{matrix}\sin\\ \cos\end{matrix}(m\phi)$$

$$\cdot\Bigg\{\mp j_n(k_0 r)\begin{bmatrix} 0 \\ (\Phi_{e_{mn}}^{N,r,1>}+\Phi_{e_{mn}}^{N,\phi,1>}) \\ (\Phi_{e_{o^{mn}}}^{N,r,2>}+\Phi_{e_{o^{mn}}}^{N,\phi,2>}) \\ (\Phi_{e_{o^{mn}}}^{N,r>}+\Phi_{e_{o^{mn}}}^{N,\phi>}) \end{bmatrix}$$

$$\mp h_n^{(1)}(k_0 r)\begin{bmatrix} (\Phi_{e_{o^{mn}}}^{N,r<}+\Phi_{e_{o^{mn}}}^{N,\phi<}) \\ (\Phi_{e_{mn}}^{N,r,1<}+\Phi_{e_{mn}}^{N,\phi,1<}) \\ (\Phi_{e_{o^{mn}}}^{N,r,2<}+\Phi_{e_{o^{mn}}}^{N,\phi,2<}) \\ 0 \end{bmatrix}\Bigg\}$$

$$+D_{mn}\frac{dP_n^m(\cos\theta)}{d\theta}\begin{matrix}\cos\\ \sin\end{matrix}(m\phi)$$

$$\cdot\Bigg\{\frac{d[rj_n(k_0 r)]}{k_0 r dr}\begin{bmatrix} 0 \\ \Phi_{e_{mn}}^{M,1>} \\ \Phi_{e_{o^{mn}}}^{M,2>} \\ \Phi_{e_{o^{mn}}}^{M>} \end{bmatrix}$$

$$+\frac{d[rh_n^{(1)}(k_0 r)]}{k_0 r dr}\begin{bmatrix} \Phi_{e_{mn}}^{M<} \\ \Phi_{e_{mn}}^{M,1<} \\ \Phi_{e_{o^{mn}}}^{M,2<} \\ 0 \end{bmatrix}\Bigg\} \tag{16b}$$

$$\begin{bmatrix} H_\phi^0 \\ H_\phi^1 \\ H_\phi^2 \\ H_\phi^3 \end{bmatrix} = \frac{ik_0^2}{4\pi}\sum_{n=1}^{\infty}\sum_{m=0}^{n} -D_{mn}\frac{dP_n^m(\cos\theta)}{d\theta}\begin{matrix}\cos\\ \sin\end{matrix}(m\phi)$$

$$\cdot\Bigg\{j_n(k_0 r)\begin{bmatrix} 0 \\ (\Phi_{e_{mn}}^{N,r,1>}+\Phi_{e_{mn}}^{N,\phi,1>}) \\ (\Phi_{e_{o^{mn}}}^{N,r,2>}+\Phi_{e_{o^{mn}}}^{N,\phi,2>}) \\ (\Phi_{e_{o^{mn}}}^{N,r>}+\Phi_{e_{o^{mn}}}^{N,\phi>}) \end{bmatrix}$$

$$+h_n^{(1)}(k_0 r)\begin{bmatrix} (\Phi_{e_{o^{mn}}}^{N,r<}+\Phi_{e_{o^{mn}}}^{N,\phi<}) \\ (\Phi_{e_{mn}}^{N,r,1<}+\Phi_{e_{mn}}^{N,\phi,1<}) \\ (\Phi_{e_{o^{mn}}}^{N,r,2<}+\Phi_{e_{o^{mn}}}^{N,\phi,2<}) \\ 0 \end{bmatrix}\Bigg\}$$

$$\mp D_{mn}\frac{m}{\sin\theta}P_n^m(\cos\theta)\begin{matrix}\sin\\ \cos\end{matrix}(m\phi)$$

$$\cdot \left\{ \frac{d[rj_n(k_0 r)]}{k_0 r dr} \begin{bmatrix} 0 \\ \Phi_{e_{mn}}^{M,1>} \\ \Phi_{e_{mn}}^{M,2>} \\ \Phi_{e_{mn}}^{M>} \end{bmatrix} + \frac{d[rh_n^{(1)}(k_0 r)]}{k_0 r dr} \begin{bmatrix} \Phi_{e_{mn}}^{M<} \\ \Phi_{e_{mn}}^{M,1<} \\ \Phi_{e_{mn}}^{M,2<} \\ 0 \end{bmatrix} \right\}. \tag{16c}$$

where $j_n(k_0 r)$ and $h_n^{(1)}(k_0 r)$ are the spherical Bessel and Hankel functions of the first kind respectively, $P_n^m(\cos\theta)$ is the associated Legendre function, and the normalization coefficient D_{mn} is given by

$$D_{mn} = \frac{(2n+1)}{n(n+1)} \frac{(n-m)!}{(n+m)!}.$$

The coefficients of the EM fields are expressed by

$$\begin{bmatrix} \Phi_{e_{mn}}^{M<} \\ \Phi_{e_{mn}}^{M,1<} \\ \Phi_{e_{mn}}^{M,1>} \\ \Phi_{e_{mn}}^{M,2<} \\ \Phi_{e_{mn}}^{M,2>} \\ \Phi_{e_{mn}}^{M>} \end{bmatrix} = \left\{ \begin{bmatrix} \Psi_{e_{13}}^{M<} + \Psi_{e_{24}}^{M<} \\ \Psi_{e_{13}}^{M,1<} + \Psi_{e_{24}}^{M,1<} \\ \Psi_{e_{13}}^{M,1>} + \Psi_{e_{24}}^{M,1>} \\ \Psi_{e_{13}}^{M,2<} + \Psi_{e_{24}}^{M,2<} \\ \Psi_{e_{13}}^{M,2>} + \Psi_{e_{24}}^{M,2>} \\ \Psi_{e_{13}}^{M>} + \Psi_{e_{24}}^{M>} \end{bmatrix} \right\} \tag{17a}$$

$$\begin{bmatrix} \Phi_{e_{mn}}^{N,r<} \\ \Phi_{e_{mn}}^{N,r,1<} \\ \Phi_{e_{mn}}^{N,r,1>} \\ \Phi_{e_{mn}}^{N,r,2<} \\ \Phi_{e_{mn}}^{N,r,2>} \\ \Phi_{e_{mn}}^{N,r>} \end{bmatrix} = \left\{ \begin{bmatrix} \Psi_{e_{13}}^{N,r<} + \Psi_{e_{24}}^{N,r<} \\ \Psi_{e_{13}}^{N,r,1<} + \Psi_{e_{24}}^{N,r,1<} \\ \Psi_{e_{13}}^{N,r,1>} + \Psi_{e_{24}}^{N,r,1>} \\ \Psi_{e_{13}}^{N,r,2<} + \Psi_{e_{24}}^{N,r,2<} \\ \Psi_{e_{13}}^{N,r,2>} + \Psi_{e_{24}}^{N,r,2>} \\ \Psi_{e_{13}}^{N,r>} + \Psi_{e_{24}}^{N,r>} \end{bmatrix} \right\} \tag{17b}$$

$$\begin{bmatrix} \Phi_{e_{mn}}^{N,\phi<} \\ \Phi_{e_{mn}}^{N,\phi,1<} \\ \Phi_{e_{mn}}^{N,\phi,1>} \\ \Phi_{e_{mn}}^{N,\phi,2<} \\ \Phi_{e_{mn}}^{N,\phi,2>} \\ \Phi_{e_{mn}}^{N,\phi>} \end{bmatrix} = \left\{ \begin{bmatrix} \Psi_{e_{13}}^{N,\phi<} + \Psi_{e_{24}}^{N,\phi<} \\ \Psi_{e_{13}}^{N,\phi,1<} + \Psi_{e_{24}}^{N,\phi,1<} \\ \Psi_{e_{13}}^{N,\phi,1>} + \Psi_{e_{24}}^{N,\phi,1>} \\ \Psi_{e_{13}}^{N,\phi,2<} + \Psi_{e_{24}}^{N,\phi,2<} \\ \Psi_{e_{13}}^{N,\phi,2>} + \Psi_{e_{24}}^{N,\phi,2>} \\ \Psi_{e_{13}}^{N,\phi>} + \Psi_{e_{24}}^{N,\phi>} \end{bmatrix} \right\}. \tag{17c}$$

4 Numerical Results

The current distributions are obtained using MoM where the relationship between the loop and wire cross-section radii is $2\ln\frac{2\pi a}{c} \geq 10$. The analytical expressions of the

current distribution are provided in the Appendix A and the convergence of the analysis is checked in details. It is realized from the computation that only four terms of the Fourier series are necessarily taken in the summation to ensure the accuracy while the fifth and higher series can be neglected.

Forty terms are considered for the numerical computation of the summation of the spherical Bessel and Hankel functions (*i.e.*, with respect to the index n). The 2-D normalized EM radiated patterns of the intermediate zones of the rectangular and square loop antennas are depicted in Figs. 3, 4 and 5 respectively. It should be pointed out that all numerical results are normalized by their maxima.

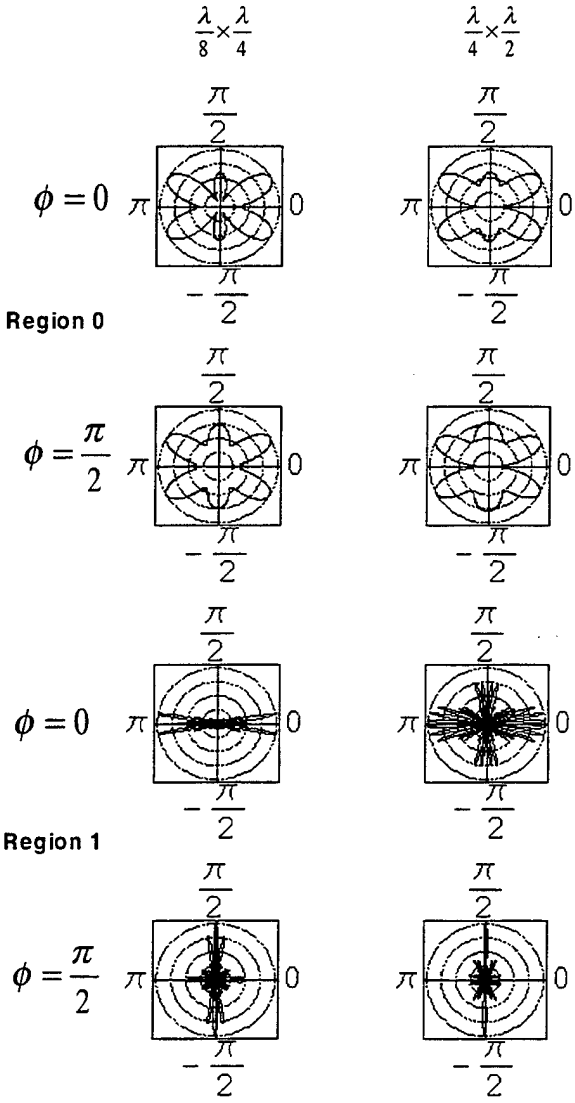

Figure 3: 2-D normalized EM radiated patterns of regions 0 and 1 of rectangular loop antennas.

5 Conclusions

This paper presents a MoM analysis of electrically large rectangular and square loop antennas. From the analysis, the radiated EM fields in both the near, far and intermediate

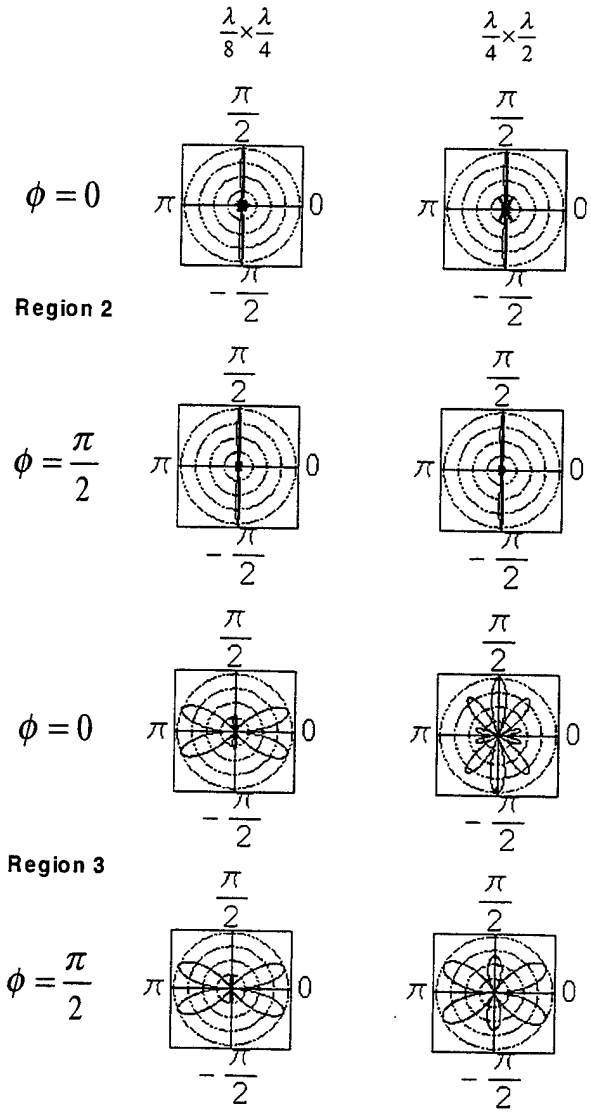

Figure 4: 2-D normalized EM radiated patterns of regions 2 and 3 of rectangular loop antennas.

zones, of thin square and rectangular loop antennas are obtained. The cosine functions are chosen as the full-domain basis and weighting functions in the Galerkin's approach. Also, the dyadic Green's function in spherical coordinates is applied in the derivation of the analytical expressions of the EM fields in the near, far and intermediate zones. The radiation patterns due to the derived current distributions are plotted in polar coordinates. The numerical results for radiation patterns in the far-field are compared with results obtained in [20, Fig. 5.52] and an excellent agreement between the two results is obtained. This confirms partially the correctness of our theoretical derivation and numerical algorithm. Some new results are also presented in the paper for the antenna patterns due to large antennas.

Appendix A: Analytical Expressions of Current Distributions

In this appendix, the current distributions along the loop antenna wires of various dimensions are provided in closed form. They are expressed in terms of the spherical azimuth angle ϕ for different loop dimensions. These formulas are extremely useful for scientists and engineers who would like to obtain full-wave characteristics of the loop antennas since they can straightforwardly use those formulas without repeating the MoM analysis.

Case I: $\frac{\lambda}{8} \times \frac{\lambda}{4}$ rectangular loop

$$\begin{aligned} I_1(\phi) &= (5.093 \times 10^{-5} + 3.043 \times 10^{-5}j) \\ &\quad +2 \times ((6.787 \times 10^{-5} - 1.221 \times 10^{-4}j)\cos(\phi) \\ &\quad +(1.040 \times 10^{-4} + 2.914 \times 10^{-5}j)\cos(2\phi) \\ &\quad +(1.642 \times 10^{-5} - 1.086 \times 10^{-5}j)\cos(3\phi) \\ &\quad +(9.660 \times 10^{-7} + 8.230 \times 10^{-7}j)\cos(4\phi) \\ &\quad +(-9.956 \times 10^{-8} + 2.220 \times 10^{-7}j)\cos(5\phi) \\ &\quad +(8.579 \times 10^{-9} + 1.316 \times 10^{-8}j)\cos(6\phi) \\ &\quad +(-4.168 \times 10^{-10} + 4.364 \times 10^{-10}j)\cos(7\phi)) \end{aligned} \tag{18a}$$

$$\begin{aligned} I_2(\phi) &= (2.187 \times 10^{-4} + 5.512 \times 10^{-5}j) \\ &\quad +2 \times ((-1.835 \times 10^{-4} - 2.148 \times 10^{-4}j)\cos(\phi) \\ &\quad +(-9.214 \times 10^{-5} - 1.196 \times 10^{-4}j)\cos(2\phi) \\ &\quad +(-2.208 \times 10^{-5} - 3.247 \times 10^{-5}j)\cos(3\phi) \\ &\quad +(-3.678 \times 10^{-6} - 6.476 \times 10^{-6}j)\cos(4\phi) \\ &\quad +(-4.591 \times 10^{-7} - 1.159 \times 10^{-6}j)\cos(5\phi) \\ &\quad +(1.991 \times 10^{-9} + 2.276 \times 10^{-7}j)\cos(6\phi)) \\ &\quad +(2.486 \times 10^{-8} - 2.546 \times 10^{-9}j)\cos(7\phi)) \end{aligned} \tag{18b}$$

$$\begin{aligned} I_3(\phi) &= (7.878 \times 10^{-5} + 5.365 \times 10^{-6}j) \\ &\quad +2 \times ((-1.634 \times 10^{-6} + 1.868 \times 10^{-4}j)\cos(\phi) \\ &\quad +(1.256 \times 10^{-4} + 3.464 \times 10^{-4}j)\cos(2\phi) \\ &\quad +(-1.388 \times 10^{-5} + 1.452 \times 10^{-5}j)\cos(3\phi) \\ &\quad +(1.428 \times 10^{-6} + 5.731 \times 10^{-7}j)\cos(4\phi) \\ &\quad +(-2.086 \times 10^{-8} + 3.035 \times 10^{-7}j)\cos(5\phi) \\ &\quad +(1.244 \times 10^{-8} + 1.202 \times 10^{-8}j)\cos(6\phi) \\ &\quad +(3.240 \times 10^{-10} - 6.533 \times 10^{-10}j)\cos(7\phi)) \end{aligned} \tag{18c}$$

$$\begin{aligned} I_4(\phi) &= (4.169 \times 10^{-5} + 2.215 \times 10^{-4}j) \\ &\quad +2 \times ((2.030 \times 10^{-4} + 1.955 \times 10^{-4}j)\cos(\phi) \end{aligned}$$

$$
\begin{aligned}
&+(-1.138\times10^{-4}-9.793\times10^{-5}j)\cos(2\phi)\\
&+(3.116\times10^{-5}+2.322\times10^{-5}j)\cos(3\phi)\\
&+(-6.261\times10^{-6}-3.749\times10^{-6}j)\cos(4\phi)\\
&+(1.111\times10^{-6}+4.192\times10^{-7}j)\cos(5\phi)\\
&+(-1.901\times10^{-7}+1.621\times10^{-8}j)\cos(6\phi)\\
&+(6.392\times10^{-9}-1.733\times10^{-8}j)\cos(7\phi)). \qquad (18d)
\end{aligned}
$$

Case II: $\frac{\lambda}{4}\times\frac{\lambda}{2}$ rectangular loop

$$
\begin{aligned}
I_1(\phi) &= (7.176\times10^{-5}+1.272\times10^{-4}j)\\
&+2\times((1.106\times10^{-4}-7.134\times10^{-5}j)\cos(\phi)\\
&+(1.665\times10^{-4}+1.213\times10^{-4}j)\cos(2\phi)\\
&+(8.318\times10^{-5}+3.618\times10^{-5}j)\cos(3\phi)\\
&+(1.937\times10^{-6}+1.318\times10^{-5}j)\cos(4\phi)\\
&+(-3.529\times10^{-6}+2.700\times10^{-6}j)\cos(5\phi)\\
&+(-2.617\times10^{-7}+5.892\times10^{-7}j)\cos(6\phi)\\
&+(-5.280\times10^{-8}+1.919\times10^{-9}j)\cos(7\phi)) \qquad (19a)
\end{aligned}
$$

$$
\begin{aligned}
I_2(\phi) &= (2.708\times10^{-4}-8.061\times10^{-5}j)\\
&+2\times((3.200\times10^{-5}-1.236\times10^{-5}j)\cos(\phi)\\
&+(1.691\times10^{-4}-3.510\times10^{-4}j)\cos(2\phi)\\
&+(1.320\times10^{-4}-1.725\times10^{-4}j)\cos(3\phi)\\
&+(5.747\times10^{-5}-4.826\times10^{-5}j)\cos(4\phi)\\
&+(1.772\times10^{-5}-8.595\times10^{-6}j)\cos(5\phi)\\
&+(4.241\times10^{-6}-6.625\times10^{-7}j)\cos(6\phi)\\
&+(7.870\times10^{-7}+1.852\times10^{-7}j)\cos(7\phi)) \qquad (19b)
\end{aligned}
$$

$$
\begin{aligned}
I_3(\phi) &= (1.458\times10^{-4}-6.315\times10^{-5}j)\\
&+2\times((6.531\times10^{-5}+1.218\times10^{-4}j)\cos(\phi)\\
&+(1.080\times10^{-4}-1.357\times10^{-4}j)\cos(2\phi)\\
&+(-6.927\times10^{-5}+4.235\times10^{-5}j)\cos(3\phi)\\
&+(1.463\times10^{-5}+3.851\times10^{-6}j)\cos(4\phi)\\
&+(-1.764\times10^{-6}-3.913\times10^{-6}j)\cos(5\phi)\\
&+(3.282\times10^{-7}+5.935\times10^{-7}j)\cos(6\phi)\\
&+(2.512\times10^{-8}-5.718\times10^{-8}j)\cos(7\phi)) \qquad (19c)
\end{aligned}
$$

$$
\begin{aligned}
I_4(\phi) &= (-2.834\times10^{-4}+9.169\times10^{-5}j)\\
&+2\times((1.635\times10^{-5}+1.242\times10^{-4}j)\cos(\phi)\\
&+(-1.204\times10^{-4}-3.554\times10^{-4}j)\cos(2\phi)
\end{aligned}
$$

$$+(1.037\times10^{-4}+1.766\times10^{-4}j)\cos(3\phi)$$
$$+(-4.708\times10^{-5}-5.054\times10^{-5}j)\cos(4\phi)$$
$$+(1.475\times10^{-5}+9.580\times10^{-6}j)\cos(5\phi)$$
$$+(-3.534\times10^{-6}-1.046\times10^{-6}j)\cos(6\phi)$$
$$+(6.586\times10^{-7}-4.669\times10^{-8}j)\cos(7\phi)). \quad (19d)$$

Case III: $\frac{\lambda}{8}$ square loop

$$\begin{aligned} I_1(\phi) &= (3.464\times10^{-5}+1.651\times10^{-5}j) \\ &+2\times((3.952\times10^{-5}-8.394\times10^{-5}j)\cos(\phi) \\ &+(2.849\times10^{-5}+1.273\times10^{-5}j)\cos(2\phi) \\ &+(-2.832\times10^{-6}+7.975\times10^{-6}j)\cos(3\phi) \\ &+(1.423\times10^{-6}+1.944\times10^{-6}j)\cos(4\phi) \\ &+(-2.106\times10^{-8}+3.319\times10^{-8}j)\cos(5\phi) \\ &+(-1.519\times10^{-9}-8.525\times10^{-10}j)\cos(6\phi) \\ &+(5.423\times10^{-11}-1.121\times10^{-10}j)\cos(7\phi)) \end{aligned} \quad (20a)$$

$$\begin{aligned} I_2(\phi) &= (4.266\times10^{-5}+1.207\times10^{-5}j) \\ &+2\times((-9.646\times10^{-5}+5.063\times10^{-5}j)\cos(\phi) \\ &+(-3.192\times10^{-5}-1.843\times10^{-5}j)\cos(2\phi) \\ &+(-8.440\times10^{-6}-5.810\times10^{-6}j)\cos(3\phi) \\ &+(2.593\times10^{-6}+6.244\times10^{-7}j)\cos(4\phi) \\ &+(3.955\times10^{-8}+2.113\times10^{-8}j)\cos(5\phi) \\ &+(1.710\times10^{-9}+1.053\times10^{-9}j)\cos(6\phi) \\ &+(1.160\times10^{-10}+8.708\times10^{-11}j)\cos(7\phi)) \end{aligned} \quad (20b)$$

$$\begin{aligned} I_3(\phi) &= (4.299\times10^{-5}-8.291\times10^{-6}j) \\ &+2\times((2.114\times10^{-5}+1.036\times10^{-4}j)\cos(\phi) \\ &+(3.434\times10^{-5}-8.589\times10^{-6}j)\cos(2\phi) \\ &+(-3.751\times10^{-6}-8.496\times10^{-6}j)\cos(3\phi) \\ &+(1.517\times10^{-6}+1.390\times10^{-6}j)\cos(4\phi) \\ &+(3.801\times10^{-9}-4.419\times10^{-8}j)\cos(5\phi) \\ &+(-1.983\times10^{-9}+6.250\times10^{-11}j)\cos(6\phi) \\ &+(2.213\times10^{-11}+1.394\times10^{-10}j)\cos(7\phi)) \end{aligned} \quad (20c)$$

$$\begin{aligned} I_4(\phi) &= (3.615\times10^{-5}+2.554\times10^{-5}j) \\ &+2\times((1.000\times10^{-4}+4.208\times10^{-5}j)\cos(\phi) \\ &+(-3.458\times10^{-5}-1.142\times10^{-5}j)\cos(2\phi) \\ &+(9.557\times10^{-6}+8.611\times10^{-7}j)\cos(3\phi) \\ &+(4.909\times10^{-7}+1.741\times10^{-6}j)\cos(4\phi) \\ &+(-3.519\times10^{-8}-2.570\times10^{-8}j)\cos(5\phi) \\ &+(1.763\times10^{-9}+8.925\times10^{-10}j)\cos(6\phi) \\ &+(-1.349\times10^{-10}-3.599\times10^{-11}j)\cos(7\phi)). \end{aligned} \quad (20d)$$

Case IV: $\frac{\lambda}{4}$ square loop

$$
\begin{aligned}
I_1(\phi) \;=\; & (6.262 \times 10^{-5} + 7.684 \times 10^{-5} j) \\
& +2 \times ((7.725 \times 10^{-5} - 6.418 \times 10^{-5} j)\cos(\phi) \\
& +(5.158 \times 10^{-5} + 5.748 \times 10^{-5} j)\cos(2\phi) \\
& +(-2.635 \times 10^{-5} + 3.153 \times 10^{-5} j)\cos(3\phi) \\
& +(-7.288 \times 10^{-6} + 2.183 \times 10^{-5} j)\cos(4\phi) \\
& +(-8.068 \times 10^{-7} + 3.686 \times 10^{-7} j)\cos(5\phi) \\
& +(-4.018 \times 10^{-8} - 6.655 \times 10^{-8} j)\cos(6\phi) \\
& +(8.524 \times 10^{-9} - 6.660 \times 10^{-9} j)\cos(7\phi)) \qquad (21a)
\end{aligned}
$$

$$
\begin{aligned}
I_2(\phi) \;=\; & (1.328 \times 10^{-4} + 3.919 \times 10^{-5} j) \\
& +2 \times ((-8.426 \times 10^{-5} - 1.476 \times 10^{-4} j)\cos(\phi) \\
& +(-4.092 \times 10^{-5} - 1.217 \times 10^{-4} j)\cos(2\phi) \\
& +(2.905 \times 10^{-6} - 6.084 \times 10^{-5} j)\cos(3\phi) \\
& +(2.019 \times 10^{-5} - 3.321 \times 10^{-6} j)\cos(4\phi) \\
& +(9.769 \times 10^{-7} + 1.072 \times 10^{-6} j)\cos(5\phi) \\
& +(4.690 \times 10^{-8} + 1.203 \times 10^{-7} j)\cos(6\phi) \\
& +(-9.835 \times 10^{-10} + 1.570 \times 10^{-8} j)\cos(7\phi)) \qquad (21b)
\end{aligned}
$$

$$
\begin{aligned}
I_3(\phi) \;=\; & (5.766 \times 10^{-5} - 3.622 \times 10^{-5} j) \\
& +2 \times ((3.725 \times 10^{-5} + 5.759 \times 10^{-5} j)\cos(\phi) \\
& +(4.172 \times 10^{-5} - 3.016 \times 10^{-5} j)\cos(2\phi) \\
& +(-1.789 \times 10^{-5} - 1.737 \times 10^{-5} j)\cos(3\phi) \\
& +(7.104 \times 10^{-6} + 1.107 \times 10^{-5} j)\cos(4\phi) \\
& +(-9.462 \times 10^{-8} - 6.786 \times 10^{-7} j)\cos(5\phi) \\
& +(-5.442 \times 10^{-8} + 1.874 \times 10^{-8} j)\cos(6\phi) \\
& +(3.616 \times 10^{-9} + 6.581 \times 10^{-9} j)\cos(7\phi)) \qquad (21c)
\end{aligned}
$$

$$
\begin{aligned}
I_4(\phi) \;=\; & (1.125 \times 10^{-5} + 1.367 \times 10^{-4} j) \\
& +2 \times ((1.247 \times 10^{-4} + 1.083 \times 10^{-4} j)\cos(\phi) \\
& +(-1.054 \times 10^{-4} - 5.352 \times 10^{-5} j)\cos(2\phi) \\
& +(4.668 \times 10^{-5} + 5.128 \times 10^{-7} j)\cos(3\phi) \\
& +(-6.577 \times 10^{-6} + 9.005 \times 10^{-6} j)\cos(4\phi) \\
& +(-2.529 \times 10^{-7} - 1.149 \times 10^{-6} j)\cos(5\phi) \\
& +(7.442 \times 10^{-8} + 8.655 \times 10^{-8} j)\cos(6\phi) \\
& +(-1.228 \times 10^{-8} - 3.989 \times 10^{-9} j)\cos(7\phi)). \qquad (21d)
\end{aligned}
$$

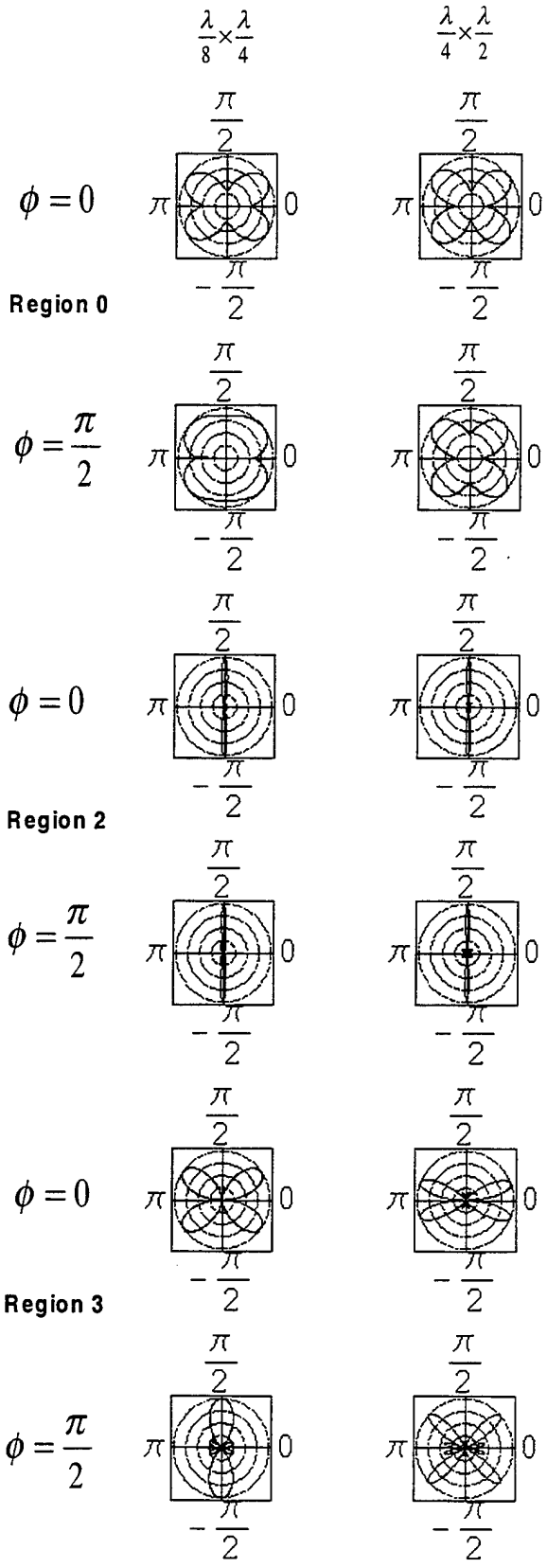

Figure 5: 2-D normalized EM radiated patterns of regions 0, 2 and 3 of square loop antennas.

Appendix B: Analytical Expressions of Coefficients of the Series

$$\begin{bmatrix} \Psi_{e_{13}}^{M<} \\ \Psi_{o_{13}}^{M,1<} \\ \Psi_{e_{13}}^{M,1>} \\ \Psi_{o_{13}}^{M,2<} \\ \Psi_{e_{13}}^{M,2>} \\ \Psi_{o_{13}}^{M>} \\ \Psi_{e_{13}}^{M>} \end{bmatrix} = \left\{ \begin{bmatrix} (\int_{-\phi_0}^{\phi_0} I_1 + \int_{\pi-\phi_0}^{\pi+\phi_0} I_3) j_n(\frac{k_0 a}{|\cos\phi'|}) \\ (\int_{-\frac{\pi}{2}+\phi_1}^{\frac{\pi}{2}-\phi_1} I_1 + \int_{\frac{\pi}{2}+\phi_1}^{\frac{3\pi}{2}-\phi_1} I_3) j_n(\frac{k_0 a}{|\cos\phi'|}) \\ \left((\int_{2\pi-\phi_0}^{-\frac{\pi}{2}+\phi_1} + \int_{\frac{\pi}{2}-\phi_1}^{\phi_0}) I_1 + (\int_{\pi-\phi_0}^{\frac{\pi}{2}+\phi_1} + \int_{\frac{3\pi}{2}-\phi_1}^{\pi+\phi_0}) I_3 \right) h_n^{(1)}(\frac{k_0 a}{|\cos\phi'|}) \\ (\int_{-\frac{\pi}{2}+\phi_1}^{\frac{\pi}{2}-\phi_1} I_1 + \int_{\frac{\pi}{2}+\phi_1}^{\frac{3\pi}{2}-\phi_1} I_3) j_n(\frac{k_0 a}{|\cos\phi'|}) \\ \left((\int_{2\pi-\phi_0}^{-\frac{\pi}{2}+\phi_1} + \int_{\frac{\pi}{2}-\phi_1}^{\phi_0}) I_1 + (\int_{\pi-\phi_0}^{\frac{\pi}{2}+\phi_1} + \int_{\frac{3\pi}{2}-\phi_1}^{\pi+\phi_0}) I_3 \right) h_n^{(1)}(\frac{k_0 a}{|\cos\phi'|}) \\ (\int_{-\phi_0}^{\phi_0} I_1 + \int_{\pi-\phi_0}^{\pi+\phi_0} I_3) h_n^{(1)}(\frac{k_0 a}{|\cos\phi'|}) \end{bmatrix} \right\}$$

$$\cdot -(2-\delta_{m0}) \frac{dP_n^m(0)}{d\theta} \begin{matrix} \cos \\ \sin \end{matrix} (m\phi') \cos(\phi') \left(\frac{a}{|\cos\phi'|} \right)^2 d\phi' \tag{22a}$$

$$\begin{bmatrix} \Psi_{e_{24}}^{M<} \\ \Psi_{o_{24}}^{M,1<} \\ \Psi_{e_{24}}^{M,1>} \\ \Psi_{o_{24}}^{M,2<} \\ \Psi_{e_{24}}^{M,2>} \\ \Psi_{o_{24}}^{M>} \\ \Psi_{e_{24}}^{M>} \end{bmatrix} = \left\{ \begin{bmatrix} (\int_{-\phi_0}^{\phi_0} I_2 + \int_{\pi-\phi_0}^{\pi+\phi_0} I_4) j_n(\frac{k_0 b}{|\sin\phi'|}) \\ 0 \\ (\int_{\phi_0}^{\pi-\phi_0} I_2 + \int_{\pi+\phi_0}^{2\pi-\phi_0} I_4) h_n^{(1)}(\frac{k_0 b}{|\sin\phi'|}) \\ (\int_{\frac{\pi}{2}-\phi_2}^{\frac{\pi}{2}+\phi_2} I_2 + \int_{\frac{3\pi}{2}-\phi_2}^{\frac{3\pi}{2}+\phi_2} I_4) j_n(\frac{k_0 b}{|\sin\phi'|}) \\ \left((\int_{\phi_0}^{\frac{\pi}{2}-\phi_2} + \int_{\frac{\pi}{2}+\phi_2}^{\pi-\phi_0}) I_2 + (\int_{\frac{3\pi}{2}+\phi_2}^{2\pi-\phi_0} + \int_{\pi+\phi_0}^{\frac{3\pi}{2}-\phi_2}) I_4 \right) h_n^{(1)}(\frac{k_0 b}{|\sin\phi'|}) \\ (\int_{-\phi_0}^{\phi_0} I_2 + \int_{\pi-\phi_0}^{\pi+\phi_0} I_4) h_n^{(1)}(\frac{k_0 b}{|\sin\phi'|}) \end{bmatrix} \right\}$$

$$\cdot -(2-\delta_{m0}) \frac{dP_n^m(0)}{d\theta} \begin{matrix} \cos \\ \sin \end{matrix} (m\phi') \sin(\phi') \left(\frac{b}{|\sin\phi'|} \right)^2 d\phi' \tag{22b}$$

$$\begin{bmatrix} \Psi_{e_{13}}^{N,r<} \\ \Psi_{o_{13}}^{N,r,1<} \\ \Psi_{e_{13}}^{N,r,1>} \\ \Psi_{o_{13}}^{N,r,2<} \\ \Psi_{e_{13}}^{N,r,2>} \\ \Psi_{o_{13}}^{N,r>} \\ \Psi_{e_{13}}^{N,r>} \end{bmatrix} = \left\{ \begin{bmatrix} (\int_{-\phi_0}^{\phi_0} I_1 + \int_{\pi-\phi_0}^{\pi+\phi_0} I_3) j_n(\frac{k_0 a}{|\cos\phi'|}) \\ (\int_{-\frac{\pi}{2}+\phi_1}^{\frac{\pi}{2}-\phi_1} I_1 + \int_{\frac{\pi}{2}+\phi_1}^{\frac{3\pi}{2}-\phi_1} I_3) j_n(\frac{k_0 a}{|\cos\phi'|}) \\ \left((\int_{2\pi-\phi_0}^{-\frac{\pi}{2}+\phi_1} + \int_{\frac{\pi}{2}-\phi_1}^{\phi_0}) I_1 + (\int_{\pi-\phi_0}^{\frac{\pi}{2}+\phi_1} + \int_{\frac{3\pi}{2}-\phi_1}^{\pi+\phi_0}) I_3 \right) h_n^{(1)}(\frac{k_0 a}{|\cos\phi'|}) \\ (\int_{-\frac{\pi}{2}+\phi_1}^{\frac{\pi}{2}-\phi_1} I_1 + \int_{\frac{\pi}{2}+\phi_1}^{\frac{3\pi}{2}-\phi_1} I_3) j_n(\frac{k_0 a}{|\cos\phi'|}) \\ \left((\int_{2\pi-\phi_0}^{-\frac{\pi}{2}+\phi_1} + \int_{\frac{\pi}{2}-\phi_1}^{\phi_0}) I_1 + (\int_{\pi-\phi_0}^{\frac{\pi}{2}+\phi_1} + \int_{\frac{3\pi}{2}-\phi_1}^{\pi+\phi_0}) I_3 \right) h_n^{(1)}(\frac{k_0 a}{|\cos\phi'|}) \\ (\int_{-\phi_0}^{\phi_0} I_1 + \int_{\pi-\phi_0}^{\pi+\phi_0} I_3) h_n^{(1)}(\frac{k_0 a}{|\cos\phi'|}) \end{bmatrix} \right\}$$

$$\cdot (2-\delta_{m0}) \frac{n(n+1)P_n^m(0)}{k_0} \begin{matrix} \cos \\ \sin \end{matrix} (m\phi') \sin(\phi') \left(\frac{a}{|\cos\phi'|} \right) d\phi' \tag{22c}$$

$$\begin{bmatrix} \Psi_{e_{24}}^{N,r<} \\ \Psi_{o_{24}}^{N,r,1<} \\ \Psi_{e_{24}}^{N,r,1>} \\ \Psi_{o_{24}}^{N,r,2<} \\ \Psi_{e_{24}}^{N,r,2>} \\ \Psi_{o_{24}}^{N,r>} \\ \Psi_{e_{24}}^{N,r>} \end{bmatrix} = \left\{ \begin{bmatrix} (\int_{-\phi_0}^{\phi_0} I_2 + \int_{\pi-\phi_0}^{\pi+\phi_0} I_4) j_n(\frac{k_0 b}{|\sin\phi'|}) \\ 0 \\ (\int_{\phi_0}^{\pi-\phi_0} I_2 + \int_{\pi+\phi_0}^{2\pi-\phi_0} I_4) h_n^{(1)}(\frac{k_0 b}{|\sin\phi'|}) \\ (\int_{\frac{\pi}{2}-\phi_2}^{\frac{\pi}{2}+\phi_2} I_2 + \int_{\frac{3\pi}{2}-\phi_2}^{\frac{3\pi}{2}+\phi_2} I_4) j_n(\frac{k_0 b}{|\sin\phi'|}) \\ \left((\int_{\phi_0}^{\frac{\pi}{2}-\phi_2} + \int_{\frac{\pi}{2}+\phi_2}^{\pi-\phi_0}) I_2 + (\int_{\frac{3\pi}{2}+\phi_2}^{2\pi-\phi_0} + \int_{\pi+\phi_0}^{\frac{3\pi}{2}-\phi_2}) I_4 \right) h_n^{(1)}(\frac{k_0 b}{|\sin\phi'|}) \\ (\int_{-\phi_0}^{\phi_0} I_2 + \int_{\pi-\phi_0}^{\pi+\phi_0} I_4) h_n^{(1)}(\frac{k_0 b}{|\sin\phi'|}) \end{bmatrix} \right\}$$

$$\cdot (2-\delta_{m0}) \frac{n(n+1)P_n^m(0)}{k_0} \begin{matrix} \cos \\ \sin \end{matrix} (m\phi') \cos(\phi') \left(\frac{b}{|\sin\phi'|} \right) d\phi' \tag{22d}$$

$$\begin{bmatrix} \Psi_{e_{13}}^{N,\phi<} \\ \Psi_{e_{13}}^{N,\phi,1<} \\ \Psi_{e_{13}}^{N,\phi,1>} \\ \Psi_{e_{13}}^{N,\phi,2<} \\ \Psi_{e_{13}}^{N,\phi,2>} \\ \Psi_{e_{13}}^{N,\phi>} \end{bmatrix} = \left\{ \begin{bmatrix} (\int_{-\phi_0}^{\phi_0} I_1 + \int_{\pi-\phi_0}^{\pi+\phi_0} I_3) \frac{d[\frac{a}{|\cos\phi'|} j_n(\frac{k_0 a}{|\cos\phi'|})]}{k_0 d(\frac{a}{|\cos\phi'|})} \\ (\int_{-\frac{\pi}{2}+\phi_1}^{\pi-\phi_1} I_1 + \int_{\frac{\pi}{2}+\phi_1}^{\frac{3\pi}{2}-\phi_1} I_3) \frac{d[\frac{a}{|\cos\phi'|} j_n(\frac{k_0 a}{|\cos\phi'|})]}{k_0 d(\frac{a}{|\cos\phi'|})} \\ \left((\int_{2\pi-\phi_0}^{-\frac{\pi}{2}+\phi_1} + \int_{\frac{\pi}{2}-\phi_1}^{\phi_0}) I_1 + (\int_{\pi-\phi_0}^{\frac{\pi}{2}+\phi_1} + \int_{\frac{3\pi}{2}-\phi_1}^{\pi+\phi_0}) I_3 \right) \frac{d[\frac{a}{|\cos\phi'|} h_n^{(1)}(\frac{k_0 a}{|\cos\phi'|})]}{k_0 d(\frac{a}{|\cos\phi'|})} \\ (\int_{-\frac{\pi}{2}+\phi_1}^{\frac{\pi}{2}-\phi_1} I_1 + \int_{\frac{\pi}{2}+\phi_1}^{\frac{3\pi}{2}-\phi_1} I_3) \frac{d[\frac{a}{|\cos\phi'|} j_n(\frac{k_0 a}{|\cos\phi'|})]}{k_0 d(\frac{a}{|\cos\phi'|})} \\ \left((\int_{2\pi-\phi_0}^{-\frac{\pi}{2}+\phi_1} + \int_{\frac{\pi}{2}-\phi_1}^{\phi_0}) I_1 + (\int_{\pi-\phi_0}^{\frac{\pi}{2}+\phi_1} + \int_{\frac{3\pi}{2}-\phi_1}^{\pi+\phi_0}) I_3 \right) \frac{d[\frac{a}{|\cos\phi'|} h_n^{(1)}(\frac{k_0 a}{|\cos\phi'|})]}{k_0 d(\frac{a}{|\cos\phi'|})} \\ (\int_{-\phi_0}^{\phi_0} I_1 + \int_{\pi-\phi_0}^{\pi+\phi_0} I_3) \frac{d[\frac{a}{|\cos\phi'|} h_n^{(1)}(\frac{k_0 a}{|\cos\phi'|})]}{k_0 d(\frac{a}{|\cos\phi'|})} \end{bmatrix} \right\}$$

$$\cdot \mp(2-\delta_{m0}) m P_n^m(0) \begin{matrix} \sin \\ \cos \end{matrix} (m\phi') \cos(\phi') \left(\frac{a}{|\cos\phi'|} \right) d\phi' \tag{22e}$$

$$\begin{bmatrix} \Psi_{e_{24}}^{N,\phi<} \\ \Psi_{e_{24}}^{N,\phi,1<} \\ \Psi_{e_{24}}^{N,\phi,1>} \\ \Psi_{e_{24}}^{N,\phi,2<} \\ \Psi_{e_{24}}^{N,\phi,2>} \\ \Psi_{e_{24}}^{N,\phi>} \end{bmatrix} = \left\{ \begin{bmatrix} (\int_{-\phi_0}^{\phi_0} I_2 + \int_{\pi-\phi_0}^{\pi+\phi_0} I_4) \frac{d[\frac{b}{|\sin\phi'|} j_n(\frac{k_0 b}{|\sin\phi'|})]}{k_0 d(\frac{b}{|\sin\phi'|})} \\ 0 \\ (\int_{\phi_0}^{\pi-\phi_0} I_2 + \int_{\pi+\phi_0}^{2\pi-\phi_0} I_4) \frac{d[\frac{b}{|\sin\phi'|} h_n^{(1)}(\frac{k_0 b}{|\sin\phi'|})]}{k_0 d(\frac{b}{|\sin\phi'|})} \\ (\int_{\frac{\pi}{2}-\phi_2}^{\frac{\pi}{2}+\phi_2} I_2 + \int_{\frac{3\pi}{2}-\phi_2}^{\frac{3\pi}{2}+\phi_2} I_4) \frac{d[\frac{b}{|\sin\phi'|} j_n(\frac{k_0 b}{|\sin\phi'|})]}{k_0 d(\frac{b}{|\sin\phi'|})} \\ \left((\int_{\phi_0}^{\frac{\pi}{2}-\phi_2} + \int_{\frac{\pi}{2}+\phi_2}^{\pi-\phi_0}) I_2 + (\int_{\frac{3\pi}{2}+\phi_2}^{2\pi-\phi_0} + \int_{\pi+\phi_0}^{\frac{3\pi}{2}-\phi_2}) I_4 \right) \frac{d[\frac{b}{|\sin\phi'|} h_n^{(1)}(\frac{k_0 b}{|\sin\phi'|})]}{k_0 d(\frac{b}{|\sin\phi'|})} \\ (\int_{-\phi_0}^{\phi_0} I_2 + \int_{\pi-\phi_0}^{\pi+\phi_0} I_4) \frac{d[\frac{b}{|\sin\phi'|} h_n^{(1)}(\frac{k_0 b}{|\sin\phi'|})]}{k_0 d(\frac{b}{|\sin\phi'|})} \end{bmatrix} \right\}$$

$$\cdot \mp(2-\delta_{m0}) m P_n^m(0) \begin{matrix} \sin \\ \cos \end{matrix} (m\phi') \sin(\phi') \left(\frac{b}{|\sin\phi'|} \right) d\phi'. \tag{22f}$$

where $\phi_1 = \sin^{-1}\frac{a}{r}$ and $\phi_2 = \cos^{-1}\frac{b}{r}$. The associated Legendre function $P_n^m(0)$ and its first-order derivative $dP_n^m(0)/d\theta$ are given by

$$\frac{dP_n^m(0)}{d\theta} = -\frac{2^{m+1}\sin\left[\frac{1}{2}(n+m)\pi\right]\Gamma\left(\frac{n+m}{2}+1\right)}{\sqrt{\pi}\Gamma\left(\frac{n-m+1}{2}\right)}, \tag{23a}$$

$$P_n^m(0) = \frac{2^m\cos\left[\frac{1}{2}(n+m)\pi\right]\Gamma\left(\frac{n+m+1}{2}\right)}{\sqrt{\pi}\Gamma\left(\frac{n-m}{2}+1\right)}. \tag{23b}$$

References

[1] M. Kanda, "An electromagnetic near-field sensor for simultaneous electric and magnetic-field measurements," *IEEE Trans. Electromagn. Compat.*, vol. EMC-26, pp. 102 – 110, Aug. 1984.

[2] G. S. Smith, "On the electrically small bare loop antenna in a dissipative medium," *IEEE Trans. Antennas Propagat.*, vol. AP-11, pp. 533 – 537, July 1963.

[3] D. Foster, "Loop antennas with uniform current," *Proc. IRE*, vol. 32, pp. 603 – 607, Oct. 1944.

[4] K. Iizuka, "The circular loop antenna multiloaded with positive and negative resistors," *IEEE Trans. Antennas Propagat.*, vol. AP-13, pp. 7 – 20, Jan. 1965.

[5] T. T. Wu, "Theory of the thin circular antenna," *J. Math. Phys.*, vol. 3, pp. 1301 – 1304, Dec. 1962.

[6] K. K. Mei, "On the integral equations of thin wire antennas," *IEEE Trans. Antennas Propagat.*, vol. AP-13, pp. 374 – 378, May 1965.

[7] R. F. Blackburn and D. R. Wilton, "Analysis and systhesis of an impedance-loaded loop antenna using the singularity expansion method," *IEEE Trans. Antennas Propagat.*, vol. AP-26, pp. 136 - 140, Jan. 1978.

[8] G. Glinski, "Note on the circular loop antennas with nonuniform current distribution," *J. Appl. Phys.*, vol. 18, pp. 638 644, July 1947.

[9] A. Richtscheid, "Calculation of the radiation resistance of loop antennas with sinusoidal current distribution," *IEEE Trans. Antennas Propagat.*, pp. 889 - 891, Nov. 1976.

[10] K. P. Esselle and S. S. Stuchly, "Resistively loaded loop as a pulse-receiving antenna," *IEEE Trans. Antennas Propagat.*, vol. 38, pp. 1123 - 1126, July 1990.

[11] G. P. Zhou and G. S. Smith, "An accurate theoretical model for thin-wire circular half-loop antenna," *IEEE Trans. Antennas Propagat.*, vol. 39, pp. 1167 - 1177, Aug. 1991.

[12] L. L. Tsai, "A numerical solution for the near and far fields of an annular ring of magnetic current," *IEEE Trans. Antennas Propagat.*, vol. AP-20, pp. 569 - 576, Sept. 1972.

[13] B. R. Rao, "Far Field Patterns of large circular loop antennas: Theoretical and experimental results," *IEEE Trans. Antennas Propagat.*, vol. AP-16, pp. 269 - 270, Mar. 1968.

[14] C. L. Chen and R. W. P. King, "The small bare loop antenna immersed in a dissipative medium," *IEEE Trans. Antennas Propagat.*, vol. AP-11, pp. 266 - 269, May 1963.

[15] K. Iizuka and F. L. Russa, "Table of the field patterns of a loaded resonant circular loop," *IEEE Trans. Antennas Propagat.*, vol. AP-18, pp. 416 - 418, May 1970.

[16] A. M. Abo-Zena and R. E. Beam, "Transient radiation field of a circular loop antenna," *IEEE Trans. Antennas Propagat.*, vol. AP-20, pp. 380 - 383, May 1972.

[17] P. L. Overfelt, "Near fields of the constant current thin circular loop antenna of arbitrary radius," *IEEE Trans. Antennas Propagat.*, vol. 44, pp. 166 - 171, Feb. 1996.

[18] D. H. Werner, "An exact integration procedure for vector potential of thin circular loop antennas," *IEEE Trans. Antennas Propagat.*, vol. 44, pp. 157 - 165, Feb. 1996.

[19] L. W. Li, M. S. Leong, P. S. Kooi, and T. S. Yeo, "Exact solutions of electromagnetic fields in both near and far zones radiated by thin circular-loop antennas: A general representation," *IEEE Trans. Antennas Propagat.*, vol. 45, pp. 1741 - 1748, Dec. 1997.

[20] W. L. Stutzman and G. A. Thiele, *Antenna Theory and Design.* New York: Wiley, 2nd ed., 1998.

[21] C. A. Balanis, *Antenna Theory: Analysis and Design.* New York: Wiley, 2nd ed., 1997.

[22] P. A. Kennedy, "Loop antenna measurements," *IRE Trans. Antennas Propagat.*, pp. 610 618, Oct. 1956.

[23] R. King, "The rectangular loop antennas as a dipole," *IRE Trans. Antennas Propagat.*, pp. 53 - 61, 1959.

[24] T. Tsukiji and S. Tou, "On polygonal loop antennas," *IEEE Trans. Antennas Propagat.*, vol. AP-28, pp. 571 - 575, July 1980.

[25] L. W. Li, C. P. Lim, and M. S. Leong, "Method of moments analysis of electrically large circular-loop antennas: Non-uniform currents," in *Dig. IEEE AP-S Int. Symp. USNC/URSI Radio Sci. Meet.*, Orlando, FL, pp. 2542 2545, July 1999.

Dielectric Cover Effect on Mutual Coupling between Cylindrical-Rectangular Microstrip Antennas using FDTD

Joonho Byun, Frances J. Harackiewicz, and Jefferson Lindsey
Department of Electrical Engineering
Southern Illinois University Carbondale

Abstract

Microstrip patch arrays find many practical applications in which they are mounted on curved surfaces such as those of aircraft and missiles, because of their major advantage of conformability. Radomes or superstrates are employed in practice to protect microstrip patch antennas from the environmental hazards such as rain, snow, and sand. The effects of this dielectric cover on the coupling between patches mounted on the curved surface can be expected to differ from those of planar models.
In this paper, the mutual coupling between cylindrical-rectangular microstrip patch antennas with dielectric overlay are investigated. This investigation is performed by using the conformal FDTD method. The method is also applied to antennas mounted on flat structures for comparison. Numerical results for the effects of superstrate permittivity and thickness on the mutual coupling between cylindrical-rectangular microstrip patch antennas are presented. The curvature effects on the mutual coupling are also shown. The presented results in this paper are useful for the rigorous analysis of microstrip antenna arrays on conformed substrates with dielectric overlay in real-world applications.

I. INTRODUCTION

Mutual coupling is always a consideration when designing microstrip antenna phased arrays especially when elements are to be spaced very close to one another. In order to accurately characterize microstrip antenna phased arrays, mutual coupling between microstrip elements must be taken into account because of its possible undesirable effects. The effect of mutual coupling can potentially cause input impedance variations with excitation and scan blindness [1]. An accurate knowledge and understanding of mutual coupling can prevent potential problems with the usage of microstrip antenna arrays.

Microstrip patch antennas many practical applications in which they are conformally mounted on curved surfaces such as those of aircraft and missiles, to avoid drag forces. Although the mutual coupling effect of microstrip patch antennas on a flat substrate have been studied by a number of authors [2]-[4], limited investigations were done for microstrip patch antennas on a curved surfaces [5]. Furthermore, there has not been a single publication regarding mutual coupling analysis between microstrip antennas on a curved surface using the FDTD method.

Indeed, radomes or substrates are employed in practice to protect microstrip patch antennas from the environmental hazards such as rain, ice, and dust. Unfortunately, this superstrate layer also causes great effects on the characteristics of microstrip structure, which have been indicated in many related reports [6]-[8]. However, these studies are mainly on the case of single patch or planar microstrip structures and the investigation on the superstrate-loaded conformal microstrip array structure is very scant. The effects of dielectric cover on the coupling between patches mounted on the curved surface can be expected to differ from those of planar models.

In this paper, the mutual coupling between two microstrip patch antennas on both flat and curved surfaces will be considered. Furthermore, the mutual coupling between cylindrical-rectangular microstrip patch antennas with dielectric overlay are investigated. This investigation is performed by using the conformal FDTD method. The method is also applied to antennas mounted on flat structures for comparison. Numerical results for the effects of substrate and superstrate permittivity on the mutual coupling between cylindrical-rectangular microstrip patch antennas are presented. The curvature effects on the mutual coupling are also shown. The effect of the superstrate on the mutual coupling of such structures will be studied. The numerical results for some cases are compared to experimental results.

II. FDTD FORMULATION

The top view of two coupled microstrip antenna patches for (a) E- and (b) H-plane configuration is shown in Fig. 1. A feed point of each radiation element is connected to a coaxial cable having a characteristic impedance of 50 Ω. The feed points were adjusted to minimize the return loss at a center frequency when the individual elements lay on an approximately infinite substrate. All the FDTD simulations ran for 16384 time steps. The patch dimensions of 10x12 mm with the substrate thickness of 0.5 mm and the relative permittivity of ε_r=2.2 was used for all the plots shown in this paper except Fig. 4 for the comparison with the

experimental data. The uniaxial perfectly matched layer was used as a boundary treatment for all simulations in this paper [9].

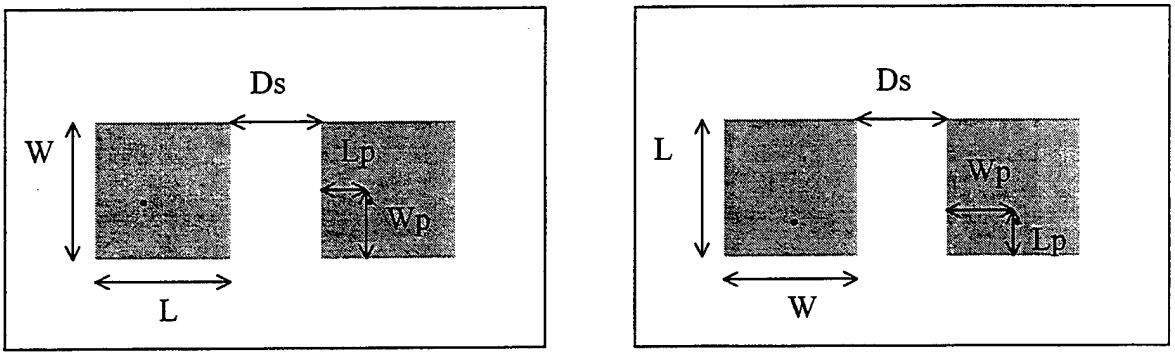

(a) (b)

Fig.1 Geometry of mutual coupling between microstrip patch antennas for (a) E- and (b) H-plane configuration.

III. Curvature Effects on Mutual Coupling between Cylindrical-Rectangular Patch Antennas

The geometries of the E- and H-plane cylindrical-rectangular microstrip antenna arrays are shown in Fig. 2. Three substrate curvatures were considered: r=16mm, 24mm, and flat. Figure 3 shows the mutual coupling coefficient versus patch separation S, where S is measured in free-space wavelengths at the resonant frequency of 8.0566 GHz. It is found that although the coupling on flat substrates is higher for small patch spacings, it falls off faster than that on curved substrates. For large patch spacings, the coupling on the most tightly curved substrate is highest. It is for these larger patch spacings that the coupling through surface waves dominates, and it may be the increase of surface waves in the axial direction of the cylinder causing this effect.

A comparison is made between the FDTD analysis and the experiment. The dual patch of 1 cm x 1 cm antenna arrays were built and measured. In the experiment, $2\lambda_0$ space was allowed from the edge of the patch. The substrate is 0.2 mm thick with a relative dielectric constant of 3.38. This geometry was

modeled using the regular FDTD and the conformal FDTD for flat and curved substrates, respectively. The simulations ran of size $(0.2\ mm)^3$. The substrate and ground plane was assumed to be infinite in the simulation. Figure 4 shows the calculated and measured mutual coupling coefficients versus the frequency for the E-plane configuration. The experimental data are less than 5 dB lower than numerical data for most of cases. This discrepancy can be explained by considering cable and connector loss which is not calibrated in the experiment. Considering as these losses are, the experimental results show the same behavior as numerical FDTD prediction and a good agreement between the measured and computed data is shown.

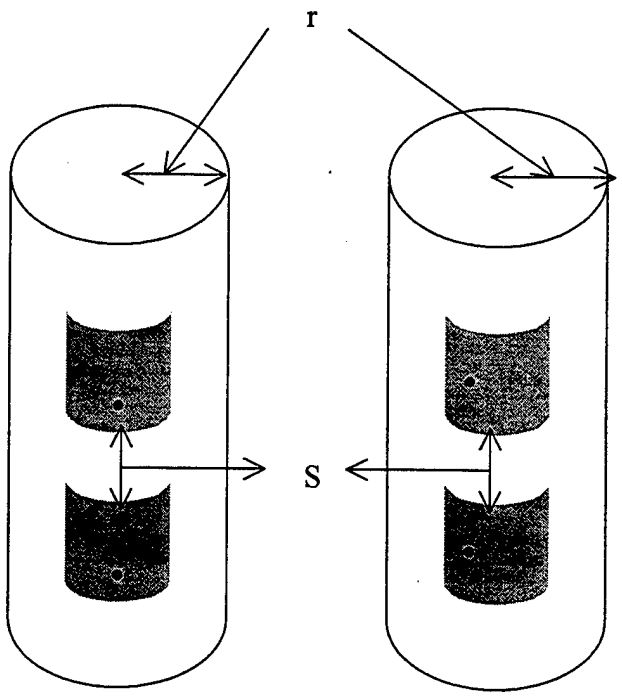

Fig. 2. (a) E- and (b) H-plane configuration of rectangular microstrip patch antennas on dielectric coated conducting circular cylinder.

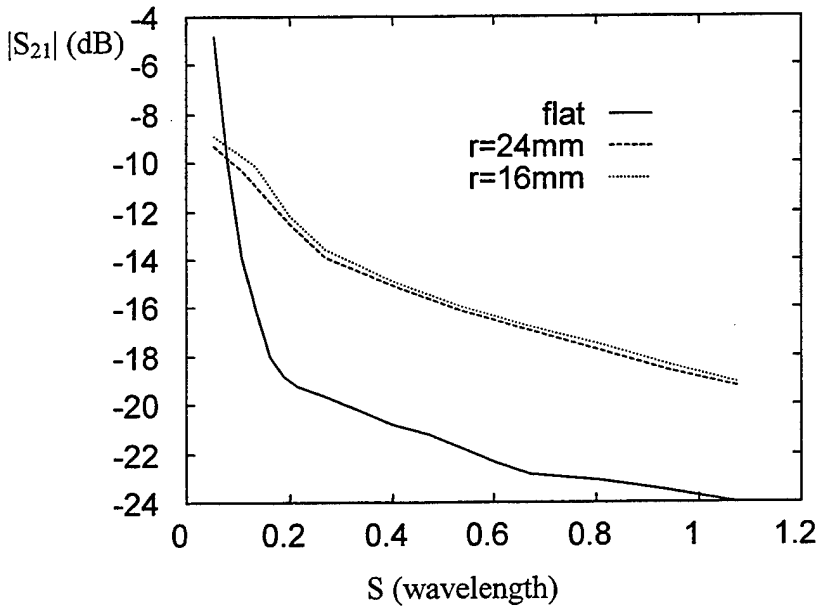

(a)

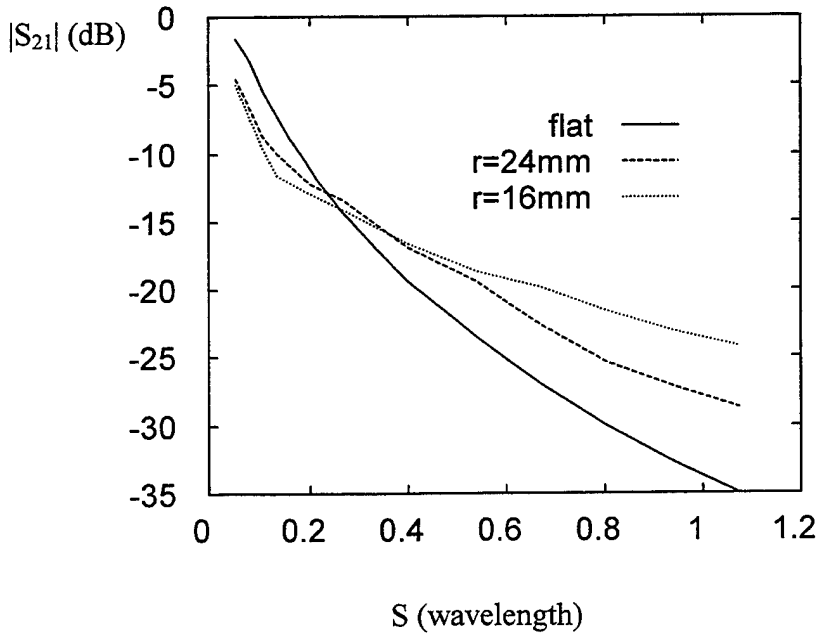

(b)

Fig. 3. (a) E- and (b) H-plane mutual coupling coefficient as a function of separation between the patches for curved and flat surfaces for $\varepsilon_r = 2.2$.

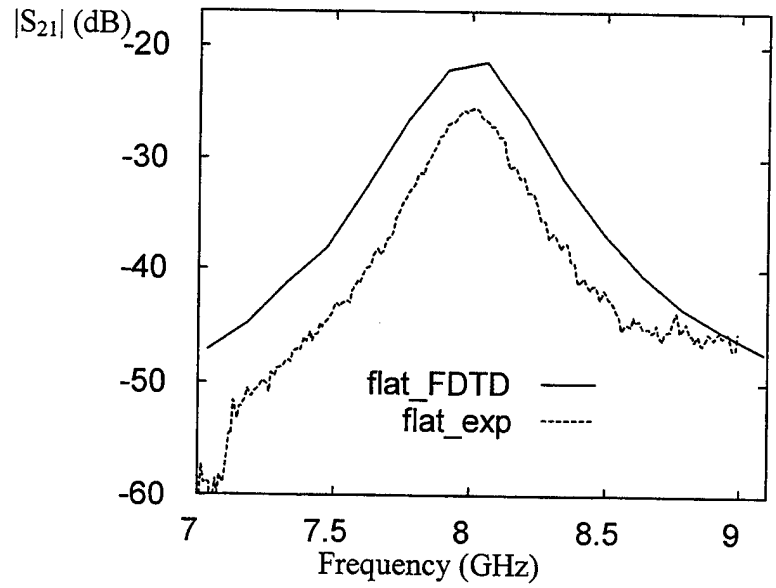

(a)

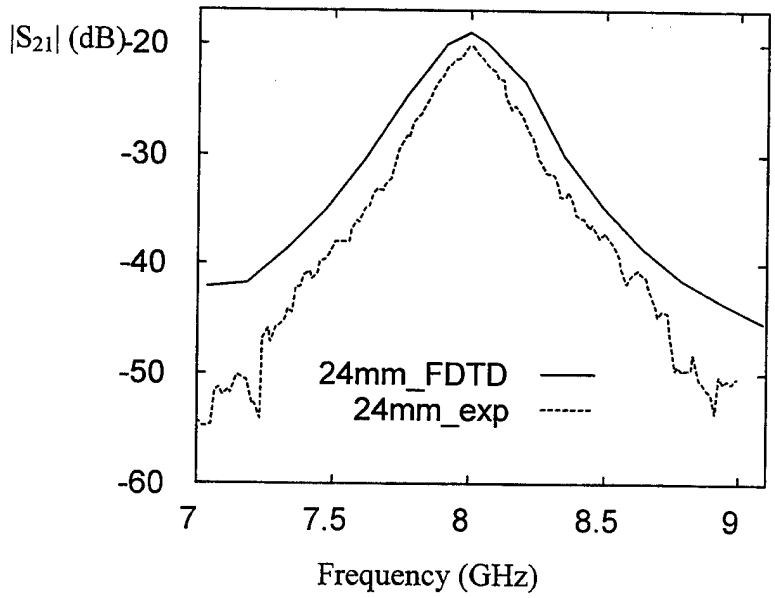

(b)

Fig. 4. Mutual coupling coefficient as a function of frequency for (a) flat and (b) curved substrate for the E-plane configuration.

IV. Superstrate Effects on Mutual Coupling between Cylindrical-Rectangular Patch Antennas

The geometry of a cylindrical-rectangular microstrip patch antenna loaded with a superstrate layer is shown in Fig. 5. The grounded conducting cylinder has radius a. A rectangular patch mounted on the substrate of thickness d (= b-a) and relative permittivity ε_{r1}. On the top of the patch is the superstrate layer of thickness t(= c-b) and relative permittivity ε_{r2}.

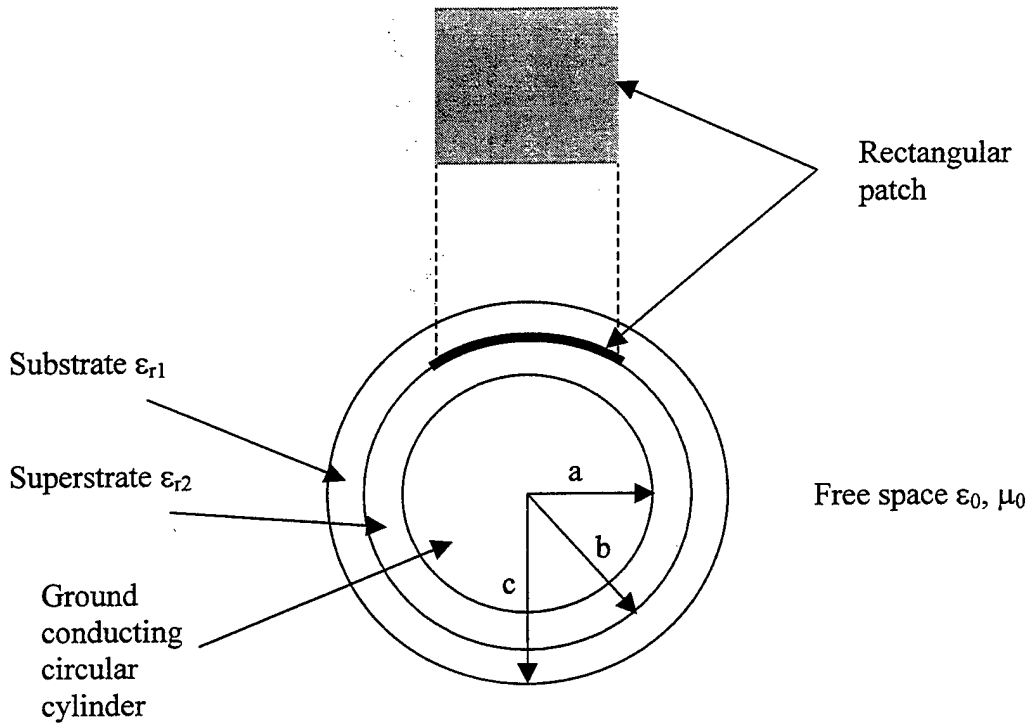

Fig. 5. Geometry of a superstrate-loaded cylindrical-rectangular patch antenna.

Without dielectric cover, the resonance was found at 8.0566 GHz and with ε_r = 2.2 and ε_r = 5.0 superstrate with the thickness of 0.5 mm, the resonance was at 7.9101 GHz and 7.6171 GHz, respectively. Fig. 6 shows the mutual coupling coefficients for the patch with and without the dielectric cover for the curved substrate. As a function of S in wavelength, the coupling is only slightly higher with a dielectric cover than one without it. In Fig. 7 and Fig. 8, a comparison is made between flat and curved substrates with dielectric covers on the mutual coupling coefficients for ε_r = 2.2 and ε_r = 5.0 substrate, respectively.

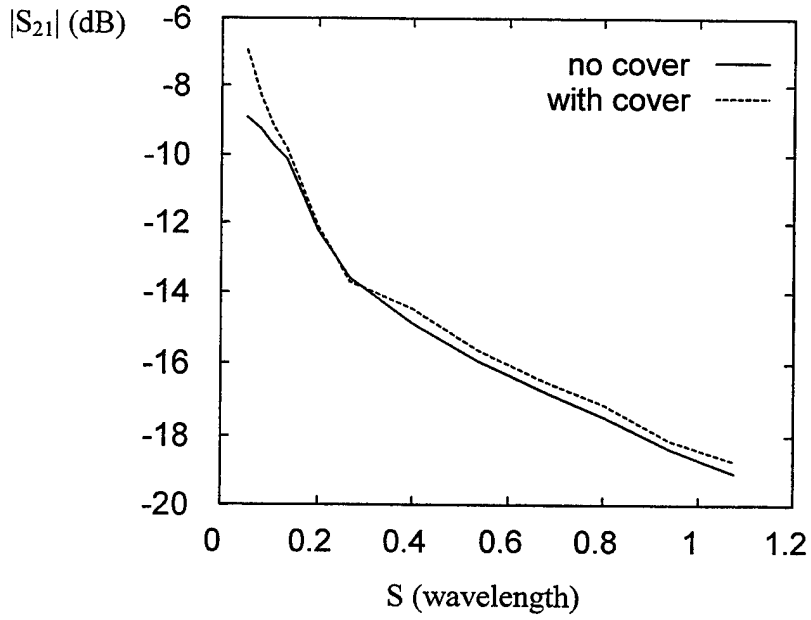

(a)

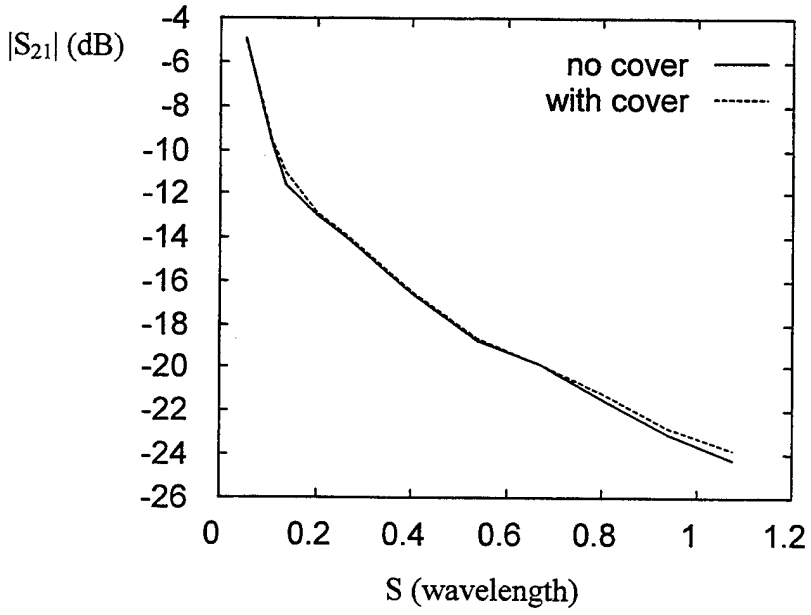

(b)

Fig. 6. (a) E- and (b) H-plane mutual coupling for curved structure with and without dielectric cover. ε_{r1}=2.2, ε_{r2}=2.2.

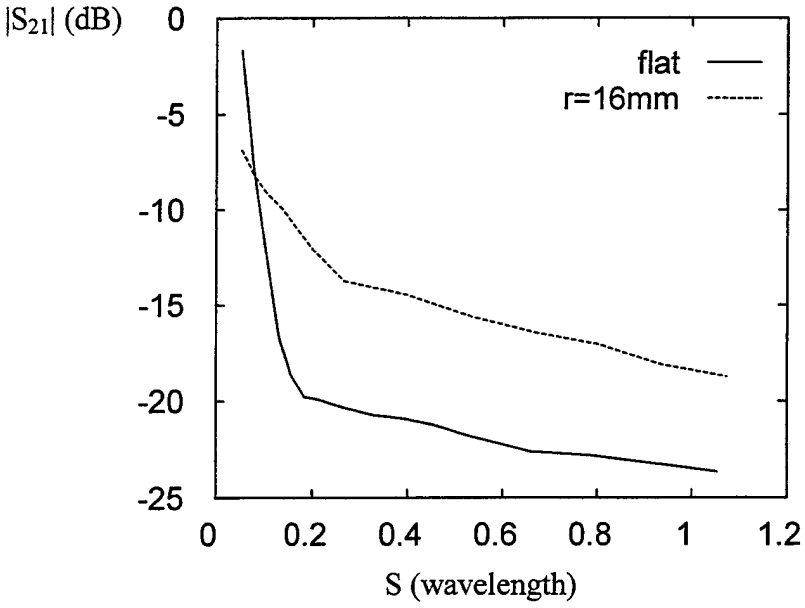

(a)

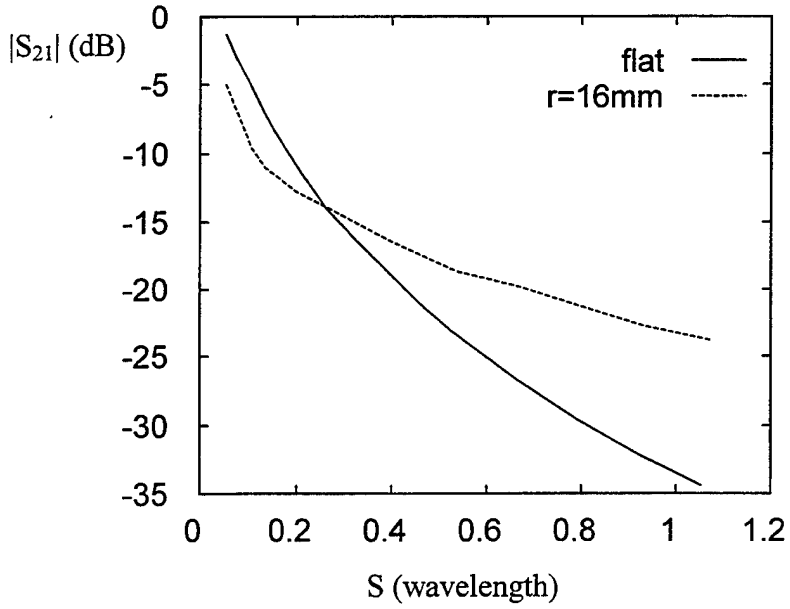

(b)

Fig. 7. (a) E- and (b) H-plane mutual coupling for flat and curved structure with dielectric cover. ε_{r1}=2.2, ε_{r2}=2.2.

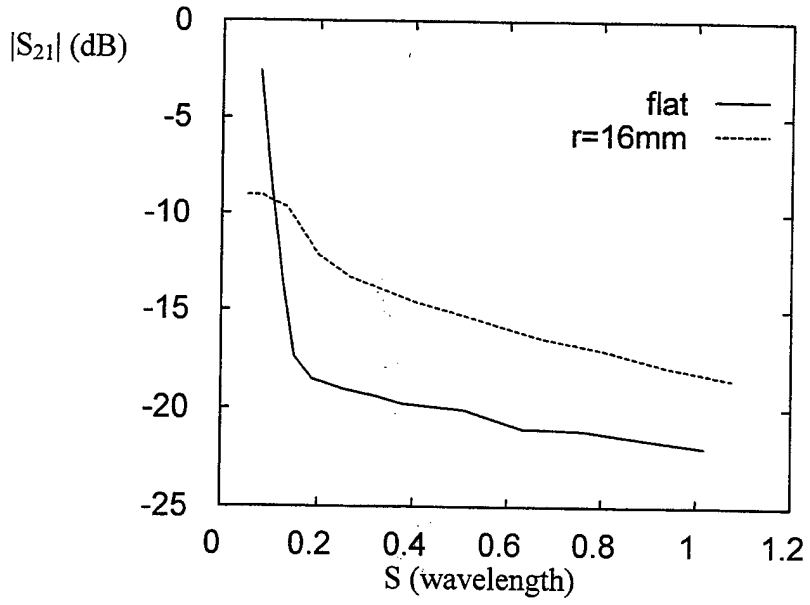

(a)

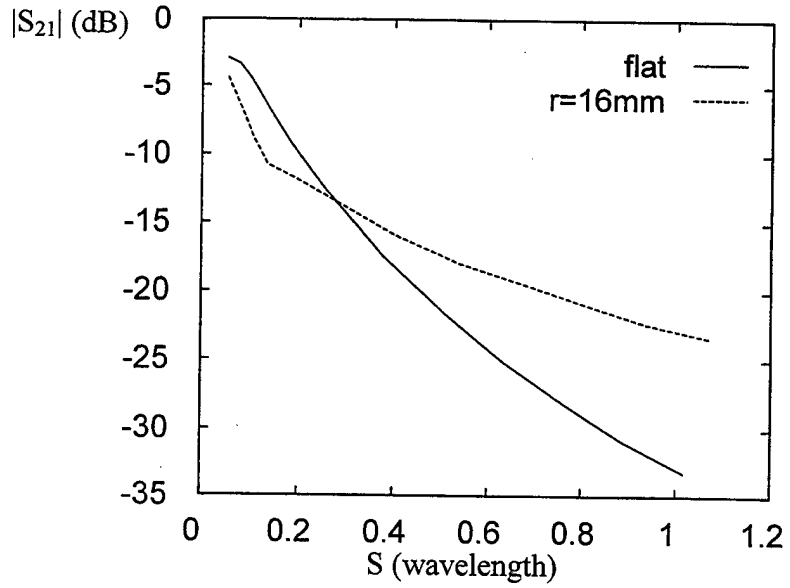

(b)

Fig. 8. (a) E- and (b) H-plane mutual coupling for flat and curved structure with dielectric cover. ε_{r1}=2.2, ε_{r2}=2.2.

V. CONCLUSION

The effect of curvature on the mutual coupling between two rectangular microstrip patch antennas fed by coaxial cable on a cylindrical structure has been calculated by using the CFDTD method. For the comparison, the microstrip patch antennas on a flat substrate structure is analyzed. The CFDTD method has been successfully applied on the curved PEC and dielectric material modeling as well. It has been observed that the mutual coupling level is strongly affected by the different shaped substrate structure. The presented results for the mutual coupling of three different substrate structures are useful for the rigorous analysis of microstrip antenna arrays on conformed substrates in real-world applications. The mutual coupling versus patch separation of H-plane configuration decreases more rapidly than that of E-plane configuration and of flat surfaces were rapidly than of curved surfaces. The mutual coupling analysis for curved substrate using the CFDTD method is compared with the experiment. The mutual coupling with dielectric cover layer shows very similar behavior as that without cover layer not only for flat but also for curved substrate.

The problem associated with this method is the large memory capacity and the long CPU time required for the calculations. The CFDTD method, however, seems to hold great promise for use in CAD systems in conjunction with a mesh generator for other curved surfaces not necessarily cylindrical.

VI. REFERENCES

[1] D. M. Pozar, "Finite Phased Arrays of Rectangular Microstrip Patches," *IEEE Trans. Antenn. Propagat.*, vol. 34, pp. 658-665, May 1986.

[2] A. Mohammadian, N. Martin, and D. Griffin, "A Theoretical and Experimental Study of Mutual Coupling in Microstrip Antenna Arrays," *IEEE Trans. Antenn. Propagat.*, vol. 37, pp. 1217-1223, October 1989.

[3] P. Haddad and D. M. Pozar, "Anomalous Mutual Coupling between Microstrip Antennas," *IEEE Trans. Antenn. Propagat.*, vol. 42, pp. 1545-1549, November 1994.

[4] C. M. Krowne, "Dielectric and Width Effect on H-Plane and E-Plane Coupling Between Rectangular Microstrip Antennas," *IEEE Trans. Antenn. Propagat.*, vol. 31, pp. 39-47, January 1983.

[5] W. Y. Tam, A. K. Y. Lai, and K. M. Luk, "Mutual Coupling between Cylindrical Rectangular Microstrip Antennas," *IEEE Trans. Antenn. Propagat.*, vol. 43, pp. 897-899, August 1995.

[6] A. Bhattacharyya and T. Tralman, "Effects of dielectric superstrate on patch antennas," *Electron. Lett.*, vol. 24, pp. 356-358, 1988.

[7] K. L. Wong, W. S. Chen, and W. L. Huang, "The absortion and coupling of an electromagnetic wave incident on a microstrip circuit with superstrate," *IEEE Trans. Electromagn. Compat.*, vol. 34, pp. 17-22, Feb. 1992.
[8] K. L. Wong, Y. T. Cheng, and J. S. Row, "Resonance in a superstrate-loaded cylindrical-rectangular microstrip sructure," *IEEE Trans. Microwave Theory Tech.*, vol. 41, pp. 814-819, May 1993.
[9] S. D. Gedney, "An anisotropic perfectly matched layer absorbing media for the truncation of FDTD lattices," *IEEE Trans. Antenn. Propagat.*, vol. 44, pp. 1630-1639, 1996.

PATCH ANTENNAS ON PHOTONIC CRYSTAL STRUCTURES

Ramón Gonzalo[+], Beatriz Martínez[+,*], Peter de Maagt[*] and Mario Sorolla[+]
[+]Microwave and Millimeter Wave Group, Universidad Pública de Navarra
Campus Arrosadia, E-31006 Pamplona, Spain
[*]Electromagnetics Division, ESTEC, European Space Agency
Postbox 299, 2200 AG Noordwijk, The Netherlands

Abstract: The microstrip patch is a very popular antenna because it is a low profile antenna, can be non-planar, is easy to manufacture and inexpensive, robust, and can be designed to produce a wide variety of patterns. However, patch antenna designs have some limitations such as restricted bandwidth of operation, low gain and surface wave losses. In order to avoid this effect, a Photonic Band Gap (P.B.G.) structure with a periodic square array of holes is proposed in this paper as a substrate. An analysis of the performance of a patch antenna on a PBG substrate has been carried out. An important reduction in the surface waves has been observed in the simulations, which consequently leads to an improvement of the antenna efficiency and a reduction of side lobe level.

1. Introduction

In this century, control over materials has spread to include their *electrical* properties. Advances in semiconductor physics have allowed to tailor the conducting properties of certain materials, thereby initiating the transistor revolution in electronics. With new alloys and ceramics, scientists have invented high-temperature superconductors and so on.

In the last decade a new frontier has emerged with a similar goal: to control the *optical* properties of materials. If we could engineer materials that prohibit the propagation of light, or allow it only in certain directions at certain frequencies, or localize light in specific areas, our technology would benefit.

Photonic Crystals, also known as *"Photonic Band Gap (PBG) Materials"* are artificial materials that have these properties, and they are the photonic analogues of semiconductors. They represent a new frontier in quantum optics and offer

many new technological applications. Unlike semiconductors, which facilitate the coherent propagation of electrons, PBG materials facilitate the coherent localization of photons.

Although one dimensional photonic crystals have been around for decades in the form of highly reflecting dielectric coatings for mirrors, the idea of making a two or three dimensional photonic crystal is only about 10 years old.

Two parameters, a spatial period (pitch or lattice constant) and the amplitude/ modulation depth of refractive index characterize a periodic structure.

In these periodic structures, electromagnetic mode distributions and their dispersion relations are generally different from those in free space. The concepts of photonic band structures can be easily explained by extending periodicity from one-dimensional space to three dimensions [1, 2, and 3].

Such photonic crystals find their application in patch antennas as substrate for suppression of surface waves excited in the substrate by the radiating element. Suppression or reduction of surface waves is expected to improve antenna efficiency, and to bring a reduction of side lobe level due to diffraction of surface waves at the edges of the antenna substrate [4, 5, 6, 7, 8 and 9].

2. Patch antenna design

There are many configurations to feed microstrip antennas, but the one used in this paper consists of a microstrip line going up to the 50Ω feeding point (see Figure 1). The patch antenna dimensions are 31.98x15.527 mm and the thickness of the substrate ($\varepsilon_r = 10$) is 12mm. With these parameters a working frequency of 1.78 GHz has been obtained (see Figure. 2). The ratio h/λ_0 is 0.07 which leads to an appreciable excitation of surface wave modes [10].

The directivity far field radiation pattern for the antenna is plotted in Figure 3. The effects of surface wave modes can be observed in the radiated power at 90 degrees and in the back radiation where a high contribution of the power coming from the surface wave is obtained. Furthermore, there is an important ripple in the main beam due to the interference of these surface wave modes in the forward direction.

3. PBG design

While the previous section has defined the patch antenna configuration for which the effect of surface mode generation has to be minimized, we now present the design of the photonic band gap substrate. Different kinds of PBG structures can be used as substrates but for simplicity, the proposed structure is a square lattice of air columns embedded in a dielectric medium, see Figure 4 [1, 11]. The dielectric material is again taken as having a dielectric constant ε_r=10.

The direct lattice of a two-dimensional structure, periodic in the x-y plane, is described by two main vectors placed in the same periodic plane. As the two-dimensional photonic crystal is formed by a square lattice, the vectors that define the direct lattice for this lattice can be written as:

$$\begin{aligned} \hat{a}_1 &= a \cdot \hat{x} \\ \hat{a}_2 &= a \cdot \hat{y} \end{aligned} \tag{1}$$

where a is any lattice size, so the structure is defined in normalized units. Another parameter that will be used to define the structure is the r/a ratio, where r is the radius of the column. With the primitive lattice vectors defined, the reciprocal lattice vectors can now be fixed. These vectors are defined as:

$$\begin{aligned} \hat{b}_1 &= \frac{2 \cdot \pi}{a} \hat{y} \\ \hat{b}_2 &= \frac{2 \cdot \pi}{a} \hat{x} \end{aligned} \tag{2}$$

The irreducible Brillouin zone for this case is defined by three special points called Γ, X and M which are corresponded respectively to $k_{\parallel} = 0$, $k_{\parallel} = \frac{\pi}{a}\hat{x}$, $k_{\parallel} = \frac{\pi}{a}\hat{x} + \frac{\pi}{a}\hat{y}$ which describe it completely. Sweeping over this zone, all directions in the k-space of the propagating incident waves will have been taken into account fully characterizing the dispersion relation for the photonic crystal.

With these definitions, the so-called "gap map" [1] for the structure was obtained by fixing the dielectric constant and sweeping the *r/a* ratio. The gap map then allows us to choose the *r/a* value to maximize the available photonic band gap for the desired frequency of operation. Figure 5 shows the TE and TM polarization

gap maps with a dielectric constant of 10. Along the horizontal axis of the gap map is the *r/a* ratio of the columns; along the vertical axis is the normalized frequency $(f \cdot a/c)$.

Using these maps and taking a working frequency of 1.8 GHz, the lattice size (*a*) can be obtained. There are different possibilities, but the selection criteria will be governed by minimizing the total device size. The only surface mode in propagation is the TM_0, so one only has to consider the TM polarization map. With these two premises, the selected *r/a* value was 0.48 together with a normalized frequency 0.27, giving a lattice period of 44.6 mm. This means that the radius value was fixed to 21.4 mm.

4. PBG antenna

The selected PBG structure was a square lattice of air holes (see Figure 1). Following the description given in 3, the distance obtained between holes is 44.6 mm and the radius of the holes 21.4 mm. The input return loss for this antenna is shown in figure 2. The working frequency is 1.81 GHz. A small frequency shift is observed in relation to the conventional patch antenna, due to the variation of the relative dielectric constant around the antenna.

Figure 2 already shows an improvement in the input return loss. An increase in the bandwidth, from 1.6 % for the conventional case to 3 % for the PBG antenna, is obtained.

Figure 6 shows the directivity far field radiation obtained for the PBG antenna. A reduction in the back radiation as well as in the radiation at 90 degrees is obtained for all cuts. The radiation pattern in the H-plane appears without ripple demonstrating again the reduced levels of surface wave modes. The other cuts present a small ripple, which can be attributed to radiation from the feeding line. Using other kinds of feeding techniques may overcome this effect.

Finally, looking at the normalization directivity values for each radiation pattern, a directivity improvement in the forward direction of 3.5 dB is obtained.

5. Conclusion

The proposed PBG structure appears to be a promising solution to avoid surface wave modes in patch antenna configurations. Improvements in input return loss, directivity, bandwidth and radiation patterns have been reported. Future

applications in array configuration are under study to improve the antenna efficiency and the reduction of the mutual coupling.

6. References

[1] Joannopoulus,J., Meade, R., Winn, J., "Photonic Crystals. Molding the Flow of Light". Princeton University Press. 1995.

[2] Yablonovitch, E., "Photonic Crystals", *Journal of Modern Optics*, 1994, Vol. 41, No 2, 173-194.

[3] Russel, P., "Photonic band gaps". *Physics World*, August 1992.

[4] Brown, E.R., Parker, C. D., Yasblonovitch, E., "Radiation Properties of a planar antenna on a photonic-crystal substrate", *J. Opt. Soc. Am. B*, Vol. 10, No. 2, February 1993.

[5] Cheng, S. D. et al., "Optimized dipole antennas on photonic band gap crystals", *Appl. Phys. Lett.* 67 (23), 4 December 1995.

[6] Kesler, M. P. et al., "Antenna Design With the Use of Photonic Band-Gap Materials as All-Dielectric Planar Reflectors", *Microwave and Optical Technology Letters*, Vol. 11, No. 4, March 1996.

[7] Sigalas, M. M., Biswas, R., and Ho, K., "Theoretical Study of Dipole Antennas on Photonic Band-Gap Materials", *Microwave and Optical Technology Letters*, Vol 13, No. 4, November 1996.

[8] Qian Y. et al., "A microstrip patch antenna using novel Photonic Band-Gap Structures", *Microwave Journal*, January 1999.

[9] R. Gonzalo, P. De Maagt and M. Sorolla, "Enhanced Patch Antenna Performance by Suppressing Surface Waves using Photonic Band-Gap substrates", IEEE-MTT, Special Issue, to be published in October 1999.

[10] J. R. James and A. Henderson. "High-Frequency behavior of microstrip open-circuit terminations". *IEE J. Microwaves, Optics and Acoustics*, Vol. 3, pp. 205-218. 1979.

[11] R. Gonzalo. "Modelling of Photonic Band Gap Structure". ESTEC Working paper 2008. December 1998.

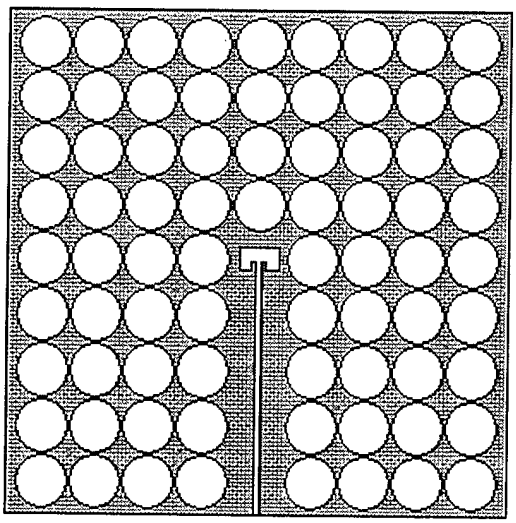

Figure 1: Schematic for PBG antenna design.

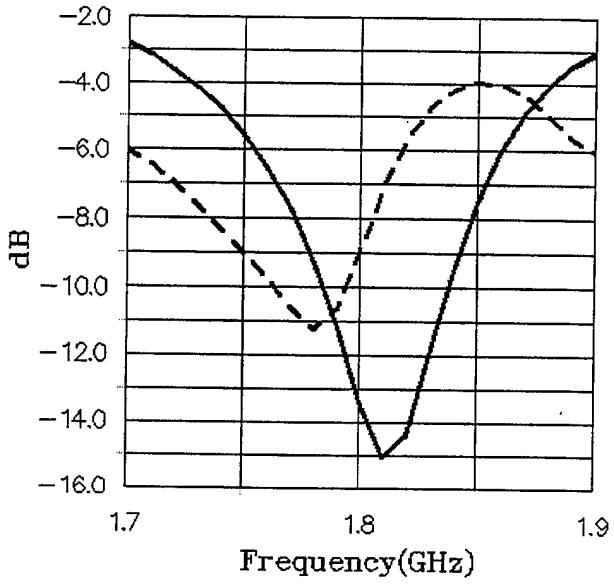

Figure 2: Input return loss (S11) for the conventional patch antenna (dashed line) and for the PBG antenna (solid line).

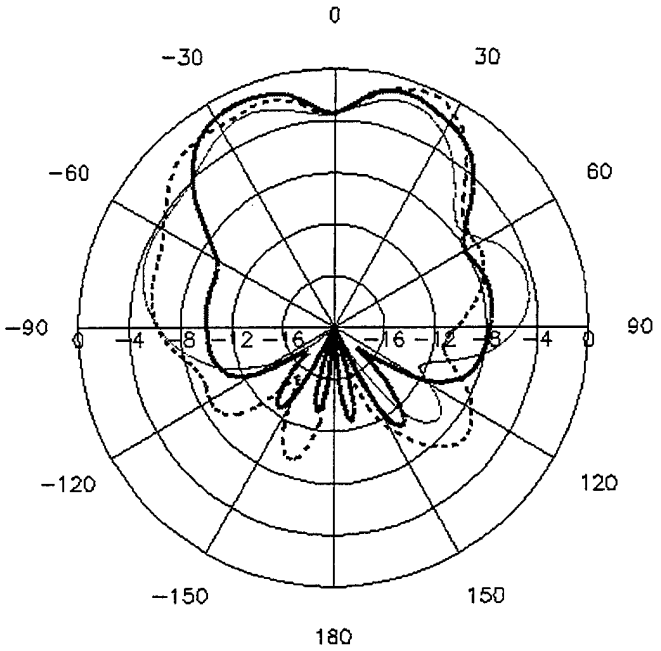

Figure 3: Directivity far field radiation pattern for the conventional patch antenna. The thick black line is the H-plane cut, the smooth line is the 45 degrees plane and the dashed line is the E-plane cut.

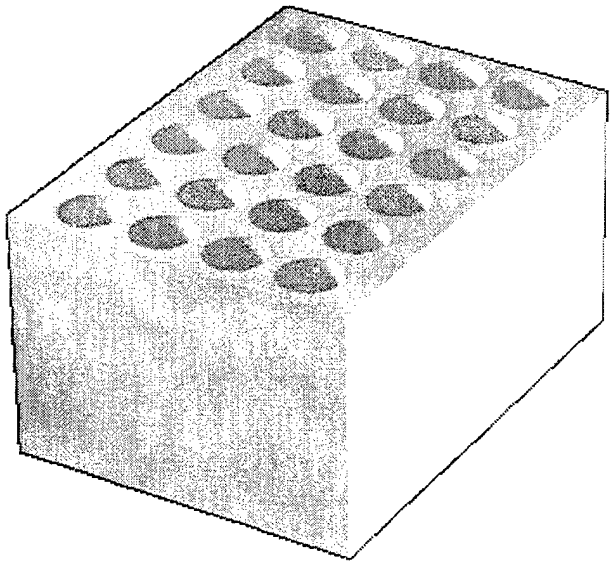

Figure 4: Two-dimensional photonic Crystal formed by a square array of air columns embedded in a dielectric medium.

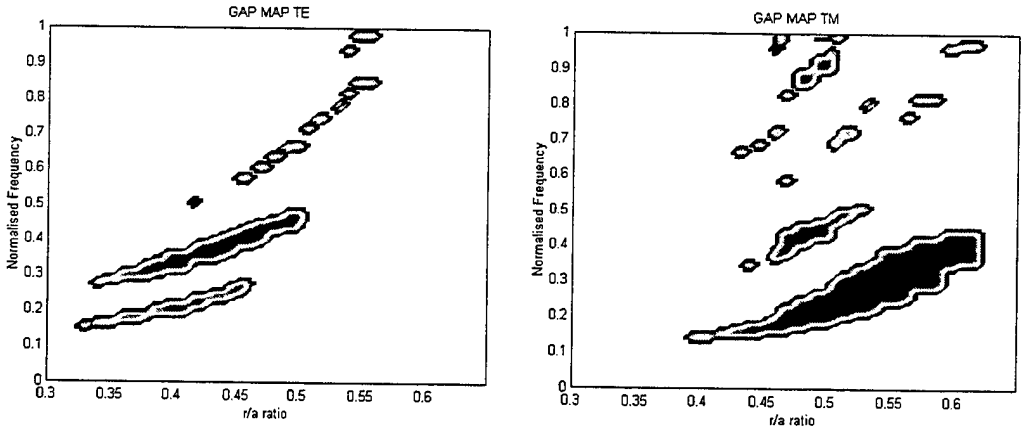

Figure 5: Gap Map for TE (left side) and TM (right side) polarizations in the case of air columns in a dielectric substrate with $\varepsilon_r = 10$.

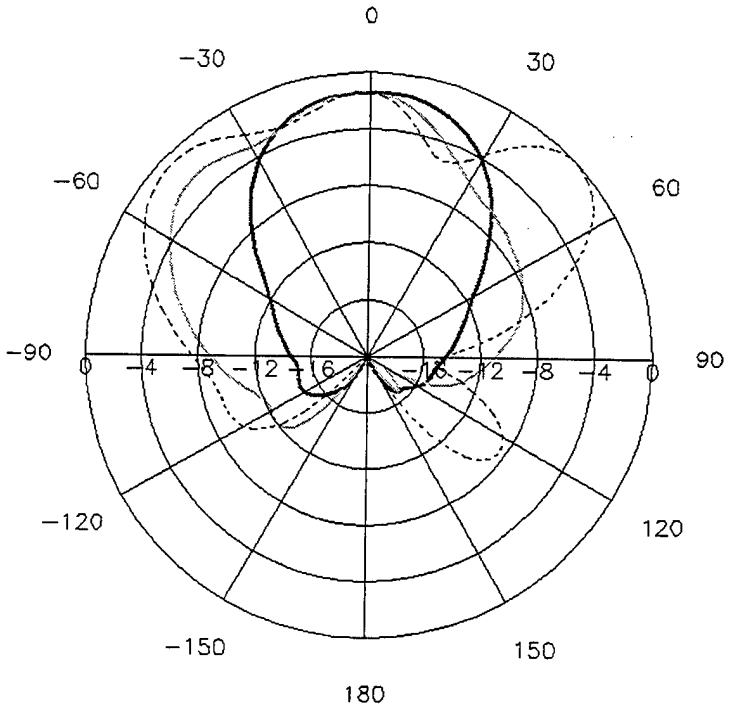

Figure 6: Directivity far field radiation pattern for the PBG patch antenna. The thick black line is the H-plane cut, the smooth line is the 45 degrees plane and the dashed line is the E-plane cut.

MEMS-SWITCHED RECONFIGURABLE MULTI-BAND ANTENNA: DESIGN AND MODELING

William H. Weedon and William J. Payne
Applied Radar, Inc. 14 Union Street, Watertown, MA 02472

Gabriel M. Rebeiz
Radiation Laboratory, University of Michigan, Ann Arbor, MI 48109

Jeff S. Herd and Michelle Champion
Air Force Research Laboratory, 31 Grenier St., Hanscom AFB, MA 01731

Abstract – Reconfigurable multi-band antennas are attractive for many military and commercial applications where it is desirable to have a single antenna that can be dynamically reconfigured to transmit and/or receive on multiple frequency bands. Such common-aperture antennas find applications in space-based radar, unmanned aerial vehicles (UAVs), communication satellites, electronic intelligence aircraft and many other communications and sensing applications. The reconfigurable antenna can be envisioned as an array of microstrip patch elements that are resonant at the highest operation frequency f_{max}, that can be connected together using switches to form groups of elements that are resonant at several lower frequencies f_{max}/α_i, where α_i, i= 1,2,...,N are scale factors related to the element groupings. It is easy to envision that an array that can be reconfigured to operate over a relative bandwidth of 100:1 would require hundreds and perhaps thousands of switches. Hence, a critical component of the reconfigurable antenna is the switches or relays used to interconnect the patch elements. Moreover, the efficiency (insertion loss) and effectiveness (isolation) of the switches will dictate the overall performance of the reconfigurable antenna array. One type of switch that has received a lot of attention recently as a candidate for reconfigurable antennas is the micro-electromechanical system (MEMS) switch. In this paper, we present design and modeling details for a prototype reconfigurable muli-band antenna using MEMS switches. A general adaptive reconfigurable (GARF) feed methodology is employed to allow various antenna configurations to have independent feed structures, and hence be tuned independently. We present computer simulations and measurement results for a small reconfigurable patch module (RPM) that may be used as a building block for a larger array in a tile architecture.

1. Introduction

Antennas for many airborne vehicles such as UAV's, satellites and ELINT aircraft are required to satisfy a diverse range of requirements imposed by radar and communications systems in order to maximize the effectiveness of the aerial platform. It is highly desirable to have a single antenna that could be automatically reconfigured [1-16] to satisfy the frequency band and gain requirements of different applications. In this manner, several communications and remote sensing systems could utilize a common antenna aperture, resulting in considerable savings in size, weight and cost.

A typical example is in a space-based radar scenario, one may want to have a satellite antenna that can be dynamically reconfigured to provide SAR at X-band, communications at L-band, and AMTI radar at S-band. Another example is the Global Hawk UAV, where it would be desirable to have a single antenna aperture that could be reconfigured to provide communications from VHF to K-band, foliage penetration (FOPEN) radar from VHF to L-band, and SAR at X-band. There are many applications in both the military and commercial arenas where it would be desirable to combine the functionality of a number of antennas.

A key enabling technology for the successful development of reconfigurable multi-band antennas is the development of switches with low-loss, high-isolation and low bias power requirements. Below approximately 1 GHz, PIN diodes [11-12] are extremely efficient and are suitable switching elements. Above 1 GHz, various photonic switches have been proposed for microwave antenna applications [5-7,13-14], but have met limited success for one reason or another. Recently micro-electromechanical system (MEMS) switches have been receiving a lot of attention [1,2,15-16] as potential antenna switching elements.

MEMS switches have several characteristics that are attractive for reconfigurable antenna development. Among these are their inherent wide bandwidth, low insertion loss (~0.2 dB), and low bias current in both the ON and OFF states. The low bias current is due to the fact that the switch operates using electrostatic force. A voltage excitation is required to actuate the switch, but once actuated, the switches hold their ON/OFF state with very little bias power. Hence, these switches can be very efficient. Another advantage is that the MEMS devices are being manufactured using silicon IC batch-processing techniques, thereby leveraging previous investments in processing facilities.

While conceptually simple, the development of a reconfigurable phased-array antenna spanning several decades of frequency bandwidth poses several design

challenges. The first design decision is the choice of the antenna elements themselves. It is anticipated that some type of an antenna patch element would be used, due to their low profile and the fact that they can be fabricated easily using PC board techniques. The design of patch radiating elements for a given board material and thickness is fairly standard [17-19]. The real challenge is developing interconnection and feed structures to connect the antenna elements, switches, and phase shift elements together in such a way that the antenna may be reconfigured to meet the needs of various applications.

Another difficulty in developing multi-band antennas with wide separation between bands is achieving a large instantaneous bandwidth in each band, particularly at the low frequency band of operation. The element to ground-plane separation imposes a bandwidth limit at the lowest frequency band due to the close proximity of the element to the ground plane. When the elements are grouped together at low frequency to form an "effective patch" consisting of a grid of smaller elements there is an additional "element fill factor" that tends to limit bandwidth. At the upper frequency band of operation, surface waves are the limiting factor.

A general adaptive reconfigurable feed (GARF) methodology is proposed for designing reconfigurable multi-band antennas such that the feeds for the various configurations may be designed and tuned independently. A reconfigurable patch module (RPM) is proposed to be used as a building block for a larger array in a tile architecture. We present design, simulations and measurement results for a dual-mode RPM capable of operating at both S-band and X-band.

2. Background on MEMS Switches

An excellent review article on RF-MEMS devices is presented by Brown [1]. Essentially, the MEMS switch is a micromachined device consisting of a membrane or strip of metal suspended over an electrode. Activation of the switch is caused by an electrostatic field induced by an applied voltage. The main advantage of these devices is that once the switch is activated, there is almost no power required to hold the switch in the activated state. Hence, the MEMS switch is an extremely efficient device.

Current MEMS Switch designs employ one of three mechanical configurations: either the cantilever, air-bridge or diaphram [1]. The cantilever switch, illustrated in Figure 1, consists of a thin strip of metal and dielectric fixed at one end and suspended over an air gap. The air-bridge, illustrated in Figure 2, is a metal/dielectric strip that is fixed at both ends and suspended over an air gap in

the middle. The diaphram consists of a metal/dielectric membrane fixed around the edges and suspended over an air gap in the middle. The circuit configurations used by the MEMS switches can be either series or parallel. Contacts are either resistive (metal-metal) or capacitive (metal-insulator-metal).

Several MEMS switches have been investigated to date with varying degrees of success. Two of the more successful approaches [1] are 1) the cantilever switch with a series-connected metal-metal contact, similar to Figure 1; and 2) the air-bridge switch similar to Figure 2 with a parallel-connected metal-insulator-metal contact. Other mechanical configurations such as diaphrams have not been successful [1].

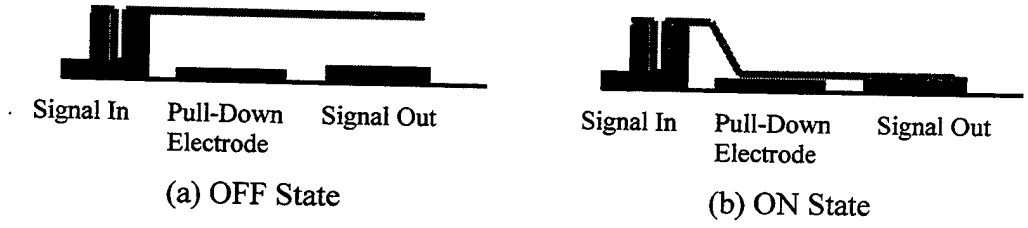

Figure 1: Illustration of cantilever MEMS switch.

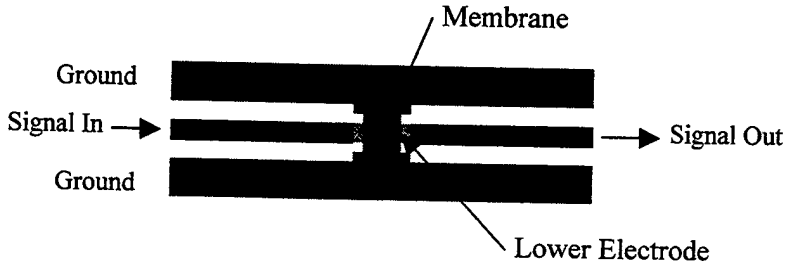

Figure 2: Illustration of air-bridge MEMS switch.

2.1 Series-Connected Cantilever Switch

Series-connected cantilever MEMS switch designs have been developed independently by both Hughes Research Lab., Malibu, CA and Rockwell Science Center, Thousand Oaks, CA. The operating principle is that electrostatic force created by an induced voltage is used to move a cantilever that series-connects the RF circuit. Both the Hughes and Rockwell switches have proven successful in achieving low insertion loss on the order of 0.2 dB from DC to 40 GHz in the ON

state and high isolation on the order of 30 dB DC – 15 GHz and 20 dB 15 GHz – 40 GHz in the OFF state. Both of these switches appear to be well-suited for reconfigurable antenna applications.

2.2 Parallel-Connected Air-Bridge

Another successful MEMS switch is the parallel-connected air-bridge switch. This switch was developed by Raytheon/TI, Dallas, TX. This switch utilizes a metal-insulator-metal bridge that in the ON state loads the center contact with a small capacitance (high impedance), and in the OFF state, shorts the center contact to ground with a high capacitance (low impedance). The insertion loss with the parallel air-bridge in the ON state is about 0.3 dB from DC – 40 GHz, comparable to the series cantilever. The isolation in the OFF state, however, is rather poor for frequencies below 15 GHz. The OFF-state isolation shows a linear trend: 30 dB at 35 GHz, 20 dB at 15 GHz, 10 dB at 5 GHz, etc. This poor isolation at low frequency is due to the fact that the switch capacitance *Cs* shunts the characteristic impedance Zo of the transmission line. The isolation *ISO* can be determined from circuit theory as [1]

$$ISO = 10 \log_{10} [1+(\omega Zo\, Cs)^2].$$

Hence, as $\omega \rightarrow 0$, $ISO \rightarrow 0$ dB.

Because of the inherent poor isolation of the parallel-connected air-bridge switches, we would expect that the series-connected cantilever switches would be more useful for reconfigurable antennas that operate below 15 GHz.

MEMS switches have several inherent limitations. The first limitation is switching speed, which is typically several microseconds [1,2]. This should not be a severe limitation, however, and would allow sufficient time for the antenna to be reconfigured for various communication and radar functions. A second problem with MEMS switches is mechanical "stiction" [1]. Since the MEMS device is mechanical in nature, the device parts can sometimes become bonded together upon physical contact. MEMS researchers are currently working vigorously to solve the stiction problem.

3. Reconfigurable Patch Module (RPM) Concepts

We now develop concepts for the reconfigurable patch modules (RPMs) that are essentially the building-blocks, or sub-array elements, in a reconfigurable antenna. The RPM utilizes one or more patch antenna elements in combination with MEMS switches to allow multi-frequency reconfiguration. Essentially, the

RPM is the fundamental building block in our reconfigurable antenna tile architecture.

We restrict our attention to microstrip patch antenna elements due to their low profile, low cost, low weight, and ease of fabrication. The antenna elements with potential for consideration are:

- Rectangular Patch
- Rectangular Resonant Patch Stack
- Printed Circuit Dipole

The primary difference between the rectangular patch and the resonant patch stack is that the resonant patch stack has a broader bandwidth.

We could consider more "coarse-grain" elements with inherent broadband characteristics such as spiral antennas and linear log-periodic elements. However, we prefer to use the "fine-grain" microstrip patch elements because there is a greater degree of flexibility in terms of configuring the array for multi-frequency and phased-array applications using fine-grain elements. Another reason for not selecting spiral elements is that spiral antennas are inherently circularly polarized, whereas linear polarization is normally used for SAR.

The design of microstrip patch elements is rather straightforward, and can be found in many texts [17-19]. The design of a reconfigurable multi-band antenna, however, involves the combination of patch elements and MEMS switches in such a way that the antenna can be reconfigured to adapt to different frequency bands. Precisely how to connect these elements together such that the module has the desired frequency bandwidth, impedance, and radiation characteristics is the problem under consideration.

Figures 3–5 illustrate possible configurations of the antenna elements in the RPMs. Figure 3 [3–5] shows a printed dipole RPM, consisting of dipole segments series-connected with MEMS switches. By symmetrically switching in dipole segments on either side of the generator, the dipole resonant frequency is changed by a scale factor.

In Figure 4 [6], a single rectangular patch is series connected with a MEMS switch to another patch segment to tune the patch. The concept of tuning a single patch with additional patch segments could be extended to include several patch segments, and hence be reconfigured for a wide range of frequency bands.

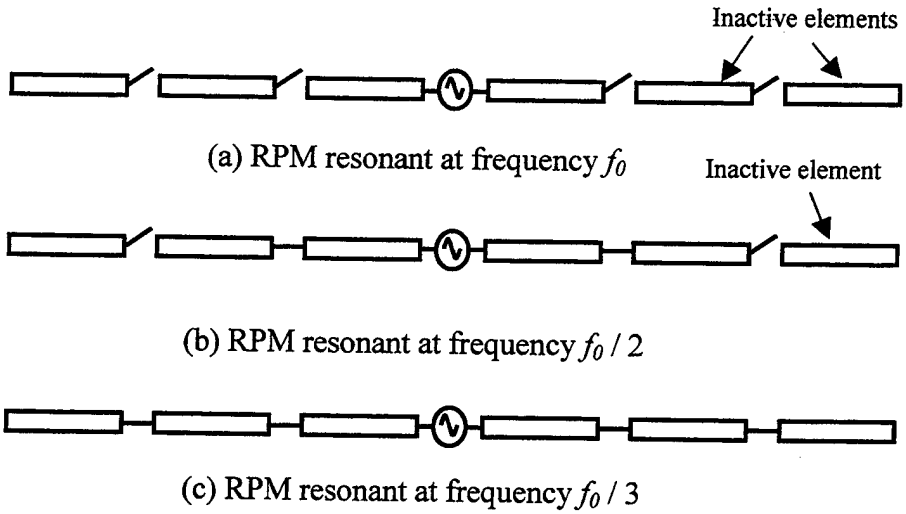

Figure 3: Printed dipole reconfigurable patch module (RPM). Printed circuit dipole segments are connected by series MEMS switches. Closed MEMS switches are indicated by solid lines connecting dipole segments. Dipole is fed by a generator at the center.

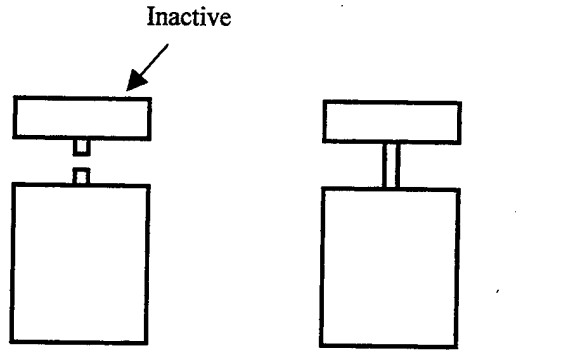

Figure 4: Single rectangular patch reconfigurable patch module (RPM). (a) RPM resonant at frequency f_0; (b) RPM resonant at frequency f_0 / p where p is a scale factor. RPM consists of two rectangular microstrip patch elements of different size connected by a transmission line and series MEMS switch.

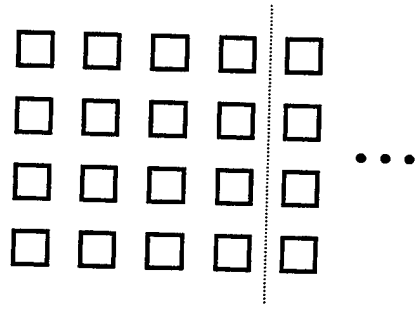

(a) RPM resonant at frequency f_0. All patch elements are active.

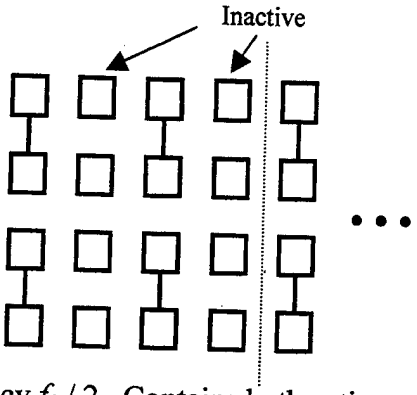

(b) RPM resonant at frequency $f_0 / 2$. Contains both active and inactive elements.

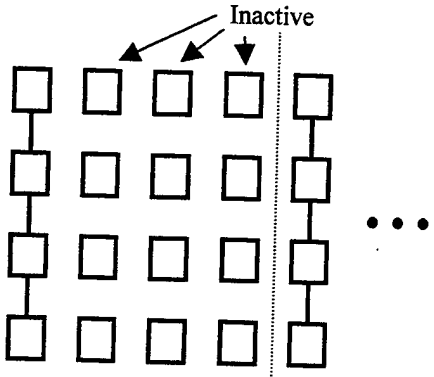

(c) RPM resonant at frequency $f_0 / 4$. Contains both active and inactive elements.

Figure 5: 4×4 Microstrip patch reconfigurable patch module (RPM). All antenna patch elements are assumed to be connected with MEMS switches. Solid line between elements indicates a closed switch, no line indicates an open switch. Dashed line separates the RPM modules.

Figure 5 illiustrates a 4×4 element microstrip patch RPM [1]. This RPM uses a symmetric 4×4 array of patch elements, where each patch is series-connected to each adjacent patch in the vertical direction with an MEMS switch. With all of the switches open, the array is resonant at frequency f_0. When two elements are connected together as in Figure 4(b), with a column of inactive elements separating each pair on connected elements, the array is vertically polarized and resonant at frequency $f_0 / 2$. Similarly, if four elements are connected together as in Figure 4(c), with three rows of inactive elements separating each row of active elements, the result is a vertically polarized array resonant at frequency $f_0 / 4$. Note that the second row of active elements would actually be located on an adjacent RPM in a tile architecture.

The RPM configurations considered in Figures 3–5 each have inactive elements in certain configurations. For example, in Figure 3(a) there are four inactive dipole segments when the dipole is resonant at frequency f_0. In figure 4(a), the patch segment is disconnected from the main patch element, and is hence inactive. In Figure 5 (b) and (c), the 4×4 patch array has columns of inactive patch elements when the array is resonant at frequency $f_0 / 2$ and $f_0 / 4$, respectively.

The examples considered in Figures 3–5 illustrate possible configurations or conceptual starting points for RPM design. Each of these designs has its own merits and advantages and disadvantages. The square or rectangular microstrip element array appears at first to be the most general and attractive configuration. However, practical design experience has shown that there are certain limitations of this approach. For example, it is difficult to obtain a large bandwidth at the low frequency band due to the height of the element above the ground plane. Another limitation is that the rectangular patch configuration is somewhat limited in the selection of frequency band due to the discrete number of patches and finite element separation. The segmented patch concept illustrated in Figure 4 may be conbined with a rectangular patch array to allow fine-tuning of the frequency band center frequency. Dipole patch arrays may offer some additional benefits as well.

4. General Adaptive Reconfigurable Feed (GARF) Methodology

Once the antenna elements themselves are chosen and designed, the RPM is not complete unless we have a method of feeding the elements with the appropriate excitation amplitude and phase in the various configurations. In addition, impedance matching must be done in order to minimize reflection loss. The design of corporate feed structures for microstrip patch arrays is straightforward [17–20]. What complicates the design is that either the same feed mechanism

must work for all array configurations, or the feed mechanism must adapt as the array is reconfigured.

Although it is possible conceptually, it is not likely that the same feed structure will be used for all array configurations. In a simple, canonical design, it is conceivable to get away with a single corporate feed. But practical design experience dictates that feed linewidths and lengths will need to be tuned in order to maximize the performance of the antenna. The likelihood that this tuning, or impedance matching, will be valid for all array configurations in a more complicated design is very small.

A more general feed design is to use an approach whereby multiple feed transmission lines are run in parallel beneath the active antenna elements. Vias are placed at selected points to bring the appropriate feed line to the appropriate microstrip patch element at the surface in the proper feed location. MEMS switches are placed directly on the patch elements themselves to connect the patch element feed points (typically somewhere on the interior of the patch elements, about 1/3 from the edge for a rectangular patch) to the feed vias. This arrangement is illustrated in Figure 6. We call this new method of feeding the antenna elements the general adaptive reconfigurable feed (GARF).

A second advantage to using the GARF approach is that it allows for a method of properly terminating unused elements in the array. That is, in addition to the parallel feed transmission lines beneath the antenna element plane, we could have several termination lines connected with various load termination impedances. As the array is reconfigured, MEMS switches will connect the unused antenna elements to vias that lead to the appropriate termination line as illustrated in Figure 7.

The GARF method conceptually provides a method of feeding the RPMs and array elements in such a way that the feed mechanism is adaptive. Each array configuration has its own feed transmission line that may be individually tuned for optimal performance. It also allows a mechanism for properly terminating unused array elements in the various configurations.

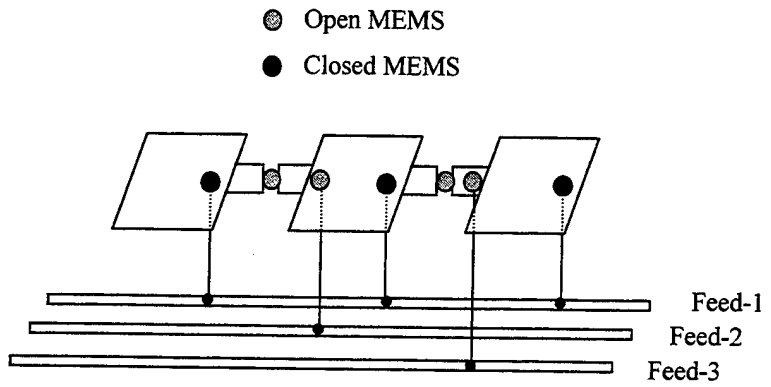

(a) RPM resonant at frequency f_0. Patches fed via Feed-1.

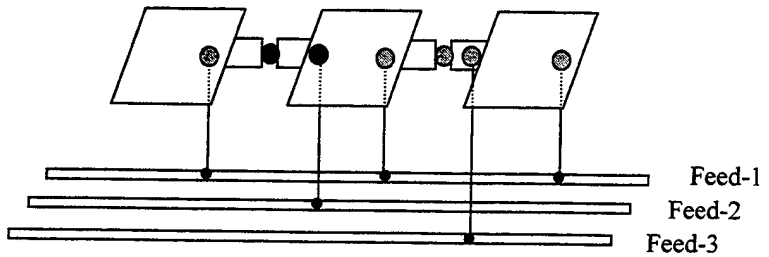

(b) RPM resonant at frequency $f_0 / 2$. Patches fed via Feed-2.

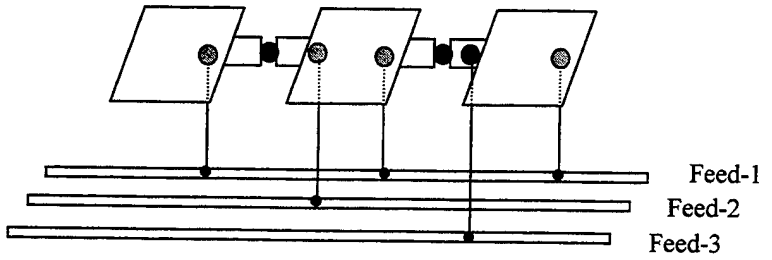

(c) RPM resonant at frequency $f_0 / 3$. Patches fed via Feed-3.

Figure 6: Illustration of General Adaptive Reconfigurable Feed (GARF) design for feeding multi-frequency reconfigurable antennas. Design allows each array configuration to be fed independently, simplifying impedance matching procedure.

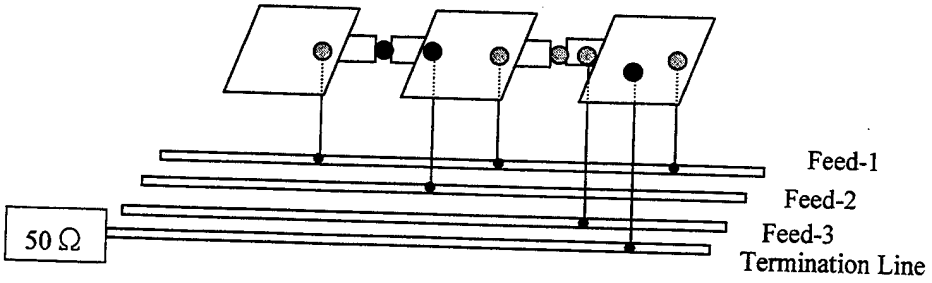

Figure 7: Illustration of General Adaptive Reconfigurable Feed (GARF) design for terminating unused elements in multi-frequency reconfigurable antennas.

5. Design, Simulation and Measurement Results

A prototype RPM was developed to operate at two distinct and widely-separated frequency bands. Our design goal was to develop and antenna that resonated at roughly 2 GHz (S-band) and 10 GHz (X-band). A square microstrip element resonating at 10 GHz was chosen as the basic antenna element. The 10 GHz patch elements were then connected together using thin microstrip lines to form the 2 GHz "effective element". Since MEMS switches were not available at this early stage, a microstrip line with or without a small gap was used to represent an OPEN or CLOSED switch.

Rogers RT/duroid 5880 material (ε_r=2.2, tanδ=.0009) was chosen as the substrate due to its low dielectric constant and loss tangent. Two substrate thicknesses were investigated: .062" and .125". Computer simulations were utilized to compute the input impedance, return loss and radiation patterns of the antenna. Several prototypes were built and tested using the .062" substrate. The .125" dielectric is currently on back-order. Therefore, measurement results are presented only for the .062" substrate.

Our initial design philosophy was to start with a square patch element on the .062" substrate, where the patch dimensions were designed to resonate at roughly 10 GHz. The patch elements were probe-fed from the bottom. The initial probe location was determined approximately using a cavity model. A more accurate computer simulation was then performed using HFSS.

5.1 Results for .062" substrate

We began by designing a single patch resonant at 10 GHz (X-band). A square patch was used with dimension .364" square on the .062" substrate. The patch was probe-fed from the bottom. The probe position was initially determined using a cavity model, then fine-tuned with HFSS. The optimized probe position was .062" from the center of the patch. Figures 8–10 show the HFSS and measured impedance, return loss and radiation patterns for the single patch. Note that there is a slight difference between the simulation and measured center frequency (9.38 GHz vs. 9.82 GHz). We believe that the simulation is limited in its ability to accurately model the resonance frequency. The measured bandwidth is 4.28% versus 4.7% for the simulation. The phase rotation between the simulation and measured smith-chart impedance is due to the electrical length of the probe feed. There was no attempt to optimize the center of the resonance frequency, since this could be trivially done by adjusting the size of the patch.

Figures 11-13 show similar simulation and measurement results for an open 3x1 patch array. In Figure 11(a), we see that the array consists of three patches identical to the single patch discussed above. The feed location is the same. Note that there are now .040" lines extending from each patch with an .050" gap to simulate an OPEN MEMS switch. The simulated and measured center frequency for the antennas are 8.48 GHz and 8.955 GHz. Note that there is a significant drop in both the simulated and measured center frequency, due to the addition of the .040" open transmission lines, which detune the patches. Again, the simulation underestimates the resonance frequency. The measured bandwidth of 4.13% was actually larger than the simulated value of 3.5%. This could be due to the higher center frequency for the measured data and the error due to the discrete simulated frequency step size.

Figures 14 and 15 show simulated and measured data for the closed 3x1 array. No radiation patterns were measured for this antenna due to the low frequency limit of the anechoic chamber. In Figure 14(a), we see that the .050" gap in the .040" transmission lines connecting the patches is now removed, simulating a CLOSED MEMS switch. The simulated and measured center frequencies are 1.905 GHz and 1.8527 GHz. Here, the simulation overestimates the resonance frequency. The simulated and measured bandwidths are 0.2% and 0.05%. These bandwidths are not acceptable for most applications, and would need to be increased. Part of the reason for this low bandwidth is that we constrained the OPEN and CLOSED feed locations to be the same. Note in Figure 15(a) that there is not a good impedance match for the CLOSED antenna. The simulated impedance match in Figure 14(b) is not a bad match, however.

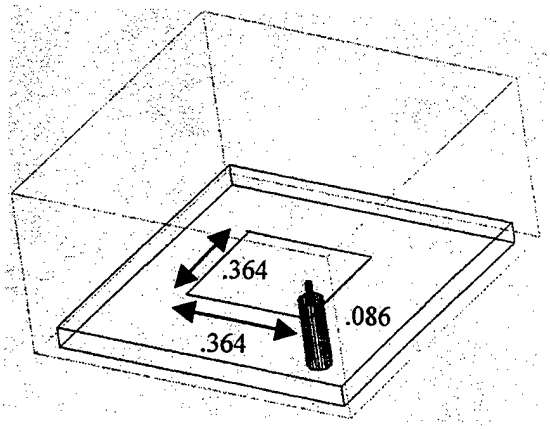

(a) Simulation Layout

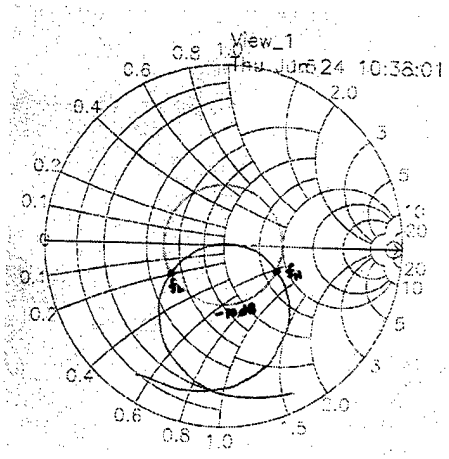

(b) Input Impedance

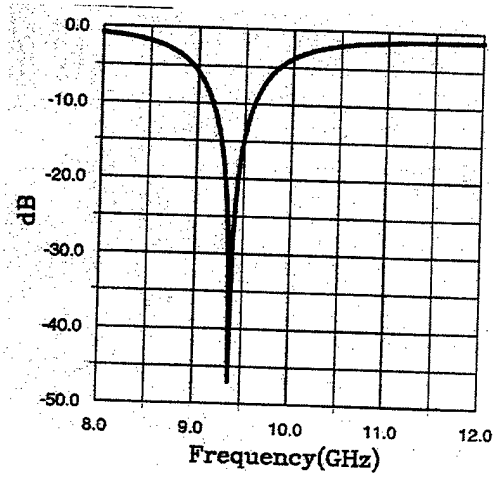

(c) Return Loss

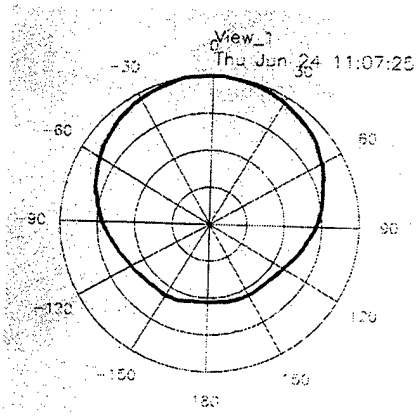

(d) Radiation Pattern

Figure 8: Simulation results for a single X-band patch. Bandwidth: f_L= 9.16 GHz; f_H= 9.60 GHz; BW= 4.7%.

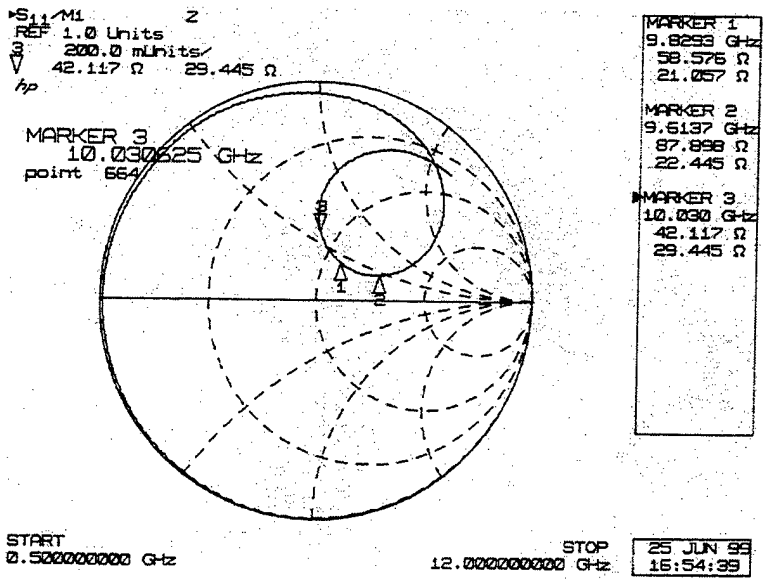

(a) Input Impedance

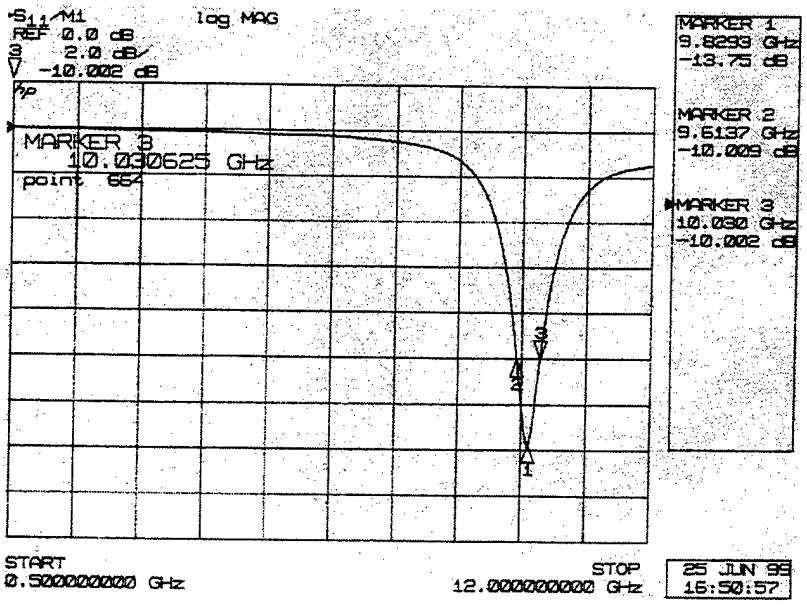

(b) Return Loss

Figure 9: Measured impedance and return loss for a single X-band patch. Bandwidth: f_L= 9.61 GHz; f_H= 10.03 GHz; BW= 4.28%

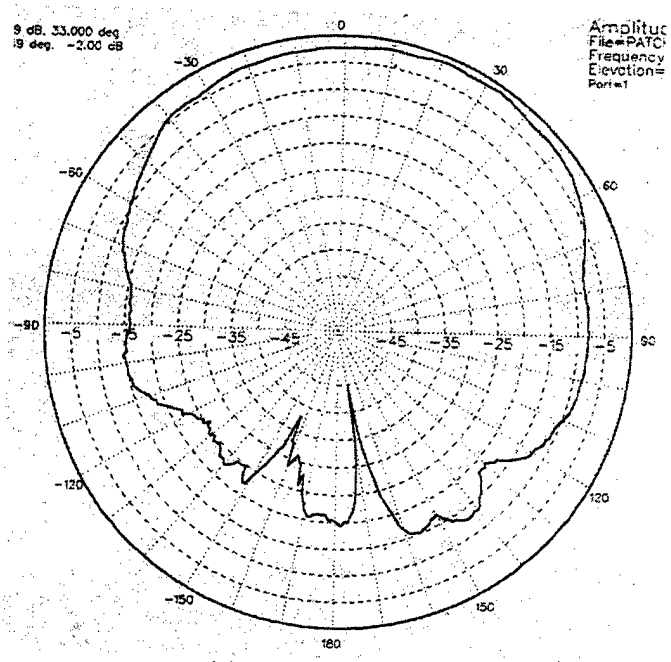

(a) E-Plane Pattern

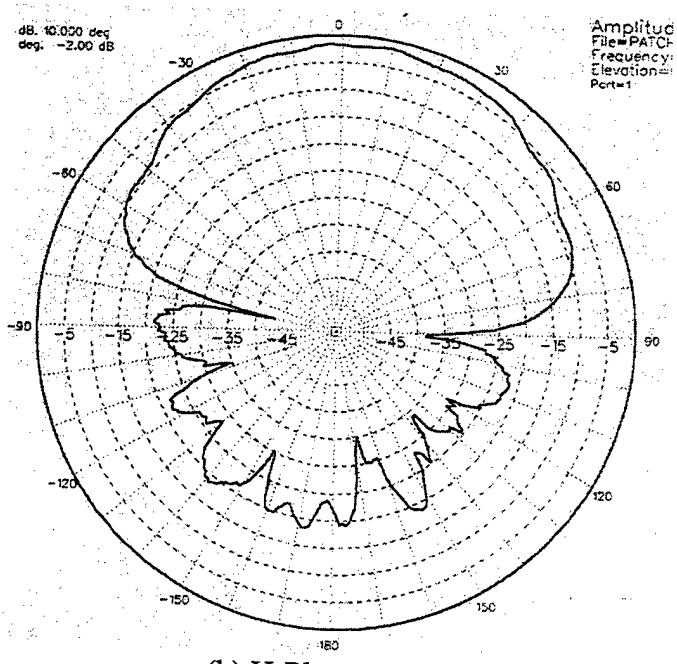

(b) H-Plane Pattern

Figure 10: Measured radiation patterns for single X-band patch. Amplitude is normalized to near 0dB at boresight.

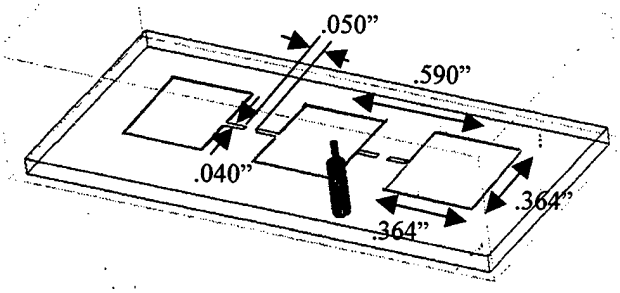

(a) Simulation Layout

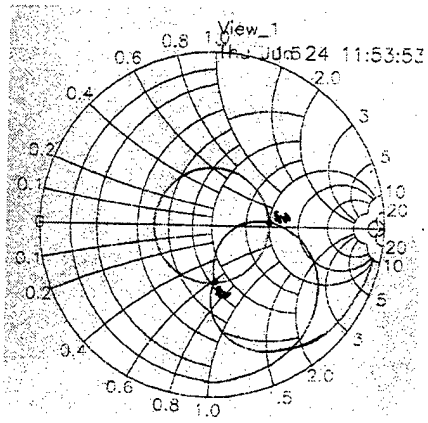

(b) Input Impedance

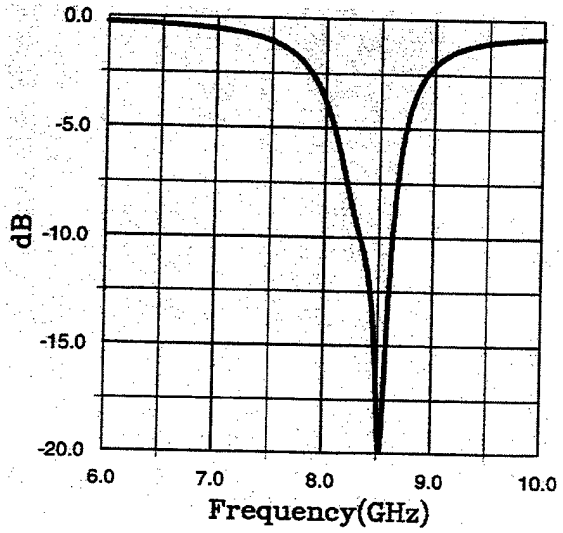

(c) Return Loss

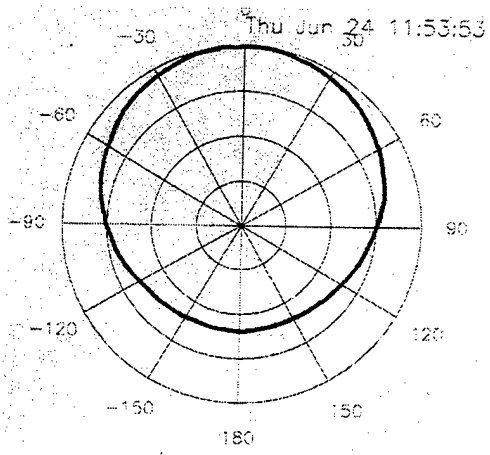

(d) Radiation Pattern

Figure 11: Simulation results for an open 3x1 patch array resonant at X-band. Bandwidth: f_L= 8.33 GHz; f_H= 8.63 GHz; BW= 3.5%.

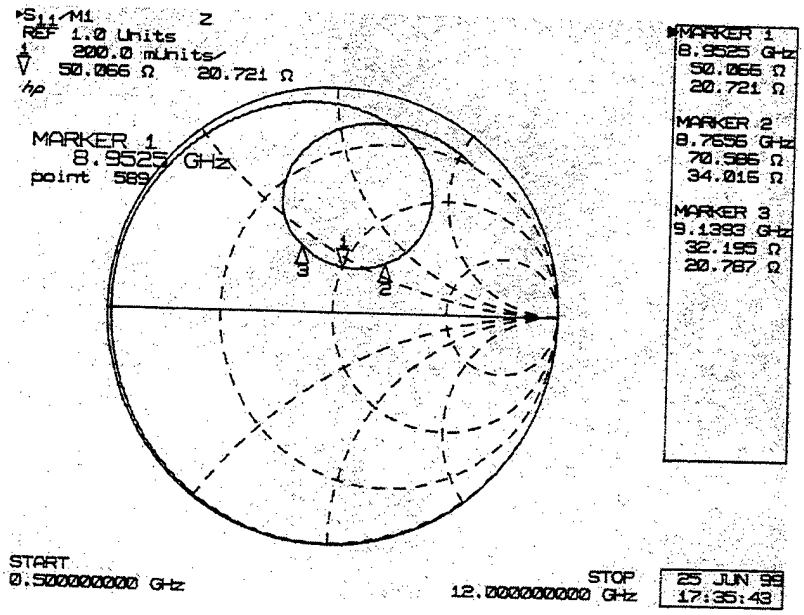

(a) Input Impedance

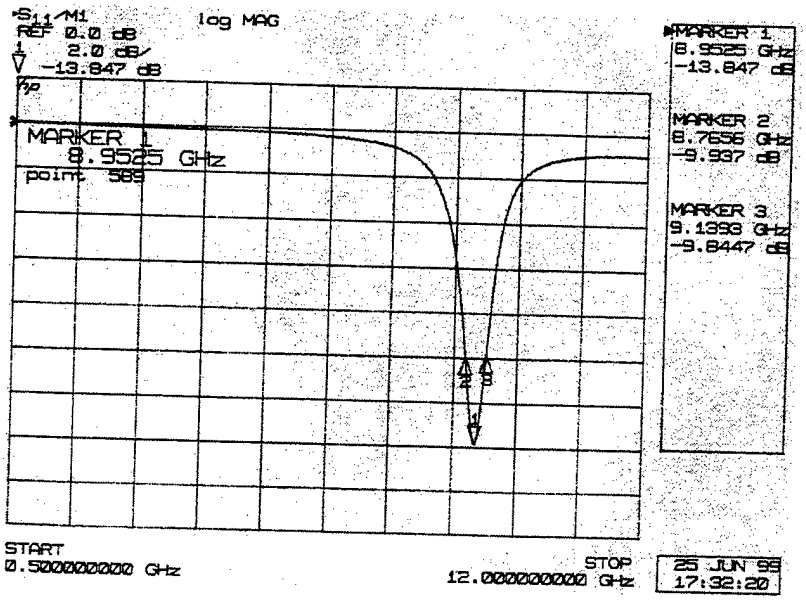

(b) Return Loss

Figure 12: Measured impedance and return loss for an open 3x1 patch array resonant at X-band. Bandwidth: f_L= 8.77 GHz; f_H= 9.14 GHz; BW= 4.13%.

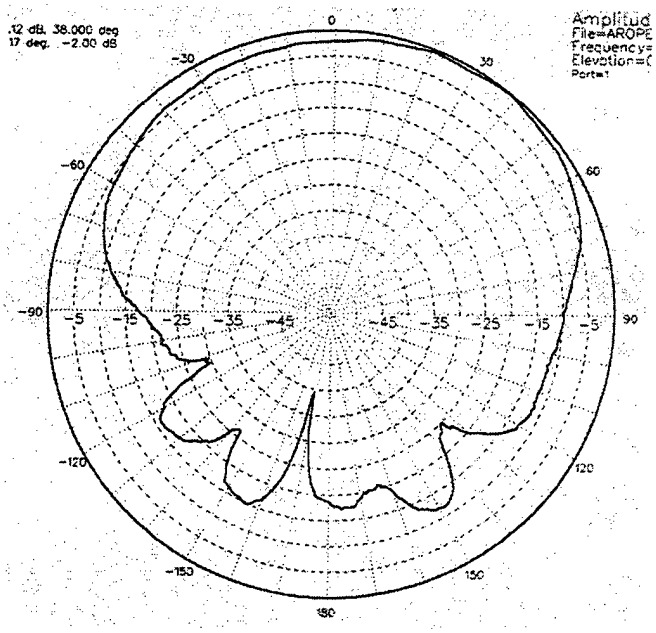

(a) E-Plane Pattern

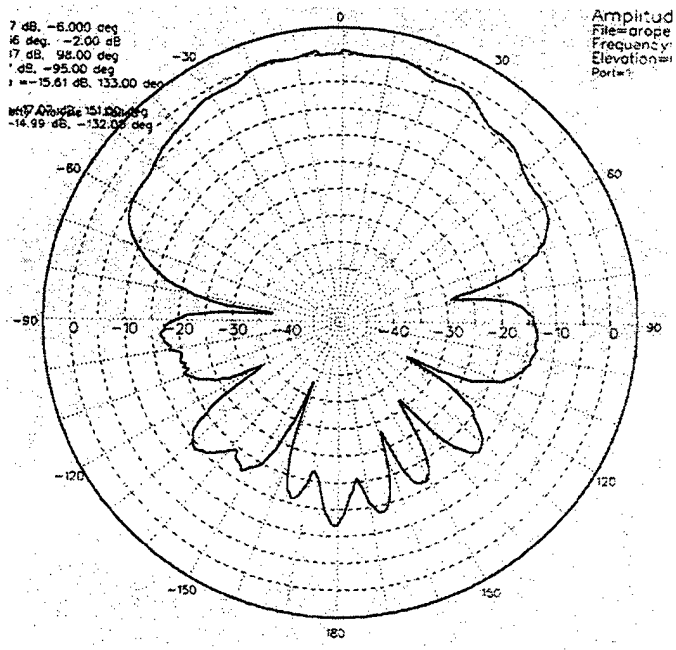

(b) H-Plane Pattern

Figure 13: Measured radiation patterns for an open 3x1 patch array resonant at X-band. Amplitude is normalized to near 0dB at boresight.

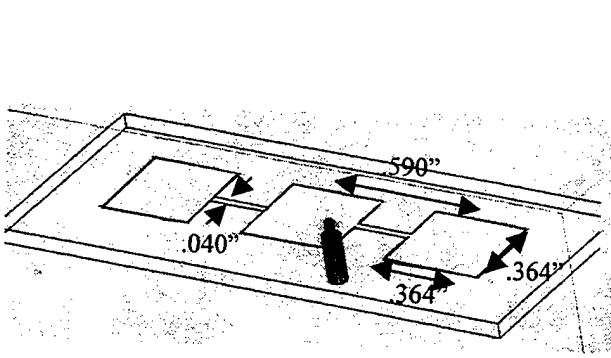

(a) Simulation Layout

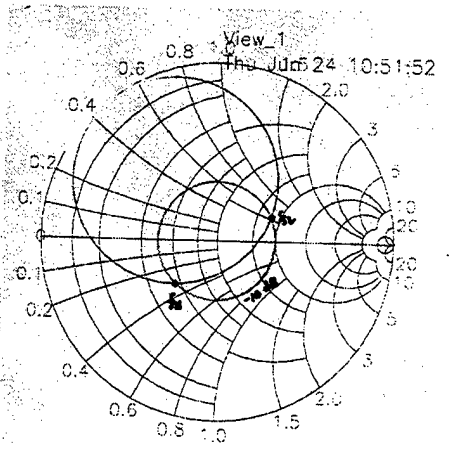

(b) Input Impedance

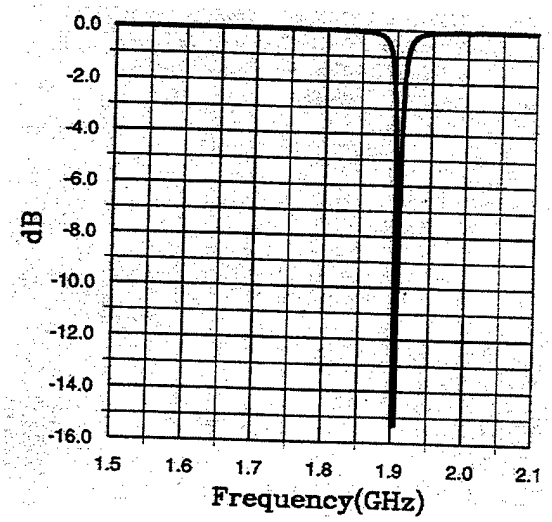

(c) Return Loss

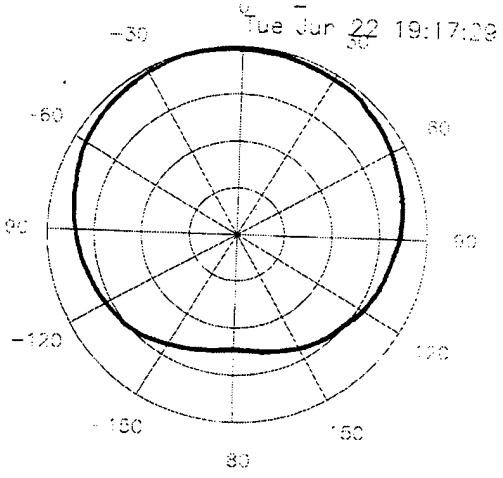

(d) Radiation Pattern

Figure 14: Simulation results for a closed 3x1 patch array resonant at S-band. Bandwidth: f_L= 1.903 GHz; f_H= 1.907 GHz; BW= 0.2%.

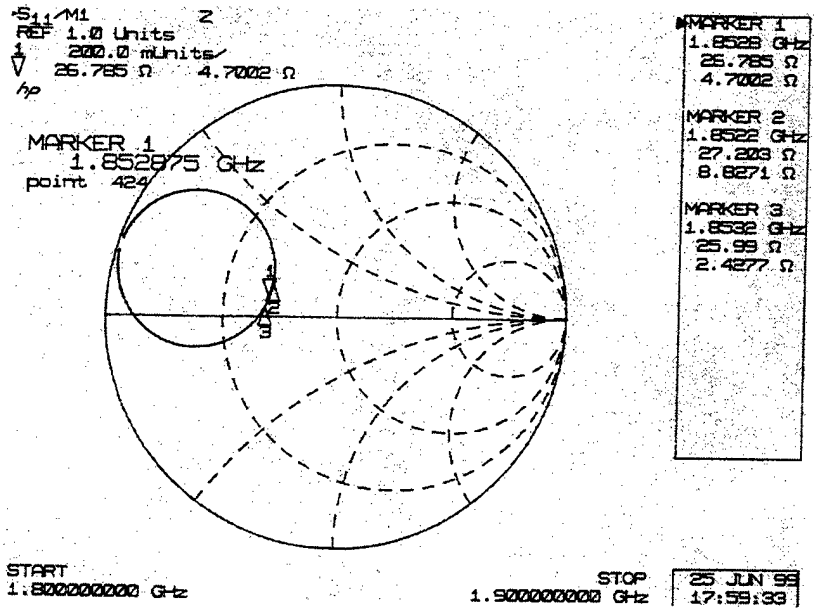

(a) Input Impedance

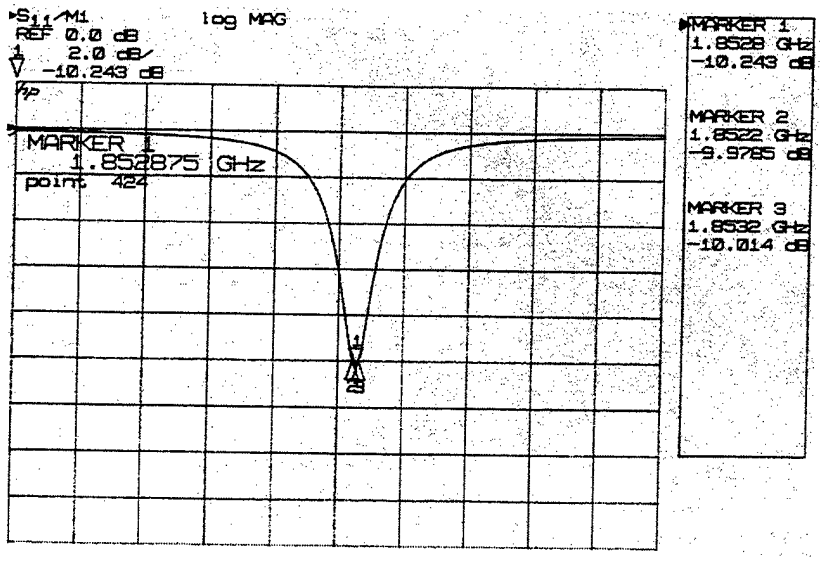

(b) Return Loss

Figure 15: Measured impedance and return loss for a closed 3x1 patch array resonant at S-band. Bandwidth: f_L= 1.8522 GHz; f_H= 1.8532 GHz; BW= 0.05%.

From the results above, it is evident that it is difficult to achieve adequate bandwidth at the low frequency band. Our initial hypothesis was this is due strictly to the height of the antenna elements above the ground plane. Further investigation proved otherwise. From Pozar [21, Fig. 1, p.158], the bandwidth of a rectangular patch at 2 GHz on .062" substrate should achieve approximately 1% bandwidth. Our simulated bandwidth (good impedance match) was a factor of 5 lower than this value, while our measured bandwidth (poor impedance match) was a factor of 20 below this value. To verify that a 1% bandwidth is achievable in practice, we built up a simple 2 GHz square patch on the .062" substrate. The patch dimensions were 1.97"x1.97" with the feed probe located .364" from the center. The measured impedance and return loss data are shown in Figure 16. We actually achieved a bandwidth of 1.22% with very little effort.

Evidently, the bandwidth limit at low frequency is not determined by the height of the microstrip substrate alone. Most likely, the bandwidth is also limited by the volume of the effective microstrip cavity resonator. The reduced volume of the "effective patch" apparently increases the Q of the resonant circuit, reducing the bandwidth. Using this reasoning, a 3x3 patch array should have a higher bandwidth than the 3x1 array.

5.2 Results for .125" substrate.

In order to increase the bandwidth at the low frequency band, we decided to experiment with .125" thick substrate. The results were computed using HFSS. General trends are similar to the .062" substrate data, with at least double the bandwidth. Measured results are not yet available at time of publication, since the substrate material is on backorder.

We first considered an X-band patch of dimension .350"x.350" fed .165" from the center, or .010" from the edge. Figure 17 shows the simulated input impedance and return loss. The 10dB bandwidth is greater than 1 GHz, or 10%.

Next, a 2 GHz square patch antenna was simulated to determine the maximum practical bandwidth achievable on the .125" substrate. The patch dimensions were 1.6"x1.6" with the feed probe .300" from the center. The computed bandwidth was 2.47%.

A single narrow rectangular patch was developed next to simulate the effect of a reduced resonator volume. The patch dimensions were 1.530"x.350". The probe location was .095" from the patch center. The measured bandwidth was .941% (f_L= 2.536 GHz; f_H= 2.560 GHz).

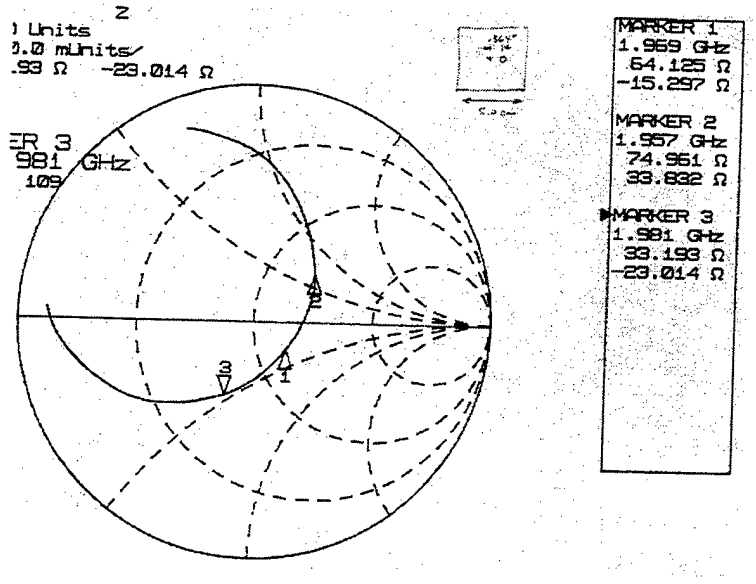

(a) Input Impedance

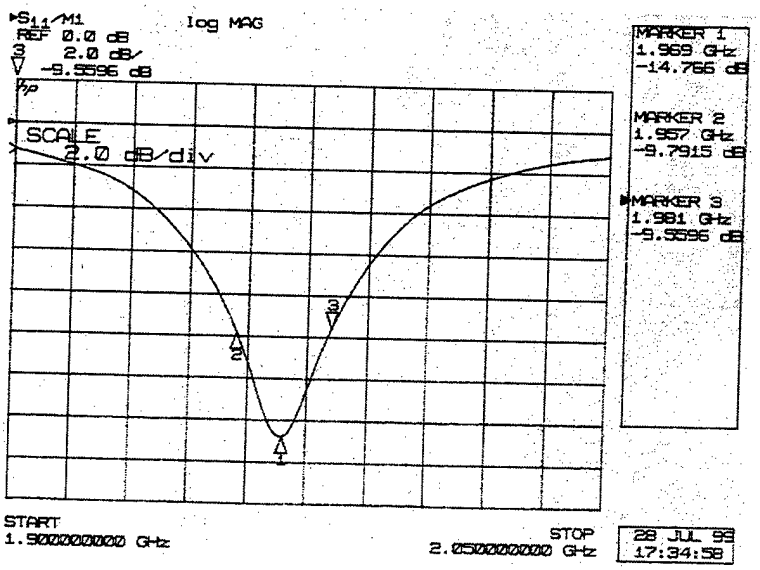

(b) Return Loss

Figure 16: Measured impedance and return loss for a square patch antenna resonant at S-band. Bandwidth: f_L= 1.957 GHz; f_H= 1.981 GHz; BW= 1.22%.

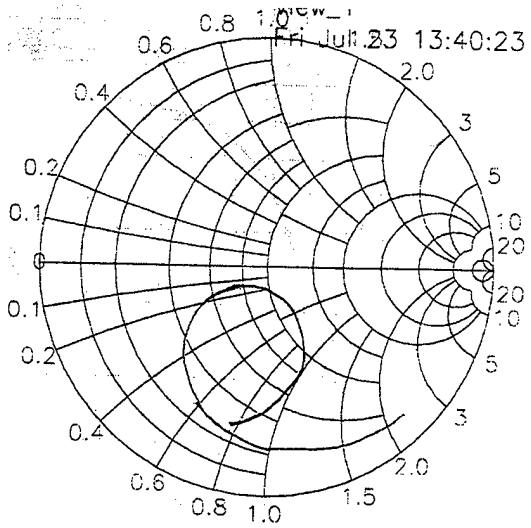

(a) Input Impedance

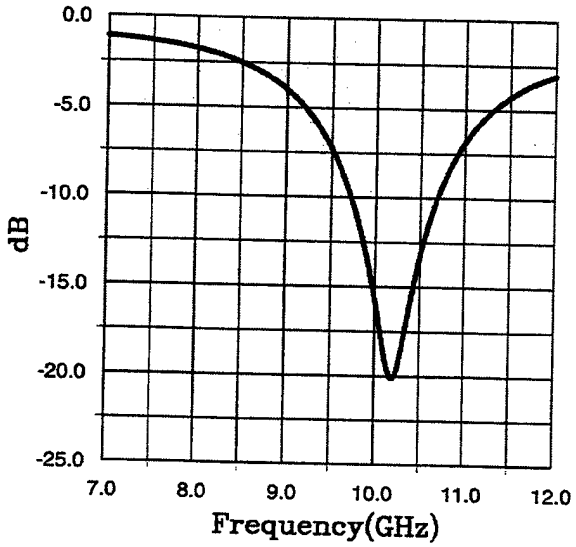

(b) Return Loss

Figure 17: Measured impedance and return loss for a square patch antenna resonant at X-band on .125" substrate. f_L= 1.8522 GHz; f_H= 1.8532 GHz (2.47%).

A closed 3x1 array of patches was simulated next on the .125" substrate. The basic patch elements were .350"x.350", with .040" connecting microstrip lines. The patches were separated by .590" on center. The center patch was fed .070" from the center. The measured bandwidth for the closed 3x1 array .519% (f_L= 1.92 GHz; f_H= 1.93 GHz).

Finally, a 3x3 closed patch array simulated using the .125" substrate. The results are shown in Figure 18. Figure 18(a) shows a diagram of the simulation layout. The patches are .370"x.370". After many simulation runs, it was determined that the optimal feed location was located .200" from the center of the center patch, which is actually located on the .040" microstrip line. Hence, the optimal feed location for the closed 3x3 array is actually not located on the patch elements themselves, but on the interconnecting microstrip line. This antenna had a 20 MHz bandwidth at 2 GHz, or roughly 1% bandwidth.

The simulation results for the .125" substrate are summarized in Table 1 below.

Table 1: Summary of Simulation Results for .125" Substrate

Configuration	**Dimensions**	**Probe Location**	**Percent B.W.**
X-Band Patch	.350x.350	.165	>10%
S-Band Square Patch	1.60x1.60	.300	2.47%
S-Band Narrow Rectangular Patch	1.53x.350	.095	.94%
S-Band Open 3x1 Array	.350x.350	.590	0.52%
S-Band Open 3x3 Array	.370x.370	.200	1.0%

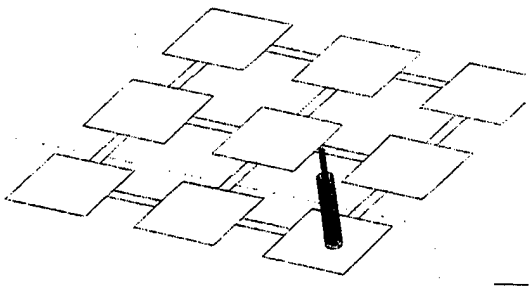

(a) Simulation Layout

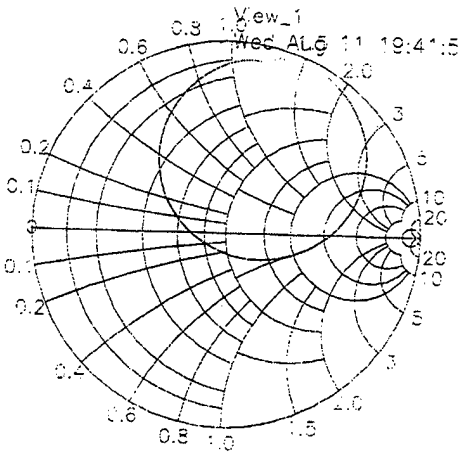

(b) Input Impedance

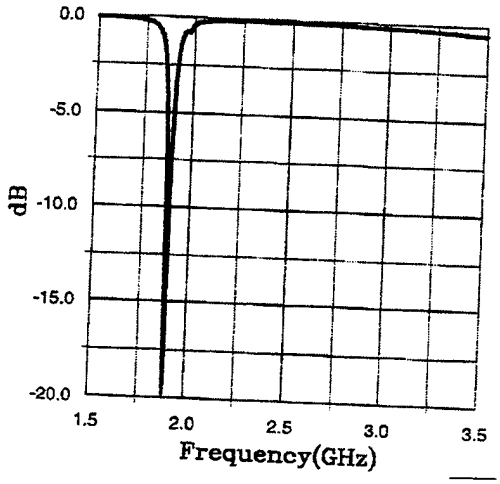

(c) Return Loss

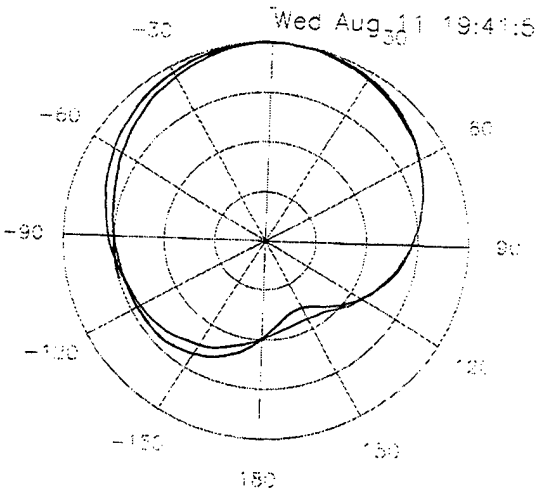

(d) Radiation Pattern

Figure 18: Simulation results for an open 3x3 patch array resonant at S-band on .125" substrate. Bandwidth: 1.0%

6.0 Conclusions

A general procedure was developed for designing reconfigurable multi-band antennas utilizing reconfigurable patch modules (RPMs) as basic elements in a tile architecture. A general adaptive reconfigurable feed (GARF) design methodology was proposed for designing and tuning the feed structure for each configuration independently. MEMS switches were discussed as possible switching elements due to their extremely low bias current and low insertion loss.

Design, simulation and measurement results were presented for a dual-mode RPM capable of operating at 10 GHz (X-band) and 2 GHz (S-band). Results were presented for both .062" and .125" thick substrate. Practical experience illustrates the difficulty of achieving a high relative bandwidth at the low frequency band. The bandwidth is limited by both the height of the element above the ground plane and the "element fill factor" determined by the volume of the resonant cavity of the "effective patch". Nevertheless, we have shown that it is possible to design a dual-mode RPM with 1% relative bandwidth at 2 GHz and 10% relative bandwidth at 10 GHz.

Since the MEMS switches are not currently available in packaged form, our current research is limited simulating the MEMS switches as ideal switches, and building separate antennas to simulate the OPEN and CLOSED configurations. We expect that samples of the MEMS switches will be available in the very near future, at which time we will incorporate these switches into our simulations and prototypes.

Acknowledgement

Support for this work is provided by a Phase-I Small Business Innovative Research (SBIR) contract from the U.S. Air Force Research Laboratory, Sensors Directorate, under contract F19628-99-C-0056.

References

[1] E. R. Brown, "RF-MEMS Switches for Reconfigurable Integrated Circuits," *IEEE Trans. Microwave Theory Tech.*, Vol. 46, No. 11, pp. 1868–80, Nov. 1998.

[2] N. S. Barker and G. M. Rebeiz, "Distributed MEMS True-Time Delay Phase Shifters and Wide-Band Switches," *IEEE Trans. Microwave Theory Tech.*, Vol. 46, No. 11, pp. 1881–90, Nov. 1998.

[3] R. C. Dempsey and R. M. Bevensee, "The Synaptic Antenna for Reconfigurable Array Applications – Description," *IEEE Antennas and Propagat. Society Symposium Digest*, pp. 760–3, 1989.

[4] R. M. Bevensee and R. C. Dempsey, "The synaptic Antenna for Reconfigurable Array Applications – Behavior," *IEEE Antennas and Propagat. Society Symposium Digest*, pp. 764–7, 1989.

[5] J. L. Freeman, B. J. Lamberty and G. S. Andrews, "Optoelectronically Reconfigurable Monopole Antenna," Electronics Lett., Vol. 28, No. 16, pp. 1502–3, July, 1992.

[6] A. S. Daryoush, K. Bontzos and P.R. Herczfeld, "Optically Tuned Patch Antenna for Phased Array Applications," *IEEE Antennas and Propagat. Society Symposium Digest*, pp. 361–4, 1986.

[7] M. L. Van Blaricum, "Photonic Antenna Reconfiguration: A Status Survey," *Proc. of the SPIE, Photonics and Radio Frequency II,* (San Diego, CA) July 21-22, 1998.

[8] D. Schaubert, F. Farrar, S. Hayes, and A. Sindoris, "Frequency-Agile, Polarization Diverse Microstrip Antennas and Frequency Scanned Arrays," US Patent #4,367,474, Jan. 4, 1983.

[9] D. Schaubert, and F. Farrar, "Microstrip Antenna with Polarization Diversity," US Patent #4,410,891, Oct. 18, 1983.

[10] F. Farrar and D. Schaubert, "Selectable-Mode Microstrip Antenna and Selectable-Mode Microstrip Antenna Arrays," US Patent #4,379,296, Apr. 5, 1983.

[11] R. Olesen, et. Al., "Quadrifilir Helix Antenna Tuning Using PIN Diodes," US Patent #4,554,554, Nov. 19, 1985.

[12] P. Bhartia and I. Bahl, "Broadband Microstrip Antennas with Varactor Diodes," US Patent # 4,529,987, July 16, 1985.

[13] K. Turk, "Digitally Reconfigurable Antenna," *Proceedings of the 1996 Antenna Applications Symposium*, Allerton Park, Monticello, IL, Sept. 18-20, 1996.

[14] R. Gilbert, G. Pirrung, D. Kopf, P. Hoefler, F. Hayes, Structurally-Integrated Optically-Reconfigurable Antenna Array, *Proceedings of the 1995 Antenna Applications Symposium*, Allerton Park, Monticello, IL, 1995.

[15] J. J. Lee, D. Atkinson, J. J. Lam, L. Hackett, R. Lohr, L. Larson, R. Loo, M. Matloubian, G. Tangonon, H. De Los Santos, and R. Brunner, "MEMS Antenna Systems: Concepts, Design and System Implications," *Nat. Radio Science Meeting*, (Boulder, CO), 1996.

[16] J. S. Herd and M. Davidovitz, "Reconfigurable Microstrip Antenna Using MEMS Switches", submitted to Electronics Letters, April 1999.

[17] D. M. Pozar, *Microwave Engineering.* Reading, MA: Addison Wesley, 1990.

[18] D. M. Pozar and D. Schaubert Eds., *Microstrip Antennas: The Analysis and Design of Microstrip Antennas and Arrays.* New York, NY: Institute of Electrical and Electronics Engineers, 1995.

[19] C. A. Balanis, *Antenna Theory, Second Ed.* New York: Wiley, 1996.

[20] R. J. Mailloux, *Phased Array Antenna Handbook.* Norwood, MA: Artech House, 1994.

[21] D. M. Pozar and D. Schaubert, "A Review of Bandwidth Enhancement Techniques for Microstrip Antennas" in *Microstrip Antennas: The Analysis and Design of Microstrip Antennas and Arrays,* D. M. Pozar and D. Schaubert Eds. New York, NY: Institute of Electrical and Electronics Engineers, 1995.

FINITE DIPOLE ARRAYS OVER A WIDEBAND

R. C. Hansen
Consulting Engineer
Tarzana, CA 91357
818-345-0770

It is known that large arrays of TEM horns have a low frequency cutoff well below that of an isolated horn. Similar results have recently been shown for the real part of impedance of a large dipole array; the reactance increases as frequency decreases, but would allow wideband performance if matched with a non-Foster circuit. This paper examines the wideband behavior of dipole arrays of finite size. In particular, the Scan Impedance and Scan Element Pattern of a 41 x 41 element array, and a 21 x 21 element array are compared with the infinite array results, for two frequencies representing a 5:1 bandwidth.

1.0 INTRODUCTION

Large arrays of TEM horns, incorrectly called notch antennas, and fancifully called Vivaldi antennas, have demonstrated a low frequency cutoff with an element spacing of the order of 1/15 wavelength, far smaller than the cutoff of an isolated TEM horn (Shin and Schaubert, 1995). Large arrays of dipoles have shown related behavior where the Scan Resistance is nearly constant with frequency, from half-wave dipole length and lattice, to several octaves lower in frequency (Hansen, 1999). This is because the infinite array Floquet unit cell formulation has only a single term for Scan Resistance (in the absence of grating lobes), with dipole length squared in the numerator, and lattice $d_x \cdot d_y$ in the denominator (Hansen, 1998). Of course the Scan Reactance is large for short dipoles. However if the reactance is cancelled at broadside then the Scan Element Pattern (array gain vs angle) is well behaved over several octaves of frequency. Such reactance cancellation might be provided by a non-Foster circuit, sometimes called a Negative Impedance Converter. These circuits were developed in the vacuum tube era, but were first applied to antennas by Mayes and colleagues, here at the University of Illinois (Poggio and Mayes, 1971). The advances in transistor circuitry with cutoffs in the hundreds of GHZ has rekindled interest in these non-Foster circuits (Skahill et al, 1998).

Clearly with both TEM horn arrays and with dipole arrays the low frequency performance degrades as the array becomes smaller. It is the purpose of this paper to briefly explore how the array parameters change from large to small arrays.

2.0 Array Simulation

For finite arrays there are no simulation tools that are as convenient and speedy as the unit cell models. Many approximate models have been developed; all suffer from a loss in fidelity to the exact results. The simulation here uses exact impedance equations for a square array of thin wire dipoles, with a square lattice. An impedance matrix is calculated using exact mutual impedances calculated in double precision Fortran, using a convenient algorithm (Hansen, 1972). The Sine and Cosine Integrals needed are calculated in double precision via a Chebyshev expansion algorithm of Luke (1975). A triangular matrix is then formed, and the resulting equations solved by a symmetric Cholesky routine. Scan Impedance is determined for the center element, or for the element nearest center. The largest array solved is 101 by 101 elements, for a total of 10,201 simultaneous equations. Matrix storage is 52 million impedances. All results were computed on an HP 64 bit UNIX workstation. Results were validated by another array code. Note that if only broadside data were wanted, the array could be folded in each dimension, resulting in a speedup of roughly 64:1. But folding is not allowed for scanning.

3.0 RESULTS

First arrays of half-wave dipoles with half-wave spacing are examined. Figs. 1-3 are for a 41 x 41 element array; shown are Scan Resistance and Reactance, and Scan Element Pattern. In all graphs, the solid line is E-plane scan, the dashed line is H-plane scan, and the dotted line is diagonal plane scan. In comparison with the infinite array results (Hansen, 1999) these are similar but with oscillations superimposed. It is interesting that the diagonal results are more oscillatory. Roughly 7 cycles occur.

Next the same elements and lattice are simulated but with 21 x 21 elements. Figs. 4-6 correspond to the first three figures. Now the oscillations are fewer in number (roughly 4 cycles) and larger in amplitude, as expected. Unexpected is a blind angle at roughly 76 deg. Note that the broadside embedded resistance is nearly the same as for the half-wave case; it is of course close to that of an isolated dipole.

To indicate behavior at a frequency of 1/5 (5:1 bandwidth) simulations were run at dipole length and lattice spacing of $.1\lambda$. Behavior of the 41 x 41 element array is shown in Figs. 7-9. Oscillations are now larger and fewer, as the array edges are closer together in wavelengths. It may be noted that the Scan Resistance value at broadside is roughly 60% of the infinite array value. Figs. 10-12 are for the 21 x 21 element array, again $.1\lambda$ dimensions. Essentially only one oscillation exists, and it is large. Broadside resistance is roughly 50% of the infinite array value. Since the isolated $.1\lambda$ dipole resistance is 2 ohms, clearly the array value is tending toward this. Additional calculations show that the broadside embedded resistance oscillates with the number of elements per side, with the oscillation amplitude and period decreasing as the number of elements increases. A rising trend matches the resistance to the infinite array value.

4.0 CONCLUSIONS

Edge effects severely limit the behavior of dipole arrays over a wideband. Arrays as large as 41 x 41 exhibit significant resistance changes over a 5:1 bandwidth; scan is probably limited to 45 deg. For smaller arrays such as 21 x 21, the useable scan range is probably less than 30 deg.

REFERENCES

R. C. Hansen, Formulation of Echelon Dipole Mutual Impedance for Computer," *Trans. IEEE*, Vol. AP-20, Nov. 1972, pp. 780-781

R. C. Hansen, *Phased Array Antennas*, Wiley, 1998

R. C. Hansen, Dipole Array Scan Performance over a Wideband," *Trans. IEEE,* Vol. AP-47, May 1999, pp. 945-957

Y. L. Luke, *Mathematical Functions and their Approximations*, Academic Press, 1975, Table 4.4

A. J. Poggio and P. E. Mayes, Bandwidth Extension for Dipole Antennas by Conjugate Reactance Loading," *Trans. IEEE*, Vol. AP-18, July 1971, pp. 544-547

J. Shin, and D. H. Schaubert, Toward a Better Understanding of Wideband Vivaldi Notch Antenna Arrays," *Proc. 1995 Antenna Applications Symp.*, Vol. 2, Sept. 1995, Allerton Park, IL, AD-A309 723, pp. 556-585

G. Skahill, R. M. Rudish, and J. Piero, Electrically Small Efficiency, Wide-band, Low-Noise Antenna Elements," *Proc. 1998 Antenna Applications Symp.*, Allerton Park, IL, AD-A364 798, pp. 214-231

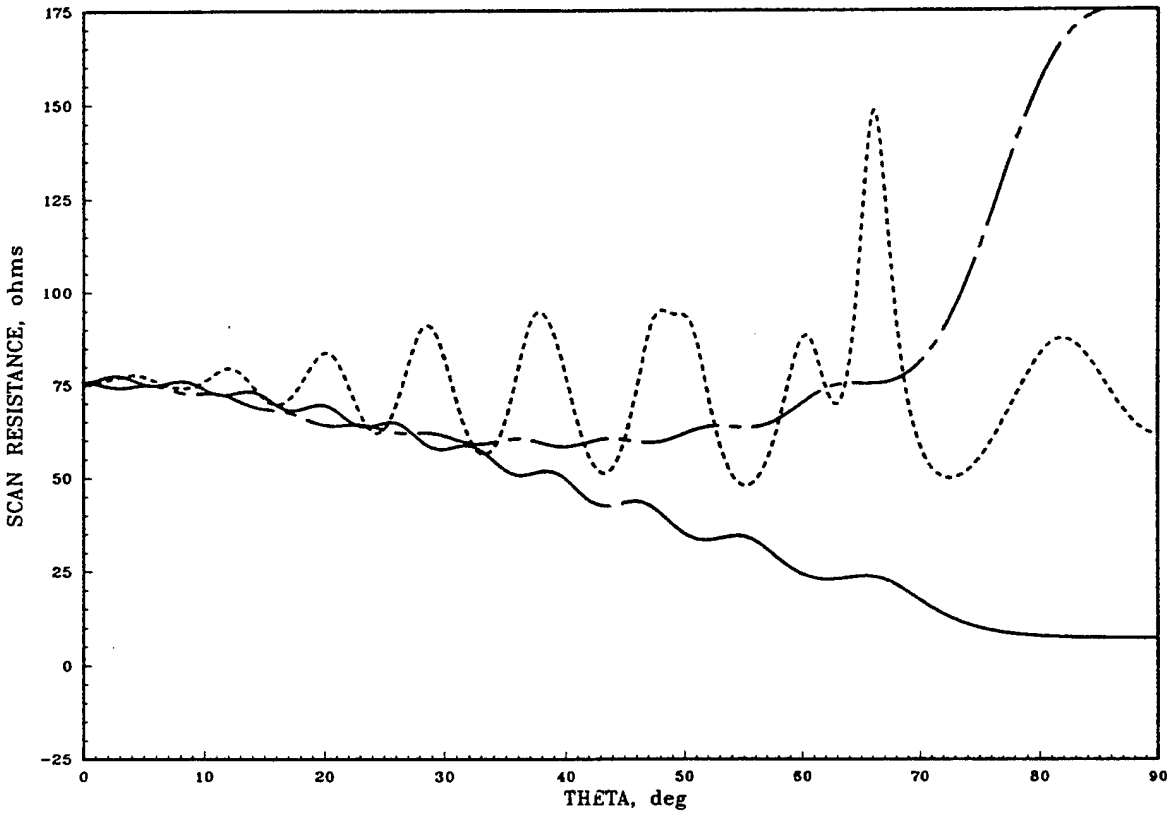

41 x 41 DIPOLE ARRAY, L=.5 wv, Dx=Dy=.5 wv

FIG. 1

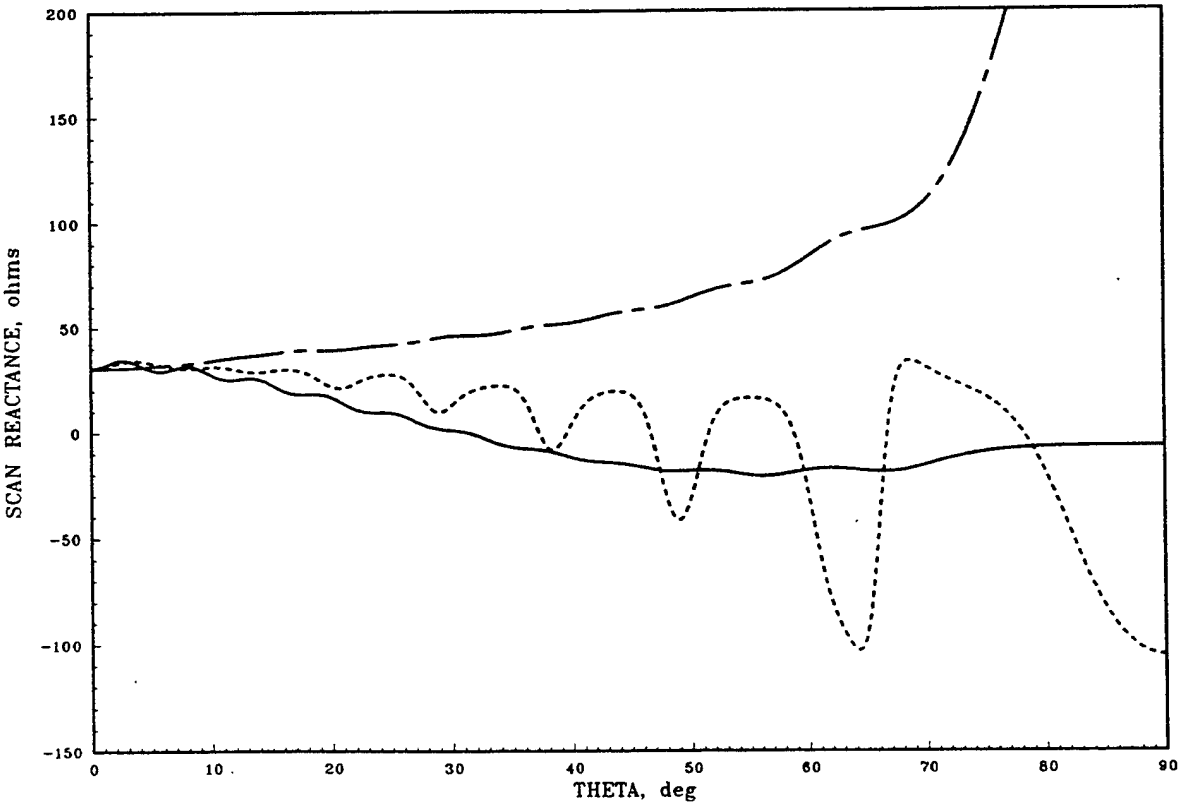

41 x 41 DIPOLE ARRAY, L=.5 wv, Dx=Dy=.5 wv

FIG. 2

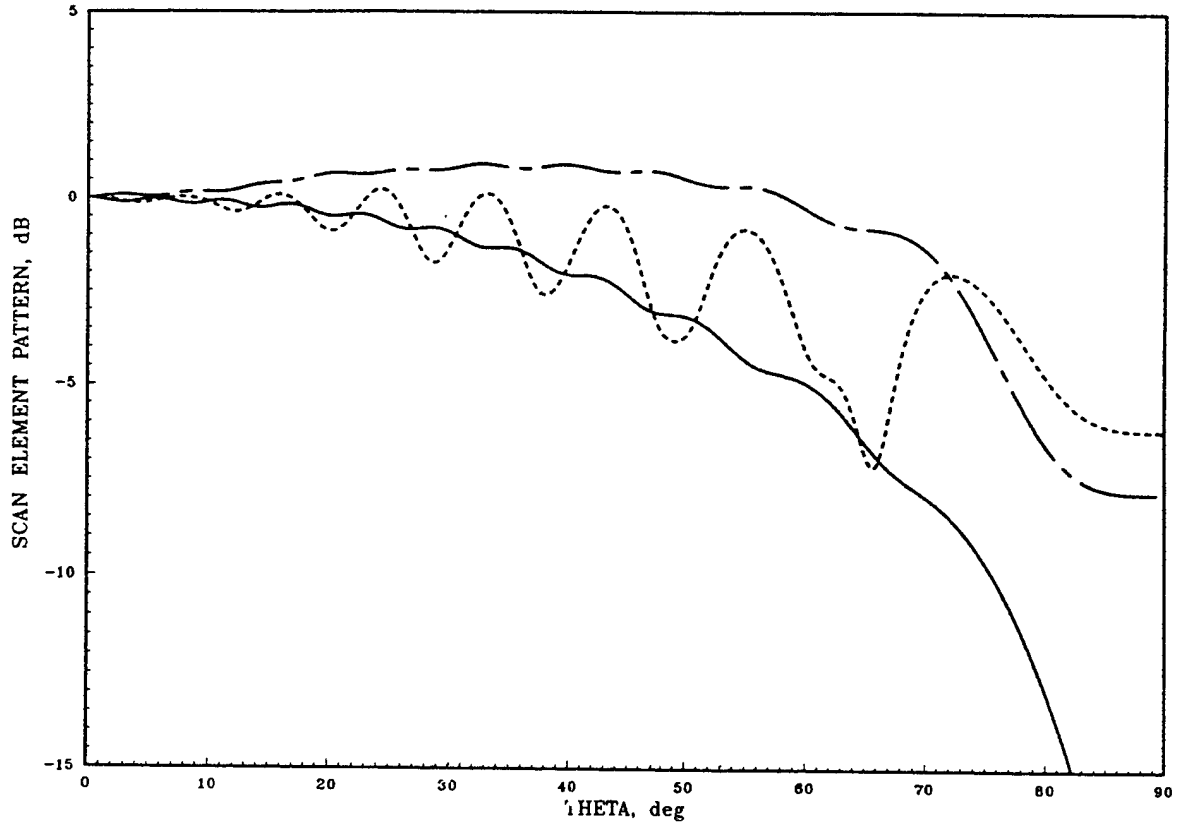

41 x 41 DIPOLE ARRAY, L=.5 wv, Dx=Dy=.5 wv

FIG. 3

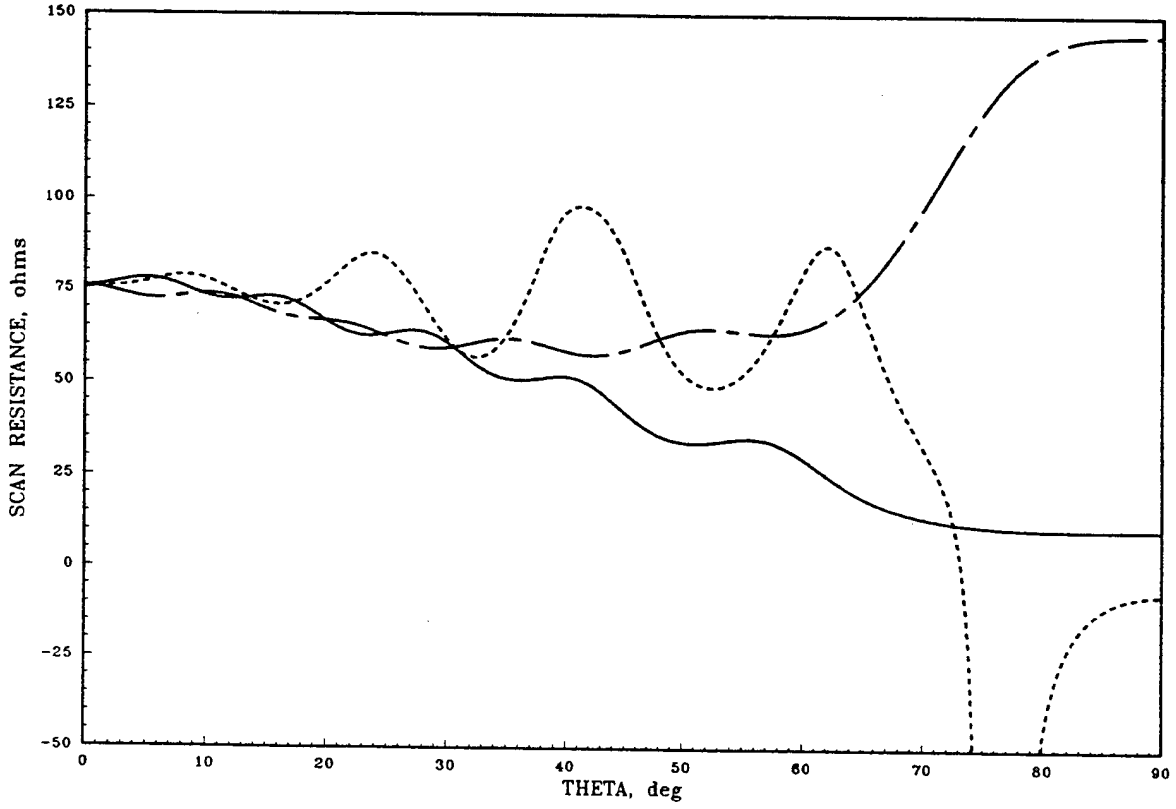

21 x 21 DIPOLE ARRAY, L=.5 wv, Dx=Dy=.5 wv

FIG. 4

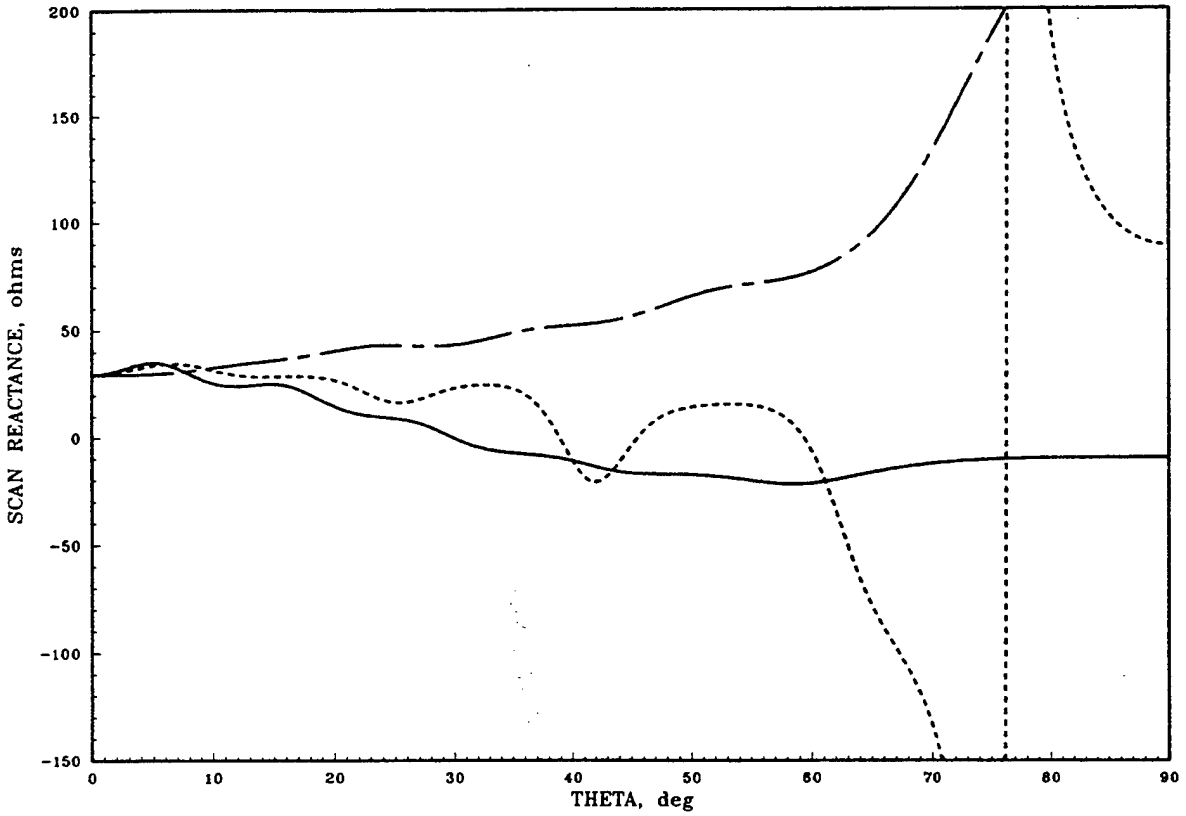

21 x 21 DIPOLE ARRAY, L=.5 wv, Dx=Dy=.5 wv

FIG. 5

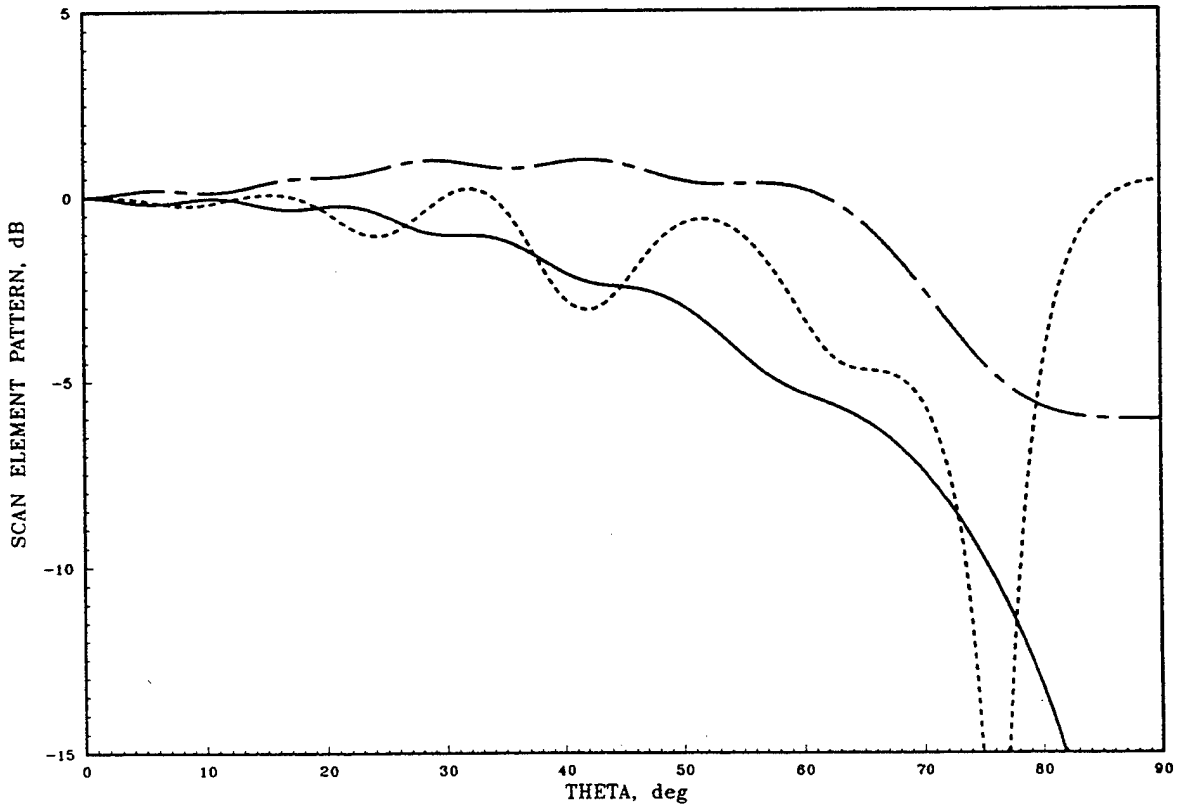

21 x 21 DIPOLE ARRAY, L=.5 wv, Dx=Dy=.5 wv

FIG. 6

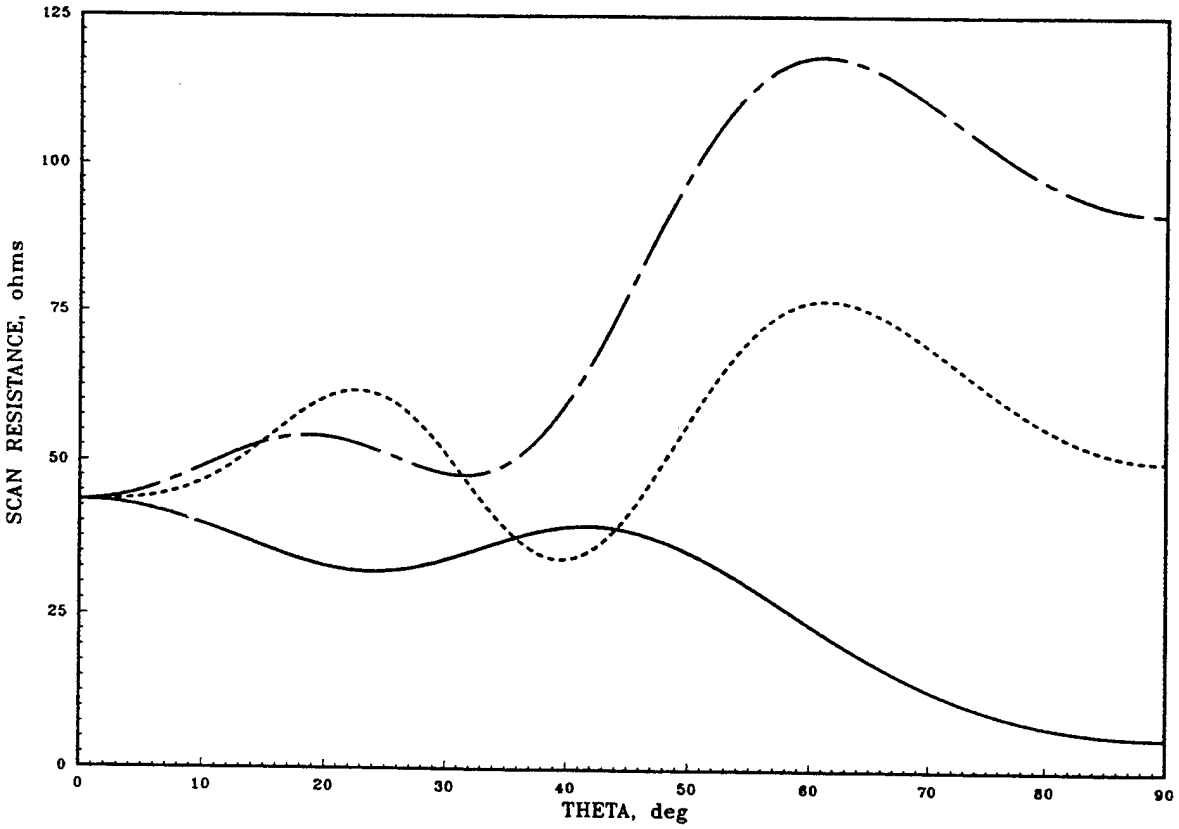

41 x 41 DIPOLE ARRAY, L=.1 wv, Dx=Dy=.1 wv

FIG. 7

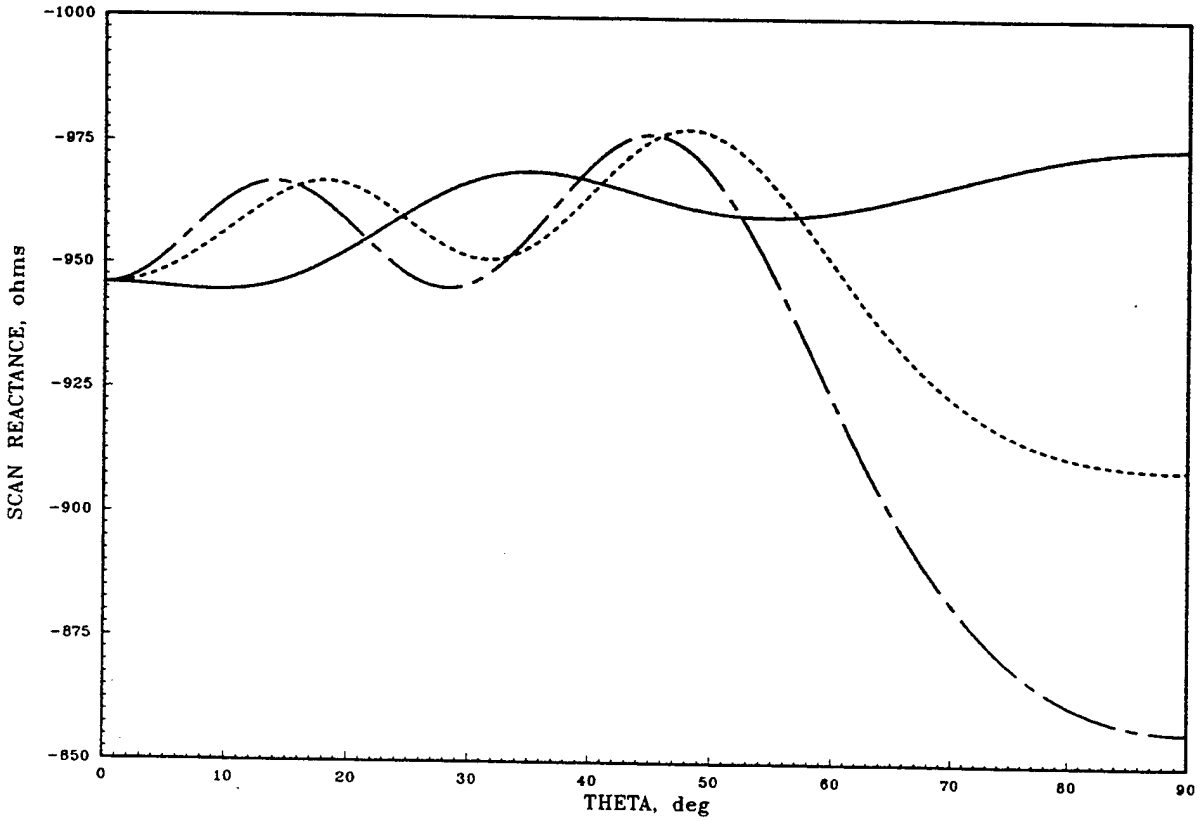

41 x 41 DIPOLE ARRAY, L=.1 wv, Dx=Dy=.1 wv

FIG. 8

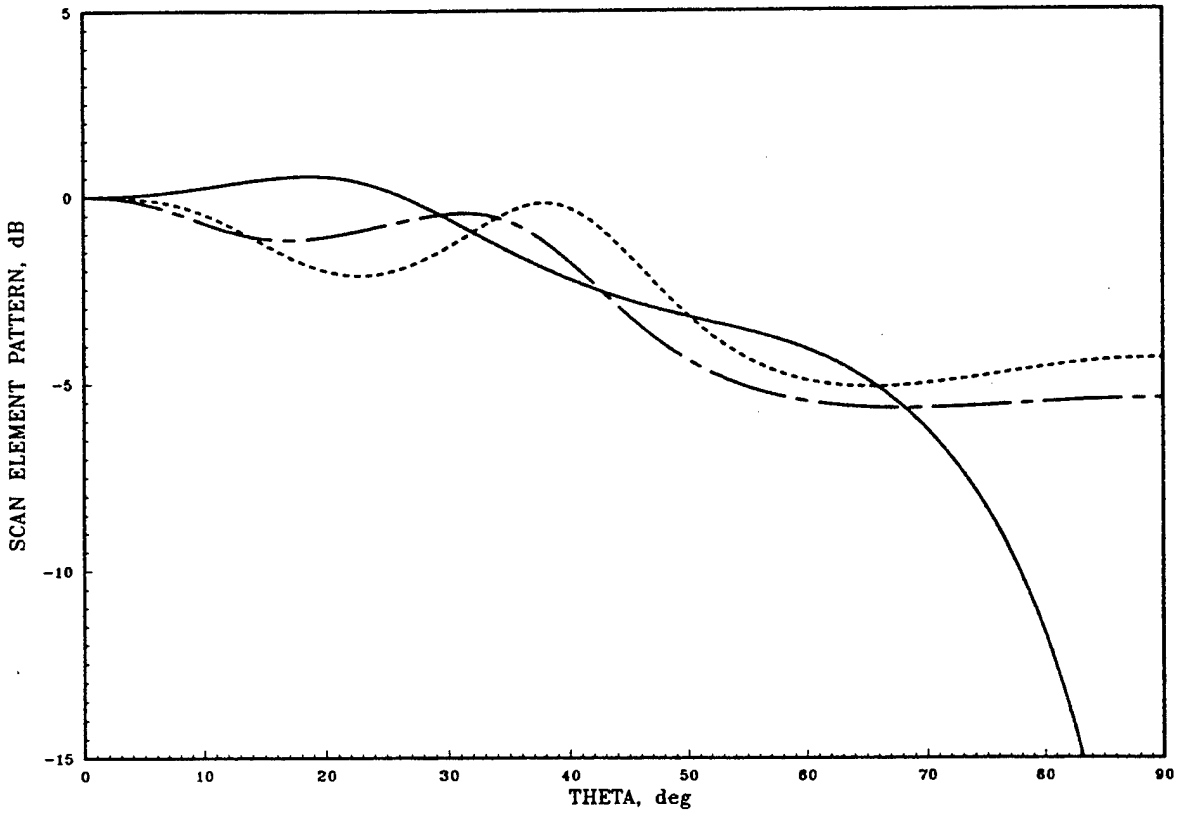

41 x 41 DIPOLE ARRAY, L=.1 wv, Dx=Dy=.1 wv

FIG. 9

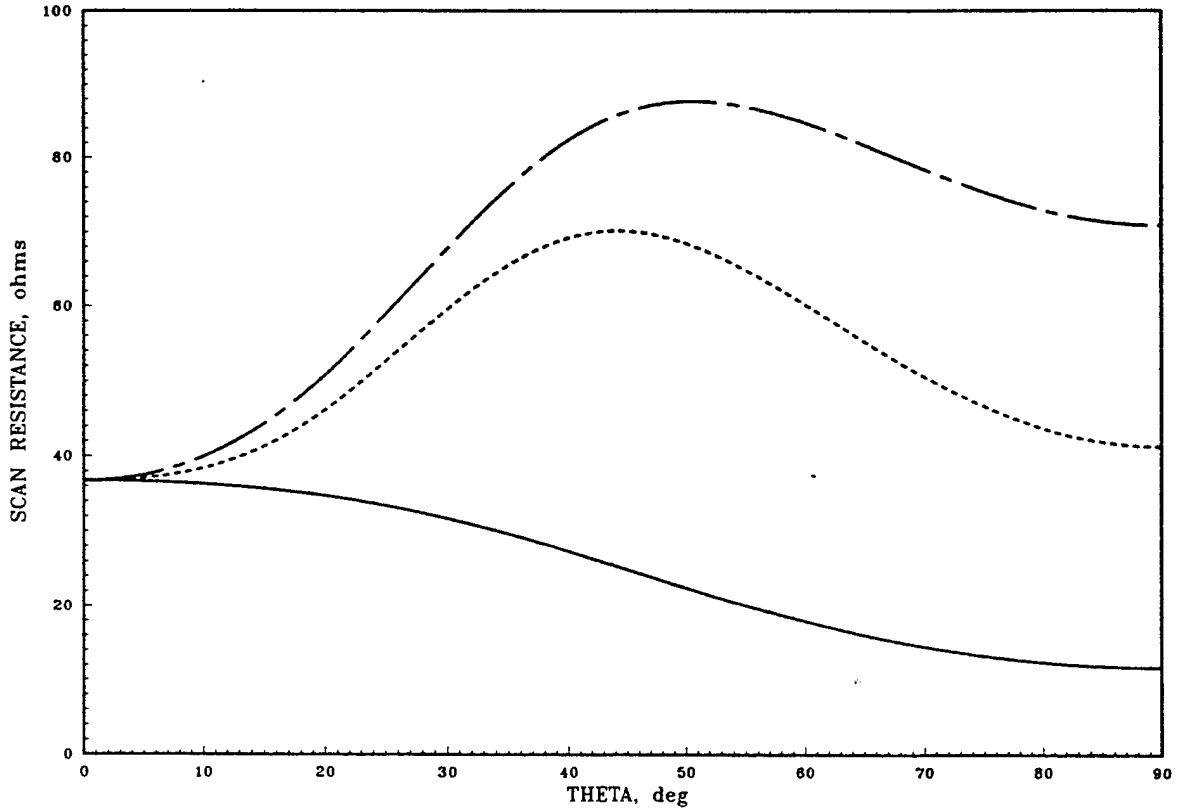

21 x 21 DIPOLE ARRAY, L=.1 wv, Dx=Dy=.1 wv

FIG. 10

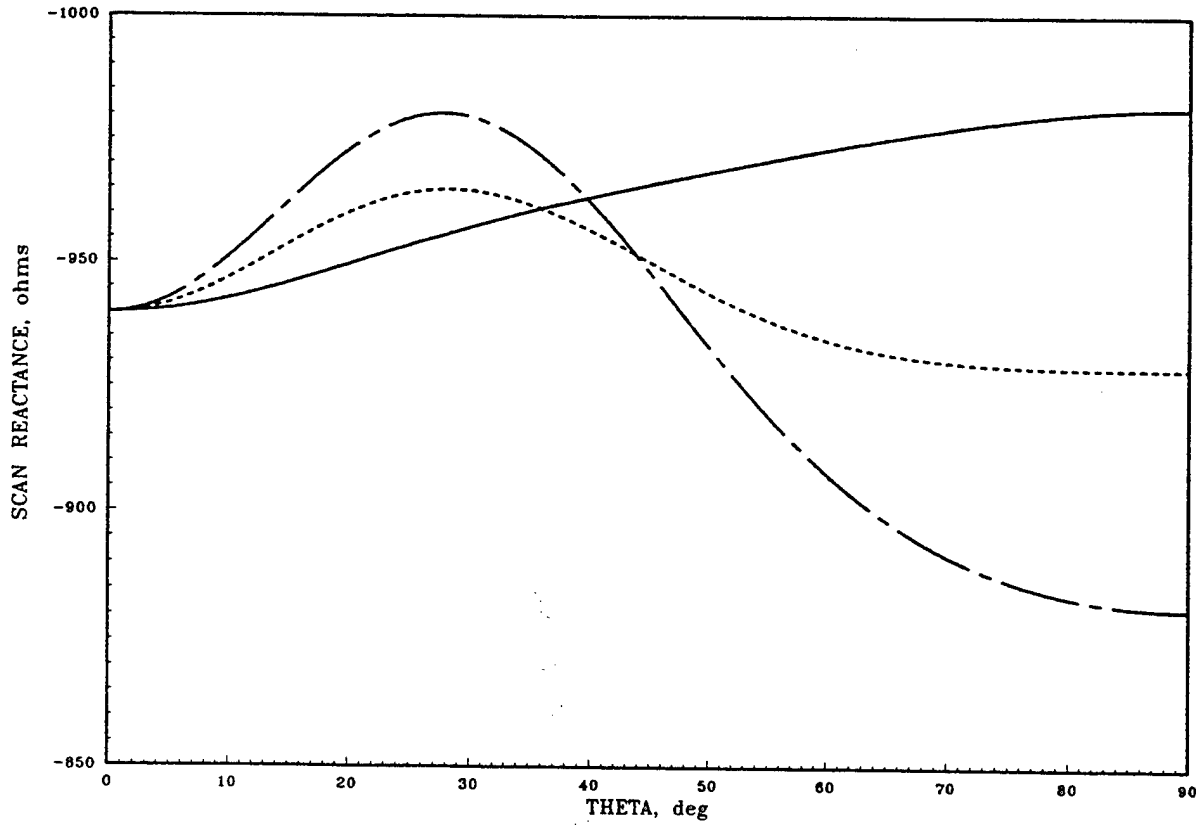

21 x 21 DIPOLE ARRAY, L=.1 wv, Dx=Dy=.1 wv

FIG. 11

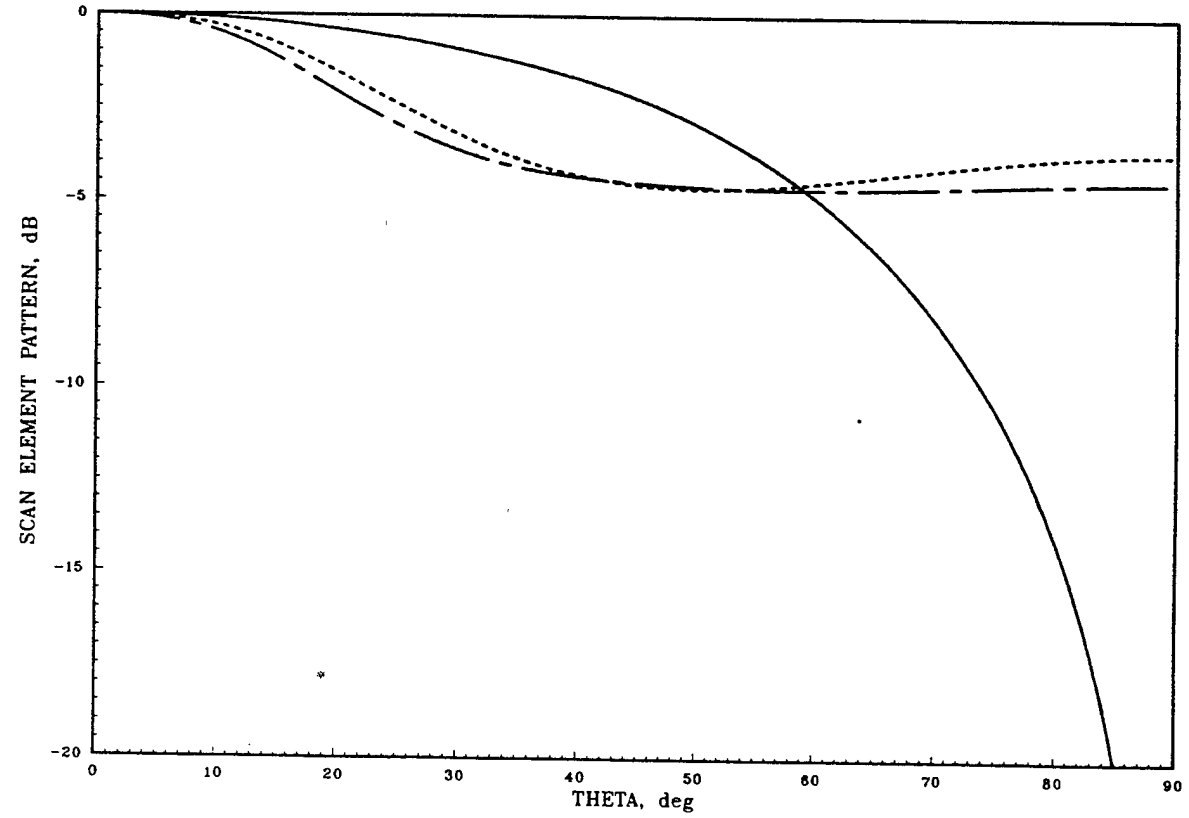

21 x 21 DIPOLE ARRAY, L=.1 wv, Dx=Dy=.1 wv

242 FIG. 12

SPINNING-ARRAY 2-D BEAM-STEERING MMW ANTENNA

V. A. Manasson, L. S. Sadovnik, V. A. Yepishin, L. Timashpolsky, R. Mino

Abstract: A new electro-mechanical beam-steering antenna for MMW imaging radar is described. The antenna is capable to synchronously steer two MMW beams in the azimuth plane and the elevation plane, 30 deg in each plane. The antenna is designed to operate at a frequency of 76.5 GHz, with arbitrary polarization, including vertical, horizontal and circular. Azimuth beam width is 1 deg, elevation beam width can be selected from the set of 3 deg, 5 deg, and 8 deg. The antenna comprises two identical components operating synchronously. Each component comprises a spinning drum carrying a set of diffraction gratings, switching parabolic reflectors and a gimbaled planar reflector. The spinning drum provides azimuth scan, the gimbaled planar reflector provides elevation beam steering. The antenna is designed to operate with imaging radar and can provide a scan rate of up to 20 frames/sec.

1.0 Introduction

Millimeter wave imaging is a fast developing technology that can provide a fair quality image even under adverse atmosphere conditions, like smog, dust, fog, and clouds. MMW radar is the main component of an active imaging system. Beam-steering antenna is an essential element of the MMW imaging radar. The traditional way to steer a MMW beam is moving the antenna back and forth using, for instance, a gimbaled reflector. Such movement is slow, and the antennas are cumbersome. In this paper we describe an antenna utilizing a novel beam-steering technology that can provide a much faster scan.

2.0 Antenna Design

The important design element that distinguishes this antenna from other antennas is a spinning drum carrying a set of diffraction gratings. Each grating represents a linear array of round holes equidistantly distributed along the drum axis. Each row has its own grating period Λ. The gratings are fed through a dielectric-rod waveguide, one grating at a time. The basic structure is shown in Fig. 1.

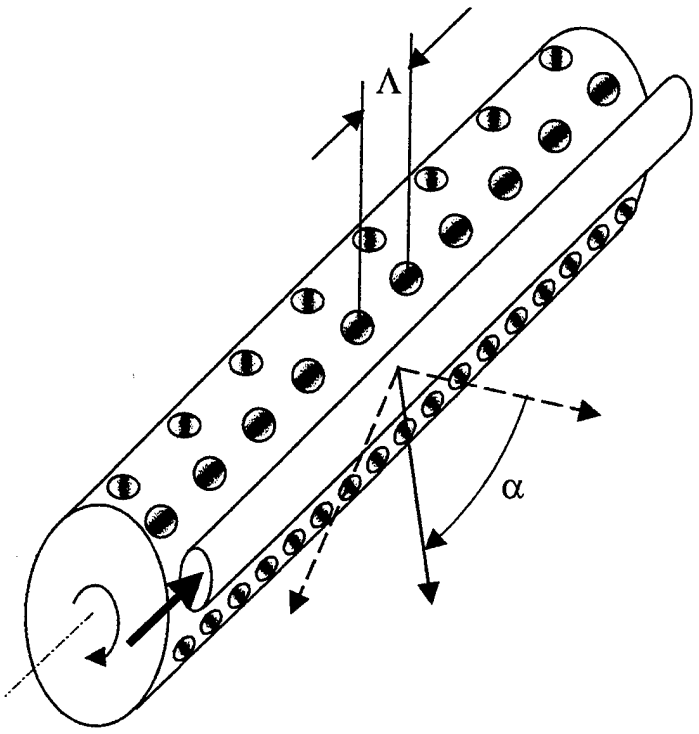

Fig.1. A spinning array fed through a dielectric rod waveguide.

The grating closest to the rod perturbs the evanescent wave supported by the dielectric rod and creates a leaky wave propagating in a specific direction at an angle α. The angle α varies with the grating period according to the formula:

$$\alpha = \arcsin(c / v_{ph} - \lambda / \Lambda), \tag{1}$$

where c is light velocity, v_{ph} is the phase velocity in the dielectric rod waveguide, λ is the free-space wavelength, and Λ is the grating period.

As the drum rotates, different gratings are consequently coming to the proximity of the rod waveguide. They have different grating periods. The variation in the grating period, caused by rotation, results in beam steering.

The feeding rod has circular symmetry, and it supports only one propagating mode. This means that all supported waves have the same phase velocity v_{ph}, independent on the polarization, so that vertically, and horizontally, and even circularly polarized waves propagate with the same phase velocity. Circular symmetry is also maintained by the shape of the holes that constitute the gratings. We found that under this geometry, the radiation angle is almost independent on the polarization as well.

Coupling efficiency between the feeding rod and the diffraction gratings depends on the size of the gap between them. By varying the gap we optimized the radiation intensity profile along the rod, and produced a bell-shaped profile that resulted in relatively low side-lobe far-field beam pattern in the azimuth plane.

Beam profile in the elevation plane was formed with the use of parabolic reflectors (Fig.2).

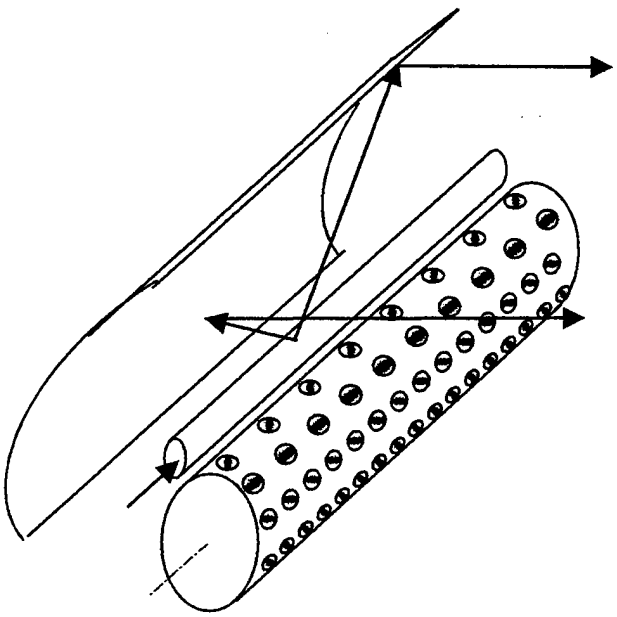

Fig.2. Parabolic reflector shapes the beam in the elevation plane.

To provide the capability of selecting the elevation beam width, we designed the antenna with a set of switched parabolic reflectors, each reflector with its own curvature (see Fig.3).

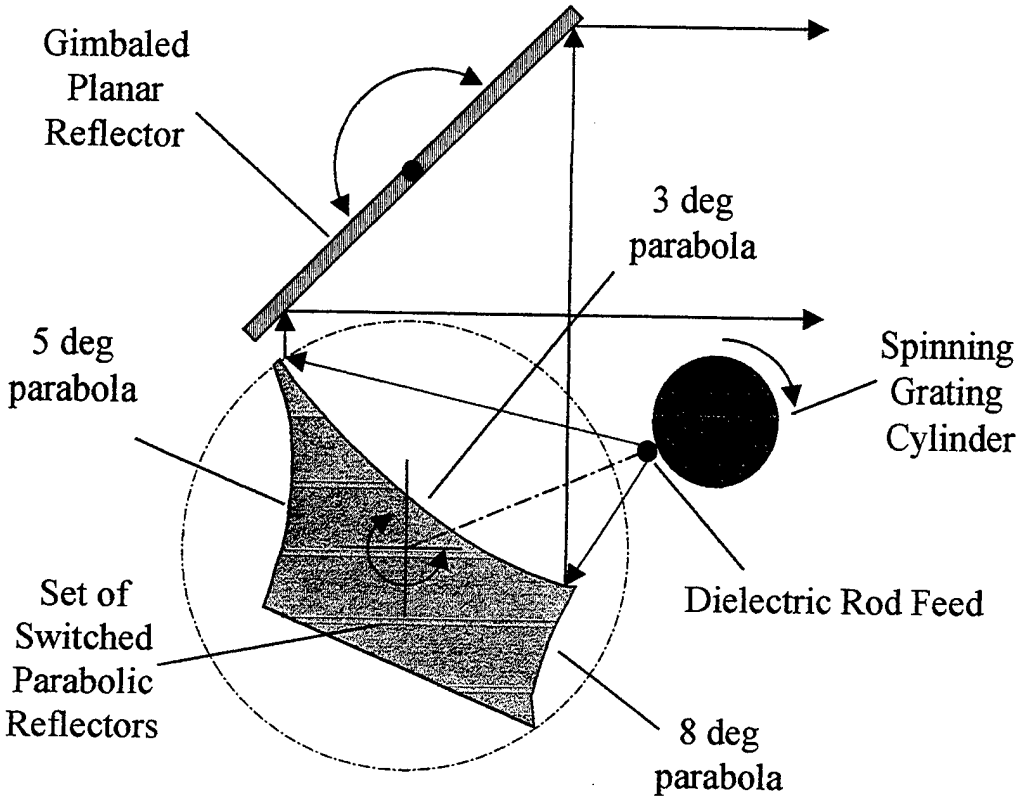

Fig.3. Antenna cross-section.
Dielectric rod feeds spinning gratings. Leaky waves originated from the rod/grating interaction illuminate the surface of one of three switched parabolic reflectors. Parabolic reflectors form the beam in the elevation plane. A gimbaled planar reflector redirects the beam into the required elevation angle.

We employed two identical synchronously moving antennas to provide a device with a capability of bistatic operation and low cross talk between the transmitting and receiving channels (see Fig.4).

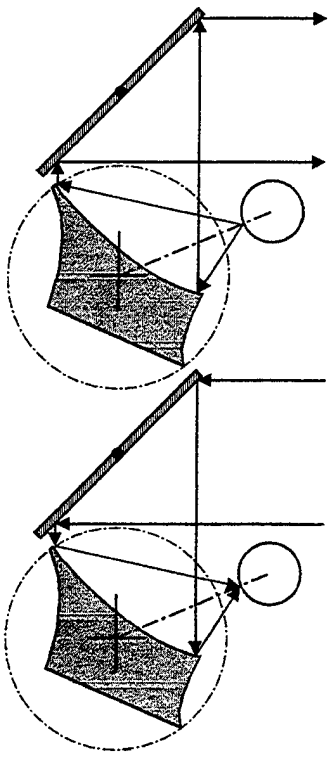

Fig.4. Two synchronously operating antennas provide duplex operation.

3.0 Experimental Results.

Azimuth beam patterns corresponding to four randomly selected drum positions for both upper and lower antennas are shown in Fig.5, left. Misalignment between the upper and lower antenna beams is smaller than 0.25 deg. Elevation plane beam patterns (Fig.5 right) are obtained with 3-deg. parabolic reflectors. Elevation plane beam patterns shown in Fig.6, are obtained with 5-deg and 8-deg parabolic reflectors, left and right respectively. All elevation patterns were taken when the planar reflector was set at 45 deg above the horizontal plane.

Azimuth beam patterns for two distinct polarizations are shown in Fig.7. The peak positions for vertical and horizontal polarizations differ by 0.3 degrees only. The fact that the beam position is insensitive to polarization is a result of the circular symmetry of the feeding rod and grating's holes. It also provides the antenna with the capability of operating with circularly polarized beams.

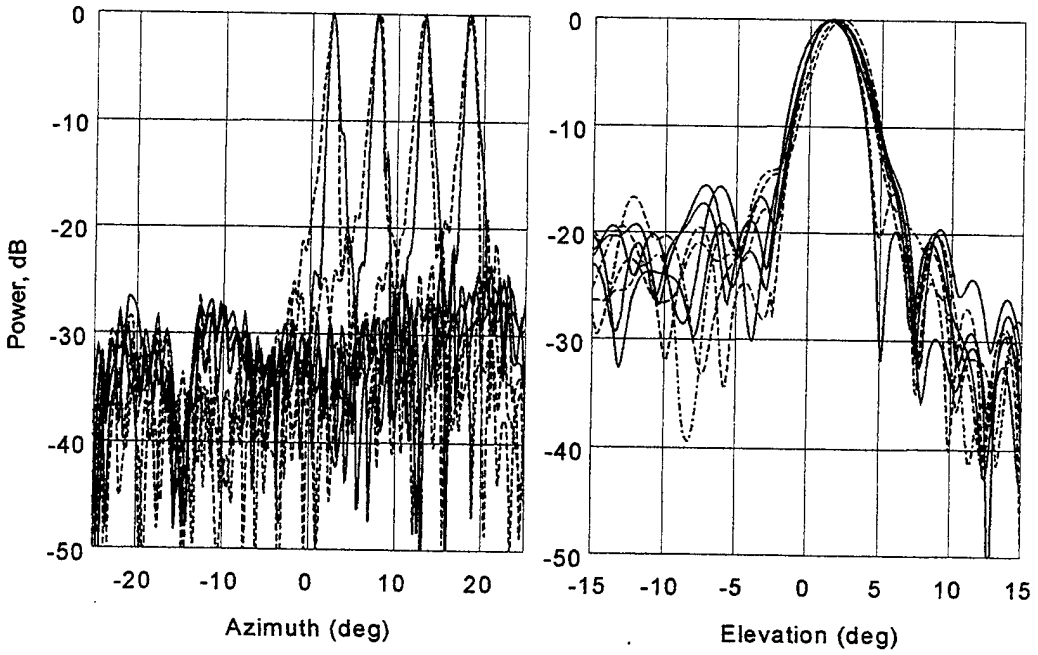

Fig.5. Beam patterns for the upper and the lower antennas at four randomly selected drum positions, produced using 3-deg reflectors.

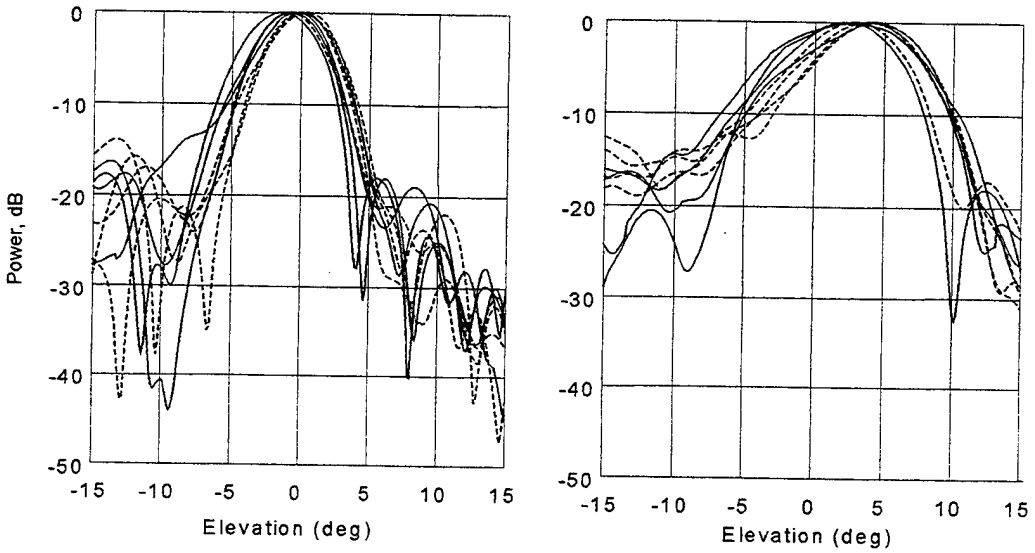

Fig.6. Elevation beam patterns for the upper and the lower antennas at four randomly selected drum positions, produced using 5-deg and 8-deg reflectors.

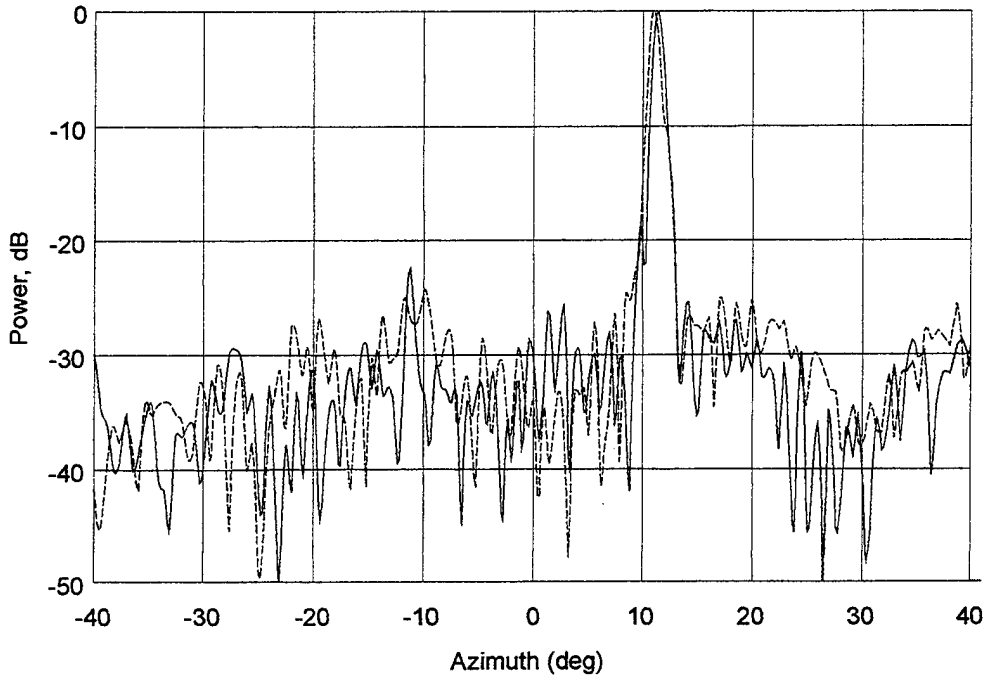

Fig.7. Azimuth beam patterns for two distinctly polarized beams: vertically polarized (solid line), horizontally polarized (dashed line).

Typical dependencies of the main lobe angle and VSWR on the frequency are shown in Fig.8.

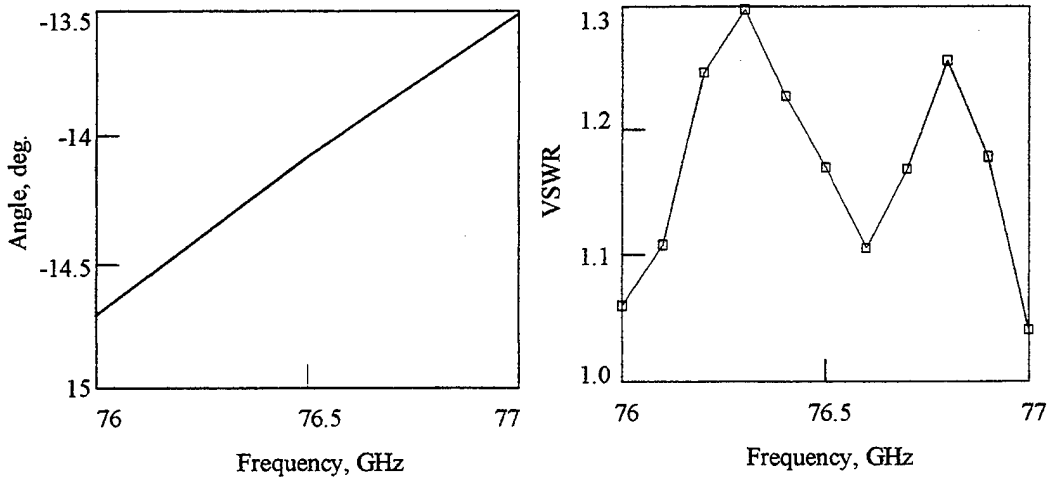

Fig.8. Radiation angle and VSWR as functions of frequency.

The radiation angle in the azimuth plane, as a function of the drum position, is shown in Fig.9. This function represents a straight line. Thus, a uniform spin of the drum also provides beam scan that is linear in time.

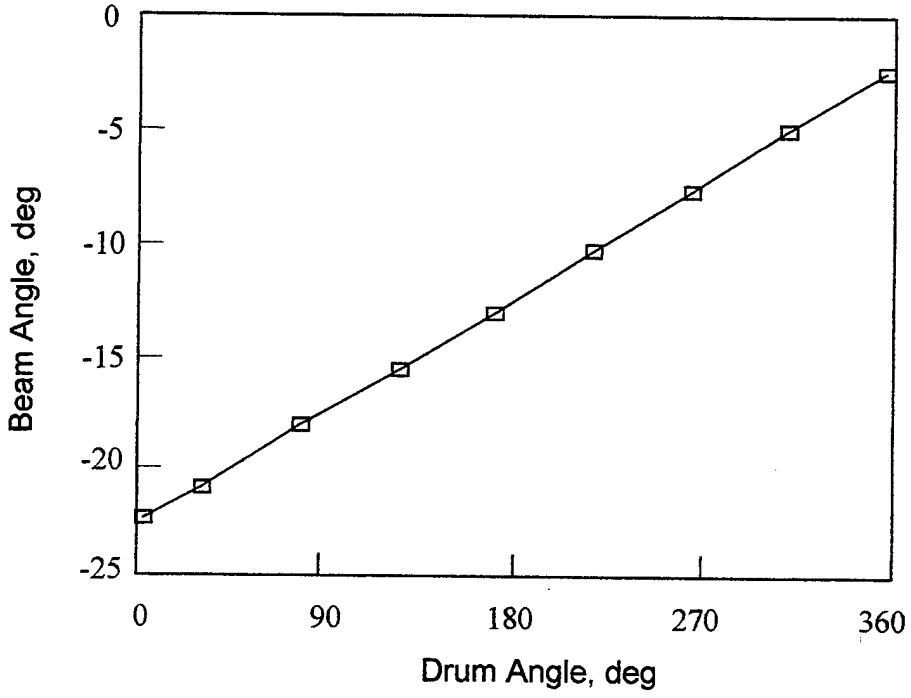

Fig.9. Azimuth main lobe direction vs. angle drum position.

4.0 Conclusion

The new antenna was successfully tested as a duplex imaging sensor coupled to a FMCW MMW radar synchronously steering two beams with a random polarization and providing a linear scan. Linear azimuth beam scanning was used for image formation. Elevation beam forming (three different parabolic reflectors) and beam steering (gimbaled planar reflector) were used to optimize radar signals.

LOW SIDELOBE PARTIALLY- OVERLAPPED FEED NETWORK FOR TIME DELAYED SUBARRAYS

Robert J. Mailloux
Sensors Directorate
Air Force Research Laboratory
31 Grenier Street
Hanscom AFB, MA 01731-3010

Abstract: Completely overlapped space fed subarrays have been shown to provide sufficient pattern control to enable (modestly) wide band arrays using time delays at the input to each subarray, and phase shifters at the array face. These configurations have been proposed for space based use, as well as for certain ground based applications that do not have severe volume constraints.

A number of applications for space based and airborne radar require compact, constrained array feed networks. However, until now there have been no appropriate networks that could be used for inserting time delay at the subarray ports without causing high sidelobes. This paper describes one such network that, at the outset, provided far lower sidelobes than the usual contiguous subarrays, but retained several high lobes near the main beam. The developments reported here show a scheme that reduces all sidelobes to levels determined by tolerance errors. An example is presented that synthesizes sidelobes at –40 dB.

1.0 INTRODUCTION

Elements of large arrays are often grouped into subarrays for the purpose of decreasing the array feed complexity or reducing the number of controls There is an increasing need for efficient, high quality subarraying techniques in systems that scan over a limited field of view (LFOV) and also in wide band scanning systems.. In an ideal LFOV system that scans to θ_{max}, using only a single phase shifter per subarray results in significant cost savings since the maximum subarray spacing "D_0" is of the order of ($D_0/\lambda=0.5/\sin\theta_{max}$) and this can be considerably larger than the approximately ($\lambda/2$ spacing used for wide angle scanning arrays. Similarly, wide band scanning systems use phase shifters at each element and time delay units or digital receivers at the subarray level, so again there is a cost savings resulting from the reduction of these devices. In this case the maximum

subarray size is approximately $D_0/\lambda = f_0/(f\sin(\theta_{max})$, where $(f/f_0$ is the fractional bandwidth. In the best practical cases subarray sizes of 80% of these spacings is usually an upper limit, and this is only approached using overlapped subarray techniques.

The fundamental need for technology in this area is to produce high quality subarray techniques that allow low sidelobe patterns to be formed and scanned, and that have compact volume.

The most compact subarraying arrangement for large subarrays is the use of contiguous, uniformly illuminated, in phase subarrays fed by constrained corporate power dividers as the basic element of large arrays. This kind of subarray is replicated across the large array. The difficulty with arrays so constructed is that they have many large grating lobes, and this limits their use in LFOV systems as well as in wide-band true- time delay scanning.

A number of useful compact (constrained) networks have been developed for forming overlapped subarrays. These networks are described in texts and survey references[1,2], and comprise a significant body of work. These constrained overlapped networks are primarily applicable to relatively smaller subarrays (of 10 elements or less) because the network complexity increases with subarray size. In addition they seem to have sidelobes with lower limit on the order of –20 dB.

Previous short communications [3,4] presented a new technique for forming large partially overlapped subarrays within large arrays. These included examples from both the LFOV and wide band applications. The subarrays are formed with fully constrained networks consisting of Butler matrices, Rotman lenses or other orthogonal beamformers, and simple power combining networks. The technique is an alternative to the well known space fed fully overlapped subarraying networks that, despite their excellent pattern control, are often not applicable to vehicle mounted ground, air, and space applications that require a large antenna with small volume. The present technique addresses a long-standing deficiency in array architecture, the ability to form large subarrays using constrained networks while maintaining excellent pattern characteristics. This paper presents the theoretical basis for the technique, but more importantly develops methods of sidelobe control that make this an approach that can produce patterns with sidelobes at the –40dB level. Examples are given for the wide band subarray case, although the results are equally applicable to the LFOV case.

Figure 1a shows the pattern an array of contiguous uniformly illuminated subarrays. An amplitude taper is used at the subarray input terminals, so that the

basic array factor is a 40 dB Taylor pattern. In this example, the elements are spaced one half wavelength.The array is scanned to 45 degrees and consists of sixteen subarrays, each 16 wavelengths in extent, and with 32 elements per subarray. There are phase shifters at each element and one time delay per subarray. The frequency is 1.03 times the center frequency, signifying the upper edge of a 6% bandwidth system. The center frequency case is not shown since it has only small grating lobes due to the quantized amplitude taper, and is otherwise the same as the 40 dB Taylor pattern. Notice that there is a significant spectrum of grating lobes at levels that would be intolerable for some systems. For comparison, Figure 1b shows initial results of the technique presented in references 3 and 4, and demonstrates significant suppression of the grating lobes that were evident in the contiguous subarray case.

The technique used to produce these results, as depicted in Figure 2, uses constrained feed networks as sections of a larger array. Although the sketch shows only three sections, the array may have numerous sections. These sections contain overlapped subarrays, made by conventional technology that has been understood for many years. The new concept partially overlaps the output of these sections by first producing more subarrays than needed, discarding some, and combining the remaining subarrays in such a way as to make use of only the best of the available ones to produce well controlled, low sidelobe patterns. In addition, it is shown in this paper that the subarrays can be further modified for sidelobe improvement, even within the subarray pattern passband.

2.0 PARTIALLY OVERLAPPED SECTIONS OF OVERLAPPED SUBARRAYS

The basic component of this technology is called a "section", which is an overlapped subarray network. The section is a self-contained dual transform system as described in several texts, and shown schematically in Figure 2. This means that two focusing systems (one much larger than the other) are used back to back. In this case, we are only concerned with systems that can replace corporate fed array elements in an array architecture, so it will be assumed that the larger focusing system is a multiple beam lens, like a Rotman or other lens implemented in parallel plate or microstrip or stripline (or optical fiber). This lens has N output terminals and M input terminals (with $M<<N$). In normal use the N output terminals would be connected to antenna elements, and a signal applied to one of the input terminals would result in a progressive phase shift across the elements. Other inputs have other rates of phase progression, corresponding to radiating beams at different directions. Exciting this multiple beam lens with a second, smaller focussing system, which could be a Butler matrix, another lens, or even a

digital Fourier transform, causes each input to the smaller network to produce a sinc-like distribution (or subarray) across all N output terminals. Each of these overlapped distributions radiates with a pulse shaped radiation pattern that performs the required grating lobe suppression. If the array were reasonably small, only one such section might be needed, and then such a system could provide good pattern control.

If the array is large enough to require more subarrays, the existing approach is to build a larger aperture, still excited by a single feed, but with more multiple beam ports. This requires more depth and volume, and may not be an acceptable solution for systems with volume constraints..

We have investigated two schemes to overcome this difficulty. The first [3] is to simply abut other overlapped subarray networks, without overlapping the abutting networks in any way. This does provide a solution, a relatively simple one that is physically compact, but has a wide region of sidelobes at approximately the –20 dB level. To overcome this deficiency while maintaining low sidelobes, the present technique [3,4] developed a methodology for partially overlapping sections. This scheme is applicable to large arrays consisting of many subarrays and several or many sections.

Figure 2 illustrates several aspects of this subarraying feed concept. Three subarraying sections are depicted, and the output terminals of the sections are combined in the manner shown. Each section is a dual transform network that forms the overlapped distributions shown aside of that section. In this example each section has 4 subarray illuminations (M=4). Notice that the edge subarray illuminations are truncated, while the two center subarray illuminations of each section have the central region and at least one sidelobe of the amplitude distribution. Although not shown, the associated subarray patterns of the central subarrays are a far better approximation of the pulse shaped ideal pattern. Implementation of this technique proceeds as indicated of the figure, where dotted, dashed and solid lines show the subarrays formed by the left, center and right sections. The combined illumination therefore uses only the best of the subarrays, to produce the best grating lobe suppression. The addition network is clearly lossy, with approximately 3 dB loss in the hybrid power divider/combiners. For this reason the concept is primarily useful after amplification on receive and before amplification on transmit. This is not seen as a significant limitation, because most such corporate feed approaches include enough loss in feed and phase shifter and /or time delay devices, that the use of active circuitry at the element is often necessary.

This description has presented the basic technique, and suggests its potential for good pattern control. This configuration however, does not meet the standard of low to very low sidelobes, and this paper addresses means to improve the performance.

2.1 Analysis

Each "section" of this array is a conventional overlapped subarray beamformer using two transform networks in cascade. The mathematics of basic overlapped subarray techniques is well established, but some of the analysis needs to be repeated here in order to explain the means of sidelobe reduction. Throughout this paper it is assumed that the larger beamformer with M input terminals and N output terminals, with N>>M, is a constrained lens of focal length F, as sketched in Figure 3, with true time delay (possibly a Rotman or Archer lens). It produces sets of progressive time delayed signals at its output which radiate as multiple beams with beam peak locations independent of frequency. The smaller MxM network could be a Butler matrix (orthogonal beam network), which produces sets of signals with progressively related phase shift at its output ports, or a true time delay constrained lens (again possibly a Rotman or Archer lens), or this MxM beamformer could be replaced by a digital beamformer that replaces either of the two types of feeds. In conventional systems the pattern performance does not depend strongly upon this choice of phase shift or time delay beamformer. Instead there are bandwidth and circuit constraints. However, in this application with partially overlapped networks, there is a significant advantage to using a true time delay beamformer for the first network.

For generality, assume the MxM multiple beam network can be either an orthogonal beam network (K=1) or a true time delay lens ($K=\lambda_0/\lambda$). Each subarray input port "m" is fed by a signal J_m which produces a series of signals I_{im} given by:

$$I_{im} = \frac{1}{(M)^{1/2}} J_m e^{-j2\pi i(m/M)K} \qquad (1)$$

Also assume that each of these signals I_{im} can be multiplied by some weighting w_i .These signals radiate from the lens feed toward the main aperture to produce the distribution below (omitting normalizing constants):

$$A_{nm} = \sum_{i=-(M-1)/2}^{(M-1)/2} w_i I_{im} e^{+j2\pi i(d_y/\lambda)\sin\phi_n} \qquad (2)$$

The angle ϕ_n, measured as shown in the figure, relates to the focal length F and the element index "n" - (N-1)/2 ≤ n ≤ (N-1)/2 as:

$$\sin\phi_n = n\, d_L/F \tag{3}$$

The expression for $A_{n\,m}$ has peak values equally spaced across the lens back face with the separation distance D, which is frequency dependent for the orthogonal matrix fed antenna, but a constant separation for the time delay feed:

$$D = \frac{F}{M}\left(\frac{\lambda}{d_y}\right)K = D_0\left(\frac{\lambda}{\lambda_0}\right)K \tag{4}$$

where the parameter D_0 is introduced as a frequency independent parameter. Since M such spacings span the lens face, then $D_0M=d_LN$. With these substitutions, and again omitting normalizing constants, the expression for A_{mn} becomes:

$$A_{mn} = J_m \sum_{i=-(M-1)/2}^{(M-1)/2} w_i\, e^{j2\pi i\left(\frac{n}{N}\frac{\lambda_0}{\lambda} - \frac{m}{M}K\right)} \tag{5}$$

In the most basic configuration, the w_i are all unity. This summation can then be done in closed form. Each subarray input port 'm', fed by a signal J_m,thus produces a series of signals A_{mn} at the output of the MXN beamformer.

$$A_{mn} = J_m \frac{\sin M\pi\left[\left(\frac{n}{N}\frac{\lambda_0}{\lambda} - \frac{m}{M}K\right)\right]}{M\sin\pi\left[\frac{n}{N}\frac{\lambda_0}{\lambda} - \frac{m}{M}K\right]} \tag{6}$$

This expression shows the overlapped sinc-like aperture distribution that radiates to form a flat subarray pattern for any given M'th subarray and shows that for the orthogonal fed system (K=1) the peaks of the distribution move as a function of frequency. For the time delayed feed however, the distribution is not orthogonal, and the location of the peaks of these distributions are fixed as a function of frequency. The whole distribution widens at the low frequency and narrows at a high frequency. Several of these amplitude distributions are plotted in the figure 4, for w_i =1, and for a particular case of M=8, N=256. For reference, these

diatributions correspond to numbered subarrays 1,2,3 and 4 of the 8 subarrays within each section. These produce in-phase sinc-like distributions across the aperture. To scan the subarray pattern to some angle given by $u_0=\sin\theta_0$ requires phase shifters at the aperture. This multiplies the aperture coefficients A_{mn} by $\exp(-j2\pi\, nu_0 d_L/\lambda_0)$. The (normalized) far field radiated from this distribution (with arbitrary w_i) is given:

$$f_m(u) = f^e(u)\, J_m \sum_{i=-(M-1)/2}^{(M-1)/2} \quad w_i e^{-j2\pi\frac{m}{M}Ki} \frac{\sin\left[(N\pi d_L)\left(\frac{u}{\lambda}-\frac{u_0}{\lambda_0}-\frac{i}{Nd_L}\right)\right]}{N\sin\left[(\pi d_L)\left(\frac{u}{\lambda}-\frac{u_0}{\lambda_0}-\frac{i}{Nd_L}\right)\right]} \qquad (7)$$

Where the element pattern $f_e(u)$ is assumed constant throughout the array. These subarrays are all pulse like, but not all are equally good patterns. Figure 5 shows the four subarray patterns corresponding to the distributions of figure 4, with $w_i=1$. The subarrays of this group nearer the center of the section have lower sidelobes, smaller ripples within the pass band, and overall better quality for use in arraying. The subarrays near the edge of the section are more distorted, since they are more severely truncated.

The array pattern is the scalar product of the vector of complex subarray excitations with elements $J_m=|J_m|\exp(-j\pi u_0 m(D_0/\lambda-D_0/\lambda_0)$, and the vector of subarray patterns. Note that this includes phase correction to remove the phase shift that is in series with the time delay.

$$F(u) = (J \bullet f) \qquad (8)$$

This arraying process sums subarrays that are separated by the distance D, and so the array factor would have grating lobes at the points $u_q = u_0 + q(\lambda/D)$, and thus are spaced 0.0625 apart in u-space at center frequency. These should be suppressed by the subarray patterns, and indeed they are for the conventional fully space fed subarray systems. However. the array pattern of Figure 6 shows the expected 40 dB sidelobes near the main beam, but has two grating lobes of height –23 dB at about 0.03 (in u-space) from the main beam . Arraying those subarrays in the manner chosen clearly produces good sidelobe suppression outside of the subarray pattern bandpass region, although not perfect because the subarrays themselves have significant wide angle sidelobes due to truncation of the sinc-like distributions. In addition, there are the –23dB sidelobes that appear within the subarray pulse region. These near sidelobes are not due to the grating lobes of the

basic subarray distance D, but rather are a direct result of the new partial overlapped technique. They arise because the subarrays themselves occur in groups of M/2 (four in this case).

Figure 7 compares two subarray patterns (3 and 4), to emphasize their slight amplitude differences. The subarray pattern phase (not shown), for these two subarrays also has different ripples about the phase center. These amplitude and phase differences mean that the set of subarrays 3,4,5,and 6 form a group that is repeated by adjacent sections, and so determines a periodicity of D/4. The resulting sidelobes (grating lobes) are not large, and as the array is scanned they vary from the –15 to –20 dB level. However, they can only be reduced further by making all the subarray patterns identical (so that each group is identical to every other), and the only periodicity is the subarray spacing D.

2.2 Control of Far Sidelobes by "Tapering" the Output Amplitudes

Far sidelobes are directly due to the truncation of the subarray pattern illumination. The partial overlapped system minimizes these effects by not using the most severely truncated edge subarrays, but even the central subarray group suffers some truncation. One way to reduce these sidelobes further, is to attenuate the output ports of each "section" using a symmetrical amplitude taper that attenuates primarily those signals near the two edges of each section. Since only the central (four) of these subarrays is used in each 8-subarray section , the major change to these subarrays is that the sidelobe region of the amplitude distribution is forced to zero at the edges. This technique , has been shown to lead to lowered far-sidelobes[4] but to no improvement in the sidelobes that are within the subarray pattern pass-band.

2.3 Control of the Near Sidelobes Using the Method of Alternating Projection

The sidelobes within the subarray pass-band are caused by the fact that the partial overlapping chooses the central M/2 (four) subarrays from each section, and then repeats this (super-subarray) grouping across the large array. These would disappear if all the subarrays were identical. The subarrays within each section are unequal because of their proximity to the edges of the section, but yet the section output port tapering that lowered the far sidelobes does not help these near sidelobes appreciably. The reason for this is that the output port tapering is symmetrical, but within each section the subarray locations are off center, so each subarray has an asymmetry in amplitude and phase center produced by the tapering. Even though truncation is eliminated by the tapering, the asymmetry leads to a change in phase center and phase ripple within the subarray passband.

Instead of tapering the output of each section, there is a second way to make the four central subarrays so similar that the super-subarray group becomes four nearly identical subarrays. This is accomplished by inserting a special set of in-phase weights between the two transform networks. The logic for employing this procedure is as follows. With uniform illumination at the feed, the feed array radiates to the main lens face in a sinc-like distribution (as shown schematically in Figure 8) . Altering the weights with, for example, a tapered distribution, would produce a lower sidelobe illumination at the main lens, and so perhaps a distribution that would not be so seriously impaired by truncation. Figure 8 illustrates the formation of a subarray illumination using a low sidelobe feed.

Since it is desired that the subarray illuminations not be truncated, the ones nearest to the end of the section should end with zero amplitude at the edge. In a section with 8 subarrays discarding the outer two on each side leaves subarrays 3 and 6 as the outermost ones, and their centers are 2.5 D_0 (or 80 elements) from each side for 32 element subarrays. So, one would formulate a new subarray synthesis situation of produce a subarray illumination that radiates with a flat top, and is centered on a lens 160 elements wide, and then achieve the goal of having no truncation at the section edges. The procedure chosen to effect this synthesis is a variation of the technique called alternating vector space projections.

The method of alternating projections (also called the intersection approach)as it is applied to antenna pattern synthesis, depends on the finite Fourier Transform relationship between an array illumination and its far field pattern.

The "projection" of a point (function) in one vector space onto another vector space, is a point (function) in the second space with least error subject to some chosen norm. For example, for an N-element array, the Fourier series synthesized array pattern is the projection of this set of all possible N-element array patterns onto the set of (in this case) one desired pattern, since its mean square error is minimum.

The procedure, as outlined schematically in Figure 9, consists of iterating a sequence of "projections" between two vector spaces (sets of functions). In this case , one set (set A), is the set of all subarray patterns that can be radiated by the weights w_i acting as feed for the modified) lens. The second set of functions, (set B), is the set defined by all the patterns that lie between the masks, also shown on that figure as between M_U and M_L. In this case the projection of set A onto B is obtained by producing a new pattern f_0' such that every point of f_0 , whose magnitude lies outside of the mask , is moved to the nearest mask limit M_U or

M_L. This is the nearest pattern to the set B, and the projection of the pattern in set A onto set B. So, values of the subarray pattern amplitude $>M_U$ are made equal to M_U, values $<M_L$ are made equal to M_L, and points within the bands are unchanged. Figure 9 illustrates this operation, with the resulting projection being the solid curve in the upper right of the figure.

For convenience we assume the MxM matrix has one beam that radiates broadside (call it m=0). This beam has signals I_1=1 (normalized) for all i. Assume that weights w_i now multiply the signals Ii. These radiate to the lens back face, but in order to force the distribution to reside only within the central 160 elements, we choose to use a smaller lens in order to avoid illuminating the edges of the larger lens with off axis beams. In keeping with the discussion in the last paragraph, we choose to assume the lens has only NN elements (NN=160 in this case) instead of the 256 elements in the real lens. With the signals $I_i w_i$ radiating from the feed, the illumination on the truncated (NN) lens is given by equation 5 directly, but equation 7 is altered below to give the radiated pattern for the smaller lens. This pattern is re-written for the same feed and a lens truncated to the NN elements wide instead of N.

$$f_m(u) = f^e(u)\, J_m \sum_{i=-(M-1)/2}^{(M-1)/2} W_i e^{-j2\pi \frac{m}{M} Ki} \frac{\sin\left[(NN\pi d_L)\left(\frac{u}{\lambda} - \frac{i}{Nd_L}\right)\right]}{NN \sin\left[(\pi d_L)\left(\frac{u}{\lambda} - \frac{i}{Nd_L}\right)\right]} \qquad (9)$$

In this expression, the "N" in the denominator occurs because the lens system itself is unchanged because the lens geometry (F/L) is unchanged, while the summation over lens elements is truncated at NN. This set of patterns is one vector space, and an example shown in the upper left of Figure 9.

Next this radiated subarray pattern (top left) is projected onto the desired mask, having an upper limit M_U and a lower limit M_L. This projection is sketched in the top right of the figure. The inverse finite Fourier transform (Fourier series) of this function yields its projection onto the set of array illuminations An'. These An' may not be achievable, given the only 8 possible values of the w_i coefficients, so they are projected to the front of the MxM network using the factor

$$w_i = \frac{1}{P} \sum_{-(NN-1)/2}^{(NN-1)/2} A_n' e^{-j2\pi np/P} f_0'(u_p) \qquad (10)$$

Having w_i, equation 7 can again be used to compute the subarray pattern. This completes one cycle of the iteration. Figure 10 shows the computed subarray patterns for four specific iterations, starting at iteration #0, the initial pattern with all weights unity. In this sequence, the outer mask is the upper mask function shown, and chosen to be the width 0.0625 in u-space, and to have near sidelobes at approximately the -30 dB is level, and decaying following a $1/(|u-u_0|)$ asymptote . Convergence is evident from the examples shown in figure 10.

In this case, at the end of the synthesis procedure, the final weights were $w_1=w_8=0.2911$; $w_2=w_7=.7529$; $w_3=w_6=1.0058$; $w_4=w_5=.9817$.

Figure 11 shows the amplitude patterns of subarrays 3 and 4, (or 6 and 5), computed directly from the final weights given above. Clearly the procedure has made the subarrays nearly identical down to the -32 dB level. The subarrays also have lower sidelobes, because of the reduced truncation.

Figure 12 shows the broadside array patterns of an array of four sections, each with eight subarrays, but using the central four and choosing the synthesized weights. This pattern shows the advantage of the subarray synthesis procedure, demonstrating sidelobes at the –40 dB design level, and all residual grating lobes below –45 dB. Notice that these remaining lobes are still spaced about 0.015 apart, indicating that they arise from the periodicity D/4.

Figure 13 compares the aperture illuminations using the initial (uniform) weights (wi=1) and the synthesized weights for two adjacent subarrays of the central four. The primary constraint imposed by the synthesizing procedure was to assure that this illumination was little effected by truncation. Indeed, the figure to the right has far smaller ripples and so the radiation patterns of the subarray at left (dotted) is very similar to the one at right (solid).

Although no distinction has been made thus far concerning the use of an orthogonal beamformer (Butler Matrix) or a true time delay beamformer (Rotman Lens) or their analog or digital equivalents, for the MxM beamformer, there is in fact a major difference in the frequency response. Figure 14 shows that the broadside radiation pattern of the network fed by an orthogonal beamformer at frequency f=1.03 f_o. has significant sidelobes at u=0.625/4=0.156 not present at center frequency. Figure 15 illustrates that this problem results from the fact that the chosen feed is an orthogonal beamformer, not a true time delay feed. With the orthogonal beamformer, at center frequency, the subarray amplitude and phase centers are evenly spaced in all of the four sections, and the sections are exactly

four subarrays apart to produce an aperture distribution with periodicity equal to the subarray separation. However, if each section is fed by an orthogonal beamformer, then the cluster of beams that excite each section has its phase center at the physical center of the section. As the frequency increases, these beams get narrower, and the whole cluster gets narrower, with its radiation peaks moving toward the broadside direction. Since each group of four has its phase center at the center of a section, the sketch at bottom shows there is imposed a periodicity of 4 D_0 across the array when the beams move together.

This periodic error is removed when a true time delay lens or digital beamformer is used as beamformer. The beams from these time-delayed networks remain equally spaced on the final aperture, and the 4D periodicity is removed. Figure 16.shows the resulting array patterns at center frequency and at 0.97 and 1.03 times the center frequency. In all cases the large grating lobes are removed, and the sidelobes are in the neighborhood of the design sidelobes except at the high end of the band. These results confirm that it is possible to reduce all sidelobes to very low design levels using the synthesis technique presented here.

6.0 CONCLUSION

Using an alternating projection technique to synthesize network weights, a new subarraying technique that uses constrained network feeds has been shown to enable the insertion of true time delayed signals without resulting in high sidelobes or grating lobes. The technique is expected to find application to arrays with volume restrictions, such as space based or airborne radar.

ACKNOWLEDGEMENT

I am grateful for the support of the Air force Office of Scientific Research, and particularly Dr. Arje Nachman of the Mathematics Directorate for sponsoring this research.

REFERENCES

[1] R. Tang. , "Survey of Time-Delay Steering Techniques," *Phased Array Antennas*, Artech House, Dedham, MA, pp.254-260, 1972

[2] S.P. Skobelev, "Methods of Constructing Optimum Phased Array Antennas for Limited Field of View," *IEEE Antennas and Propagation Magazine*, Vol. 40, No.2, April 1998, pp. 39-50

[3] R. J. Mailloux, "Constrained Feed Technique for Subarrays of Large Phased Arrays," IEEE Electronic Letters, Vol 34, No. 23, pp 2191-2193, 12 November 1998

[4] R.J. Mailloux, "Constrained Feed Techniques for Limited Field of View Scanning or Time Delay Steering," *IEEE AP-S International Symposium Proceedings*, IEEE Conf. Publ, pp. 740-743, 1998

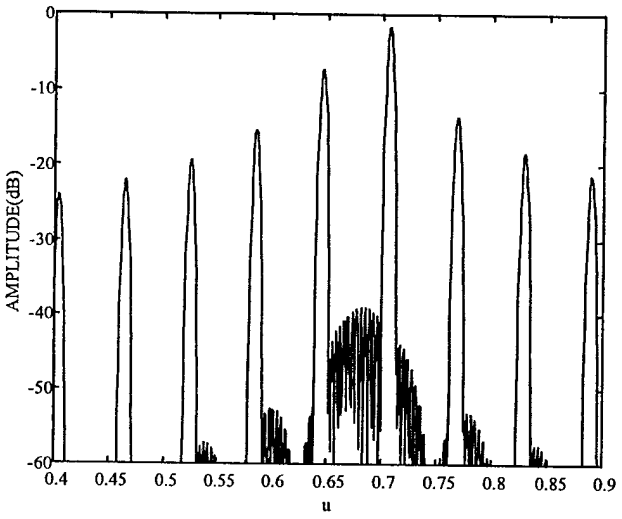

A. Contiguous Subarrays

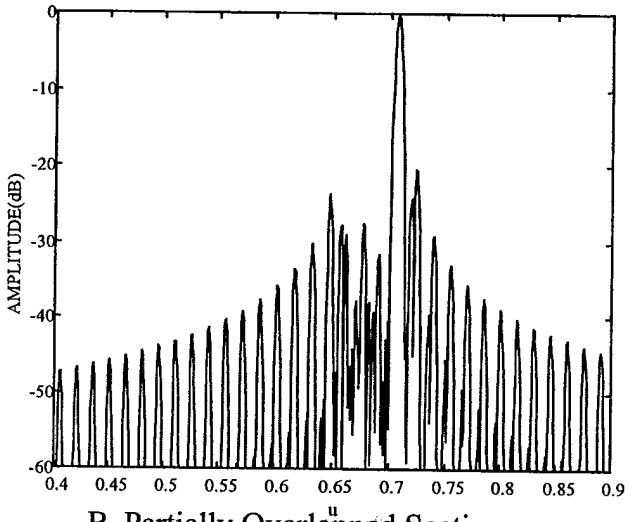

B. Partially Overlapped Sections of Overlapped Subarrays

Radiation Patterns of Contiguous Subarrays and Partially Overlapped Sections of Overlapped Subarrays

16 subarrays, 32 elements each

Figure 1

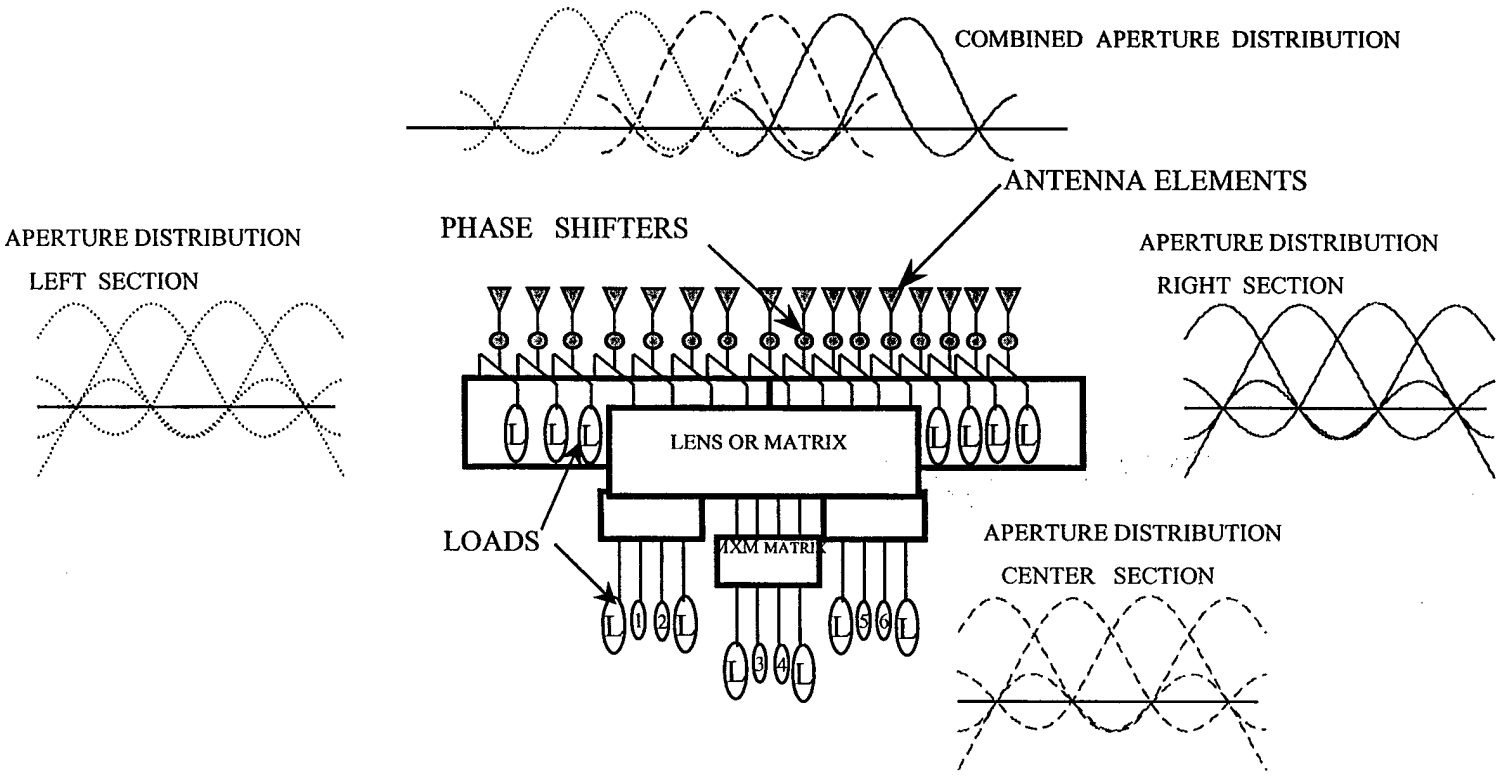

Figure 2. Partially Overlapped Sections of Overlapped Subarrays

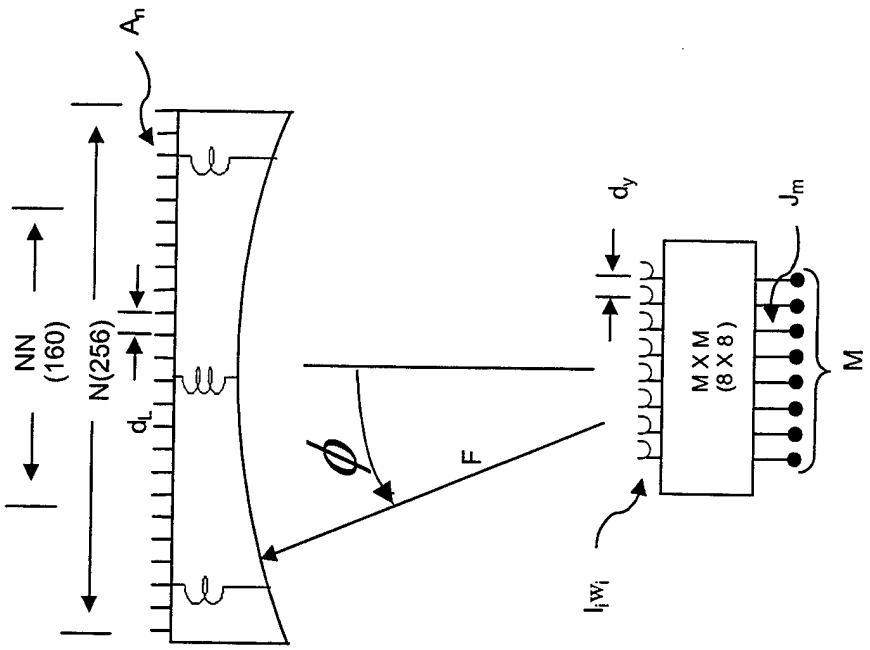

Figure 3

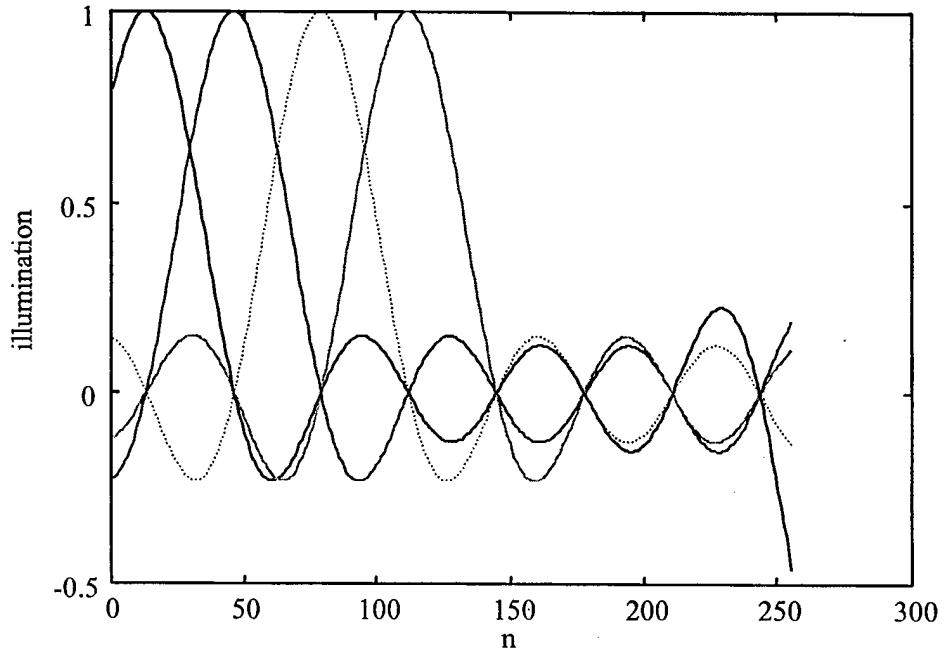

Selected Subarray Illuminations in Section of 8-Subarrays and 256 Elements

Figure 4

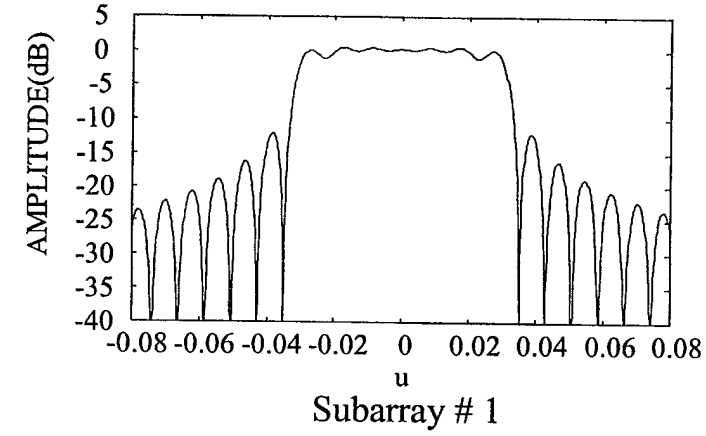

Subarray # 1

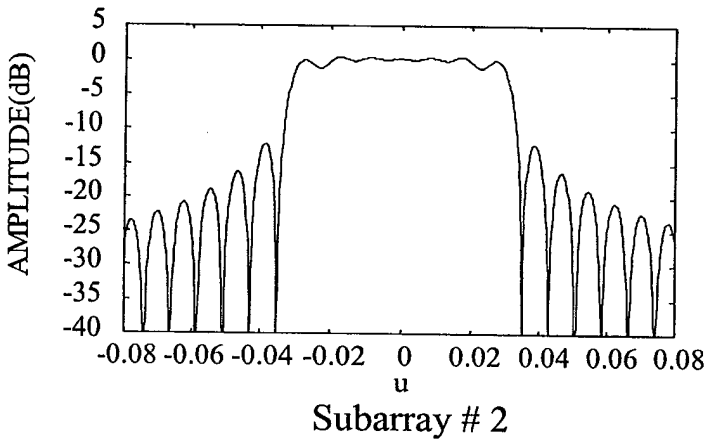

Subarray # 2

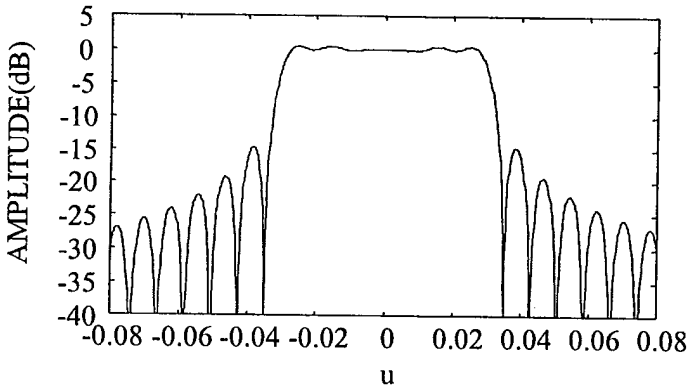

Subarray # 3

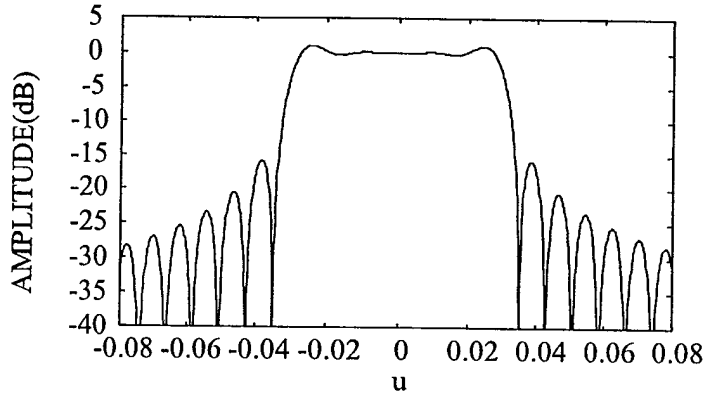

Subarray # 4

Figure 5. Selected Subarray Radiation Patterns for Section of 8 Subarrays

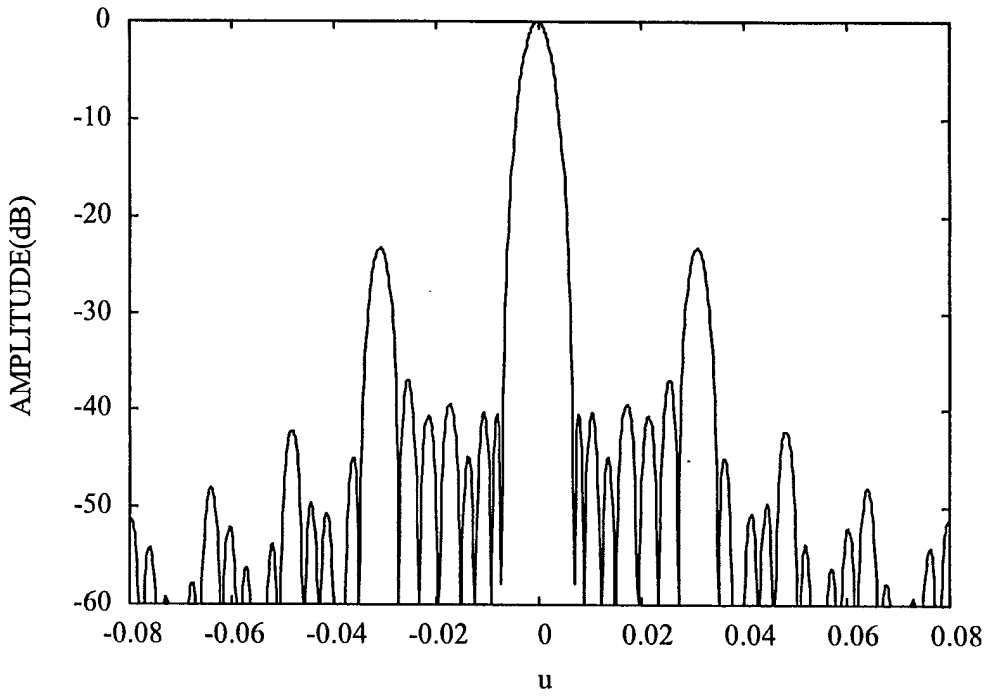

Figure 6. Broadside Radiation Pattern of Array of 4 Partially Overlapped Sections with 16 Subarrays

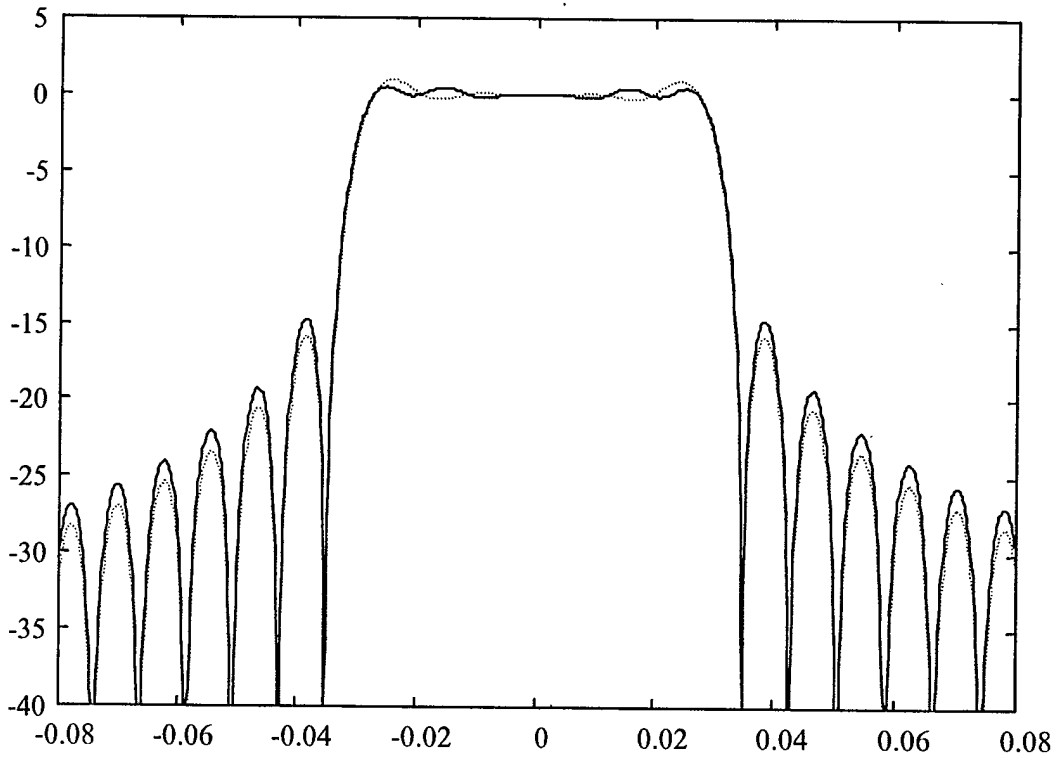

Radiation Patterns of Subarrays 3 and 4 (also 6 and 5)
of Section with 8 - Subarrays

Figure 7

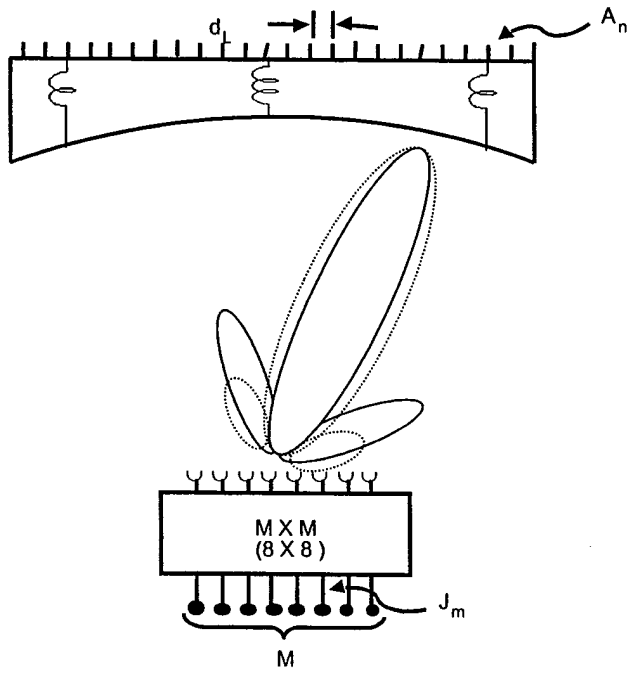

Feed Pattern Sidelobes Determine the Truncation
of Subarray Aperture Illumination

Figure 8

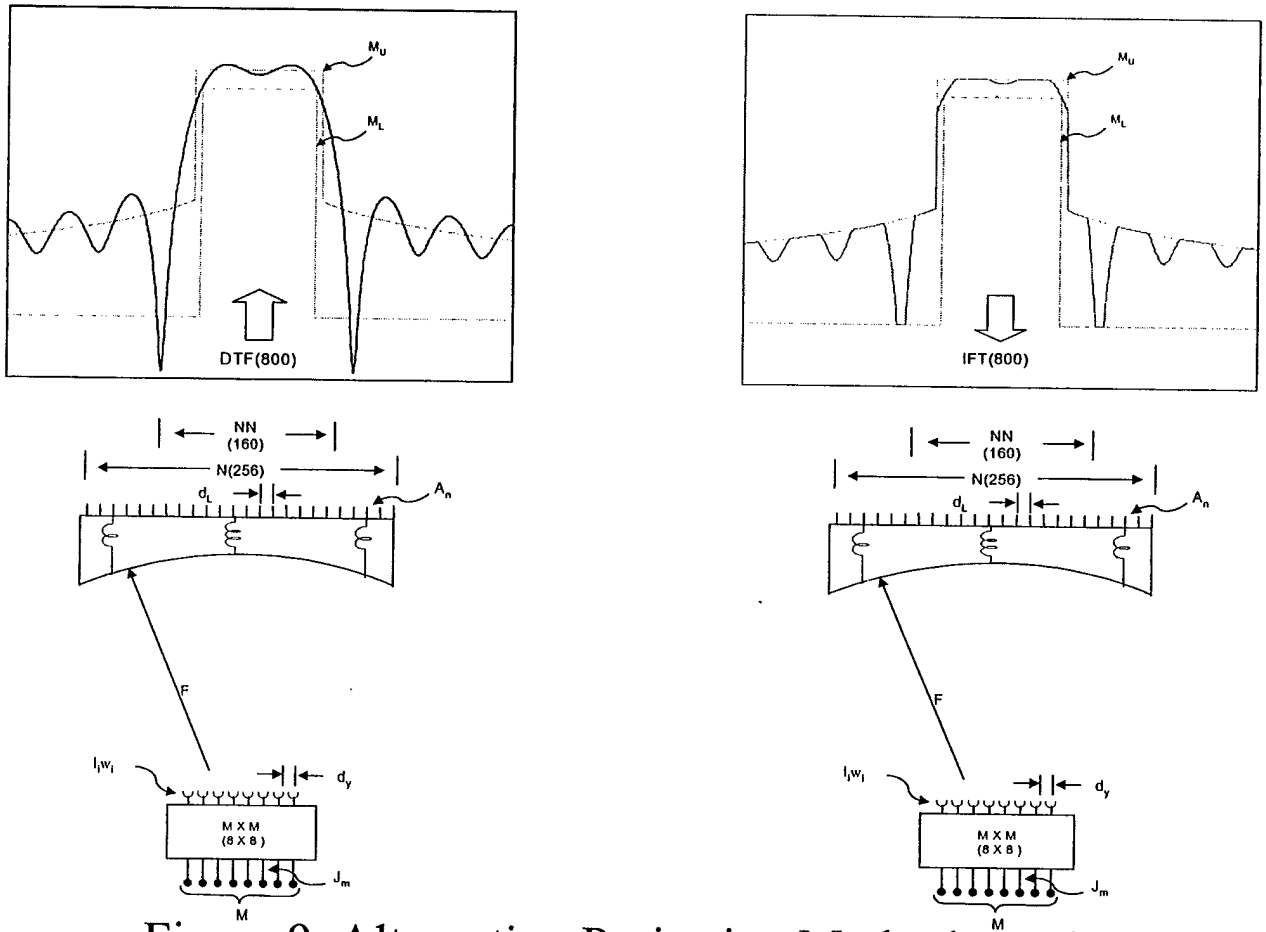

Figure 9. Alternating Projection Method Used to Reduce Subarray Truncation by Iterating Weights w_i

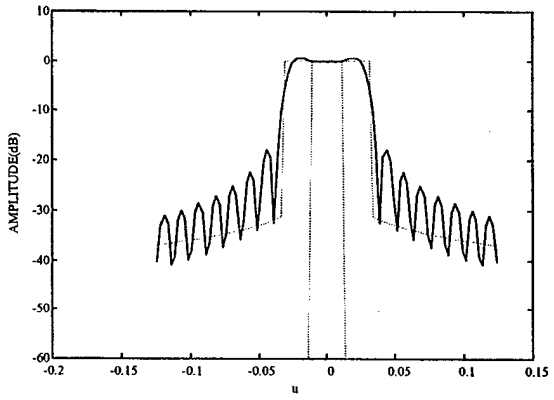

#3

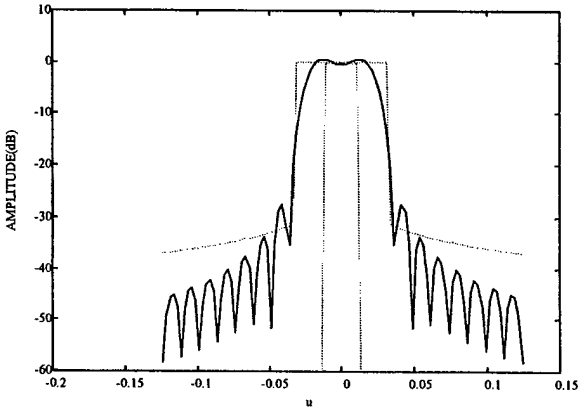

#13

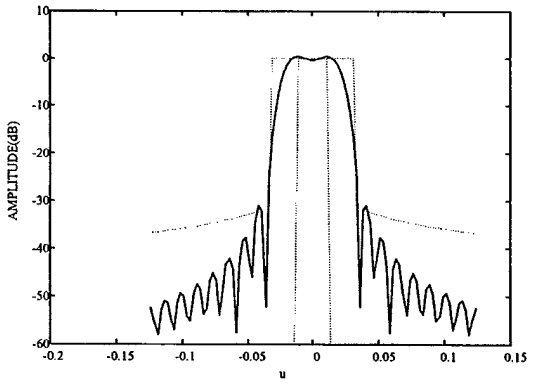

#23

Figure 10

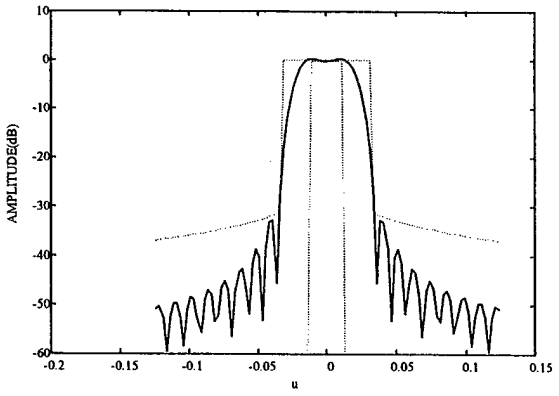

#33

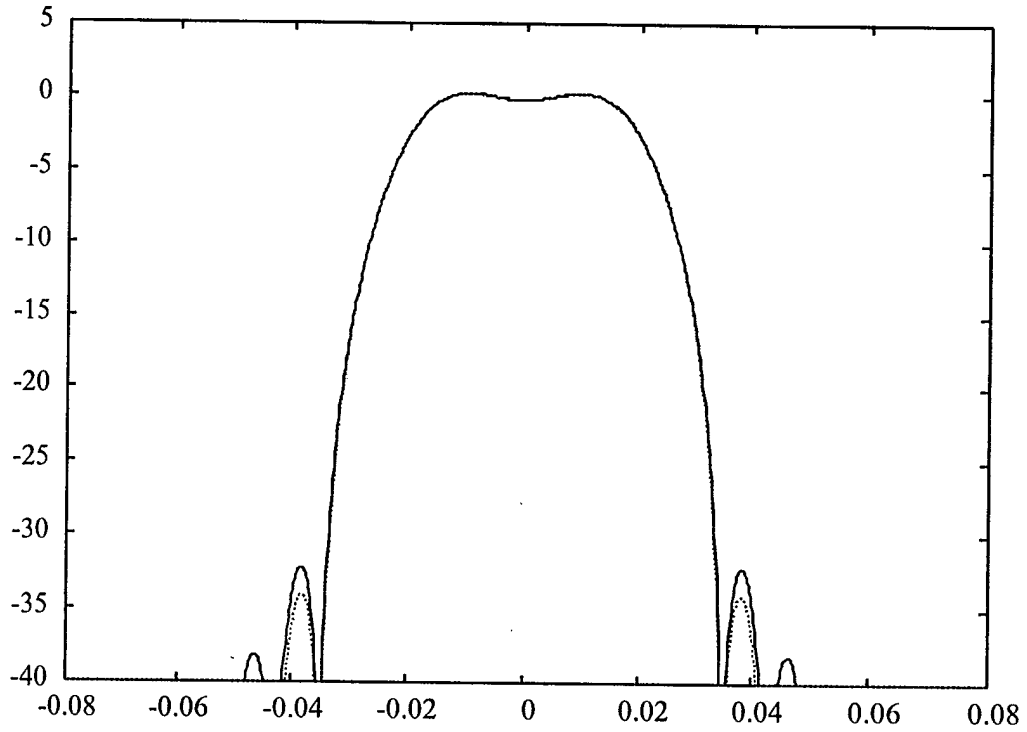

Radiation Patterns of Subarrays 3 and 4 (also 6 and 5)
of Section with 8 - "Optimized" Subarrays
Figure 11

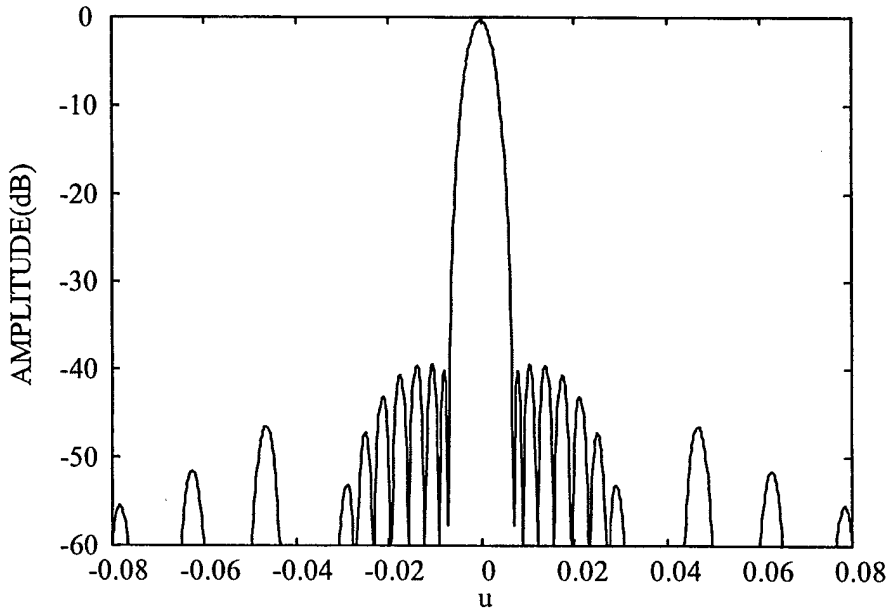

Broadside Radiation Pattern of Array
of 4 "Optimized" Partially Overlapped Sections with 16 Subarrays
Figure 12

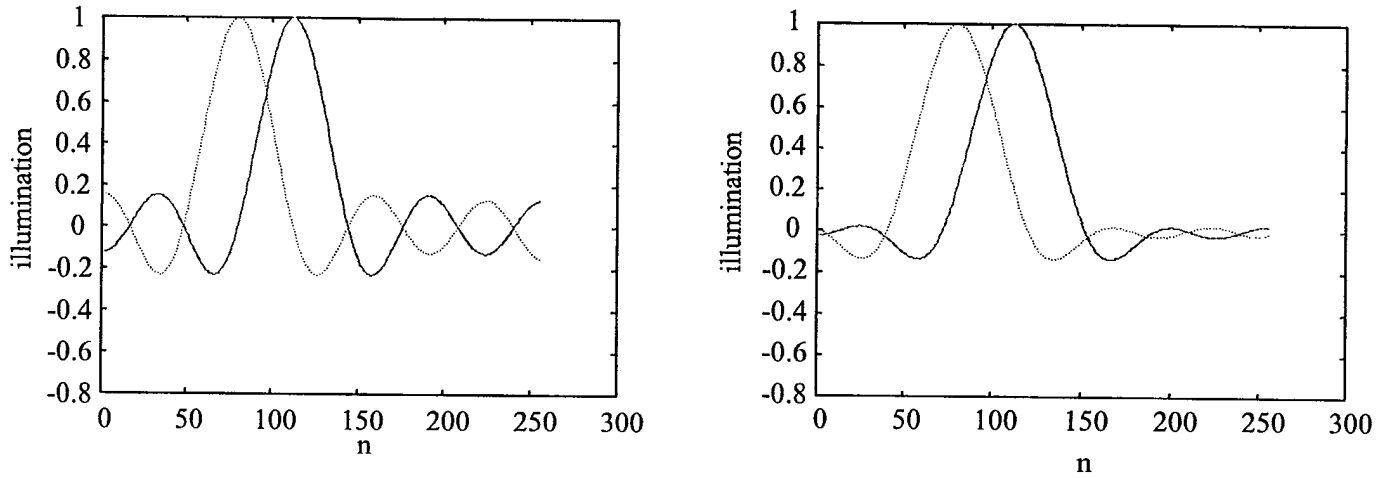

Comparison of Aperture Illuminations
using Initial Weights (w_i) and "Optimized" Weights (w_i)

Figure 13

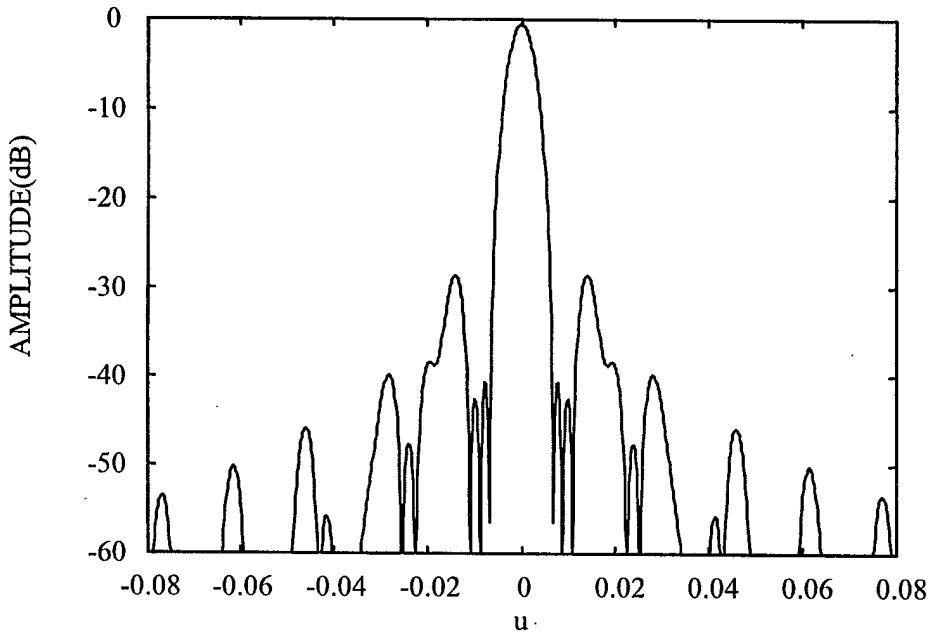

Broadside Radiation Pattern of Array of 4 "Optimized"
Partially Overlapped Sections at $f/f_o = 1.03$.
Using M x M Orthogonal Feed Matrix
Figure 14

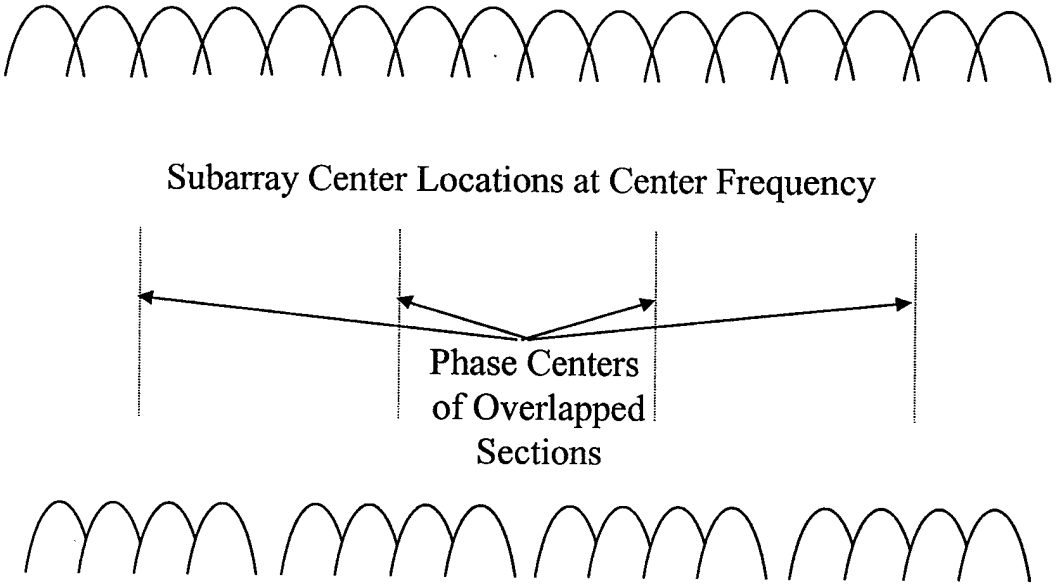

Subarray Clustering for Orthogonal(phase shift)
Feed Matrix

Figure 15

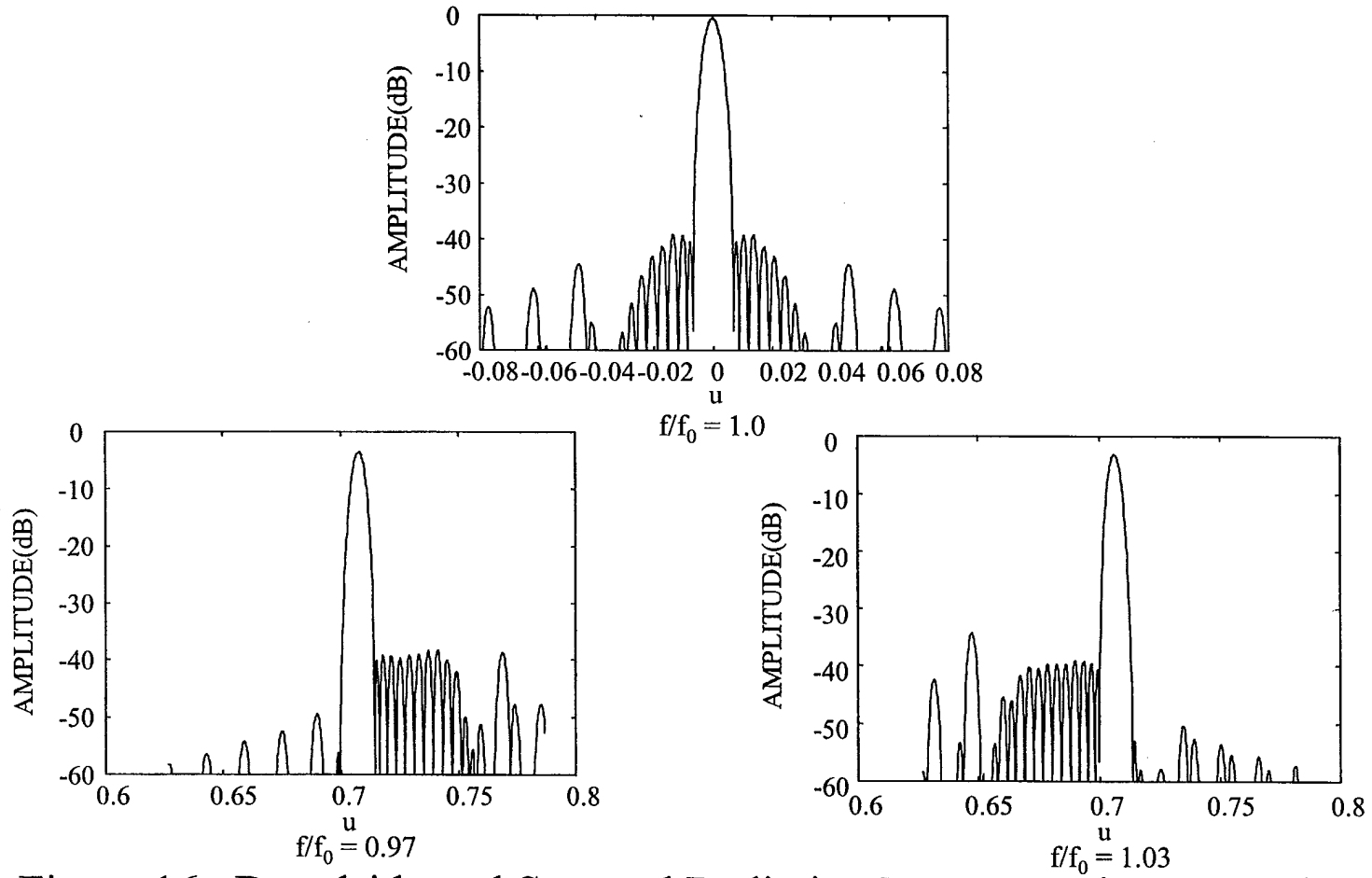

Figure 16. Broadside and Scanned Radiation Patterns Using True Time Delay Lens Feed